TECTONICS, GEOCHEMISTRY AND GEOCHRONOLOGY OF THE LADAKH BATHOLITH, TRANS - HIMALAYA

A THESIS

Submitted in fulfilment of the requirements for the award of the degree of

DOCTOR OF PHILOSOPHY

in

EARTH SCIENCES

By

RAJEEV KUMAR

DEPARTMENT OF EARTH SCIENCES
INDIAN INSTITUTE OF TECHNOLOGY ROORKEE
ROORKEE-247 667 (INDIA)

JANUARY, 2005

INDIAN INSTITUTE OF TECHNOLOGY ROORKEE
ROORKEE

CANDIDATE'S DECLARATION

I hereby certify that the work which is being presented in the thesis entitled **"TECTONICS, GEOCHEMISTRY AND GEOCHRONOLOGY OF THE LADAKH BATHOLITH, TRANS-HIMALAYA"** in fulfillment of the requirement for the award of the Degree of Doctor of Philosophy and submitted in the Department of Earth Sciences, Indian Institute of Technology Roorkee, Roorkee is an authentic record of my own work carried out during the period from July, 1999 to January, 2005 under the supervision of **Dr. Sandeep Singh and Prof. A. K. Jain**

The matter presented in this thesis has not been submitted by me for the award of any other degree of this or any other Institute.

Rajeev Kumar.
(RAJEEV KUMAR)
24/1/05

This is to certify that the above statement made by the candidate is correct to the best of our knowledge.

Sandeep Singh 24/1/2005
AK Jain 24/1/2005

Date: 24/01/2005

Dr. Sandeep Singh
(Assistant Professor)
Department Of Earth Sciences

Dr. A. K. Jain
(Professor)
Department Of Earth Sciences.

The Ph. D. viva voce examination of **Mr. Rajeev Kumar**, Research Scholar, has been held on July 8, 2005.

Sandeep Singh 8th July 2005 | AK Jain 8/7/2005 | V. N. Singh | Anchal Ray

Signature of Supervisor(s) **Signature of H.O.D.** **Signature of External Examiner**

ABSTRACT

The Himalaya is a unique example of young continent to continent collision. The geodynamics of the Himalaya has been described in terms of its large-scale continental convergence along the suture zones. During Mesozoic the Tethyan oceanic crust, attached to the Indian Plate, has subducted beneath the Eurasian Plate and collided against the latter along the Indus Tsangpo Suture Zone (ITSZ) and Shyok Suture Zone (SSZ) during Cenozoic. This collision has caused intense crustal shortening and deformation either along southerly migrating thrusts viz. The Main Central Thrust (MCT), the Main Boundary Thrust (MBT), and the Main Frontal Thrust (MFT) as well as large scale strike slip faults in Tibet.

The area of study incorporates the Trans-Himalayan Batholithic complex lying to the north of the Indus Tsangpo Suture Zone (ITSZ) in the Ladakh district of Indian Territory. The batholithic complex has been variously called as the Kohistan Batholith and Ladakh Batholith in the northwest, the Kailas tonalite and Gangdese pluton in Tibet and the Lohit Batholith in Arunachal Pradesh. The Ladakh Batholith occurs as a WNW-ESE trending linear belt of about 600 km long and 30-80 km wide with about 3 km of exposed thickness and forms a part of the calc-alkaline Andean-type magmatic pluton. Within this batholith, three crucial sections have been selected for lateral and temporal variation in geochemistry and geochronology. The sections are (i) Leh-Khardung La section, (ii) Kharu-Chang La section and the (iii) Lyuma-Hanle section, the first one being the westernmost section and the last being the extreme easternmost section within the batholith with the Kharu-Chang La section in the middle.

The work undertaken in the present thesis aims at the objective of looking into

(a) the lateral petrological and geochemical variations through the three crucial sections mentioned above.

(b) the depth of emplacement of the Ladakh Batholith by using Al content in Hornblende geobarometer.

(c) constraining the age of crystallization of the Ladakh Batholith using Rb-Sr dating technique on Thermal Ionization Mass Spectrometer and

(d) the cooling and exhumation history of the Batholith.by integrating the Rb-Sr biotite ages and the Fission Track apatite and zircon ages.

In the present study, systematic work has been carried out for temporal and lateral variations of petrography and geochemistry, along three sections of the Ladakh Batholith, viz. Leh-Khardung La, Kharu-Chang La and Lyoma-Hanle. For this purpose 53 samples have been selected from these three sections (Leh- Khardung La: 30 samples; Kharu-Chang La: 13 samples and Lyoma-Hanle: 10 samples). The petrographic studies (Chapter 3) clearly indicate three main types of rocks-diorite (16 samples), granodiorite (27 samples) and granite (10 samples). Similar picture has emerged from the Quartz-Alkali Feldspar-Plagioclase (Q-A-P) normative calculation plot of Streicksen (1976). The major oxide plots, in particular the SiO_2 vs (K_2O+Na_2O) plot indicates its sub-alkaline, SiO_2 vs K_2O plot indicates medium to high K- bearing rocks and AFM plot indicates its calc-alkaline character. In the discrimination Rb vs (Y+Nb) and Rb vs (Yb+Ta) plots of Pearce et al. (1984) the batholith falls in the Volcanic Arc Granite (VAG) field. The normalized spiderplots and REE plots show enrichment of LREE-LILE and depletion of HFSE which are characteristic of subduction-related magmatism (Saunders et al., 1980; Holm, 1985). Typical signature of negative Nb anomaly for subduction zone environment (Wood et al., 1979) is also characterized by the spiderplot of the samples from the Ladakh Batholith. Similar character of REE pattern has been reported by Honneger et al. (1982), Dietrich et al. (1983), and Ahmad et al. (1998) from the study of the Ladakh Batholith from different sections.

Based on the Al-content in hornblende geobarometer, the batholith appears to have been crystallized at depth between 14.27 and 7.3 km over a vertical section of around 2 km with diorite indicating lower crustal depth around 14.30 km and granodiorite around 7.35 km. When the crustal depths are plotted against the elevation, a good correlation between crustal depths with elevation has been obtained indicating that the diorites at lower elevation have crystallized first. Also, if the total depth difference is considered, it comes out be~7 km whereas the elevation difference is ~ 2 km. It can be inferred that this body has undergone either magmatic compression or denudation by tectonic removal within this section.

For obtaining the crystallization age as well as biotite cooling ages, Rb-Sr systematics on 21 whole rock and 7 whole rock-biotite pairs from the Ladakh Batholith have been attempted. All $^{87}Rb/^{86}Sr$ and $^{87}Sr/^{86}Sr$ values have been determined in newly-established TIMS Laboratory at IIT Roorkee. The $^{87}Rb/^{86}Sr$ and $^{87}Sr/^{86}Sr$ ratios show a fair amount of spread and make it very difficult to obtain an isochron. But on close observation four points from the Kharu-Chang La section give an isochron age of 61.59±0.05 Ma with initial $^{86}Sr/^{87}Sr$ ratio of 0.70417±0.000006 and MSWD value of 0.92 depicting a good quality fit. Seven biotite fractions separated from these samples analyzed in the same way as the whole rock give a range of ages from 36.71±0.05 to 52.38±0.05 Ma.

Fission track dating of the Ladakh Batholith on 30 apatite and 3 zircon samples from three sections show a good correlation of FT-apatite age with elevation except in Lyoma-Hanle section and provide invaluable data on the exhumation rate of the batholith. The ages range from 9.21 Ma to 25.35 Ma. However, FT zircon ages are 41.73Ma, 43.37 Ma and 31.71 Ma from west to east and show younging towards east. FT zircon and apatite ages from 3 widespread sections through the Ladakh Batholith reveal its exhumation history through low temperature geotherms of 220±25°C and 110±10°C around 43.37±3.66 Ma and 25.35±2.57 Ma, as is evident from the oldest FT zircon and apatite ages. Extremely good correlations

have been established between the elevation and age for FT apatite in two profiles of the Ladakh Batholith and provide a very slow average exhumation rates of 0.11 mm/yr between 25.35 Ma and 9.21 Ma, irrespective of any assumed values for geothermal gradient, annealing temperatures and present-day temperatures. When the Rb-Sr biotite cooling ages FT zircon and FT apatite ages are clubbed together with the available published data of different thermochronometers complete cooling picture of the Ladakh Batholith comes out. It shows the cooling trend from crystallization temperature of about 750^{0}C to 110^{0}C and to present.

Comparison of exhumation history of the continental lithosphere of the UHP Tso Morari terrain in the south, which has subducted to a depth of about 100 km around 53 Ma with the part of the Ladakh Batholith reveals that the later has exhumed as a piggy-back sequence along north-dipping ITSZ. Since its emplacement around 60 Ma till 43 Ma exhumation has been calculated at a rate between 0.55mm/yr in the initial stages to 4.42 mm/yr subsequently. The Ladakh Batholith has crossed 220±25^{0}C geotherm at ~ 43 Ma, as is indicated by average FT zircon age and 110±10^{0}C at around ~25 Ma - the oldest apatite age from the batholith. In comparison to the available FT zircon and apatite ages from any other tectonic units of the Himalaya, the Ladakh Batholith reveals an almost uniform and slow exhumation pattern between ~25 to 9 Ma at an average rate of about 0.11mm/a. Exhumation paths of the Tso Morari and the Ladakh Batholith are almost identical since ~ 53 Ma and older when compared to the exhumation of the Higher Himalayan Crystallines further south.

ACKNOWLEDGEMENTS

This work has been carried out under the supervision of **Dr. Sandeep Singh** and **Prof. A. K. Jain** whose suggestions, advices, ideas and criticisms at all stages of the work, right from the formulation of the problem through field and laboratory works to the completion of the final draft of the thesis have made it possible for me to complete this work. Especially memorable were the months of joint field work together and the intriguing discussion sessions.

I am deeply grateful to **Prof. V. N. Singh, Prof. A. K Awasthi and Prof. B. Parkash,** the present and former Heads of the Department, respectively, for extending all the possible facilities during the course of the research work.

My sincere thanks are to **Prof. Nand Lal**, Department of Earth Sciences, Kururkshetra University, Kurukshetra for introducing and teaching me patiently the intricacies of the Fission Track Dating technique at his coveted laboratory. **Dr. R. C. Patel** needs a special mention for making my stay at Kurukshetra congenial and fruitful with his superb elderly vigil and discussions. Fruitful suggestions are also acknowledged with **Dr. Devender Kumar and Dr. Ashok Thakur.**

I am very much obliged to **Prof RM. Manickavasagam** and **Prof. A. K. Choudhary** for their expert guidance and helpful discussions during the geochronological work on Thermal Ionization Mass Spectrometer at the Institute Instrumentation Centre, IIT Roorkee.

Dr. Pulak K. Mukherjee, Wadia Institute of Himalayan Geology (WIHG), Dehra Dun is thankfully acknowledged for his encouragement, help and discussions which were useful in elucidating the geochemistry. The Director, WIHG is thankfully acknowledged for arranging the geochemical analysis. **Dr. P. P. Khanna, Dr. N. K. Saini** and other scientists from WIHG are highly appreciated for providing facilities for geochemical analysis on XRF.

Dr. V. Balaram, Scientist, National Geophysical Research Institute (NGRI), Hyderabad and the Director NGRI are also extended heartfelt gratitude towards extending the facilities to generate good quality geochemical data on ICP-MS.

This thesis forms a part of the HIMPROBE Programme on 'Tectonics, P-T Constraints and Timing of India Asia Collision along the NW Himalayan Geotransect' (Grant No. 5724-14-44) of the Department of Science and Technology **(DST)**. I owe my gratitude to **Prof. Manickavasagam** for extending the financial support to me from this project and to

Council of Scientific and Industrial Research **(CSIR)**, New Delhi (Grant No. 7877-14-44) for the **Senior Research Fellowship**.

My sincere appreciation goes to **Prof. S. S. Srivastava and Dr. A. K. Saraf** of the Department of Earth Sciences, IITR for their encouragement and kind words of wisdom.

The help extended by the technical and non-technical staffs of the Department especially **Ramesh Chand, Subodh Mishra, R. K. Agrawal, Nair ji, Kamesh Gupta, Rahil, Om Prakash, Raj Kumar, and Ram Karan** are duly acknowledged. **Rameshji, Bhim Singh, Manoj, and Jagadish** need special mention for their company during the strenuous field work in the rugged terrains and hostile environment. Sincere thanks are due to **Ramdal Mishra, Bhim Singh, Surendra** and **Somdutt** who have helped a lot during the thin section preparation and geochronological analysis.

I express my heartfelt appreciation to my my seniors, **Dr. J. R. Sahoo, Dr. P. R. Pujari, Dr. Pramanand Mishra, Ashutosh Shandilya** and **Shekhar Gupta** for their encouragement and moral support during the course of the research work.

I am extremely thankful to **Yogesh, Om Prakash** and **Rajesh Sakalani** at Kurukshetra for keeping patience with me and making my stay at Kurukshetra enjoyable and fruitful while generating the FT dataset.

I express my heartfelt appreciation to my friends **Amit Sahay, Ashis Patra, Ashis Saha, Debdutta Mohanty, Rakesh Bora, Satvinder Singh, Umesh Haritashya, Sudesh, Subhash, Dhiraj Khatod,** and **G. C. Joshi** for their cheerful and affectionate company during this study.

I am thankful to my lab mates, **Nidhi, Soumyajit, Biswajayee, Nikunj** and **Chandramauli** for their continuous support, cooperation and encouragement. The last moment impetus and completion deadline has given them sleepless nights to them too. Helping hands extended by them at that moment are beyond any expression.

Finally, I am indebted to my parents, brothers, wife and relatives for their unknown sacrifices, frequent help and constant encouragement. Without their everlasting love, affection and inspiration, I would not have completed this thesis.

(RAJEEV KUMAR)

CONTENTS

LIST OF TABLES

LIST OF FIGURES

CHAPTER–1

INTRODUCTION

1.1 INTRODUCTION

The Himalaya is a unique example of young continent to continent collision. It stretches uninterruptedly along a regional strike of about 2400 km in length, from west to east between Nanga Parbat (33° 15' N; 74° 36' E; 8126 m) to Namche Barwa (29° 37' N; 95° 15' E; 7756m). The width varies from north to south between 230 and 300 km with an average of about 270 km. Among the different orogenic belts, the Himalaya is the highest having 10 out of 14 peaks above 8,000m, with Everest at 8848m and large contrast in relief over short distances. Some of the longest rivers nourish the oceans. In the north, lies the highest plateau of Tibet with a crustal thickness of 60-80 km, and in the south, the Indian Peninsular Shield has a general crustal thickness of 35-40 km. The curved disposition of Himalaya is a very striking feature of this range (Fig. 1.1).

The evolution of the Himalayan Arc has created immense interest among the geoscientists all over the world because of its large-scale continental convergence along the Suture Zones. The Tethyan oceanic crust attached to the Indian Plate has subducted beneath the Eurasian Plate and the Indian Plate collided against the Eurasian Plate along the Indus Tsangpo Suture Zone (ITSZ) and Shyok Suture Zone (SSZ) (Gansser, 1964; Dewey & Bird, 1970; Dewey & Burke, 1973; Le Fort, 1975, 1986; Thakur, 1993; Searle et al. 1988; Jain et al., 2002, 2003). The parts of the Indian Plate now forming the Himalaya were part of the Gondwanaland and known as the Greater India (Veevers et al., 1975; Tapponier and Molnar, 1976; Powell, 1979). After the break up from the Gondwanaland at around 200 Ma, the continued northward movement of Indian Plate for some 100 Ma progressively narrowed the

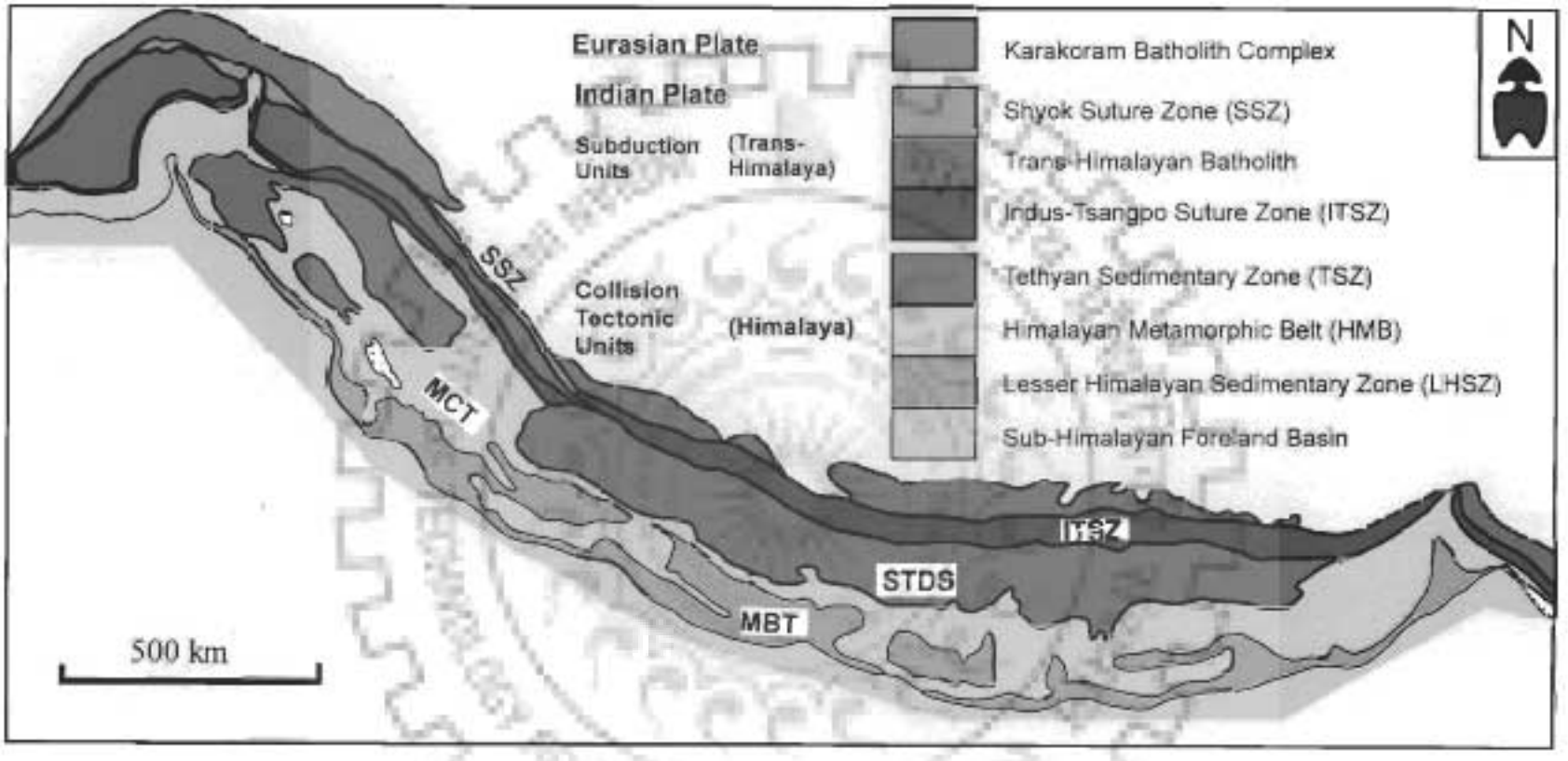

Figure 1.1: Simplified regional geological framework of the Himalaya in plate tectonic framework. Abbreviations: SSZ-Shyok Suture zone, ITSZ-Indus Tsangpo Suture Zone, STDS-Trans Himadri shear System, MCT-Main Central Thrust, MBT-Main Boundary Thrust (after Jain et al., 2002).

Tethyan Ocean (Le Fort, 1989). The closure of Tethys was followed by subduction of the continental crust below the Eurasian Plate up to a depth of at least 90 Km (de Sigoyer et al., 2000; Guillot et al., 2003; Sachan et al., 2004; Singh et al., 2003; Leech et al., in review).

Due to the continued northerly movement of the Indian Plate the closure of Tethys Ocean ended and the Indian Plate collided with the Eurasian Plate along the ITSZ. This collision event can be constrained on the basis of biostratigraphy of collision-related sediments on either side of the ITSZ and palaeomagnetic data (Klootwijk et al., 1992; Rowley, 1996; Guillot et al., 2003). Stratigraphic constraints indicate that the collision began in northern Pakistan at around 52 Ma and progressed eastward until its end around 41 Ma near eastern syntaxis (Rowley, 1996). There is a range of geochronological data from 65 to 40 Ma to interpret the onset of collision in the NW Himalaya. The best estimations are based on stratigraphy of the Zanskar region, where collision-related deposition started in Early Eocene (50-51 Ma) with deltaic red beds containing ophiolitic detritus and the marine sedimentation ended by the Early-Middle Eocene (49-46 Ma) (Gaetani and Garzanti, 1991; Rowley, 1996). However, onset of collision of India and Eurasia has been placed at ~55±1 Ma from the palaeomagnetic determination of an abrupt slowdown of northward velocity of the Indian Plate from 180±50 mm/a to 134±33 mm/a (Klootwijk et al., 1992; Guillot et al., 2003).

Analysis of the Cenozoic magnetic anomalies in the Indian Ocean shows that India's northward movement slowed down from pre-collision rate of about 18-19.5 cmy^{-1} to a post-collision rate of about 4-5 cmy^{-1} or less (Molnar and Tapponier, 1975; Patariarch and Achache, 1984; Molnar, 1987). According to Klootwijk et al. (1992), this occurred at about 55 Ma indicating the completion of suturing between India and Asia.

The collision is followed by the obduction of ophiolitic nappes and generation of eclogites in the Tso Morari and Khagan sector of the Northwestern Himalaya (O'Brien, 2001,

Guillot et al., 2003; Singh et al., 2003; Leech et al., in review). A reasonable estimate of the total post-collisional crustal shortening between the stable parts of the Eurasian and Indian Plates is of the order of 1100 km (Guillot et al., 2003 and references therein).

The continued collision and crustal shortening have resulted in the overthrusting of the frontal part of the Indian continent block and leading to doubling of the thickness of the continental crust to about 70-80 km. The total crustal shortening has been compensated by the detachment, block rotation and sideways extrusion along large-scale strike-slip faults in the Eurasian plate to the north of the ITSZ (Molnar and Tapponier, 1975), and within the Himalayan orogenic segment south of the ITSZ. A part of the shortening within the Himalayan segment has been attributed to a number of thrusts viz; the Main Central Thrust (MCT), the Main Frontal Thrust (MFT) and the Main Boundary Thrust (MBT). These south-directed thrusts appear to sole into a common decollement; the Main Himalayan Thrust (MHT) (Zhao et al., 1993; Brown et al., 1996; Nelson et al., 1996). The MCT separates high grade gneisses from lower grade sedimentary sequences (Heim and Gansser, 1939). The MBT juxtaposes the low grade metamorphosed sedimentary sequences against the unmetamorphosed Miocene-Pleistocene molasse (the Siwalik Group). It has been observed by certain workers that thrusting is active even within the Quaternary sediments (Singh, 1999). The sedimentation within the Sub-Himalayan unit; Indo-Gangetic Plains, the megafans of the Arabian Sea and Bay of Bengal, the present-day seismicity in the Himalayan and adjoining areas, the exhumation of deeply-buried rocks and ensuing extensional tectonics- all are related to the collision-tectonics (Gansser, 1964; Le Fort, 1975; Honegger et al., 1982; Coward et al., 1982; Searle, 1983; Valdiya, 1980, 1989; Thakur, 1993; Hodges, 2000; Yin and Harrison, 2000, Jain et al., 2002, 2003).

1.2 TECTONIC ZONES OF HIMALAYA

The Himalaya rises abruptly from the Indo-Gangetic Plains to high mountain peaks south of the Indus Tsangpo Suture zone. From south to north the Himalaya can be separated into the following longitudinally continuous lithotectonic zones.

1.2.1. Sub-Himalayan Zone (SHZ): The SHZ consisting of the Cenozic sedimentary rock sequence represent the 'Himalayan Foreland Basin'. It is bounded to the north by the MBT and towards south; it is separated from the undeformed Indo-Gangetic foreland basin by the north-dipping Main Frontal Thrust (MFT).

1.2.2. Lesser Himalayan Zone (LHZ): It contains the Lower Proterozoic to Lower Paleozoic sediments and very low grade sedimentary sequence lying between the MCT and the MBT. At places, the LHZ has thick section of the Precambrian metasediments metamorphosed up to amphibolite facies (Le Fort, 1989). The determination of definitive age relation and lateral correlations in the LHZ are difficult and uncertain due to the lack of fossils, paucity of exposures in many areas and later structural complications.

1.2.3. Higher Himalayan Crystalline Zone (HHCZ): The north-dipping MCT, active since 25-20 Ma (Hodges et al., 1996), places the 10-15 km thick Higher Himalayan Crystalline Zone over the Lesser Himalayan Zone. It occupies the area between the MCT and the South Tibetan Detachment System (STDS). The rocks of the HHCZ are highly deformed and metamorphosed and represent the leading edge of the Precambrian Indian crust which has been reactivated, remobilized, metamorphosed and intruded by the Miocene leucogranite during the Cenozoic Himalayan orogeny (Jain and Anand, 1988; Searle et al., 1992; Jain and Manickavasagam, 1993, Patel et al., 1993; Jain et al., 2002 and references therein). In the NW Himalaya, the Zanskar Shear Zone (ZSZ), separates the HHC from Neo Proterozoic to Eocene sediments of the Tethys Himalaya. This zone is variably

referred to as the Central Crystallines, the Jutogh/Vaikrita Groups, the Tibetan Slab, Darjeeling gneisses and by other different names in different sectors (e.g., Pilgrim and West, 1928; Heim and Gansser, 1939, Gansser, 1964; Le Fort, 1975; Valdiya, 1980).

1.2.4. Tethyan Sedimentary Zone (TSZ): This zone is composed of sedimentary rocks of Neoproterozoic to Eocene age. These rocks were deposited on the leading edge of the northerly-moving Indian Plate. The TSZ is bound to the north by the ITSZ and towards south by the STDS. Structurally, it is complex zone with south vergent recumbent folds, north vergent back-folds and back thrusts, and extensional structures (Searle, 1983; Burg and Chen, 1984, Herren, 1987; Patel et al., 1993).

1.2.5 Trans-Himalayan Zone: Further north lies the Trans-Himalayan Zone, which includes the Ladakh, Karakoram and Mansarovar ranges. The Trans-Himalayan Zone has the conspicuous feature of two suture zones; the Indus Tsangpo Suture Zone and the Shyok Suture Zone, separating the two huge batholithic masses-the Ladakh Batholith and the Karakoram Batholith (Fig. 1.2). Details of their geological framework are given in Chapter 2.

1.3 SCOPE OF THE WORK

The Himalayan orogeny, the youngest in the history of the Earth, relates to the formation of the Himalayan Mountains. The Himalayan rocks have drawn global attention of a large number of geoscientists as these carry the present and past records of the collision tectonics. In fact, this range is the best example living laboratory to study the intricacies of plate tectonic theory, especially the continental collision.

In the established framework of continent-continent collision of the Indian and the Eurasian Plates, the present study aims at enhancing the existing knowledge of lateral and

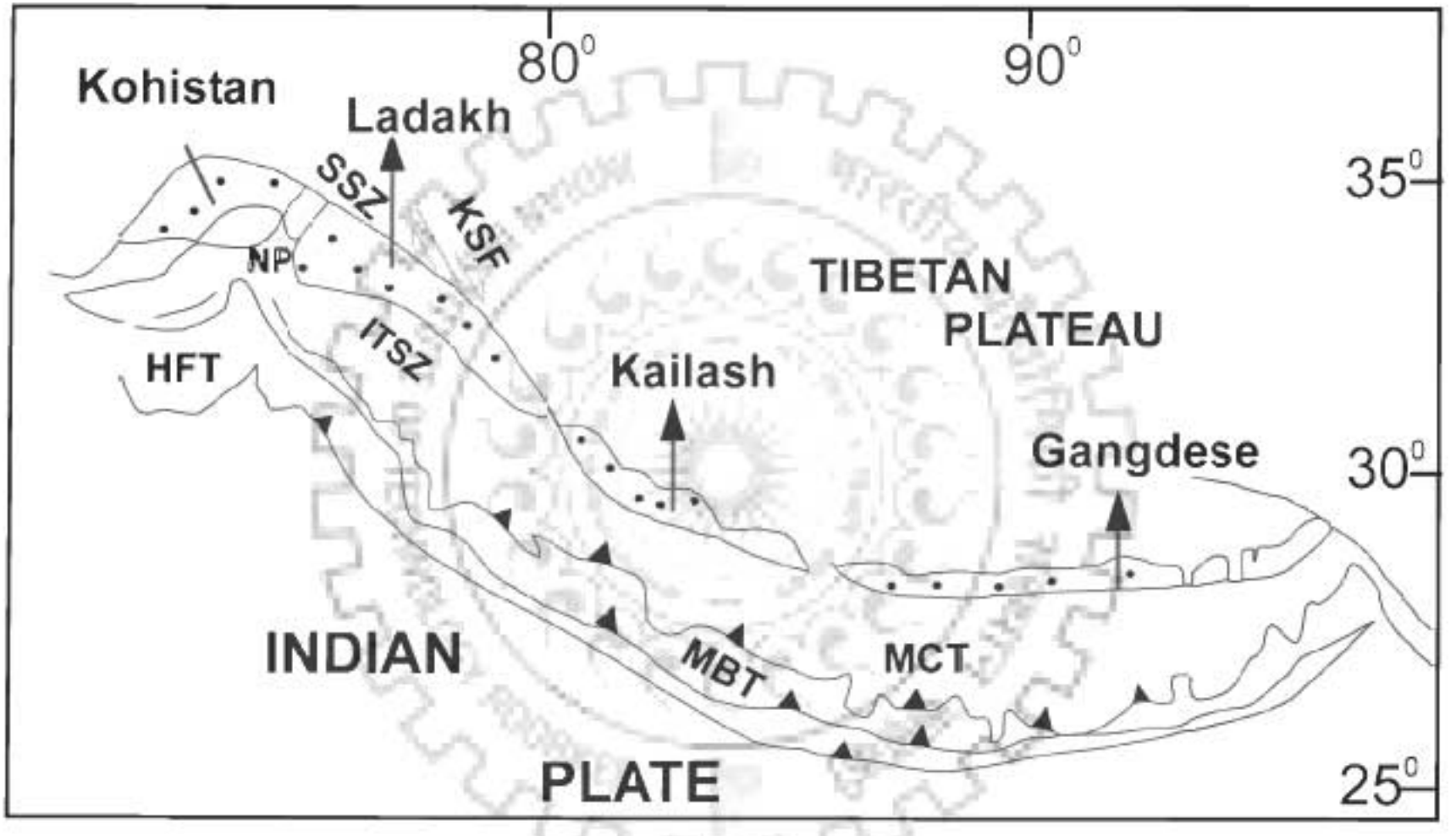

Figure 1.2: Simplified geological map of the Himalaya showing distribution of the Trans-Himalayan Batholith and its nomenclature.

temporal, petrological and geochemical variations of the Trans-Himalayan Ladakh Batholith and its cooling, exhumation and denudation history.

1.3.1. Petrology and Geochemistry: The limited petrological and geochemical data of the Ladakh Batholith suggest that the majority of the rocks range in composition from diorite to granite with occasional occurrence of more basic varieties like norite and gabbro in the Kargil area (Rai and Pande, 1978; Rai, 1983; Raz and Honegger, 1989). Though differentiated varieties have been observed in this part of the Himalaya, it is still not clear whether such differentiated products occur both laterally and temporally. Therefore, an attempt has been made to study the Ladakh Batholith in the present work, both petrographically and geochemically, across three sections to understand the lateral and temporal variations in major oxides, trace elements and rare earth elements and also to characterize its magmatic evolution and depth of crystallization. Three extensive field trips were undertaken during 1998, 1999 and 2001 along the following sections (Fig. 1.3):

(i) Leh–Khardung La section,

(ii) Kharu-Chang La section,

(iii) Lyoma-Hanle section.

1.3.2 Fission track thermochronology: One aspect of the Himalaya that has particularly drawn much attention in recent years is its history of exhumation and denudation because quantitative knowledge of these processes sheds light on various geological phenomena, including (i) inherent link among thermotectonic processes, styles of strain accumulation, and deep crust- mantle interactions, (ii) development of mountain landscape, drainage patterns, and dynamics of foreland sedimentary basins, (iii) geochemical changes in

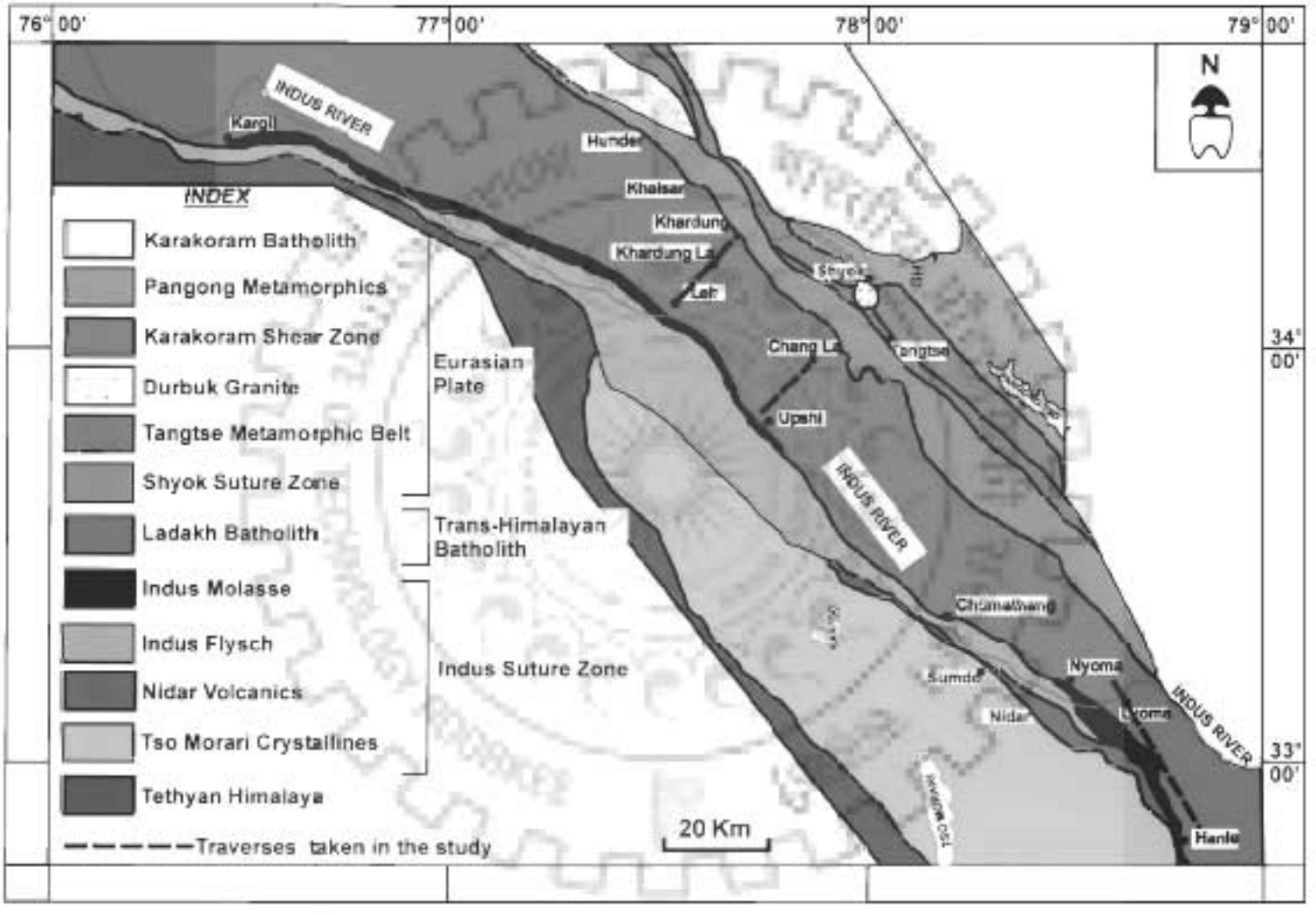

Figure 1.3: Geological map of the Ladakh Batholith in parts of Kargil-Leh-Hanle sector, Trans - Himalaya showing location of the traverses in Ladakh (Compiled after Thakur, 1993, Jain et al., 2003).

the atmosphere and the oceans; and (iv) Cenozoic ecological and climatic changes on a continent- to globe scale associated with the Alpine- Himalayan orogeny.

Going by the vastness and complexity of this orogenic belt and usefulness of fission track (FT) mineral ages, such work is required from many parts of the Himalaya to avoid generalization of the concepts from incompetent data. The work embodied in the present thesis, incorporates thermal and exhumation history of the Trans-Himalayan Ladakh Batholith, using FT thermochronology along these traverses.

1.3.3. Rb-Sr geochronology: Though good quality geochronological data set is currently available from the various segments of the Higher Himalayan Crystalline zone, yet, the Ladakh Batholith has remained poorly constrained in terms of its age of emplacement, crystallization and exhumation. The work undertaken in the present thesis attempts to fill in this gap in the existing knowledge from the main sections of the Ladakh Batholith using Rb-Sr geochronology.

1.3.4. Depth of emplacement: After getting the age of emplacement it is imperative to look into the depth of emplacement of this huge batholithic mass. For this purpose hornblende geobarometry has been used to decipher the depth of emplacement of the Ladakh Batholith.

1.3.5. Data integration, summary and conclusions: Finally the data generated in this work has been critically interpreted to characterize the geochemistry, age and depth of emplacement of the Ladakh Batholith and its exhumation for the late Mesozoic-Cenozoic geodynamic evolution of the Trans-Himalaya.

1.4 METHODOLGY

(i) Field work and systematic geological mapping of the various tectonic units have been carried out using parts of Survey of India toposheet nos. 52F/10-16, 52G/9, 52G/13-15, 52K/2-4, and 52K/6-8 on 1:50,000 scale along with sampling.

(ii) Preparation of thin sections for detailed textural and petrographic studies.

(iii) Powdering of selected samples for the determination of major oxides by XRF, trace element and REEs by the ICP- MS as well as whole rock Rb–Sr dating technique by Thermal-Ionization Mass Spectrometer (TIMS).

(iv) Standard crushing of selected samples for the separation of apatite and zircon for Fission Track dating and, biotite for Rb- Sr dating to determine the cooling and exhumation history of the Ladakh Batholith.

(v) Mineral chemistry of hornblende for the determination of depth of crystallization using Electron Probe Micro Analyzer (EPMA).

CHAPTER–2

GEOLOGICAL FRAMEWORK

2.1 INTRODUCTION

The area of study is a part of the Trans-Himalayan zone lying to the north of the Indus Tsangpo Suture Zone (ITSZ) in the Ladakh district of Indian Territory. Lithotectonic units of the Trans-Himalaya represent the subduction-related processes and represent an initial island arc having fore arc and back arc sediments, ophiolite emplacement and late Mesozoic Andean-type Ladakh Plutonic Complex. They also include the Kohistan sequence in Pakistan Himalaya, whereas, the ophiolite sequence along with the flyschoidal and molassic sediments of Kailas range forms the eastern continuity.

2.2 PREVIOUS WORK

The earliest reference to the geology of Ladakh is available from the works of Thompson (1852), Stoliczca (1866), Drew (1857) and Lydekker (1880, 1883). Subsequent description came from the work of Hayden (1907), Middlemiss (1911), Dainelli (1933, 1934), De Terra (1935) and Auden (1935) who have taken traverses across Ladakh. Later, Wadia (1937) and Berthelsen (1953) carried out comprehensive studies including mapping of different sectors of Ladakh. Sahni and Sastri (1956) and Sahni and Bhatnagar (1958) reported *Ohiolina*, fresh water mollusca and plant remains in the molassic sediments from Kargil area and assigned them a Tertiary age. Later on Raiverman and Misra (1974), Shankar et al. (1974) and Shah et al. (1976) have looked into the structural and plate tectonic aspect of the Ladakh area in the western parts near Kargil and Dras. The detailed study of the suture zone was undertaken in two significant publications by Gansser (1977, 1980). Honegger et al. (1982) carried out

detailed geochemical and isotopic studies of various litho units of the Indus Tsangpo Suture Zone and the Trans-Himalayan Ladakh Batholith. Thakur and Sharma (1983) published the edited volume entitled 'Geology of the Indus Suture Zone of Ladakh.' In the year 1984, Scharer and co-workers, published new dates of the Trans-Himalayan Ladakh Batholith. In between Rai (1982) gave an account of the status of Shyok Suture Zone in the collision tectonic framework and again in the year 1986, he provided an account of the Karakoram Metamorphics. Based on the extensive field observations Raz and Honegger (1989) described the tectonic and magmatic evolution of the Ladakh block. Searle and co-workers (1983, 1990, 1993, 1998) have contributed immensely in the understanding of the Ladakh Himalaya and integrated the field observations with structural, geochemical and geochronological aspects. Thakur (1993) has compiled a book on the geology of Western Himalaya giving an extensive account of the geology of the all the tectonic units of Himalaya. Sorkhabi et al. (1994) incorporated fission track and Ar-Ar ages of the Trans-Himalayan Batholith and tried to work out its cooling history. Recently, Upadhyaya and Sinha (1998), Ahmed et al. (1998) Upadhyaya et al. (1999), Chandra et al. (1999), Weinberg and Dunlap (2000), Rolland et al. (2000), Rolland (2002), Dunlop and Wyasoczanski, (2002) have published works on the suture zones, Trans-Himalayan Batholith, Karakoram Metamorphics and Karakoram Batholith covering various integrated aspects. Jain et al. (2003) have produced an excellent account of geology and tectonics of different sectors of the Ladakh Himalaya right from the ITSZ to the Karakoram Ranges.

2.3 GEOLOGY OF THE AREA

The general geology of the study area and its adjoining boundaries from south to north is described below:

2.3.1 Indus Tsangpo Suture Zone (ITSZ): The ITSZ occupies a unique position in the Himalaya because of its characteristic rock assemblage and role during the evolution of the Himalaya. The suture represents a major tectonic crustal lineament from Hindukush to Mishmi Hills of Assam for about 2500 km along which the Indian Plate has subducted below the Eurasian Plate during late Mesozoic. It follows the course of Indus River in the west and the Tsangpo River in eastern Tibet. It separates the Indian Plate to the south and Lhasa and Xangtang blocks of Tibet to the north (Gansser, 1964, 1977; Dewey and Bird, 1970; Windley; 1983; Searle 1983). It is bounded by the Trans-Himalayan sequences in the north, followed by Neo-Tethys oceanic sediments and Indian plate sequences in the south. The continental arc segments containing volcanic arc and the passive margin have merged together at the time of India-Eurasia collision during Mesozoic and formed the Indus-Tsangpo Suture Zone. The allocthonous suture zone sediments occur as klippen and half-klippen, which is deformed by backfolds and backthrusts subsequently during collision in Miocene and younger ages (Searle, 1983, 1990, 1991; Thakur, 1983, 1987, 1993). The ITSZ is recognized by (i) the occurrence of blue schist metamorphism in general but the degree of metamorphism in the suture zone ranges from lowest greenschist facies in south to prehnite-pumphelyite facies in the north, (ii) coloured tectonic melanges, (iii) ophiolites (iv) flysch deposits and (v) the Dras volcanics (Virdi, et al. 1977; Thakur, 1981, 1993; Honegger et al., 1982; Scharer et al., 1984; Jain et al., 2002).

This zone comprises mainly of the Mesozoic deep sea sediments like the Lamayuru Formation (shale, siltstone and graded sandstone), the Indus Group (conglomerate, sandstone, siltstone and shale); the Nindam Formation (alternating sandstone, siltstone and shale), the Kargil Formation (conglomerate and sandstone), the Dras volcanics of Upper Jurassic to Upper Cretaceous times (andesite and basaltic lavas) and the Shergol mélanges (serpentinite, peridotite and dunite) within jasperoid shale, chert, pillow lavas and basic rocks together with

blocks of mica schist, limestone lenses and discrete bands of sandstone, grit conglomerate and glaucophane schist) (Thakur and Misra, 1984; Thakur, 1993). A very striking sequence of conglomerate and sandstone occurs within the suture zone and is called the Hemis Group. These molasses dip southerly and nonconformably overlie the Ladakh Plutonic Complex. The ITSZ is bounded by the Dras Thrust in the south while most of the contacts between different Formations within the ITSZ are imbricated (Thakur, 1981). Thakur (1983) deduced the deformational pattern associated with the ITSZ and identified three distinct deformational phases. D1 has produced thrusts leading to the emplacement of ophiolitic rocks over the continental margin sediments of Zanskar sedimentary zone. D2 phase caused the folding of the thrust into antiformal and synformal structures. Due to the D3 deformational phase cross-folds with NE-SW axial traces are generated.

The Shergol mélange rocks are metamorphosed to blueschist facies indicating a high pressure metamorphism due to oceanic subduction within the ITSZ. The age of the mélanges is considered to be Jurassic to Late Cretaceous on the basis of *foraminiferal* and *radiolarian* fossils (Shah and Sharma, 1977; Upadhyaya and Sinha, 1998). Pessagno (1977) assigned them an Albian age, and on the basis of the presence of *radiolarian* Satouru et al. (2001) approved it.

2.3.2 The Trans Himalayan Batholith: The Ladakh Batholith occurs as a WNW-ESE trending linear belt of about 600 km long, 30-80 km wide and about 3 km in exposed thickness, and lies immediately to the north of the ITSZ. The batholith continues from Astor-Deosai-Skardu region (Auden, 1935; Wadia, 1937; Desio, 1977) eastwards through Leh, Upshi and Nyoma to Hanle and further southeast into the southern Tibet. The Ladakh Batholith is a part of the calc-alkaline Andean-type Trans-Himalayan complex that extends for 2500 km from Afghanistan in the west (the Kohistan Batholith) to east of Lhasa in Tibet (Honegger et al., 1982). The batholith has been variously called as Kohistan

batholith and Ladakh batholith in the northwest, Kailas tonalite and Gangdese pluton in Tibet and Lohit Batholith in Arunachal Pradesh (Thakur and Jain, 1975; Sharma et al., 1991). It is composed of multiple calc-alkaline intrusions that vary from norite and gabbro to granite (Honegger et al., 1982). The batholith has resulted from melting related to the north-directed subduction of the Tethyan oceanic crust below an island arc situated along the southern margin of Eurasia (Scharer et al., 1984). A large sliver of sedimentary sequence within the Ladakh Batholith led Raz and Honegger (1989) to suggest that it may have developed in a transitional environment between the Kohistan island arc in the west and the continental margin of Eurasia.

The Trans-Himalayan plutonic complex is partly covered by fore-arc rocks and continental molasse sedimentary rocks. These assemblages are derived from uplift of magmatic rocks and their subsequent erosion. The igneous complex consists of I-type lithologies, including gabbros, diorites, granodiorites and granites. The belt has intrusive relationship with the volcanics of island arc like Dras volcanics and Khardung volcanics (Srimal et al., 1982; Sharma and Gupta, 1983; Choudhry, 1983). Sharma (1983) and Sharma and Choubey (1983) recognized four phases of magmatic activity within the Ladakh Batholith. After a detailed survey of the batholith Singh (1993) divided the Ladakh Granitoid Complex into five distinct units: diorite-tonalite, granodiorite-quartzmonzodiorite, biotite-hornblende granite, leucogranite and pink porphyritic granite. Though several types of igneous bodies have been reported, predominant rock type is biotite- and hornblende-bearing granodiorite throughout the body. Formation of the complex is thought to have occurred in several phases between 110 and 40 Ma with a dominant phase around 60 Ma (Honegger et al., 1982). Partial melting of a subducting Neo-Tethyan slab beneath the Asian plate is thought to have resulted in these magmas (Sorkhabi 1999).

The northern slope of this batholith is exposed in the Shyok Valley and is in juxtaposition with the Khardung and Shyok Volcanics. Intrusive relationship is well documented at many places. In the south central part of the Shyok valley, between Diskit and Chandmarg, the batholith has intruded into the sediments and ophiolotic mélange (Rai, 1983). Near the intrusive contact with the volcanics, an intrusive breccia has developed (Rai, 1980).

The Ladakh Batholith was emplaced into an unmetamorphosed thick pile of basic and acid volcanics, (Dras Volcanics). Therefore, the batholith has crystallized under a thick pile of volcanics and reached at the shallow depth. Radiometric dating on the Ladakh Batholith shows a late Cretaceous-Eocene body representing an Andean-type pluton, which was formed by magma accumulation as a result of northward subduction of the Mesozoic oceanic crust beneath Tibet. Relatively low $^{87}Sr/^{86}Sr$ initial ratios (0.707) and high $^{143}Nd/^{144}Nd$ ratios (0.5126) support the derivation of these magmas from partial melting of subducted mantle material which was possibly contaminated by a small amount of crustal material (Allegre and Othman,1980, Honegger et al. 1982).

The Ladakh Batholith is largely undeformed and has escaped intense penetrative deformation to a very large extent. However, diffused deformation zone to the north of Leh and intense penetrative ductile shear fabric within this batholith has been observed by Weinberg and Dunlap (2000) within NNW-trending dextral Thanglaso Shear Zone. Observations of Jain et al. (2003) on the deformation pattern reveal intense development of mylonitized gneiss having large-scale ellipsoidal enclaves of the country rocks which trend almost N90° to N 120° with steep dips towards north. The presence of NW-trending ductile shear zone having top-to-southwest overthrust sense of shearing along with other brittle-ductile to brittle in character have also been observed and reported by Jain et al., (2003). Numerous dolerite dykes cut almost orthogonal across the deformed batholith.

Weinberg and Dunlap (2000) obtained U-Pb SHRIMP ages of 58.1±1.6 Ma from zircon cores and a younger 49.8±0.8 Ma rim age from Leh, and interpreted these as the crystallization age of the source igneous rock and a subsequence crystallization phase followed by rapid generalized cooling and dyke intrusion at 46±1 Ma. In another significant work Singh et al. (2003) combined the U-Pb SHRIMP ages and hornblende geobarometry to give the depth of crystallization to be 9-10 km.

2.3.3 Shyok Suture Zone (SSZ): The northern boundary of the Ladakh Batholith is demarcated by another suture zone - the Shyok Suture Zone (SSZ). It was first described by Gansser, 1964 and later by many other workers (Tahirkheli et al., 1979; Brookfield and Reynolds., 1981; Rai, 1982; Thakur and Mishra, 1984; Srimal, 1986; Brookfield and Reynolds, 1990; Chandra et al. 1999; Upadhyaya et al. 1999; Rolland et al. 2000, 2002). Two contrasting views place the main trace of the suture zone either to the north of Saltoro range along Saltoro river (Gansser,1980), or more commonly along the Shyok River, south of Saltoro range (Srimal,1986). In the Shigar Valley of Baltistan the SSZ has been investigated by Hanson, (1989), who defines it as a simple fault containing a few pods of serpentinite and separating the Paleozoic sedimentary rocks of the Eurasian Plate from the Dras island arc. Marine sediments of Cretaceous age suggest a small ocean basin between the two terrains. It is also known as Main Karakoram Thrust (MKT) in Pakistan. The SSZ comprises of dismembered bodies of ultramafics, gabbro, basalt and sediments within tectonic mélange. It demarcates the southern margin of the Karakoram Batholith Complex (KBC), which intrudes the Paleozoic-Mesozoic platform sediments of the Eurasian Plate.

The Shyok Volcanics consist of basalt and andesite and are overlain by flysch (Rai, 1982). Chloritization, epidotization and decalcification of plagioclase are frequently observed, and at contacts with the granitic intrusions thermal metamorphism has led to the formation of hornfelses. The lithology shows low grade of metamorphism. The volcanics are

poor in K_2O and SiO_2 and the composition is comparable to that of the Dras volcanics (Thakur, 1993, Rolland, 2000). The basalts have high Mg-content and are tholeiitic in nature suggesting chemical affinity between primitive N-MORB to E-MORB. The andesites are calc-alkaline having resemblance with transitional basalt between E-MORB to OIB (Chandra et al., 1999).

The Khardung volcanics consists of lava flows and tuffs of Eocene or early Oligocene age (38±2 Ma) (Sharma et al., 1978) and hence younger than Shyok volcanics. Main constituents are rhyolite and dacite with subordinate ignimbrite. The basal rhyolite has yielded an age of 67.4±1.1 Ma U-Pb SHRIMP zircon age while a feeder porphyritic sill gave a weighted mean age of 60.5 ± 1.3 Ma. Both these ages have been interpreted as the age of eruption and intrusion respectively (Dunlap and Wysoczanski, 2002).

The flysch and ophiolitic mélange form a thin and discontinuous belt of fine, pink grey and black shales and phyllites with grey massive limestone. The rocks are folded and thrust over the Shyok Volcanics. These sediments have yielded marine fauna of Upper Cretaceous to Eocene age in the Saltoro Hills (Rai, 1982) and *Orbitelina* around Chusul in the east (Srikantia et al., 1982). Upadhyaya et al., (1999) called them the Saltoro Formation and assigned an age of upper Cretaceous to lower Eocene.

The molasse lithology is mainly confined to the central part of the Saltoro Hills and contains mainly the clastic sediments of post-Oligocene age (Rai, 1986). The belt runs NW-SE for about 50 km and dips due northeast. To the east and west, thickness of the Saltoro molasse varies from 2 to 3 km but becomes 5 to 6 km in the central part. It lies in tectonic contact with the flysch and the Shyok Volcanics in the south. Contemporaneous volcanism is represented by discrete andesite horizon within molasses (Rai, 1983; Srimal, 1986).

Along the Shyok Valley as well as in the Chang La sector, intrusive contacts of various lithologies of the SSZ are intruded by apophyses and small stocks of the Ladakh Batholith. A

thin sequence of slate-phyllite and thin limestone intercalations is exposed around Diskit-Khalsar and can be traced beneath the overthrust Karakoram Batholith Complex (KBC) around Sati. An intervening succession of ophiolite and sedimentary rocks is exposed in the Saltoro Range (Rai, 1983) and appears to truncate against the Karakoram Shear Zone (KSZ). In the Chang La sector in southeastern parts, enormously thick imbricated sequence of ultramafics, volcanics, conglomerate, sandstone and chert is exposed between Tsoltak and Darbuk and may represent the most accessible section through the SSZ. On the turn and along the left flank of the Tangtse valley, an interesting long linear belt of diorite-granodiorite has been observed by Jain et al. (2003), which abuts against the frontal part of the Karakoram sequence. This belt extends towards northwest along the Shyok Valley where diorite-granodiorite bodies intrude the slate-phyllite sequence around Tirit-Diskit-Khalsar-junction of Nubra-Shyok Rivers.

2.4 GEOLOGICAL OBSERVATIONS

The observations in the study area in all the three sectors, namely Leh-Khardung La section, Kharu-Chang La section and Lyoma-Hanle Section are described under separate heads as per the traverses.

2.4.1 Leh–Khardung La section: In this section the traverse has been taken along the main road section from Leh to Khardung La and-Khalsar, where the batholith is covered by the vast alluvium of the Indus River in the south and the Khardung Volcanics in the north. Vast hornblende-biotite granodiorite (Fig. 2.1 a) occurs as the main rock type with regional strike of NW-SE and steep dips towards north. Remnants of dioritic and gabbroic bodies, intruded by the granodiorite are seen in the southern parts while ascending to Khardung La. Aplitic veins (Fig. 2.1 b) intruding the main mass are common, while numerous dolerite undeformed dolerite dikes cut across the deformed granodioritic mass and show chilled

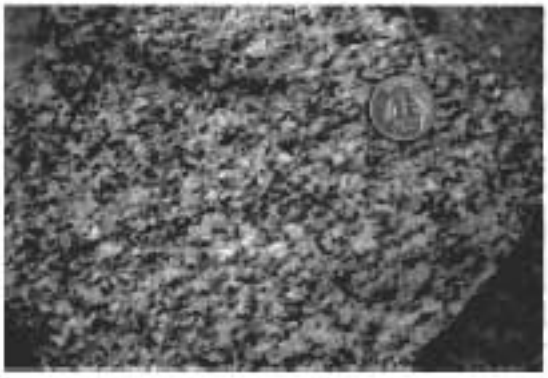

Hb-rich Granodiorite

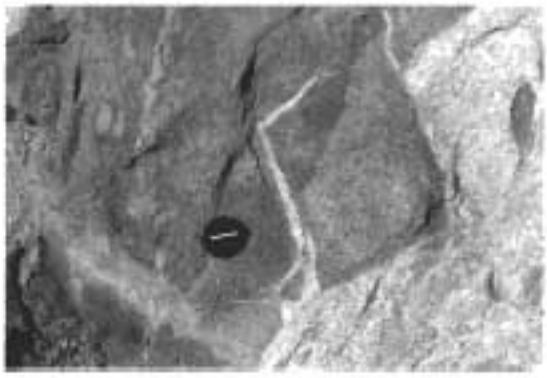

Aplitic veins

Sheared enclaves

Andesite

Reddish Rhyolite

Exposure of the foliated Batholith

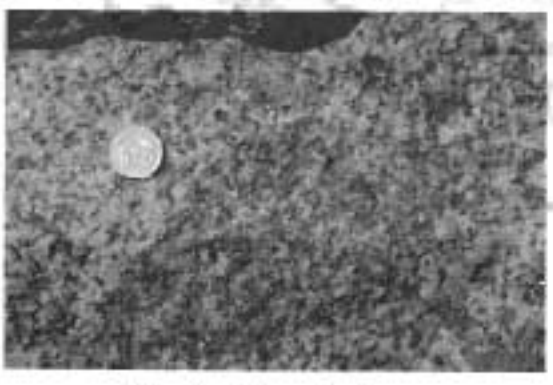

Garnite at Khardung La

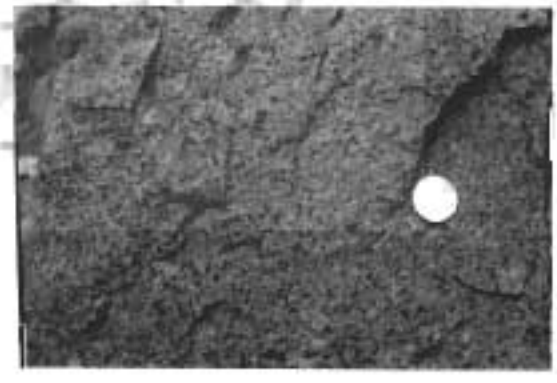

Pink Porphyritic Garnite

Figure 2.1: Field photographs of Ladakh Batholith from Leh Khardung la Section

contact. Presence of sheared enclaves (Fig: 2.1 c) within mylonitized granodiorite is characteristic of this traverse and indicate the extension of Thanglaso Shear Zone along the road section where main foliation within the batholith trends almost $N110^0$ with steep dips towards north. The enclaves show a distinct contact with granitic body. Some of the enclaves are concentrates of biotite and seem to be remnants of the biotite schist, the original mass into which the batholith has intruded. On both side of North-Pulu locality, the Ladakh Batholith shows unconformable relationship with the Khardung Volcanics which are younger rhyolite and andesite (Fig.2.1 d, e). Towards the extreme northern extent between Khardung and Khoksar Villages rock types are mainly volcanics (rhyolite, andesite), agglomerate, gravelly sandstone and conglomerate intercalations and reddish rhyolite (Fig.2.1 e). Except for light colored small exposures of granite and leucogranite sheets near Khardung La, traverse is dominated by hornblende-rich granodiorite (Fig. 2.1 f, g).

2.4.2 Kharu -Chang La section: In this section the southern margin of the Ladakh Batholith is again covered by the vast alluvium of the Indus River within the ITSZ, while its northern margin is demarcated by the SSZ. In the southern extremity near village Igu, lithology is dominated by purple green shale-sandstone-conglomeratic mass of the Indus Group of the ITSZ, while the ophiolitic sequence of the ITSZ occurs further southwards. The Hemis conglomerate overlies nonconformably the Ladakh Batholith and dips southwards. While going north of the village, massively foliated granitic body of the Ladakh Batholith are encountered having regional strike of NW-SE with very steep dip. Sheared enclaves are also observed near the village Igu. Numerous doleritic dikes cut across the batholith at places in this traverse. The mafic phase of the batholith in the form of dioritic masses is concentrated near Kharu and continues upto a distance of almost 1.5 km in the lower parts. While moving towards Chang La in the main section, the pink porphyritic granite (Fig.2.1 h) as described by Singh, (1993) are encountered Chang La. The granitic mass is jointed and weathered at

places. It is by and large a monotonous sequence of the batholith. Along the weak planes, batholith is marked by the growth of chlorite and epidote veins. At the northern extremity across Chang La and Tsoltak check post, vast pile of imbricated sequence of ultramafics, volcanics, gabbro, peridotite, conglomerate, sandstone, and chert is exposed. This sequence marks the appearance of the Shyok Suture Zone, the northern limit of the Ladakh Batholith. This sequence extends upto Laga village near Darbuk.

2.4.3 Lyoma-Hanle section: This section lies almost parallel to the mega lineament of the ITSZ and comprises the southern margin of the Ladakh Batholith. Along the main road section between Nyoma and Lyoma through the Indus River and from Lyoma to Rhongo and further east along the Hanle River, typical coarse and undeformed granodiorite is exposed near Gangla with thin dolerite intrusives. Lithologies of the ITSZ are very poorly exposed along the Hanle River due to vast alluvium between Losar and Hanle, and they include dismembered bodies of conglomerate, sandstone, shale and chert along with peridotite, gabbro and basalt. Near Hanle are the metamorphics of Tso Morai Crystalline (TMC); all the units are characteristically steeply dipping.

CHAPTER–3

GEOCHEMISTRY

3.1 INTRODUCTION

The occurrence of granite in the field and its relationship with country rock is very important aspect in understanding its petrogenesis. Apart from the field relationship, petrographic study of the rocks is also necessary step to understand the evolutionary trend along with the classification of rocks. It is prerequisite for geochemical and geochronological studies of any area. The constituent minerals and their modal proportion are the key parameter. The texture of any rock type throws light on the function of bulk composition of the magma from which the minerals crystallize and the relationship between temperature, pressure and time. The degree of cooling below the liquidus determines many criteria such as grain size, grain shapes, inclusion relationships, intergrowth and corona, which are useful in determining the sequences of crystallization of minerals in any igneous rock (Clarke, 1992). The inferences deduced on this criterion are not always unique (Flood and Vernon, 1988), e.g. fine and coarse grain sizes of the crystals suggest the rapid and slow rates of crystallization, respectively, but the relative grain size has nothing to do with the order of crystallization. Moreover, the large crystals are necessarily those that have crystallized earliest (Clarke, 1992).

The geochemistry of magmatic rock throws light on the type of melting processes, degree of partial melting and nature of the source rock. The processes involved in the rock generation frequently modify the chemical composition of the primary magma due

to the process of partial melting of source through fractional crystallization, magma mixing, contamination, individually or in combination of these processes. These processes, in a way, govern the behaviour of major, trace and rare earth elements. (Hall, 1987; Wilson, 1989; Rollinson, 1993).

The limited data of the Ladakh Batholith suggest that the majority of the rocks range in composition from diorite to granite with occasional occurrences of more basic varieties like norite and gabbro in the Kargil area (Rai and Pande, 1978; Honneger et al. 1982; Rai, 1983; Raz and Honneger; 1989, Singh, 1993). Though differentiated varieties have been observed in this part of the Himalaya, it is still not clear whether such differentiated products occur both laterally and temporally. Keeping this thing in mind an attempt has been made to study the Ladakh Batholith, both petrographically and geochemically, in three crucial sections (Figure 3.1) to understand the lateral and temporal variations in major oxides, trace elements and rare earth elements and its magmatic evolution.

3.2 PETROGRAPHY

53 samples spreading over all the three sections have been selected for the petrographic studies and further geochemical analysis. Figure 3.1 shows the location of these samples through the traverses taken across the Ladakh Batholith (Fig. 3.1). The westernmost section from Leh-Khardung la contains 30 samples of different lithologies (Fig. 3.1b), while 13 samples have been collected from the central Kharu-Chang La section (Fig. 3.1c) and 10 samples from the extreme easternmost section between Lyoma-Hanle (Fig. 3.1d). Further eastward, sampling could not be performed due to logistic difficulties. Individual samples were critically studied under the petrological microscope

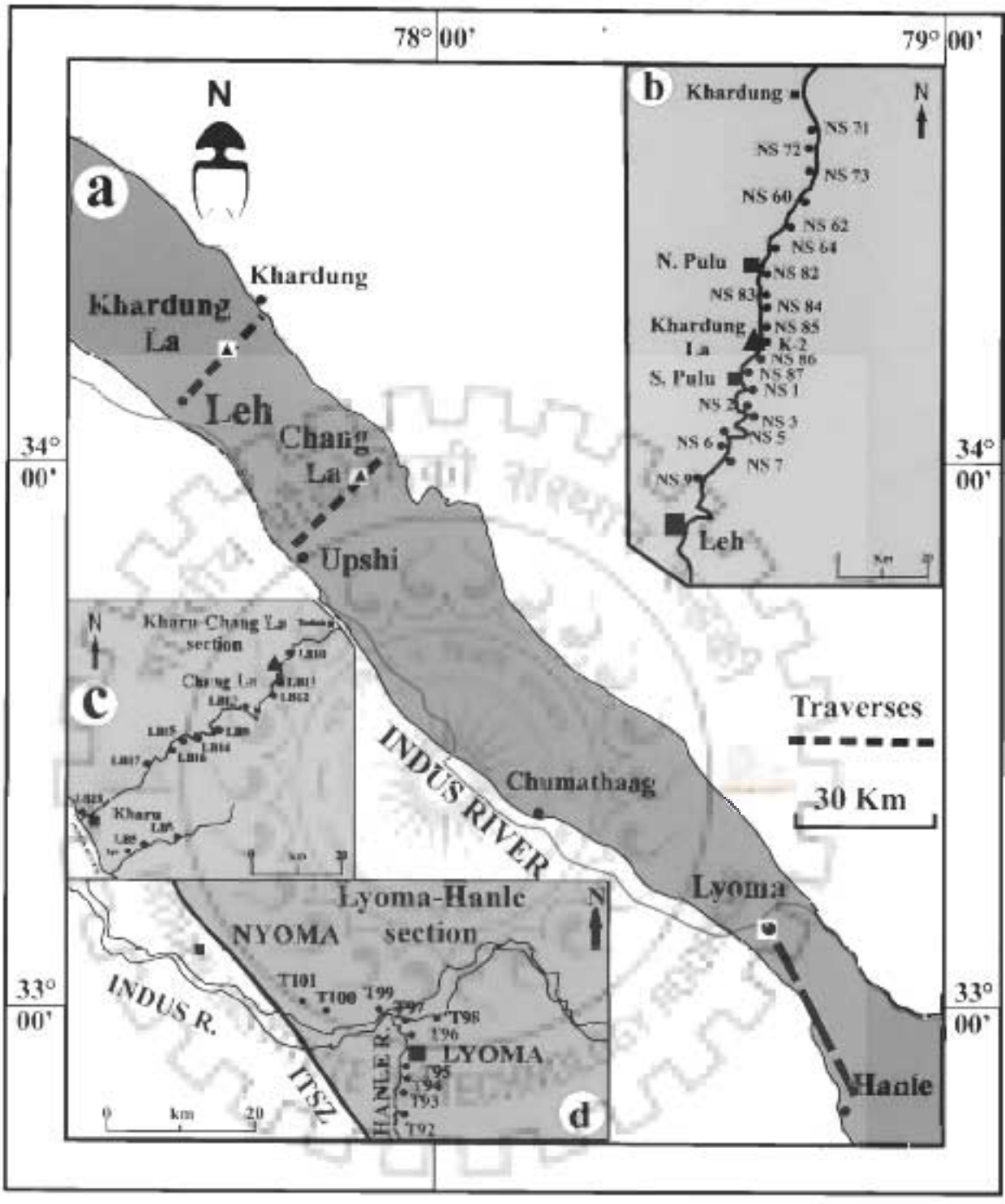

Figure 3.1: Location map of samples from the Ladakh Batholith for geochemistry. (a) Map of the Ladakh Batholith. (b) Leh-Khardung La section. (c) Kharu-Chang La section. (d) Lyoma-Hanle section.

(Appendix I). On the basis of these petrographic studies three main types of rocks have been identified and include diorite (16), granodiorite (27) and granite (10) with granodiorite being the most dominant.

In general, the rocks are medium to coarse grained. All the samples contain plagioclase, alkali feldspar, quartz, amphibole and biotite in variable proportions depending on the whole rock composition. The accessory minerals include apatite, zircon and opaque with altered chlorite. In many of the samples, opaque is present in considerable amount. These mafic minerals constitutes <5% in more leucocratic varieties and are as high as >25% in diorite.

Feldspar: Subhedral plagioclase feldspar is generally coarser than K-feldspar and occurs as euhedral to subhedral grains having lamellar twinning. Sometimes, the twin lamellae are partially erased due to deformation. Zoning is commonly observed in this variety of feldspar. Inclusions of fine prismatic zircon grains have also been observed in some of the grains. Feldspar shows maximum extinction angle of 22°-25° indicating andesine composition. Modally, it occurs as a major component in diorite, more or less in equal amounts with K-feldspar in granodiorite and in subordinate amounts in granite. Both varieties of alkali feldspars occur. Orthoclase is dominant over microcline except in coarse-grained varieties. Microperthite and perthite are common in granite. Andesine in diorite becomes more albitic to oligoclase in composition towards granodiorite. Myrmekites are developed along the margins of plagioclase as well as orthoclase and at the contact of quartz.

Quartz: Quartz grains are anhedral and, sometimes, stretched and elongated. Most of the quartz is looking strain-free, but undulose extinction is common. Quartz

content increases towards granodiorite to granite variety. They also occur as inclusions in plagioclase and alkali feldspar.

Amphibole: Amphibole is mainly of hornblende variety and occurs as euhedral to subhedral grains. It is present in almost all samples and many times the crushed margins show the development of altered chlorite.

Biotite: Biotite occurs in small amount, both brown as well as green biotite, green biotite indicating I-type of nature. Bending of flakes of biotite indicate evidences of deformation.

3.3 GEOCHEMISTRY

For geochemical analysis, all the fresh and unweathered 53 samples were selected for crushing. Approximately 5 kg of the fresh samples have been taken for sample processing. The samples were washed with distilled water to remove dust and other impurities, which might have been attached with the samples while collecting them from the field. After drying, the samples were broken into small chips of about 1.0 to 2.0 cm size. After thorough homogenization one quarter of the chipped samples was taken after proper coning and quartering for crushing. Jaw crusher with adjustable jaw spaces has been used to crush the samples up to -60 to -80 mesh size. Coning and quartering was again performed to collect 250 gm of the fine crushed samples for powdering in a ball mill grinder to -250 mesh size. Utmost care has been taken at every step to avoid any cross contamination. Samples were then analyzed by X-ray Fluorescence (XRF) Spectrometry for major oxide determination and the Inductively Coupled Plasma–Mass Spectrometer (ICP-MS) for trace and rare earth elements (REEs). For XRF the

instrument was calibrated by Test Sample analysis on BHVO-1; (Hawaiian Basalt USGS, USA), GSN (Granite, CRPG FRANCE) and GSR-1(Biotite granite, IGGE CHINA) XRF analysis was carried on Siemens, SRS 3000 XRF at Wadia Institute of Himalayan Geology (WIHG) Dehradun. Perkin Elmer ICP-MS was used for the analysis of REEs at National Geophysical Research Institute (NGRI), Hyderabad. The instrument was calibrated GSJ standard of granite, JG-2 and JG-3.

3.3.1 Analytical techniques: Major elemental abundance of the samples was carried out using Energy dispersive X-ray Flourescence (XRF) Spectrometry, which worked at at 12 kv tube voltage, 40 μA tube current in VAC with no filtered path. The sample was subjected to a live time of 200 seconds. The emission intensity of this particular radiation is measured with the suitable X-ray spectrometer (Potts, 1987) using international reference standards BHVO-1; (Hawaiian Basalt USGS, USA), GSN (Granite, CRPG FRANCE) and GSR-1(Biotite granite, IGGE CHINA) (Govindraju, 1989). Pressurized powder pellets of samples were prepared to measure the major oxide abundance. For the preparation of pellets about 5 gm of powdered sample was taken in an agate mortar, 1-2 drops of polyvinyl alchohol was added to the sample and was thoroughly mixed with pestle. It was then transferred to a steel cylindrical structure on boric acid pellet base with cover on which 4-5 lb hydraulic pressure was applied. This setup was left for 5 minutes to give the mixture an optimum binding time. After that time pressure was released and the sample was taken out from the cylinder in the form of a pellet. This pressurized pellet has been used for analysis with measurement accuracy better than 5% for major elements.

Utmost care was taken throughout the sample preparation, i.e. very fine powdering and proper homogenization. The major elemental oxide data have been listed in Table 3.1.

The ICP- MS used in this work, was ELAN DRC II Perkin- Elmer Sciex Instrument, USA controlled by an IBM-PC-XT microcomputer and associated software. Proper matching standard reference materials (GSJ standard of granite, JG-2 and JG-3.) were used for calibration along with dissolution method (Balaram, 1996). These standard reference materials helped in minimizing matrix and other interferences that are encountered in routine analysis and also help in checking measurement precision. The operating parameters were optimized to minimize the potential polyatomic and doubly–charged ion interferences. The mass spectrometer was operated in mass scanning mode. The detailed operation of the ICP-MS have been described by Balaram et al. (1995). 100 mg of sample were dissolved in Teflon beakers by HF, HNO_3 and $HClO_4$, using the procedure described by Balaram et al. (1996). Clear solutions were obtained in all cases. GSJ rock standards were also prepared in a similar way for calibrating the instrument and to assess the accuracy of measurements for different elements. ^{103}Rh was used as internal standards at a concentration level of 100 ng/ml to allow drift corrections to make each mass spectral region distinct. Couple of procedural blanks were also prepared. The blank, calibration standards and samples were run in a sequence along with two minutes wash of the nebulizer-spray chamber system with 5% HNO_3 in between ten samples. Data acquisition and reduction were done under software control. Altogether, 33 trace elements including 13 REEs were obtained by the ICP- MS and listed in Table no.3.2 and 3.3.

Table 3.1: Major element abundance data of Ladakh Batholith

	Granodiorite												
	N 53/5	NS 5/12	NS 5/14	NS 7/19	NS 9/20	NS 82/156	NS 83/157	NS 84/158	NS 85/161	NS 86/163	NS 87/164	NS 60/110	NS 71/126
SiO_2	69.61	75.02	66.99	66.62	68.43	72.12	70.28	66.89	72.25	69.9	67.77	75.91	67.81
TiO_2	0.51	0.17	0.67	0.74	0.63	0.31	0.38	0.62	0.26	0.53	0.64	0.13	0.46
Al_2O_3	14.5	12.64	15	15.17	14.95	14.1	14.3	15.24	14.37	14.73	14.63	12.8	14.99
$Fe_2O_3(T)$	3.13	0.75	3.49	4.61	4.02	2.21	2.63	3.96	1.64	3	4.24	1.56	3.13
MnO	1.21	0.34	1.3	1.53	1.27	0.83	1.07	1.85	0.79	1.67	1.76	0.28	1.3
MgO	2.18	1.65	3.21	3.94	3.04	2.13	1.78	2.2	1.7	2.02	2.75	1.2	2.16
CaO	4.6	4.52	5.04	4.81	5.01	4.34	3.97	4.8	4.62	4.23	5.04	4.66	5.7
Na_2O	3.12	2.66	1.93	1.72	1.83	2.89	3.53	2.51	3.88	3.89	1.74	3.65	1.85
K_2O	0.08	0.02	0.05	0.13	0.11	0.04	0.05	0.14	0.06	0.11	0.11	0.06	0.12
P_2O_5	0.2	0.04	0.32	0.33	0.23	0.07	0.09	0.23	0.08	0.16	0.26	0.03	0.16
Total	99.13	97.81	98.15	99.6	99.53	99.04	98.08	98.93	99.65	100.18	98.92	100.28	97.86
Norm. Qtz	26	36.47	23.59	23.93	25.57	31.3	30.29	22.46	26.83	25.13	25.26	32.99	22.13
Norm. Or.	20.4	16.55	13.01	11.79	12.18	18.36	23.2	17.08	24.31	25.4	11.85	22.5	17.33
Norm. Pl.	53.6	46.97	63	64.28	62.25	50.34	46.51	60.46	48.86	49.46	62.89	44.51	65.53
A/CNK	0.98	0.95	0.93	0.9	0.95	1	1.05	0.98	0.97	0.99	0.96	0.93	0.96

Table 3.1 continue..

Table 3.1 continue..

	Granodiorite													
	NS 72/129	NS 73/131	T 94/335	T 97/343	T 99/346	T 100/350	LB 8/23	LB 9/27	LB 10/28	LB 11/29	LB 12/30	LB 13/31	LB 14/32	LB 15/33
SiO_2	75.74	76.37	62.85	60.01	65.19	77.73	62.24	72.84	64.93	62.85	64.36	73.22	72.76	75.43
TiO_2	0.05	0.13	0.84	0.92	0.82	0.12	0.21	0.29	0.48	0.76	0.79	0.42	0.19	0.14
Al_2O_3	12.86	12.65	15.18	15.5	15.08	12.84	15.91	14.01	15.18	15.67	14.59	13.91	14.67	13.94
$Fe_2O_3(T)$	0.87	0.76	5.94	6.32	5.75	1.06	5.56	1.88	3.31	6.1	5.5	2.21	1.23	1.17
MnO	0.27	0.32	3.07	3.38	2.66	0.22	0.15	0.04	0.12	0.16	0.17	0.06	0.06	0.04
MgO	2.02	0.79	4.99	5.12	4.22	0.77	2.04	0.83	1.65	2.01	2.52	2.21	1.23	1.17
CaO	5.48	4.89	2.78	2.62	2.91	4.92	4.17	2.3	3.79	4.12	2.88	2.8	1.76	1.31
Na_2O	1.58	3.74	2.7	2.94	3.28	3.93	4.27	5.5	4.81	4.69	3.66	4.44	4.68	4.36
K_2O	0.01	0.02	0.09	0.1	0.09	0.02	1.78	1.09	1.78	1.86	2.55	1.73	3.6	3.96
P_2O_5	0.01	0.02	0.16	0.19	0.13	0.01	0.17	0.03	0.14	0.2	0.11	0.05	0.05	0.02
Total	98.89	99.69	98.6	97.09	100.14	101.64	97.02	98.81	96.34	98.39	97.12	99.53	99.61	100.84
Norm. Qtz	35.27	32.73	24.11	20.11	24.83	32.65	21	30.2	21.8	19.48	26.15	33.48	26.09	26.52
Norm. Or	9.82	22.88	20.03	22.61	23.35	23.63	12.2	6.79	12.9	12.77	17.92	10.79	21.94	24.65
Norm. Pl	54.91	44.39	55.86	57.28	51.82	43.72	66.8	63.01	65.3	67.75	55.93	55.73	51.97	48.83
A/CNK	0.9	0.94	0.92	0.92	0.95	0.94	0.92	0.98	0.92	0.91	1.04	0.98	0.99	1.01

Table 3.1 continue..

	Diorite															
	NS 1/1	NS 2/4	K-2	NS 84/160	NS 85/162	NS 62/112	NS 62/113	NS 64/116	T 95/339	T 96/342	T 98/345	T 101/351	LB 5/14	LB 9/25	LB 17/35	LB 18/36
SiO_2	61.83	57.35	57.68	59.96	54.54	59.91	59.1	56.82	51.46	53.36	61.97	63.04	50.17	48.61	53.47	54.35
TiO_2	0.9	1.08	1.29	0.99	1.41	0.73	0.81	0.31	1.05	1.03	0.9	0.71	1.32	0.46	0.97	0.99
Al_2O_3	16.92	18.28	15.33	16.6	15.31	16.85	17.86	12.38	15.49	16.25	16.94	15.97	15.8	8.69	14.96	15.2
$Fe_2O_3(T)$	4.83	5.91	8.2	6.56	8.49	6.25	6.88	9.51	10.82	9.48	4.86	6.08	11.7	9.88	9.65	8.85
MnO	2.21	2.57	5.59	3.48	6.04	2.28	2.19	9.48	6.32	6.86	2.29	3.13	0.22	0.15	0.22	0.15
MgO	3.99	5.7	6.14	5.36	6.66	6.48	6.11	6.62	8.74	8.83	3.98	4.47	6.3	14.73	6.94	6.14
CaO	4.45	4.38	3.68	5	3.41	3.6	3.51	3	2.52	2.65	4.51	3.45	7.75	14.42	5.79	6.64
Na_2O	2.11	1.93	1.74	1.15	1.73	1.54	2.38	0.18	1.14	1.17	2.14	2.99	3.09	0.79	3.12	2.99
K_2O	0.14	0.15	0.22	0.25	0.22	0.11	0.13	0.14	0.18	0.15	0.14	0.12	1.44	0.25	1.84	1.94
P_2O_5	0.31	0.37	0.43	0.42	0.49	0.39	0.31	0.01	0.12	0.17	0.31	0.15	0.22	0.11	0.19	0.14
Total	97.7	97.52	100.3	99.78	98.1	98.15	99.29	98.4	97.83	99.95	98.05	100.11	98.02	98.09	97.33	97.38
Norm. Qtz	17.74	8.52	10.14	11.19	6.35	18.41	13.72	14.47	3.79	4.69	17.17	18.5	6.21	4.89	12.1	12.1
Norm. Or.	15.11	14.3	15.01	8.8	15.99	11.56	17.41	1.98	11.65	11.91	15.3	21.78	13.02	5.02	16.11	16.62
Norm. Pl.	67.15	77.18	74.85	80.01	77.66	70.13	68.87	83.55	84.56	84	67.53	59.72	80.77	90.09	71.59	71.28
A/CNK	1	0.91	0.81	0.86	0.77	0.87	0.92	0.72	0.73	0.75	1	0.94	0.76	0.33	0.85	0.8

Table 3.1 continue..

Table 3.1 continue..

	Granite									
	NS 1/2	NS 2/3	NS 84/159	NS 3/7	NS 72/127	NS 72/128	NS 72/130	T 93/334	T 96/341	LB 16/74
SiO_2	73.19	74.95	77.51	76.54	74.34	75.96	75.33	69.17	68.59	73.5
TiO_2	0.29	0.25	0.18	0.07	0.1	0.07	0.07	0.75	0.68	0.19
Al_2O_3	14.01	13.05	12.22	12.66	13	12.84	12.78	13.67	13.69	14.35
$Fe_2O_3(T)$	2.3	1.59	1.23	0.69	0.88	0.68	0.91	5.05	4.97	1.4
MnO	0.86	0.61	0.39	0.19	0.35	0.18	0.26	2.4	1.97	0.07
MgO	1.42	1.14	0.88	0.6	0.7	0.59	0.62	2.91	2.94	1.4
CaO	4.22	3.87	3.1	4.67	4.59	4.66	4.46	2.49	2.59	0.86
Na_2O	4.13	4.43	5.17	4.32	4.2	4.46	4.4	4.02	4.11	4.54
K_2O	0.12	0.03	0.03	0.02	0.02	0.02	0.02	0.09	0.07	4.74
P_2O_5	0.07	0.06	0.03	0.01	0.02	0.01	0.01	0.14	0.1	0.04
Total	100.61	99.98	100.75	99.73	98.2	99.46	98.85	100.69	99.71	100.16
Norm. Qtz	29.18	33	37.59	32.24	30.79	31.24	31.82	31.97	30.67	25.76
Norm. Or	25.92	27.38	31.29	26.27	25.98	27.16	27.03	27.7	28.16	29.53
Norm. Pl.	44.9	39.62	31.12	41.5	43.23	41.6	41.15	40.33	41.17	44.71
A/CNK	1	0.99	0.99	0.95	0.97	0.95	0.97	0.99	0.97	1.02

Table 3.2: Trace elemental abundance data of Ladakh Batholith

	Granodiorite													
	NS 3/5	NS 5/12	NS 6/14	NS 7/19	NS 9/20	NS 82/156	NS 83/157	NS 84/158	NS 85/161	NS 86/163	NS 87/164	NS 60/110	NS 71/126	NS 72/129
Sc	1.257	2.288	3.668	10.62	3.322	1.881	3.632	6.341	2.439	5.943	6.199	2.043	3.285	2.335
V	8.678	8.912	47.83	62.02	16.99	16.17	23.65	42.37	41.07	41.67	46.55	5.224	17.23	2.979
Cr	0.922	0.925	12.4	12.97	2.431	0.798	13.25	12.96	0.57	14.78	14.84	0.549	0.988	0.764
Co	1.903	16.95	13.21	43.92	41.58	4.496	3.074	5.166	2.913	4.042	3.939	29.71	38	16.41
Ni	2.488	2.285	5.441	4.533	2.36	3.714	10.5	4.127	2.035	3.565	4.519	1.689	2.311	2.22
Cu	0.883	0.775	4.418	4.836	0.845	1.573	6.405	5.796	1.016	4.652	7.232	0.593	1.114	1.229
Zn	12.01	23.79	57.43	61.52	47.11	50.95	40.98	56.12	31.48	53.2	59.5	18.31	27.71	17.88
Ga	14.94	14.32	15.56	15.89	19.91	15.19	12.13	16.32	17.79	14.87	15.63	17.87	19.31	15.97
Rb	32.34	71.44	38.22	46.63	51.31	56.72	56.81	67.21	118.9	91.48	45.72	136.2	56.82	167.2
Sr	128.9	90.47	291.8	312.8	177.6	147.6	223.5	231.2	99.69	187.6	242.1	51.9	135.6	19.43
Y	8.113	10.81	16.81	24.1	24.33	6.239	8.005	46.13	32.09	27.43	31.64	21.68	25.36	27.19
Zr	2.155	1.92	37.21	63.97	6.926	3.818	23.83	25.42	6.015	27.02	31.44	10.64	13.63	7.398
Nb	3.005	5.94	9.492	8.158	7.6	3.466	4.564	12.44	11.41	10.25	6.89	12.2	11.02	15.15
Cs	0.481	0.732	1.102	1.488	1.584	1.199	1.244	2.43	1.653	2.226	1.891	4.896	1.267	1.005
Ba	167.9	324.3	453.8	413.4	282.7	1639	4274	391.5	316.9	515.4	310.6	294.1	347.8	129.9
Hf	0.084	0.041	1.26	2.53	0.19	0.063	0.573	1.297	0.21	1.217	1.261	0.337	0.27	0.246
Ta	0.183	0.275	0.97	1.967	0.416	0.207	0.637	1.792	0.744	1.481	1.103	1.183	0.891	1.275
Pb	9.076	9.496	7.527	8.145	9.871	13.84	18.98	26.23	11.49	29.78	27.9	13.62	9.375	16.44
Th	5.063	5.142	5.23	7.952	4.209	5.506	18.03	14.24	8.964	13.78	10.06	15.21	5.313	10.81
U	0.505	0.383	0.862	1.814	0.506	0.407	0.638	1.862	1.722	0.921	0.697	2.476	1.027	1.627

Table 3.2 continue..

Table 3.2 continue..

	Granodiorite												
	NS	T	T	T	T	LB	LB	LB	LB	LB	LB	LB	LB
	73/131	94/335	97/343	99/346	100/350	8/23	9/27	10/28	11/29	12/30	13/31	14/32	15/33
Sc	2.129	10.75	11.34	9.219	2.28	8.683	2.113	9.631	13.82	10.02	1.556	2.236	1.792
V	5.702	115.8	122.2	100.1	5.663	73.2	8.975	43.93	82.68	58.2	13	8.303	6.948
Cr	0.686	60.36	83.02	78.03	1.802	57.9	0.757	46.77	46.93	65.67	0.906	0.075	0.723
Co	44.69	26.52	32.27	33.81	1.082	8.117	2.859	5.24	7.286	8.033	2.798	2.317	1.644
Ni	1.86	20.73	19.01	16.84	1.746	4.509	2.432	4.318	4.401	8.424	3.228	1.802	1.718
Cu	1.048	9.954	8.207	7.386	0.469	3.408	0.779	3.01	3.943	3.798	0.627	0.971	0.477
Zn	23.59	101.7	112.6	102.4	12.63	88.81	23.23	68.12	87.36	113.8	30.1	24.78	14.48
Ga	16.32	15.32	16.46	15.59	16.02	15.69	17.26	15.25	15.99	15.8	16.57	16.49	13.93
Rb	134	108.5	116.2	139	178.2	50.58	28.84	42.76	45.93	91.29	45.61	82.76	77.2
Sr	43	246.4	252.7	232.7	17.09	301.5	131.4	267.3	243.8	226.7	173.4	108.1	65.39
Y	26.94	35.44	37.71	33.67	19.84	47.01	8.988	31.24	66.74	35.75	11.03	11.02	3.068
Zr	8.185	20.79	18.11	16.9	13.28	21.42	4.108	15.66	25.55	13.1	4.505	5.01	2.966
Nb	9.272	9.315	10.08	11.06	14.55	11.28	3.188	6.124	12.79	9.66	8.448	6.113	4.28
Cs	0.819	7.702	8.124	16.14	3.305	2.371	0.969	1.012	1.114	2.137	0.959	0.818	0.75
Ba	104.8	266.7	307.1	317.9	38.2	269.6	237.1	350.6	325	400.6	207.8	347.7	312.7
Hf	0.235	0.518	0.801	0.942	0.456	1.183	0.143	0.732	1.477	0.735	0.139	0.132	0.078
Ta	0.553	1.054	0.821	1.256	0.741	1.126	0.092	0.321	0.733	0.73	0.551	0.272	0.163
Pb	13.45	0.99	29.53	25.38	15.05	17.68	12.24	19.89	17.64	18.48	10.13	11.5	10.81
Th	10.45	82.2	22.23	15.48	19.32	8.502	26.32	3.817	6.776	5.373	15.27	9.356	3.128
U	1.044	15.53	1.458	3.493	1.368	3.034	0.488	0.899	1.505	1.684	1.021	0.484	0.404

Table 3.2 continue..

	Diorite															
	NS 1/1	NS 2/4	K-2	NS 84/160	NS 85/162	NS 62/112	NS 62/113	NS 64/116	T 95/339	T 96/342	T 98/345	T 101/351	LB 5/14	LB 9/25	LB 17/35	LB 18/36
Sc	5.525	15.25	21.43	15.34	23.13	7.364	6.925	10.24	22.11	15.88	9.552	9.968	18.39	49.17	17.5	15.11
V	69.07	91.22	134.4	91.77	137.2	37.23	39.36	61.08	196.4	165.4	103.4	109.1	203.7	177.4	195	165.6
Cr	13.22	14.72	13.8	10.53	12.29	2.112	0.954	4.204	64.22	99.5	60	79.65	51.95	442.3	41.14	74.94
Co	7.033	8.1	15.11	9.707	16.24	25.7	28.23	53.9	42.31	47.48	12.94	13.64	17.16	64.42	16.37	20.1
Ni	6.031	4.694	6.894	3.987	8.48	6.084	21.04	56.92	21.05	21.23	12.39	14.89	6.291	88.55	5.875	14.09
Cu	6.275	7.397	8.059	8.977	9.126	512	2.858	1.361	10.15	15.04	5.155	6.027	7.267	23.69	6.101	11.43
Zn	67.25	76.13	91.97	70.68	93.18	66.47	65.79	39.65	139.4	118.6	91.66	102.4	156.9	83.83	138.7	100.4
Ga	19.55	20.14	19.02	17.12	18.57	9.62	20.78	11.74	17.52	16.42	14.59	15.59	18.22	8.484	17.61	16.42
Rb	84.3	58.33	41.06	33.56	36.65	6.27	81.44	6.692	39.79	66.77	87.55	93.57	34.13	3.778	32.37	53.4
Sr	380.4	457.9	371.4	263.6	375.3	189	207.8	76.82	311.2	392.6	280.5	276.5	433.8	164.8	431.4	386.7
Y	22.19	44.93	47.41	40.65	55.98	33.86	32.56	8.07	33.12	30.76	35.99	38.44	45.27	18.14	44.09	30.21
Zr	20.77	72.15	76.52	35.69	78.69	16.88	38.15	12.83	98.1	125.5	55.9	44.4	36.02	66.18	36.48	35.77
Nb	17.21	10.82	10.52	9.587	13.39	6.137	9.13	2.96	4.354	5.275	11.17	11.79	5.29	0.919	5.457	5.227
Cs	3.112	2.31	1.816	1.958	2.555	1.635	3.241	0.369	4.712	11.17	3.612	3.852	1.457	0.276	1.422	2.452
Ba	348.4	320.8	325.5	205.4	271.2	166.4	296.5	77.23	172.5	170.6	346.5	376.8	223.3	89.76	215.3	286
Hf	0.747	3.343	1.707	1.973	4.22	0.862	1.09	0.535	0.45	0.426	1.73	1.869	1.926	1.978	1.923	2.03
Ta	1.953	1.413	1.191	1.116	1.393	1.503	0.674	0.241	3.115	4.589	0.806	0.922	0.328	0.061	0.424	0.437
Pb	7.398	7.547	16.37	26.21	26.92	38.62	45.21	41.59	0.451	0.462	19.79	24.86	17.18	13.55	15.51	21.66
Th	2.818	7.037	7.582	2.914	6.786	3.978	5.191	0.861	72.89	23.01	12.27	13.18	2.806	0.918	1.599	8.39
U	1.367	2.07	1.251	0.38	1.017	0.777	0.582	0.253	4.093	4.471	1.887	1.917	0.684	0.239	0.644	1.338

Table 3.2 continue..

Table 3.2 continue..

	Granite									
	NS 1/2	NS 2/3	NS 84159	NS 3/7	NS 72/127	NS 72/128	NS 72/130	T 93/334	T 96/341	LB 16/34
Sc	2.485	2.319	1.435	4.718	2.842	2.409	2.499	9.418	9.828	1.751
V	12.58	11.3	8.37	35.28	4.205	2.813	7.054	96.36	95.62	7.479
Cr	0.824	0.859	0.711	12.27	0.742	0.715	0.824	24.03	25.94	0.841
Co	3.573	2.064	1.597	3.17	19.67	19.41	19.63	21.57	24.15	1.843
Ni	2.695	2.413	1.44	20.85	1.262	1.386	2.604	14.11	13.13	2.268
Cu	1.002	0.975	0.992	8.548	0.842	0.819	0.901	4.284	5.768	0.856
Zn	38.05	24.11	27.5	48.06	14.46	10.68	14.54	57	51.47	19.38
Ga	17.3	15.98	12.52	15.35	17.96	15.93	16.73	16.37	15.51	15.63
Rb	126.7	91.62	105.3	75.67	154.4	166.3	171.8	219.6	198.6	73.97
Sr	95.39	75.62	102.2	232.3	15.57	12.19	13.29	140.8	152.3	40.92
Y	14.12	15.81	2.166	9.49	33.99	20.05	28.46	48.23	39.67	11.6
Zr	4.89	3.611	1.171	16.61	14.34	7.263	9.608	60.21	50.19	3.635
Nb	9.09	11.06	3.628	6.33	18.4	11.93	14.27	19.74	15.01	4.62
Cs	1.463	0.978	0.992	1.552	1.902	0.984	1.027	13.52	14.06	0.595
Ba	401	372.4	1667	511.9	133.1	128.3	119.8	214.9	231.1	204
Hf	0.109	0.107	0.074	0.583	0.531	0.259	0.338	3.975	3.628	0.098
Ta	0.253	0.373	0.053	0.63	0.945	1.259	1.346	4.58	3.604	0.287
Pb	11.49	10.25	11.57	8.367	13.67	14.76	14.87	37.27	32.63	13.72
Th	9.232	10.47	4.381	11.03	13.7	10.66	10.99	55.74	106.2	9.815
U	0.438	0.362	0.72	0.883	1.757	1.471	1.633	5.22	14.3	0.387

Table 3.3: Rare Earth Element (REE) abundance data of Ladakh Batholith

	Granodiorite												
	NS	T	T	T	T	LB	LB	LB	LB	LB	LB	LB	LB
	73/131	94/135	97/141	99/146	100/350	8/23	9/27	10/28	11/29	12/30	13/31	14/32	15/33
La	27.312	23.419	21.753	20.006	14.694	13.078	96.309	11.589	19.376	12.17	84.364	28.352	6.103
Ce	52.184	58.469	55.974	50.374	38.174	38.631	164.67	29.256	55.962	35.113	139.14	52.452	10.133
Pr	5.139	8.013	7.827	6.992	3.57	5.855	15.254	4.158	8.577	5.13	12.724	4.988	0.912
Nd	18.55	27.437	27.686	24.151	13.623	21.631	51.24	15.111	32.028	18.608	41.516	17.605	3.221
Sm	3.11	5.667	5.855	5.228	2.518	5.128	6.039	3.666	7.83	4.284	4.246	2.86	0.656
Eu	0.385	1.101	1.214	1.067	0.118	1.28	0.796	0.953	1.587	1.041	0.727	0.481	0.41
Gd	2.609	4.573	4.701	4.216	2.225	4.319	5.053	3.169	6.734	3.548	3.872	2.233	0.442
Tb	0.406	0.935	0.951	0.859	0.334	0.992	0.414	0.703	1.523	0.794	0.52	0.277	0.064
Dy	2.917	4.792	5.144	4.619	2.262	5.659	1.745	4.116	8.911	4.485	1.51	1.556	0.328
Er	1.211	3.008	3.102	2.748	0.961	3.875	0.398	2.643	5.567	2.999	0.55	0.473	0.146
Tm	0.184	0.489	0.483	0.456	0.138	0.696	0.033	0.422	0.905	0.509	0.065	0.05	0.018
Yb	1.925	3.223	3.281	2.986	1.432	5.014	0.285	2.751	5.979	3.591	0.707	0.495	0.232
Lu	0.315	0.508	0.538	0.491	0.235	0.813	0.046	0.44	0.926	0.565	0.121	0.075	0.041
ΣREE	116.25	141.63	138.56	124.17	80.284	106.97	342.28	78.977	155.9	92.832	291.86	111.9	22.706
Eu/Sm	0.12	0.2	0.21	0.2	0.05	0.25	0.132	0.26	0.203	0.243	0.171	0.168	0.625
(La/Lu)N	9.2924	4.0513	4.3333	4.3668	6.7013	1.724	224.39	2.8228	2.2425	2.3085	74.723	40.514	15.953
(La/Yb)N	10.18	4.32	4.76	4.81	7.36	1.871	95.28	3.022	2.325	2.431	85.59	41.08	18.87
(La/Sm)N	5.67	2.32	2.4	2.47	3.77	1.646	10.29	2.041	1.598	1.864	12.83	6.4	6.006
Eu/Eu*	0.4132	0.6866	0.7074	0.6948	0.1524	0.8315	0.4405	0.8548	0.6682	0.8163	0.5482	0.5819	0.6484

Table 3.3 continue..

	Granodiorite												
	NS	T	T	T	T	LB	LB	LB	LB	LB	LB	LB	LB
	73/131	94/335	97/343	99/336	100/350	8/23	9/27	10/28	11/29	12/30	13/31	14/32	15/33
La	27.312	23.419	21.753	20.006	14.694	13.078	96.309	11.589	19.376	12.17	84.364	28.352	6.103
Ce	82.184	58.469	55.974	50.374	38.174	28.631	164.67	29.256	55.962	35.113	139.14	52.452	10.133
Pr	5.139	8.013	7.877	6.992	3.57	5.855	15.254	4.158	8.577	5.13	12.724	4.988	0.912
Nd	18.55	27.439	27.686	24.151	13.623	21.631	51.24	15.111	32.025	18.608	43.516	17.605	3.221
Sm	3.11	5.667	5.855	5.228	2.538	3.128	6.039	3.666	7.83	4.284	4.246	2.86	0.656
Eu	0.385	1.101	1.214	1.067	0.118	1.28	0.796	0.953	1.587	1.041	0.727	0.481	0.41
Gd	2.609	4.573	4.701	4.216	2.225	4.319	5.053	3.169	6.734	3.548	3.872	2.233	0.442
Tb	0.406	0.935	0.953	0.859	0.334	0.992	0.414	0.703	1.523	0.794	0.32	0.277	0.064
Dy	2.917	4.792	5.144	4.619	2.262	5.659	1.745	4.176	8.911	4.485	1.51	1.556	0.328
Er	1.211	3.008	3.102	2.748	0.961	3.875	0.398	2.643	5.567	2.999	0.55	0.473	0.146
Tm	0.184	0.489	0.483	0.436	0.138	0.696	0.033	0.422	0.905	0.509	0.065	0.05	0.018
Yb	1.925	3.223	3.281	2.986	1.432	5.014	0.285	2.751	5.979	3.591	0.707	0.495	0.232
Lu	0.315	0.508	0.538	0.491	0.235	0.813	0.046	0.44	0.926	0.565	0.121	0.075	0.041
ΣREE	116.75	141.63	138.56	124.17	80.284	106.97	342.28	78.977	155.9	92.837	291.86	111.9	22.706
Eu/Sm	0.12	0.2	0.21	0.2	0.05	0.25	0.132	0.26	0.203	0.243	0.171	0.168	0.625
(La/Lu)N	9.2924	4.0513	4.3333	4.3668	6.7013	724	224.39	2.8278	2.2425	2.3085	74.723	40.514	15.953
(La/Yb)N	10.18	4.32	4.76	4.81	7.36	871	95.78	3.022	2.325	2.431	85.59	41.08	18.87
(La/Sm)N	5.67	2.32	2.4	2.42	3.77	646	10.29	2.041	1.598	1.814	12.83	6.4	6.006
Eu/Eu*	0.4132	0.6866	0.7074	0.6948	0.1524	0.8315	0.4405	0.8548	0.6682	0.8163	0.5482	0.5819	0.6484

	Diorite												
	NS 1/1	NS 2/4	K-2	NS 88/160	NS 85/162	NS 62/112	NS 62/113	NS 64/116	T 95/339	T 96/342	T 98/345	T 101/351	LB 5/14
La	13.183	31.35	36.84	25.626	36.631	22.626	27.506	4.141	10.262	14.068	23.419	24.759	11.47
Ce	26.448	68.3	78.46	58.619	83.796	48.262	55.284	8.366	27.631	36.599	58.469	62.027	34.5
Pr	3.329	8.819	10.02	7.465	10.717	5.554	6.261	0.938	4.215	5.38	8.013	8.574	5.621
Nd	13.379	35.16	39.11	28.119	41.618	24.596	26.313	3.934	16.235	20.204	27.437	29.514	22.94
Sm	3.378	7.964	8.65	6.518	9.466	5.325	5.718	0.921	4.141	4.67	5.667	5.94	5.952
Eu	1.409	2.334	2.144	1.471	2.271	1.139	1.5	0.202	1.197	1.221	1.101	1.189	1.695
Gd	2.998	7.17	7.851	5.764	8.845	4.619	4.694	0.86	3.528	3.913	4.573	4.926	4.983
Tb	0.544	1.273	1.331	1.014	1.525	0.755	0.749	0.148	0.804	0.788	0.935	0.972	1.116
Dy	3.296	7.097	7.492	6.113	8.838	5.073	5.076	1.066	4.527	4.291	4.792	5.244	6.3
Er	1.862	3.952	4.196	3.786	5.192	1.938	1.799	0.433	2.872	2.678	3.008	3.18	3.961
Tm	0.264	0.537	0.59	0.541	0.717	0.245	0.225	0.067	0.446	0.422	0.489	0.507	0.618
Yb	2.476	5.032	5.064	5.097	6.569	2.392	2.106	0.707	2.976	2.677	3.223	3.352	4.242
Lu	0.361	0.697	0.709	0.696	0.878	0.405	0.31	0.114	0.45	0.426	0.508	0.535	0.654
∑REE	72.927	179.7	202.4	150.85	217.08	122.93	137.54	21.937	79.281	97.237	141.63	150.72	104.1
Eu/Sm	0.308	0.293	0.248	0.23	0.24	0.21	0.26	0.22	0.29	0.26	0.19	0.2	0.285
(La/Lu)N	3.9137	4.82	5.569	3.946	4.4714	5.9874	9.5094	3.893	2.444	3.5392	4.9407	4.9598	1.879
(La/Yb)N	3.819	4.469	5.218	3.61	4	6.79	9.37	4.2	2.47	3.77	5.21	5.3	1.939
(La/Sm)N	2.519	2.541	2.749	2.54	2.5	2.74	3.11	2.9	1.6	1.95	2.67	2.69	1.244
Eu/Eu*	1.0000	0.9443	0.7954	0.7337	0.7588	0.7021	0.8852	0.6939	0.8732	0.6612	0.9574	0.6720	0.9515

Table 3.3 continue..

Table 3.3 continue..

	Diorite						Granite						
	LB 9/25	LB 17/35	LB 18/36	NS 1/2	NS 2/3	NS 84/159	NS 3/7	NS 72/127	NS 72/128	NS 72/130	T 93/334	T 96/341	LB 16/34
La	3.091	9.315	13.699	33.951	40.282	16.492	23.82	32.122	26.181	24.244	44.21	73.602	22.076
Ce	8.457	29.643	37.879	70.402	75	23.483	44.727	63.649	50.433	47.196	98.535	141.89	46.08
Pr	1.442	5.017	5.484	6.96	7.48	1.752	4.931	6.528	5.006	4.727	12.294	15.881	4.632
Nd	6.269	21.076	20.347	25.772	27.25	5.468	17.369	23.687	18.102	16.975	44.7	52.381	16.54
Sm	1.983	5.421	4.643	4.023	4.251	0.921	2.963	4.606	3.052	3.29	9.641	9.323	2.985
Eu	0.588	1.627	1.079	0.64	0.553	0.624	1.267	0.192	0.161	0.163	1.044	0.927	0.238
Gd	1.847	4.756	3.723	3.205	3.393	0.533	2.451	3.819	2.675	3.132	8.171	7.991	2.363
Tb	0.45	1.068	0.754	0.402	0.422	0.047	0.293	0.616	0.384	0.515	1.355	1.259	0.297
Dy	2.529	6.028	4.139	2.113	2.328	0.236	1.463	4.232	2.61	3.642	7.564	6.547	1.702
Er	1.606	3.812	2.64	0.579	0.689	0.095	0.81	1.587	0.94	1.32	4.202	3.559	0.505
Tm	0.258	0.614	0.441	0.059	0.084	0.013	0.107	0.232	0.13	0.184	0.589	0.476	0.066
Yb	1.698	4.151	2.919	0.546	0.637	0.153	1.087	2.32	1.354	1.913	5.516	4.455	0.623
Lu	0.264	0.652	0.489	0.096	0.088	0.033	0.179	0.362	0.23	0.316	0.74	0.607	0.088
∑REE	30.48	93.48	98.236	152.8	162.46	49.85	101.47	143.85	111.27	107.62	238.56	318.9	98.195
Eu/Sm	0.297	0.3	0.232	0.157	0.13	0.678	0.428	0.04	0.05	0.05	0.11	0.1	0.08
(La/Lu)N	1.2548	1.5312	3.0024	4.8202	49.058	53.561	14.262	9.51	12.2	8.2225	6.4029	12.995	26.886
(La/Yb)N	1.306	1.61	3.366	49.86	45.36	77.37	15.72	9.93	15.87	9.09	5.75	11.85	25.42
(La/Sm)N	1.007	1.109	1.905	6.015	6.117	11.56	5.19	4.6	5.52	4.76	2.96	5.1	4.774
Eu/Eu*	0.9398	0.9796	0.7934	0.5415	0.4451	0.3790	0.5820	0.1415	0.1720	0.1552	0.3596	0.3283	0.2340

3.3 2 Results and discussions:

3.3.2.1 Major element geochemistry: The Ladakh Batholith exhibits a wide major elemental compositional range from basic to acid (SiO_2-48.61 wt.% to 76.37 wt.%) indicating wide variation in terms of degree of partial melting. It also indicates meta-aluminous character having A/CNK ($Al_2O_3/CaO+Na_2O+K_2O$) ratio <1.1 (Zen,.1986; Chappel and White, 1992). The range of A/CNK ratio is 0.76 to 1.05 indicating I-type affinity with sub-alkaline character. The normative data of all varieties of rock from the batholith plot in the field of granite, granodiorite, quartz-monzodiorite, monzodiorite and quartz-diorite and diorite in the Quartz–Alkali Feldspar–Plagioclase (Q-A-P) normative plot (Fig.3.2) of Streikeisen (1976). Large number of samples lie in the granodiorite (twenty seven) field, few in granite field (ten) and sixteen in more mafic dioritic or monzodioritic and quartz dioritic varieties. However, the AFM (Al2O3-FeO*-MgO) plot (Fig. 3.3) indicate calc-alkaline series of magmatism (Irvine and Barager, 1971). Further K_2O vs. SiO_2 diagram (Fig. 3.4) indicate medium to high-K type rock (Le Maitre et al., 1989) of calc-alkaline series (Rickwood, 1989). The SiO_2 content of granodiorite ranges from 77.73 to 60.01 wt% with lower range of 63.04 to 48.61 wt% for diorite and almost similar range of 77.51 wt.% to 68.59 wt.% for granite. MgO content is maximum in diorite ranging between 14.73 to 3.98 wt.% with lower in granodiorite (4.99 to 1.20 wt.% and lowest in granite (2.94 to 0.60 wt.%). Similarly, CaO content is maximum in diorite with 14.42 wt.% to 21.52 wt.% and lower in granodiorite (5.70 to 1.31 wt.%) and granite (4.66 to 0.86 wt.%). The major elemental data define an almost linear trend in the Harker's variation binary diagram, where SiO_2 has been used as a differentiation index against TiO_2 (Fig. 3.5 a), MgO (Fig. 3.5 b), Al_2O_3 (Fig. 3.5 c), CaO (Fig. 3.5 d), Fe_2O_3

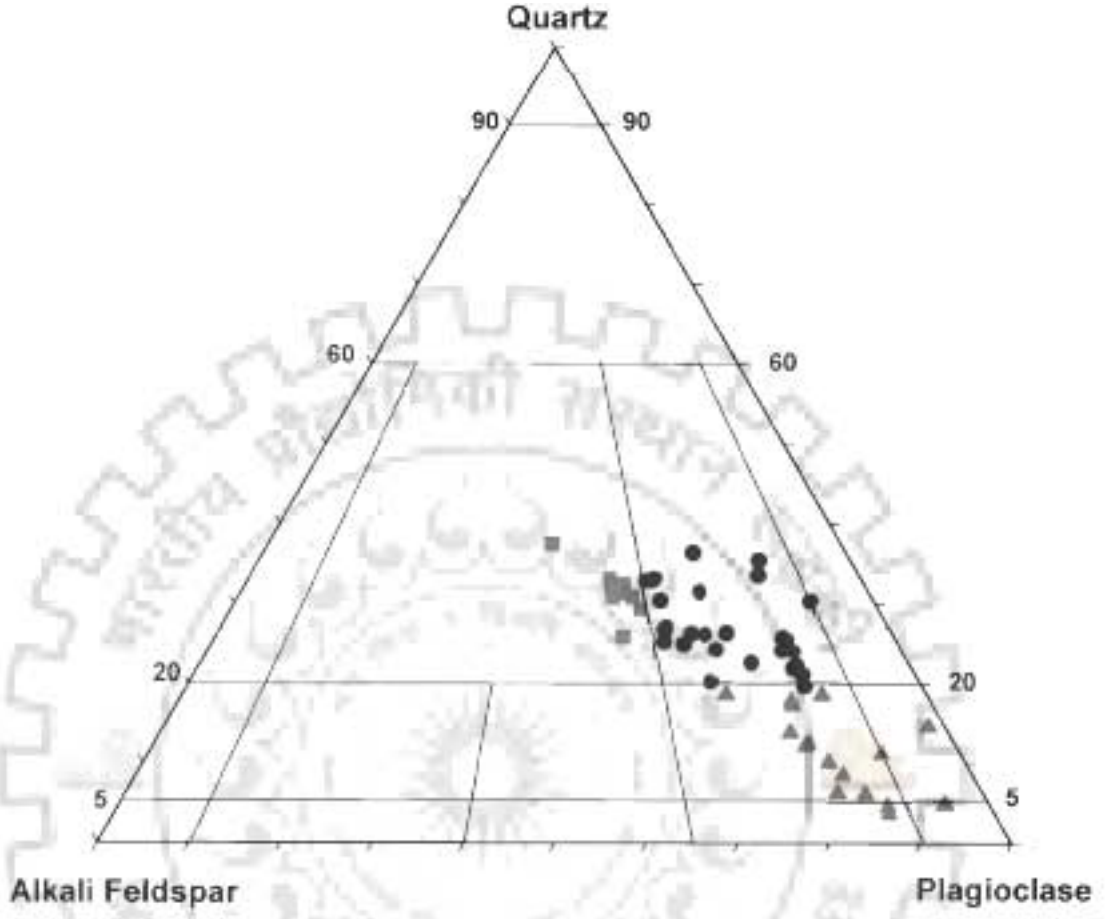

Figure 3.2: QAP plot of the Ladakh Batholith (After Strieckensen, 1976)

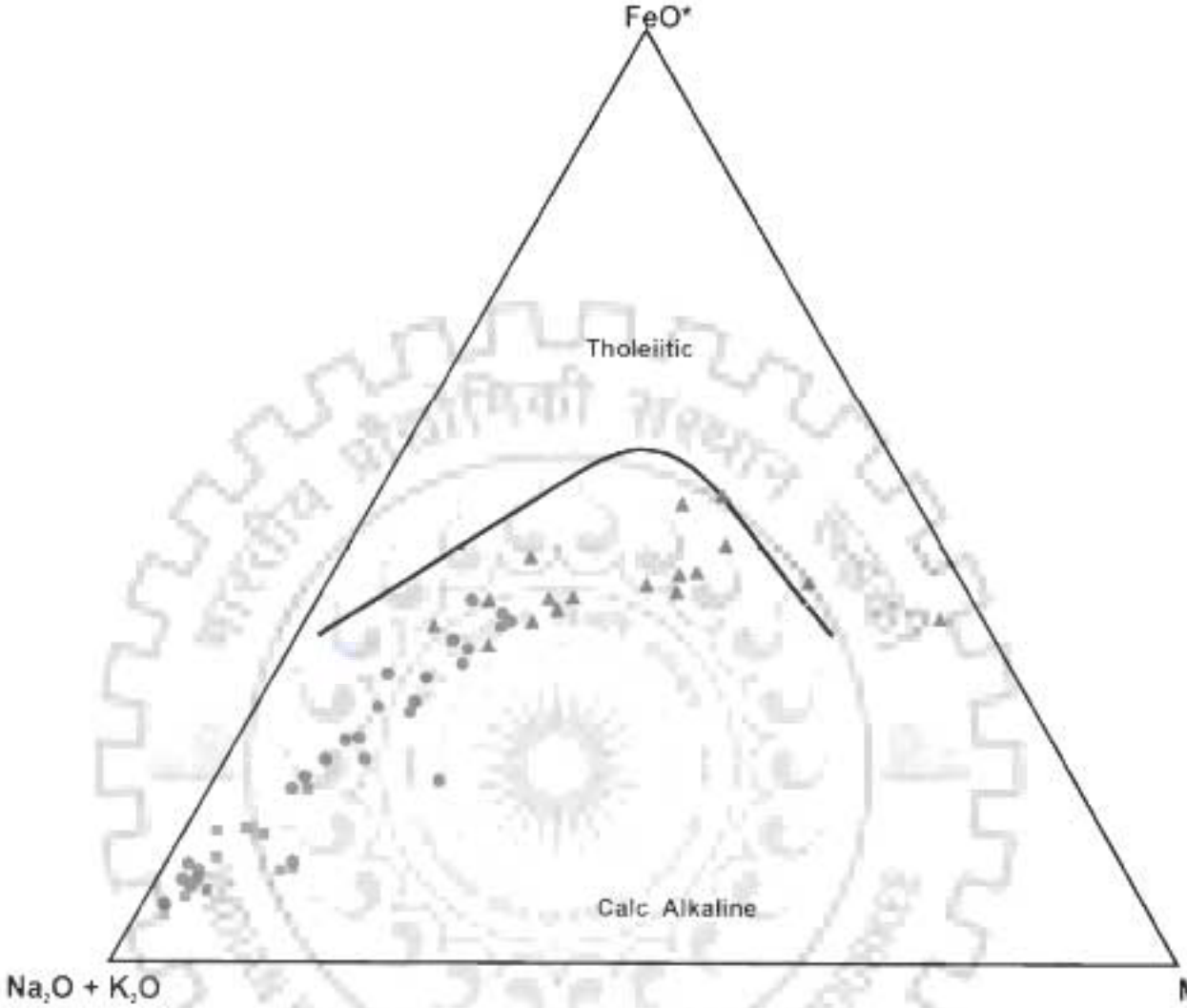

Figure 3.3: AFM Plot for Ladakh Batholith, (fields after Irvine & Baragar 1971

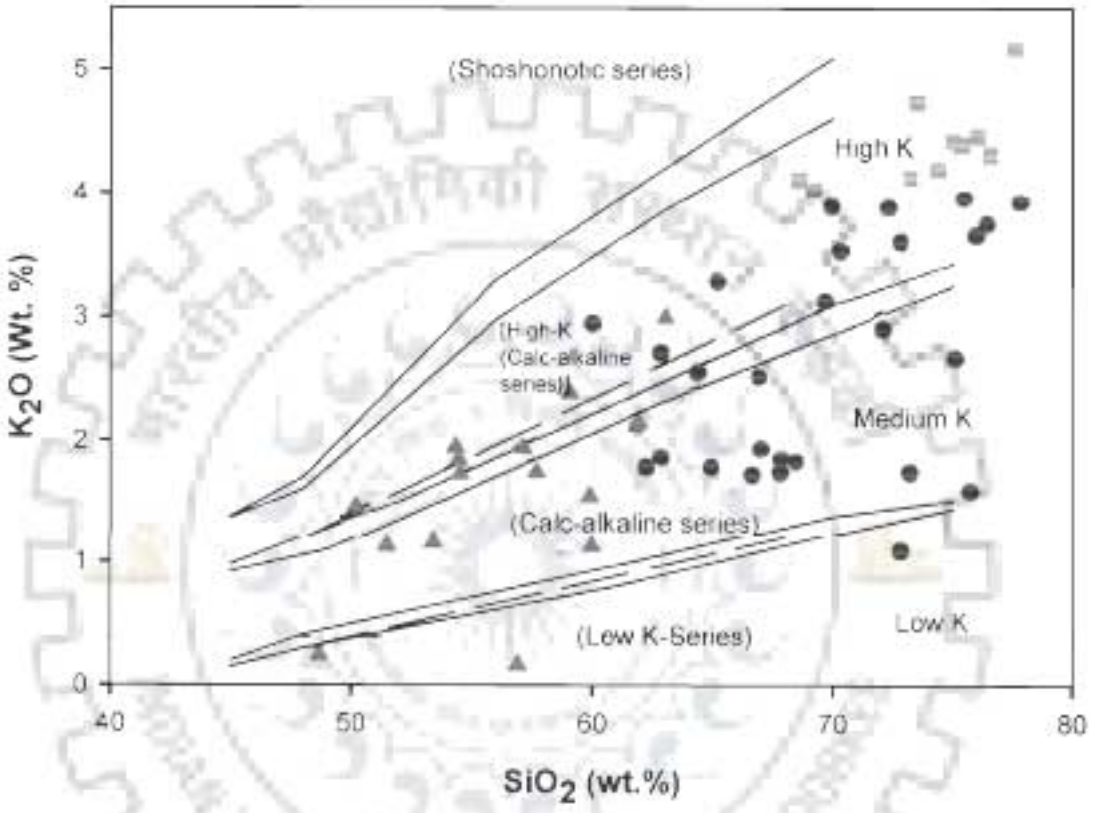

Figure 3.4: SiO_2 vs. K_2O plot of the Ladakh Batholith (fields after Le Maitre et al., 1989 and Rickwood, 1989)

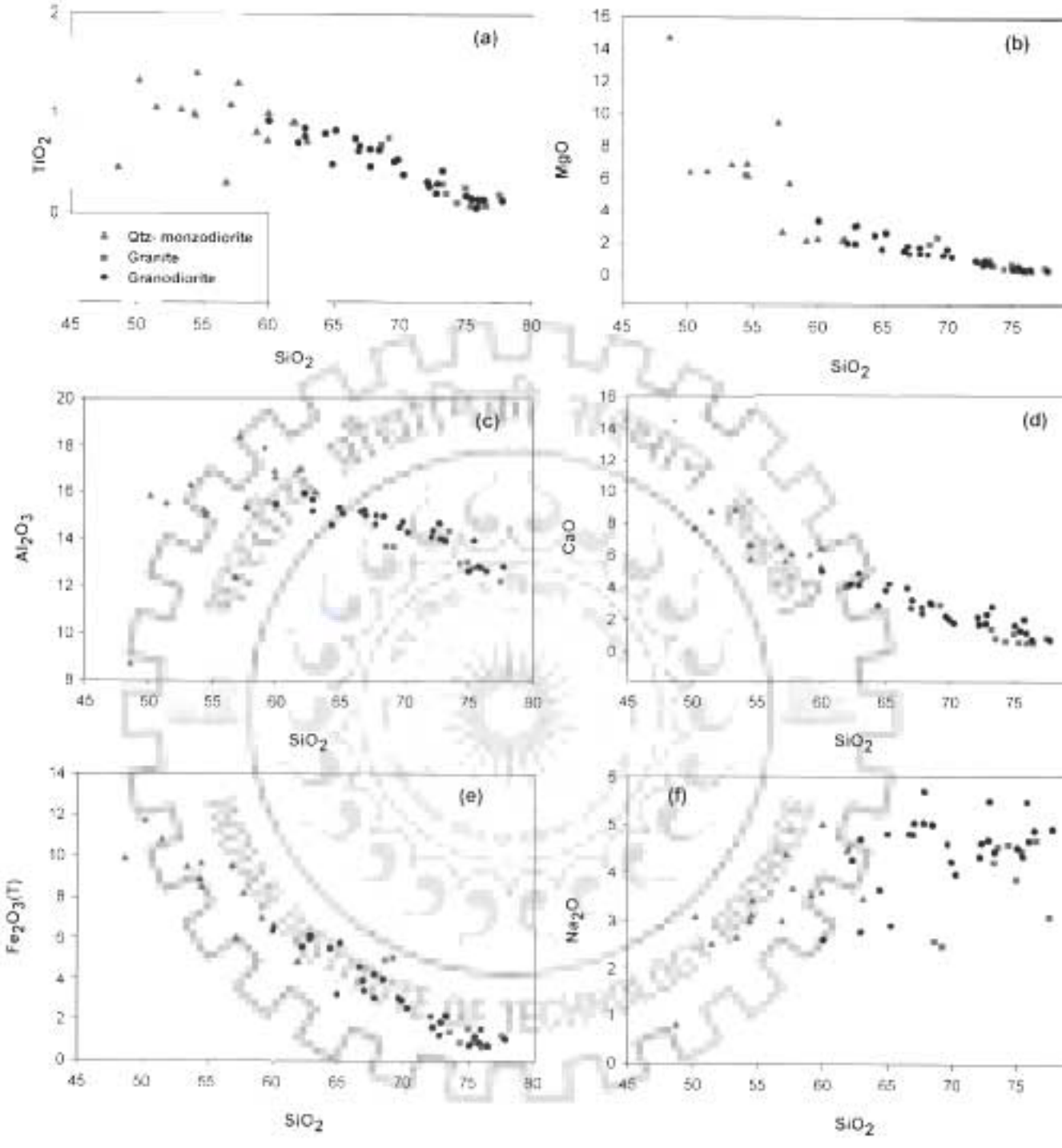

Fig. 3.5: Harker variation plot of Ladakh Batholith showing correlation between SiO_2 and (a) TiO_2, (b) MgO, (c) Al_2O_3, (d) CaO, (e) Fe_2O_3 (T) and (f) Na_2O.

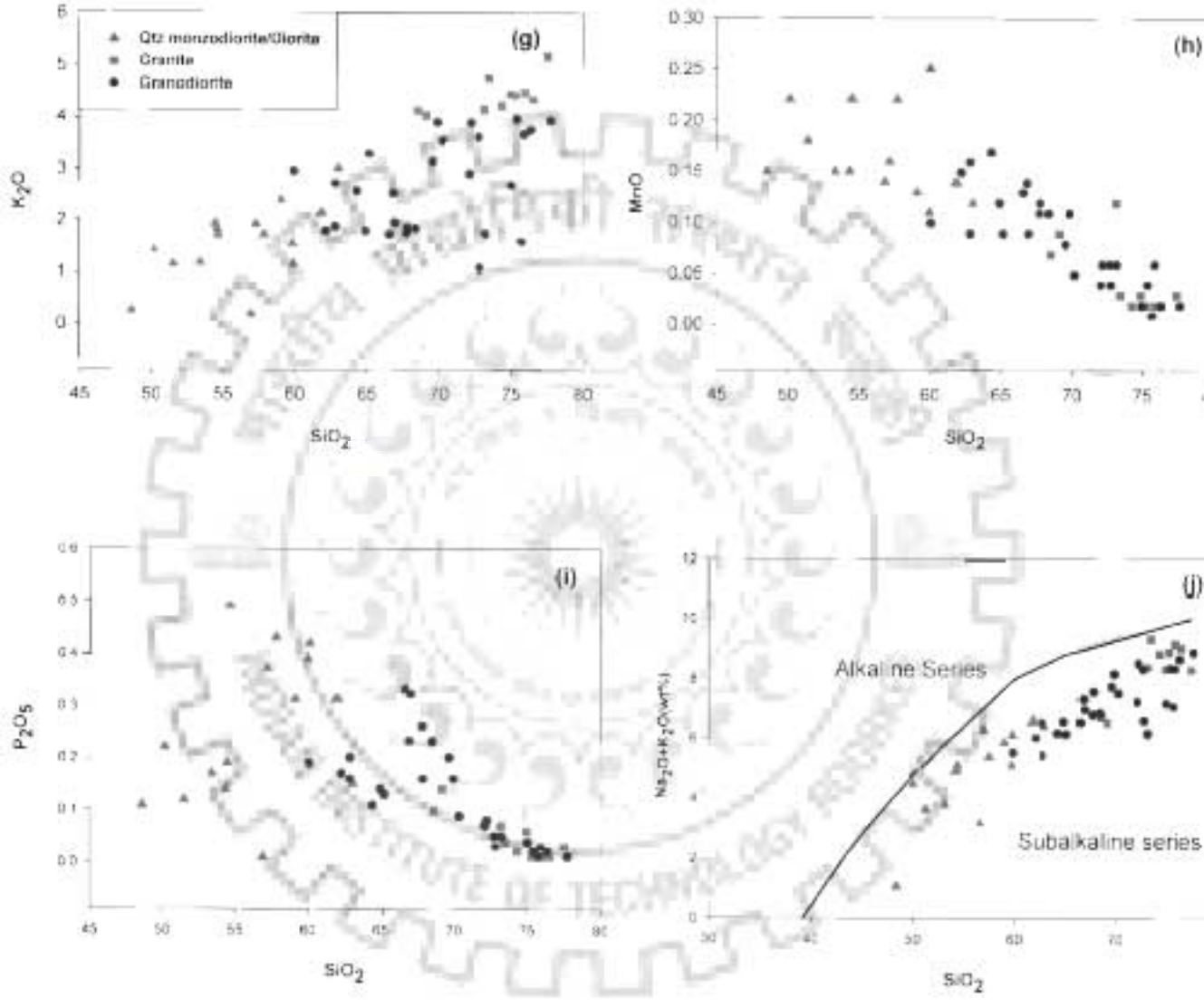

Fig. 3.5: Harker variation plot of Ladakh Batholith showing correlation between SiO_2 and (g) K2O, (h) MnO, (i) P_2O_5 and (j) Na_2O+K_2O (*Boundaries after Irvine and Baragar, (1971)*).

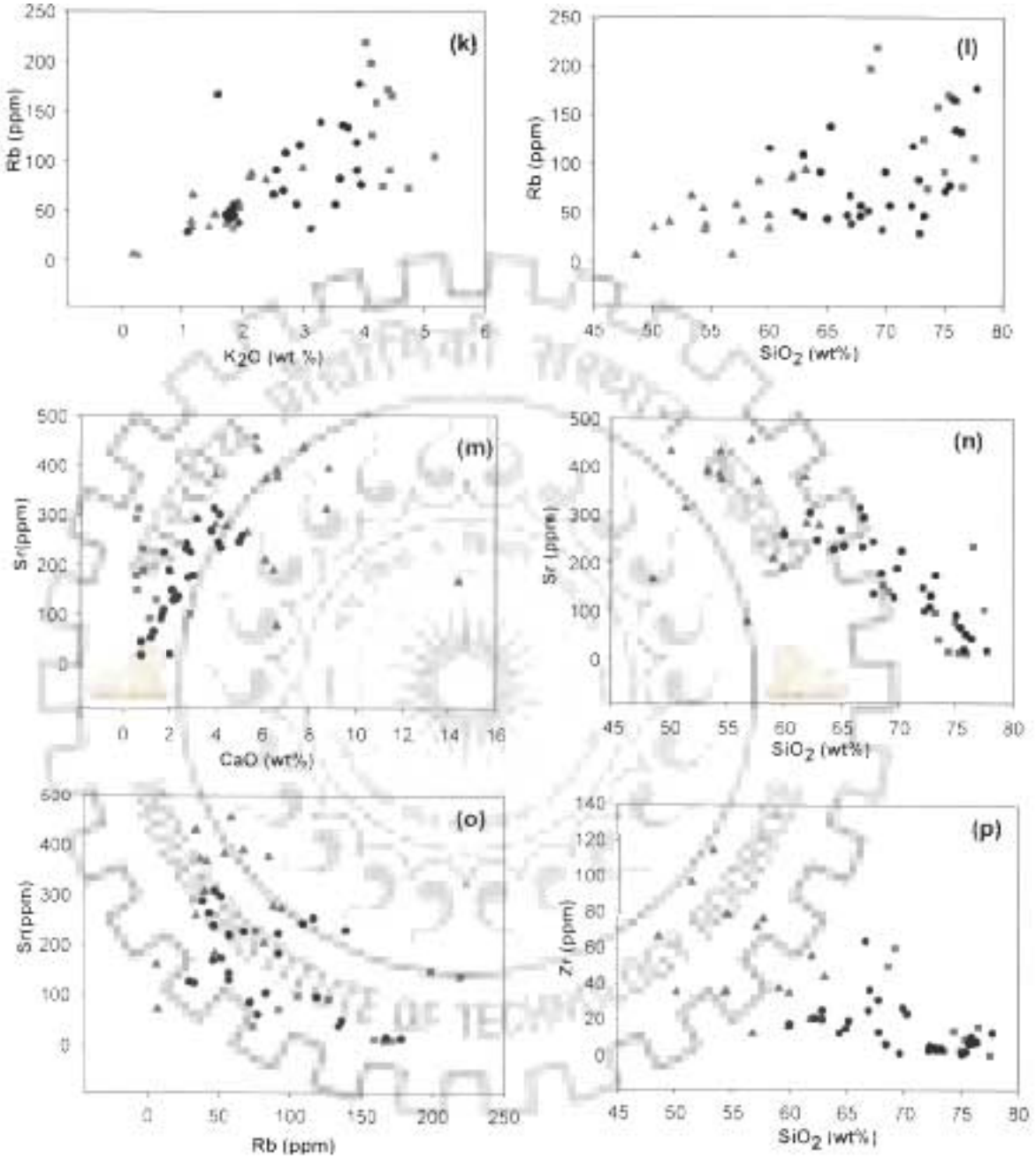

Fig. 3.5: Harker variation plot of the Ladakh Batholith showing correlation between (k) K20 and Rb, (l) SiO_2 and Rb, (m) CaO and Sr, (n) SiO_2 and Sr, (o) Rb and Sr and (p) SiO_2 and Zr.

(as total Fe - Fig. 3.5 e), Na_2O (Fig. 3.5 f), K_2O (Fig. 3.5 g), MnO (Fig. 3.5 h), P_2O_5 (Fig. 3.5 i). The variation diagram between SiO_2 and K_2O indicate a positive correlation along with moderate content of Na_2O+K_2O which also indicates a positive correlation indicating evolution within sub alkaline series with field after Irvine and Barager (1971) (Fig.3.5 j) indicate subalkaline composition. The negative correlation of TiO_2 and SiO_2 indicate role of Fe-Ti oxides in the fractionation process (Fig. 3.5 a). The CaO vs. SiO_2 trend represent assimilation and early crystallization of calcic plagioclase (Fig. 3.5 d), whereas P_2O_5 vs SiO_2 trend indicate formation of apatite mineral (Fig. 3.5 i).The increase in K_2O and Na_2O with increase in SiO_2 content can be attributed to the formation of K-feldspar and biotite (Fig. 3.5 f and g). Apart from Na_2O and K_2O all other major oxides show negative correlation. With increasing SiO_2 content Al_2O_3 content decreases indicating formation of feldspar (Fig. 3.5 f) and negative trend of Fe_2O_3 (T) and MgO as compared to SiO_2 increase suggest high fractionation of mafic minerals like hornblende, biotite, magnetite etc. (Fig. 3.5 b, e).

*3.3.2.2 **Trace element geochemistry:*** The binary variation diagram for Rb and SiO2 indicate positive trend (Fig. 3.5 k) attributed to K-feldspar formation, this is also in conjunction with positive trend of K2O vs. SiO2. The Rb vs SiO2 trend also indicate that Rb content increased during diorite formation and then slightly depleted during granodiorite formation suggesting appearance of K-feldspar during granodiorite formation (Fig. 3.5 l). Sr indicate negative trend with SiO2 indicating assimilation and early crystallization of calcic plagioclase (Fig. 3.5 m). This observation is also being supported by the major elemental variation diagram of SiO2 vs Sr (Fig. 3.5 n). The Rb vs Sr pattern indicates that crystal fractionation is the most viable mechanism for trace

elemental variation (Fig. 3.5 o). Zr shows a negative trend with respect to SiO2 content indicating formation of zircon, the trend also indicate magmatic process rather than post crystallization alteration processes (Fig. 3.5 p).

The spidergram plots have been made using incompatible-compatible elemental composition normalized to Primordial Mantle composition of Sun and Mc Donough (1989). The plot indicates a slight enrichment of mobile LILE from diorite to granodiorite to granite composition (Fig. 3.6). The concentration pattern of Nb can be attributed to the higher concentration of hornblende and biotite within the body. However, the Nb anomaly/trough can be attributed to subduction related magmatism. The Sr anomaly/trough is indicative of plagioclase formation or low Sr concentration in the melt/source.

3.3.2.3 REE geochemistry: The REE are a group of 15 elements with atomic numbers ranging from 57 (Lanthanum- La) to 71 (Lutetium- Lu). Out of these, 14 elements occur naturally. The REE are generally classified as the light REE (LREE) and middle or heavy REE (HREE) based on their atomic numbers. The REE are normally presented on a concentration versus atomic number diagram on which concentrations are normalized to the chondritic reference value, expressed as the logarithm to the base 10 of the value. Concentrations at individual points on the graph are joined by straight lines. This is referred to as the *Masuda- Coryell diagram* after original proponents of the diagram (Masuda, 1962; Coryell et al. 1963). Trends on the REE diagram are usually referred to as REE 'patterns' and the shape of an REE pattern is of considerable petrological interest. The raw data are normalized with C1 chondrite in order to refine the data (Sun and Mc Donough, 1989). Chondritic meteorites are chosen as common

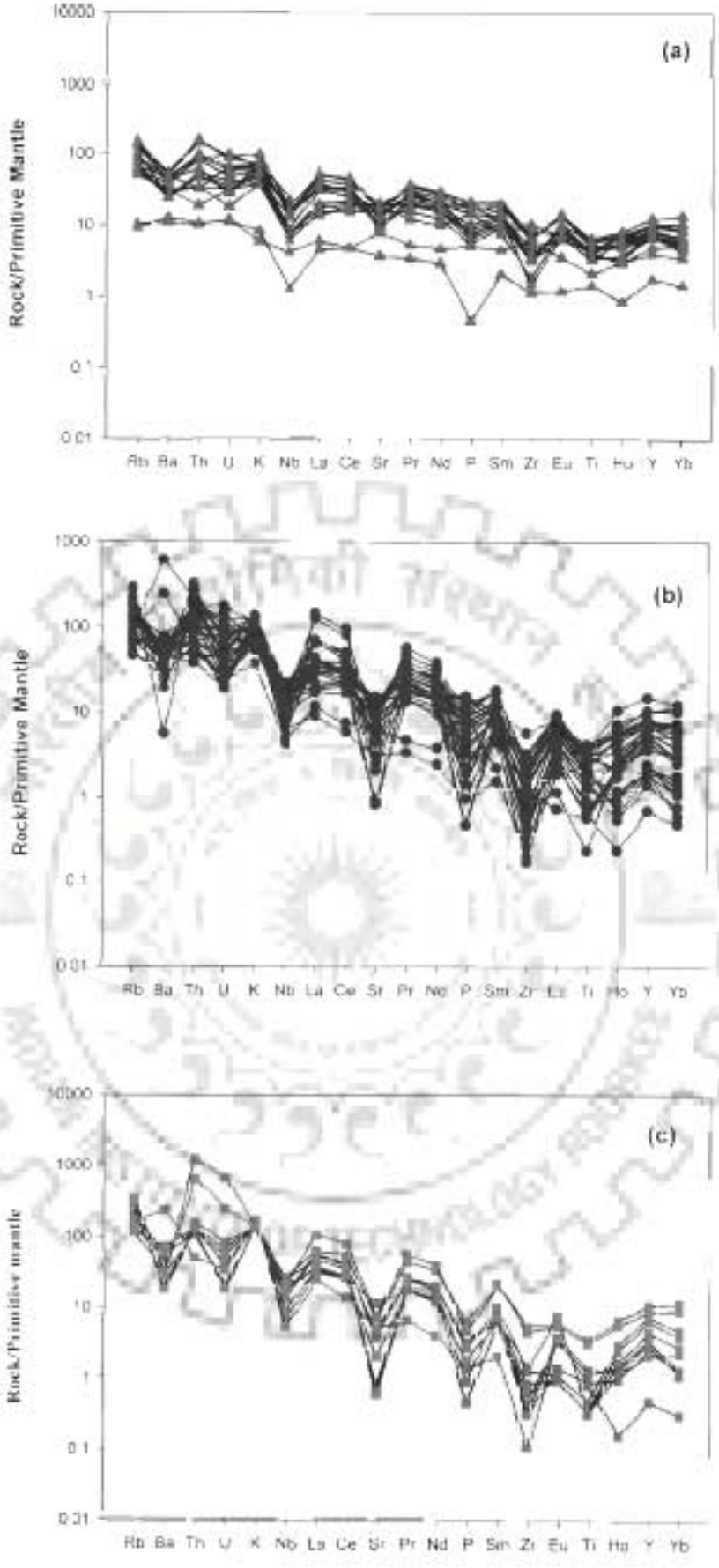

Fig 3.6 Spiderplot of Ladakh Batholith (a) diorite, (b) granodiorite and (c) granite

reference for standard normalizing because they are considered to be relatively unfractionated samples of the solar system dating from the original nucleosynthesis. Thus, the chondritic normalization has two important functions;

(a) Firstly, it eliminates the abundance variation between odd and even atomic number elements (Oddo- Harkins effect) and

(b) Secondly, it allows any fractionation of the REE group relative to the Chondritic meteorites to be identified.

The chondrite normalized REE plot for all the three rock types indicate similar elemental concentration pattern. The dioritic rocks show slight enrichment in LREE and nearly a flat trend in HREE without any prominent Eu anomaly (Fig. 3.7 a), whereas the granodiorite show similar pattern as that of diorite but with a slight overall enrichment in the REE and negative Eu anomaly (Fig. 3.7 b). However, granite shows more enrichment in LREE and relative depletion in HREE from granodiorite and diorite (Fig. 3.7 c). Negative Eu anomaly is more prominent in granites and less significant in other varieties suggesting early crystallization and removal of plagioclase during fractionation process. The Eu-anomalies are chiefly controlled by feldspars, particularly in felsic magmas, for Eu (present in the divalent state) is compatible in plagioclase and K- feldspar, in contrast to the trivalent REE which are incompatible. Thus, the removal of feldspar from a felsic melt by crystal fractionation or the partial melting of a rock in which feldspar is retained in the source will give rise to a negative Eu anomaly in the melt. To a lesser extent hornblende, sphene, clinopyroxene, orthopyroxene and garnet may also contribute to a Eu anomaly in the felsic melts, although in the opposite sense to that of the feldspars. Also,

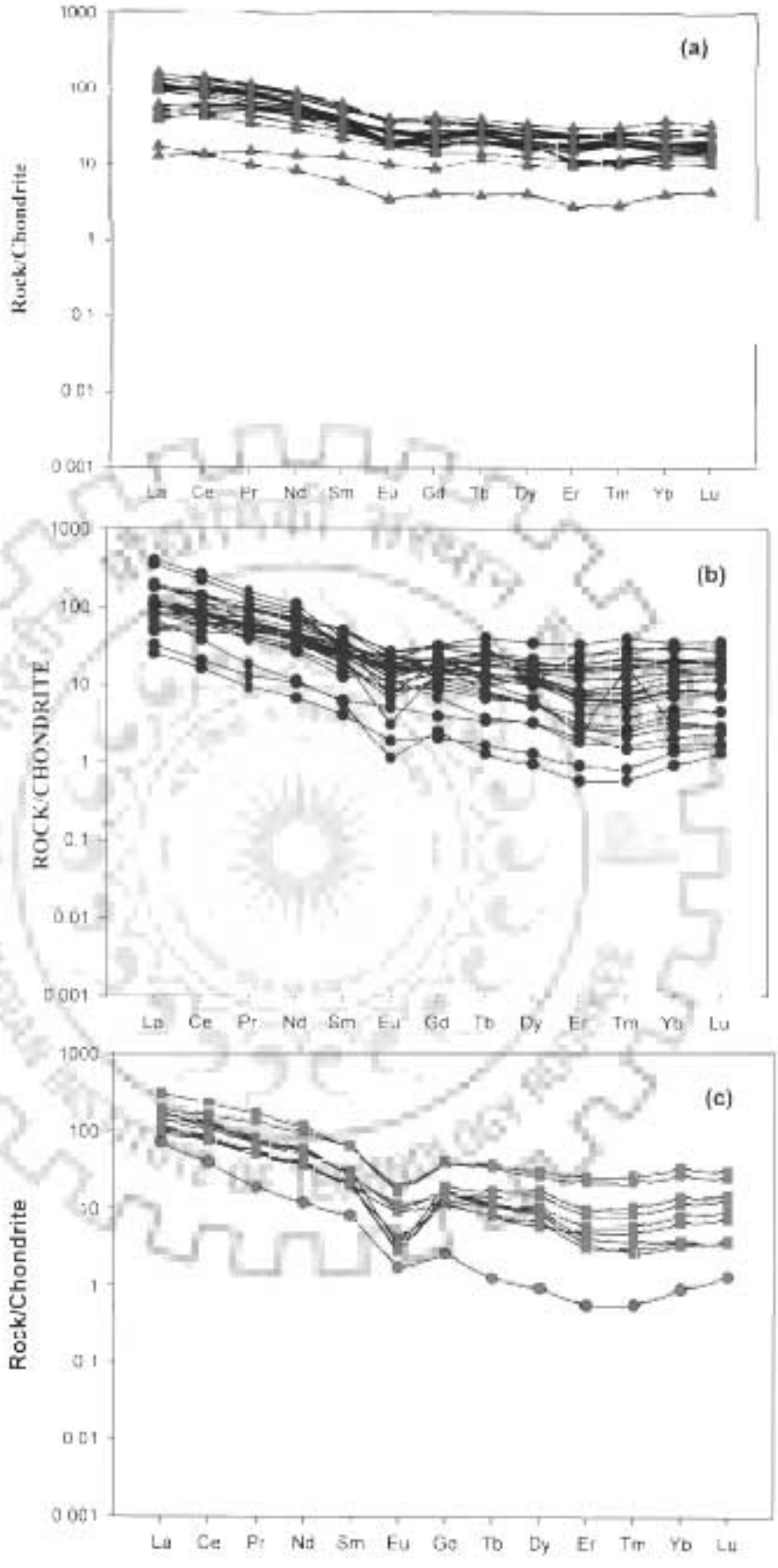

Figure 3.7: REE normalised plot of Ladakh Batholith (a) diorite, (b) granodiorit and (c) granite

the overall increase in the LREE with depletion in HREE from intermediate to acidic varieties also indicates fractional crystallization.

In the discrimination diagram of Rb vs. (Y+Nb) and Rb vs (Yb+Ta) of Pearce et al. (1984) diorite, granodiorite and granite fall within the volcanic arc granite field (Figs. 3.8 a and b).

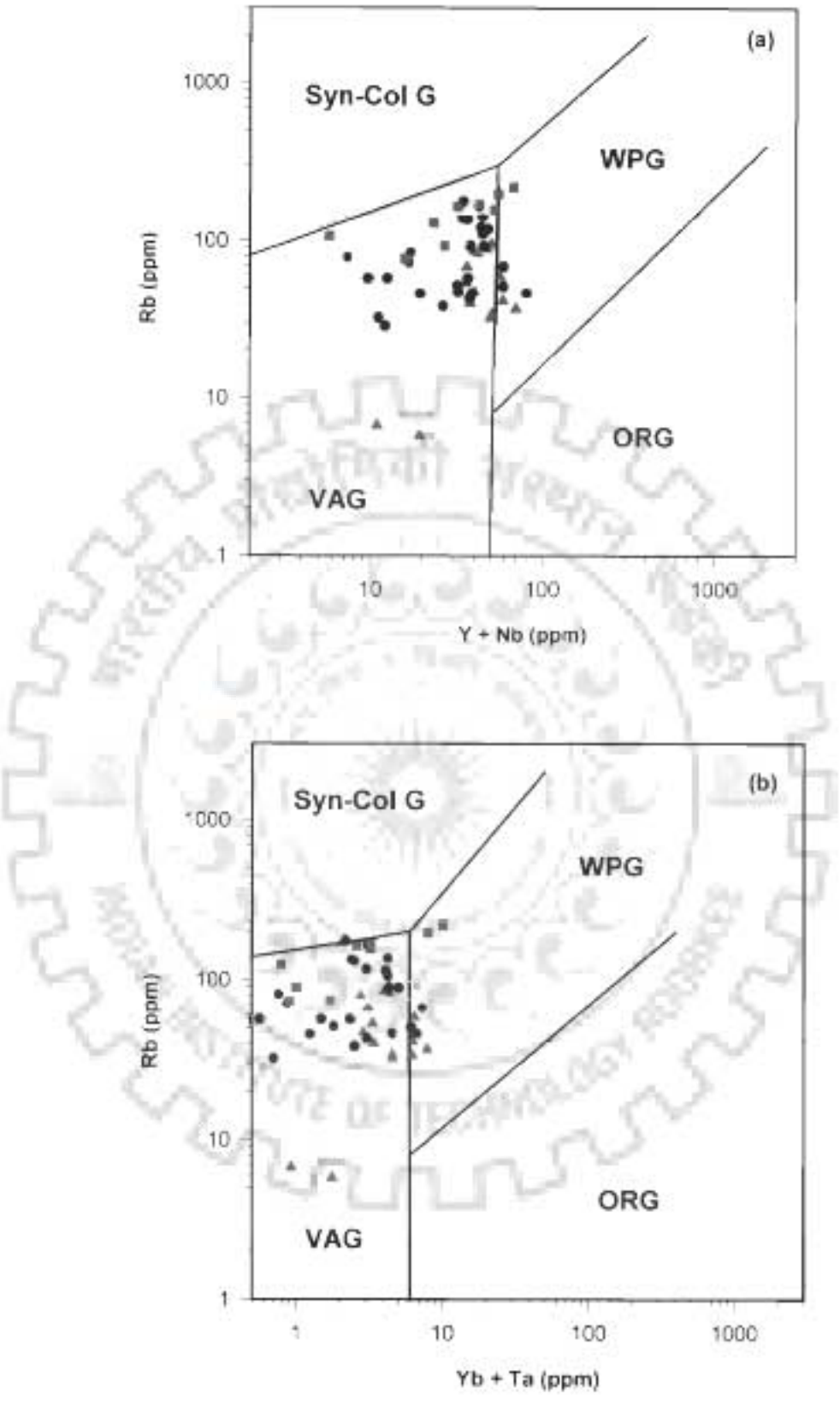

Figure 3.8: Discrimination plot of Pearce et al. (1984) for the Ladakh Batholith with symbols as in figure 3.5 (a) Rb vs. (Y+Nb) and (b) Rb vs. (Ta+Yb)

CHAPTER–4

DEPTH OF EMPLACEMENT

4.1 INTRODUCTION

Among the various granitoid belts in Himalaya, the Trans-Himalayan Ladakh Batholith in the Indian sector is the largest plutonic complex within the Himalayan orogenic belt. The most striking feature of this batholith is the emplacement of enormous volume of magma. Hornblende is the most commonly amphibole observed in this calc-alkaline granitoid, as has been shown in the preceding chapter. This chapter aims at constraining the depth of emplacement of the batholith using hornblende geobarometer (Schmidt, 1992), which will give the pressure of crystallization and the depth of emplacement.

The depth of crystallization can be obtained from the relationship:

$$P = h\rho g$$

Where, P is the pressure, h is the depth of crystallization, and ρ is the density of the overlying column of rock mass (3.0) and g the acceleration due to gravity (9.81 m sec^{-2})

$$P = 3 \times 9.81 \times 10^{6} h \ Nm^{-2}$$

$$= 0.2943 \times 10^{8} h \ Nm^{-2}$$

$$\text{or, } P = 0.2943h \text{ Kbar} \qquad (4.1)$$

The quantitative estimation of the pressure of crystallization of the Ladakh Batholith has been attempted using Al-in-hornblende barometry of Schmidt (1992), which corresponds to the Al^{T} content of magmatic hornblende (Wones, 1981) with crystallization pressure of intrusion, as has been calibrated experimentally under water-saturated conditions at pressure 2.5–1.3 kbar and 700-655° C. Data on natural rock and experimental data using natural rock as the starting materials show that composition of amphibole varies with bulk composition, pressure, temperature and oxygen fugacity (Raase,, 1974; Spear, 1981; Wones and Gilbert, 1982; Helz, 1982; Laird and Albee, 1981; Hammarstrom and Zen, 1986). The term hornblende is used here in a more generalized manner as been used by Hawsthorne (1983) rather than the true definition of amphibole, as has been given by the International Mineralogical Association Subcommission (Leake, 1978), and may include edenite, magnesiohornblende and pargasite.

4.2 Al-IN-HORNBLENDE GEOBAROMETER

The amphibole group minerals are the chain silicates, with structure consisting of two parallel cross-linked chains with a structural unit of T_4O_{11}. The general formula for amphibole group of minerals is $(A_{0-1}) M4_2M3M2_2M1_2T_8T2_8O_{22}(OH,F,Cl)_2$. The A-site is a 12 co-ordinated site occupied by Na and K where cation varies from 0 to 1. M4 site is a 8- co-ordinated site occupied in Ca, Na, Mg, Fe^{++}, Mn and occasionally Li. M1, M2, M3 sites are 6- co-ordinated and have been designated as M1, M2, M3 in order of increasing size between cation-oxygen distance. There are in total 2 M1-sites, 2 M2-sites and 1 M3-sites. These sites are occupied, by a variety of cations including, Mg, Fe^{2+}, Fe^{3+}, Al, Mn, Cr and Ti. Here Al, Fe^{3+}, Cr^{3+} and Ti^{4+} are the 4- co-ordinated sites form

the T_4O_{11} chain system in the amphibole and contains Si and Al in the T1-site and only Si in T2-site. Amphibole classification has dealt in detail in a paper published by the International Mineralogical Association Working Group on Amphiboles (Leake et al., 1997). In this paper, they have outlined the latest complex classification of the amphibole group minerals on the basis of several parameters including B-site occupancy (8 fold M4-site), $Mg/(Mg+Fe^{2+})$ ratios, number of Si-cations per 23 oxygens and the relative abundances of octahedrally co-ordinated aluminum (Al^{VI} = aluminum in the C-site: these 6-fold sites of M1, M2, and M3) and ferric iron (Fe^{3+} in C-site).

On the basis of B-site occupancy in term of cation per 23 oxygen, four major amphibole subdivisions have been proposed. The classification rules, in terms of cations per 23 oxygens, are:

(1) ***Magnesium-iron-manganese-lithium amphiboles***

$(Ca+Na)_B < 1$ and $(Mg+Fe2+Mn+Li)_B \geq 1$

(2) ***Calcic amphiboles***

$(Ca+Na)_B >= 1$ and Na_B less than 0.5

(3) ***Sodic-calcic amphiboles***

$(Ca+Na)_B >= 1$ and $Na_B = 0.5 - 1.5$

(4) ***Sodic amphiboles***

$Na_B >= 1.5$

Based on the $Mg/(Mg+Fe^{2+})$ ratio the Mg-Fe-Mn-Li amphiboles are further divided into two groups on the basis of symmetry of amphiboles, i.e. orthorhombic amphiboles; and monoclinic amphiboles details of which have been depicted in the following diagram:

In amphiboles the major substitutions depend on pressure, temperature, oxygen fugacity and system composition. All aspects of the amphibole chemistry depend on the bulk composition of the system and the Mg number [Mg/(Mg+Fe(2+)] depends largely on system composition and to a significantly lesser extent on temperature. In contrast, the tschermaks substitution $[Al]_C + [Al]_T = [X(2+)]_C + [Si]_T$ increases with increasing pressure (*i.e.*, the amphiboles become more Al-rich with increasing pressure). Similarly, the edenite substitution $[Na]_A + [Al]_T = [VAC]_A + [Si]_T$ increases with increasing temperature (*i.e.*, the amphibole becomes increasingly sodic and aluminous with increasing temperature). However, substitution of ferric iron for aluminum in the C-sites also increases with increasing oxygen fugacity.

Given these substitutions, it is possible that Al-content of an amphibole could be used to indicate pressure of formation of hornblende which formed during crystallization of the rock. A quantitative application of this idea was presented by Hammerstrom and Zen (1986), based on an empirical study of total aluminum content (on a cations per 23 oxygen basis) of amphiboles in granitic intrusives. The emplacement pressures were confirmed by application of conventional metamorphic geobarometry using the thermal contact aureoles around the granitic plutons. The granite has the mineral assemblage plagioclase (An20-40) + K-felespar + quartz + hornblende + biotite + titanite + magnetite (or ilmenite). Their analyses deduced a simple equation for the crystalization pressure of an amphibole in terms of the number of Al-cations in its structure (23 oxygen basis)

$$P\ (kbar) = 5.03\,Al_T - 3.92 \qquad (4.2)$$

Hammerstrom and Zen (1986) were of the opinion that the pressure had dominant control on the total Al-content of amphibole, however, the effect of temperature and oxygen fugacity created some scatter in their data set. Their results led to several experimental studies which improved the calibration of the Al-in-hornblende geobarometer (*i.e.* Johnson and Rutherford, 1989; Thomas and Ernst, 1990; Schmidt, 1992) resulting in the calibration equation:

$$P\ (kbar) = 4.76\,Al_T - 3.01 \qquad (4.3)$$

4.3 ANALYTICAL PROCEDURE

To have a critical look at the distribution of pressure of crystallization based on Al- in hornblende geometry 8 samples were selected along the Kharu-Chang La section (Fig.4.1). Thin sections from the Ladakh Batholith were polished with good quality alumina powder. Hornblende occurs as euhedral to subhedral megacrysts (Fig. 4.2)

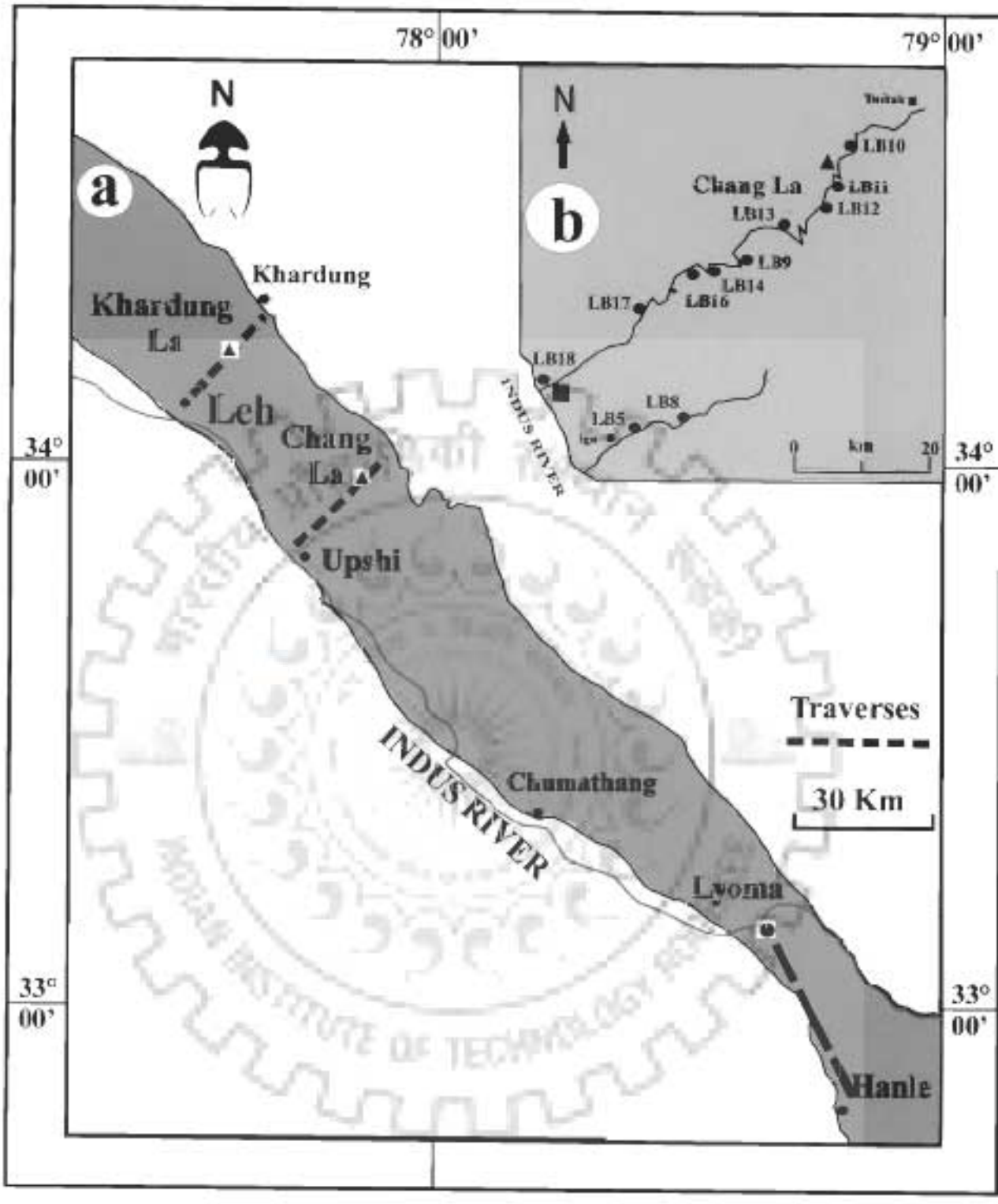

Figure 4.1: Location map of samples from the Ladakh Batholith for Hornblende geobarometry. (a) Map of the Ladakh Batholith. (b) Kharu-Chang La section.

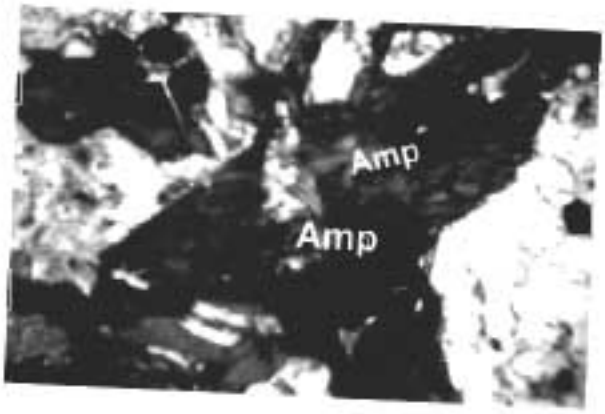

LB5/14

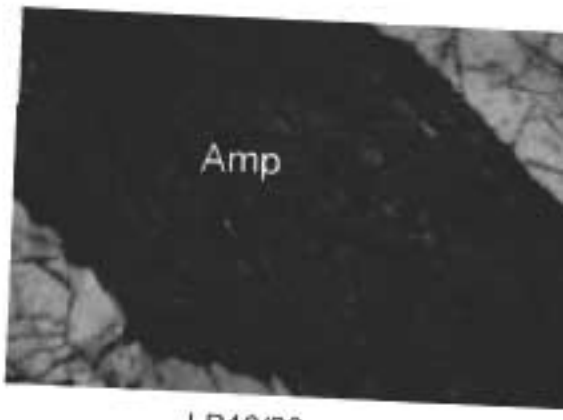

LB10/28

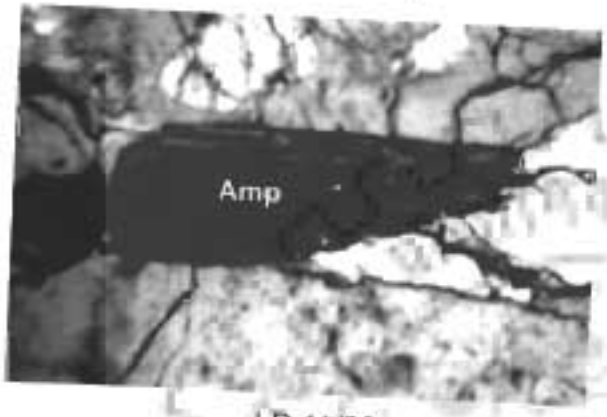

LB 11/29

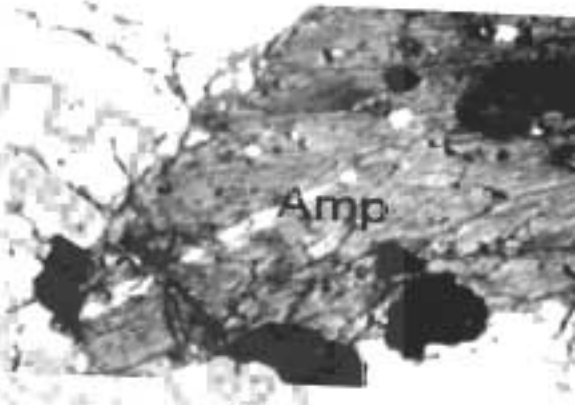

LB 13/31

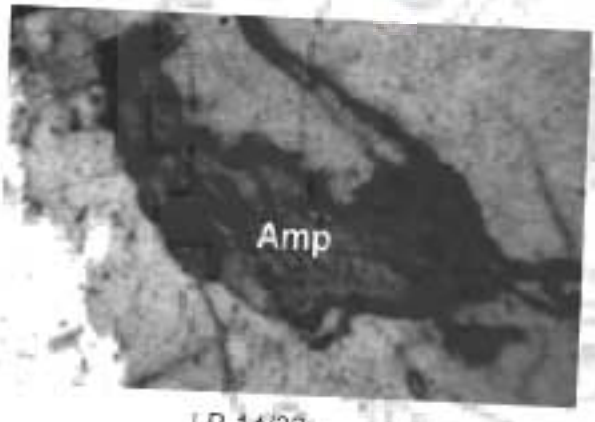

LB 14/32

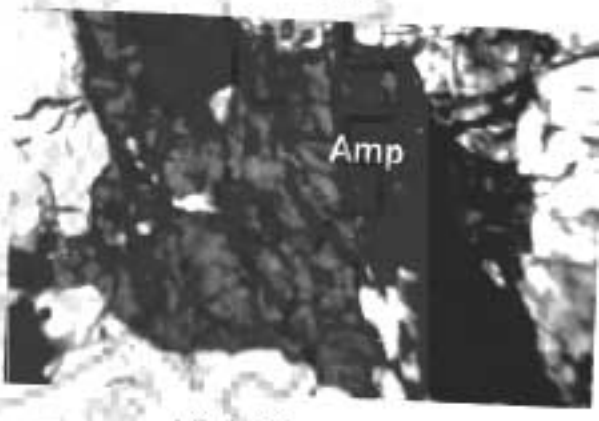

LB 15/33

LB 17/35

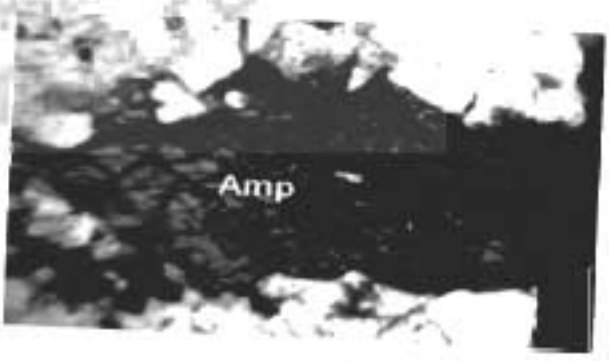

LB 18/36

Fig 4.2 Photomicrograph of the amphibole grain analysed from Kharu-Changla Section

having variable pleochroic scheme.Hornblende analysis was performed on 40 points on unaltered grains from 8 samples using JEOL – JXA - 8600M Electron Probe Micro-Analyzer (EPMA) at the Institute Instrumentation Center at Indian Institute of Technology Roorkee, Roorkee. A probe current of 20 nA at the 15 Kev with a beam size of 2 um were used to get the data after using ZAF correction of Philibert (1963), which is inbuilt in the machine. Standardization of the machine was done against synthetic and natural standards before analysis.

4.4 RESULTS

The EPMA data from Hornblende have been listed in Table 4.1. Table 4.2 presents the estimation of [P (kbar) = 4.76 Al_T-3.01 of Schmidt (1992)] along with the rock type and altitude of the sample.The primary magmatic hornblende has been used. The hornblende described as late on the textural grounds and composition representing late stage alternating imposing Leake's (1971) proposed limit of Si ≤ 7.5 with Ca≥1.6for "igneous" hornblende have been omitted for pressure calculation. All hornblendes reported show textural evidence of coexistence with quartz and the analyses were made on the rim compositions of hornblende to provide true picture of composition with the last melt remaining in the rock. Hornblende from the rocks crystallized at low pressure have higher Mg/(Mg+Fe) than those for high pressure rocks along with some overlap in Mg/(Mg+Fe) between low and high pressure samples (Fig 4.3a). The data points fall mainly in Edenite field on modified IMA recommended Mg/(Mg+Fe) vs Al^{IV} plot (Fig.4.3 a). The Al^{IV} vs Al^{T} plot shows a strong correlation among themselves with regression line having equation of $Al^{IV} = 0.133+0.82\ Al^{T}$ and r^2 value to be 0.96. The data point fall mainly between line $Al^{IV}=0$ and $Al^{IV}<0.6Al^{IV}+0.25$ (Fig.4.3 b).

Table 4.1: EPMA Analysis of hornblende with data at oxygen base 23 with pressure calculated based on formula of Schmidt (1992)

Sample No.	LB 5/14		LB 10/28			
	1st point	2nd point	1st point	2nd point	3rd point	4th point
SiO_2	44.452	43.018	42.126	42.531	43.544	43.179
Al_2O_3	8.179	8.389	6.505	6.655	6.433	6.234
FeO	18.427	19.255	13.036	13.534	13.008	13.401
MgO	11.083	10.243	13.167	12.679	14.218	13.473
MnO	0.666	0.557	0.564	0.388	0.484	0.489
CaO	10.927	10.701	11.473	11.389	11.226	11.517
K_2O	0.811	0.550	0.494	0.410	0.460	0.418
Na_2O	1.167	1.264	0.720	1.027	1.065	0.739
TiO_2	0.547	0.479	1.524	1.598	1.535	1.420
Cr_2O_3	--	--	--	--	0.011	--
Total	96.285	94.456	89.660	90.206	91.974	90.890
Cations (23 Oxygen)			Cations (23 Oxygen)			
Si	6.8122	6.7548	6.8024	6.8295	6.8315	6.870
Al	1.4775	1.5526	1.2381	1.2597	1.1822	1.1692
Fe	2.3617	2.5286	1.7605	1.8176	1.7068	1.7832
Mg	2.5318	2.3977	3.1693	3.0335	3.3251	3.1956
Mn	0.0864	0.0741	0.0772	0.0528	0.0643	0.0659
Ca	1.7943	1.8005	1.9851	1.9596	1.8871	1.9634
K	0.1587	0.1102	0.1017	0.0840	0.0921	0.0888
Na	0.3467	0.3849	0.2256	0.3199	0.3241	0.2279
Ti	0.0662	0.0565	0.1911	0.1930	0.1811	0.1699
Cr	--	--	--	--	0.0013	--
Total	15.6355	15.6599	15.5510	15.5496	15.6011	15.5339
Pressure (kbar)	**4.02**	**4.38**	**2.88**	**2.98**	**2.64**	**2.55**
Al^{iv}	1.1878	1.2452	1.1976	1.1705	1.1685	1.13
Mg/Fe+Mg	0.517	0.487	0.643	0.625	0.661	0.642

Sample No	LB11/29				
	1st point	2nd point	3rd point	4th point	5th point
SiO_2	43.894	45.021	45.029	44.918	42.873
Al_2O_3	5.737	5.444	5.876	5.893	5.958
FeO	15.376	14.81	12.672	16.0761	15.239
MgO	12.446	12.6	13.79	12.427	11.993
MnO	0.777	0.696	0.546	0.772	0.663
CaO	11.635	11.814	10.835	11.711	11.559
K_2O	0.333	0.299	0.566	0.43	0.476
Na_2O	0.628	0.673	0.869	0.687	0.643
TiO_2	1.005	0.625	0.976	0.789	1.187
Cr_2O_3	0.024	0.035	0.067	--	0.021
Total	91.855	92.010	91.225	93.703	90.615
	Cations (23 Oxygen)				
Si	6.9706	7.097	7.073	7.0016	6.9154
Al	1.074	1.0115	1.088	1.0827	1.1328
Fe	2.0421	1.9525	1.6647	2.0957	2.0557
Mg	2.9463	2.961	3.229	2.8875	2.8838
Mn	0.1046	0.0929	0.0726	0.102	0.0906
Ca	1.9798	1.9955	1.8236	1.956	1.9979
K	0.0674	0.0589	0.1134	0.0855	0.0979
Na	0.1933	0.2058	0.2646	0.2077	0.2019
Ti	0.12	0.074	0.1153	0.0925	0.144
Cr	0.0031	0.0043	0.0083	--	0.0027
Total	15.502	15.4534	15.4525	15.5111	15.5227
Pressure (kbar)	**2.10**	**1.80**	**2.16**	**2.14**	**2.38**
Al^{iv}	1.0294	0.903	0.927	0.9984	1.0846
Mg/Fe+Mg	0.591	0.603	0.659	0.579	0.584

Sample No	LB13/31					
	1st point	2nd point	3rd point	4th point	5th point	6th point
SiO_2	44.654	39.531	41.189	39.707	41.702	41.250
Al_2O_3	6.276	6.077	6.980	6.909	5.977	6.228
FeO	15.831	13.928	15.849	15.689	15.120	15.471
MgO	11.410	11.986	11.932	11.746	12.668	12.014
MnO	0.866	0.799	0.811	0.810	0.807	0.728
CaO	10.820	11.861	11.661	11.704	11.740	11.722
K_2O	0.340	0.444	0.482	0.468	0.468	0.388
Na_2O	0.841	0.767	0.893	0.901	0.837	0.750
TiO_2	0.531	1.479	1.106	0.668	1.011	0.750
Cr_2O_3	--	0.007	--	0.007	--	--
Total	91.568	86.878	90.901	88.609	90.330	89.423
	Cations (23 Oxygen)					
Si	7.0924	6.6870	6.6819	6.6336	6.7834	6.7853
Al	1.1749	1.2117	1.3346	1.3604	1.1460	1.2076
Fe	2.1028	1.9704	2.1503	2.1921	2.0569	2.1283
Mg	2.7014	3.0224	2.8855	2.9253	3.0718	2.9460
Mn	0.1165	0.1144	0.1114	0.1146	0.1112	0.1014
Ca	1.8414	2.1498	2.0270	2.0951	2.0462	2.0660
K	0.0689	0.0957	0.0997	0.0997	0.0970	0.0814
Na	0.2590	0.2516	0.2807	0.2919	0.2640	0.2393
Ti	0.0634	0.1881	0.1350	0.0839	0.1237	0.1078
Cr	--	0.0009	--	0.0009	--	--
Total	15.4207	15.6922	15.7060	15.7975	15.7003	15.6634
Pressure (kbar)	**2.60**	**2.76**	**3.34**	**3.47**	**2.45**	**2.74**
Al^{iv}	0.9076	1.313	1.3181	1.3664	1.2166	1.2147
Mg/Fe+Mg	0.562	0.605	0.573	0.572	0.599	0.581

Sample No.	LB13/31		LB14/32			
	7th point	8th point	1st point	2nd point	3rd point	4th point
SiO_2	41.007	40.768	40.811	41.760	41.380	44.028
Al_2O_3	6.175	6.283	6.639	6.093	7.307	5.746
FeO	15.110	15.547	16.185	15.083	16.331	13.559
MgO	12.485	12.418	10.933	11.644	11.934	12.924
MnO	0.842	0.812	0.713	0.763	0.651	0.682
CaO	11.719	11.783	11.757	11.723	11.740	11.923
K_2O	0.396	0.344	0.546	0.337	0.528	0.319
Na_2O	0.722	0.791	0.801	0.635	0.847	0.574
TiO_2	0.722	0.791	1.255	1.080	1.087	0.589
Cr_2O_3	--	0.007	--	0.031	--	--
Total	89.443	89.373	89.640	89.149	91.805	90.343
Cations (23 Oxygen)			Cations (23 Oxygen)			
Si	6.7422	6.7265	6.7332	6.8624	6.6531	7.0411
Al	1.1967	1.2218	1.2911	1.1802	1.3848	1.0832
Fe	2.0778	2.1453	2.2332	2.0728	2.1959	1.8135
Mg	3.0601	3.0544	2.6888	2.8523	2.8604	3.0811
Mn	0.1173	0.1135	0.0996	0.1062	0.0887	0.0928
Ca	2.0646	2.0832	2.0788	2.0641	2.0226	2.0431
K	0.0831	0.0724	0.1149	0.0708	0.1084	0.0651
Na	0.2301	0.2531	0.2563	0.2023	0.2640	0.1779
Ti	0.1220	0.0768	0.1558	0.1335	0.1314	0.0708
Cr	--	0.0009	--	0.004	--	--
Total	15.6940	15.7841	15.6511	15.5486	15.7098	15.4680
Pressure (kbar)	**2.69**	**2.81**	**3.14**	**2.61**	**3.58**	**2.18**
Al^{iv}	1.2578	1.2735	1.2668	1.1376	1.3469	0.9589
Mg/Fe+Mg	0.596	0.587	0.546	0.579	0.566	0.629

Sample No	LB15/33					
	1st point	2nd point	3rd point	4th point	5th point	6th point
SiO_2	41.214	38.967	39.254	37.607	39.266	40.849
Al_2O_3	7.280	7.526	7.374	7.480	7.273	6.280
FeO	15.785	16.332	15.588	14.919	15.940	14.652
MgO	12.601	12.011	11.780	11.115	11.656	12.901
MnO	0.748	0.665	0.622	0.619	0.614	0.743
CaO	11.722	11.697	11.884	11.290	11.930	11.649
K_2O	0.436	0.549	0.532	0.541	0.564	0.292
Na_2O	1.121	0.967	0.770	0.461	0.556	0.996
TiO_2	1.252	1.174	0.795	0.862	1.097	1.484
Cr_2O_3	--	--	0.021	0.062	0.066	
Total	92.161	89.901	88.621	84.958	88.962	89.846
	Cations (23 Oxygen)					
Si	6.5951	6.4492	6.5561	6.5393	6.5430	6.6889
Al	1.3732	1.4682	1.4517	1.5332	1.4285	1.2093
Fe	2.1125	2.2606	2.1774	2.1696	2.2214	2.0020
Mg	3.0065	2.9632	2.9328	2.8812	2.8954	3.1420
Mn	0.1014	0.0932	0.0881	0.0912	0.866	0.1029
Ca	2.0100	2.0743	2.1268	2.1036	2.1302	2.0393
K	0.0890	0.1160	0.1134	0.1201	0.1200	0.0608
Na	0.3477	0.3104	0.2494	0.1553	0.1797	0.3154
Ti	0.1506	0.1461	0.0999	0.1128	0.1375	0.1823
Cr	--	0.0018	0.0027	0.0086	0.0086	
Total	15.7860	15.8829	15.7982	15.7147	15.7508	15.7276
Pressure (kbar)	**3.52**	**3.97**	**3.90**	**4.28**	**3.78**	**2.74**
Al^{iv}	1.4049	1.5508	1.4439	1.4607	1.457	1.311
Mg/Fe+Mg	0.587	0.567	0.574	0.570	0.566	0.611

Sample No.	LB15/33			LB17/35		
	7th point	8th point	9th point	1st point	2nd point	3rd point
SiO_2	40.909	38.614	38.748	49.094	48.310	48.216
Al_2O_3	6.290	8.493	6.579	6.189	6.677	6.165
FeO	14.863	15.119	12.782	14.104	13.960	16.680
MgO	13.072	11.968	12.463	15.151	14.465	15.239
MnO	0.634	0.560		0.319	0.284	0.406
CaO	11.838	11.514	10.791	10.474	10.189	10.059
K_2O	0.425	0.435	0.436	0.202	0.260	0.150
Na_2O	0.433	0.584	0.927	1.096	1.086	0.914
TiO_2	0.254	1.056	.237	0.663	0.670	0.576
Cr_2O_3	0.010	0.052		0.011	--	0.047
Total	89.727	88.396	84.484	97.303	95.899	95.454
	Cations (23 Oxygen)				Cations (23 Oxygen)	
Si	6.4341	6.8194	6.8949	7.1827	7.1664	7.1771
Al	1.2123	1.6679	1.3367	1.0672	1.0393	1.1674
Fe	2.0325	2.1069	1.8426	1.7258	1.7319	1.7030
Mg	3.1862	2.9728	3.2022	3.3044	3.1987	3.3814
Mn	0.0877	0.0791	0.0761	0.0396	0.0357	0.0512
Ca	2.0759	2.0557	1.9930	1.6420	1.6195	1.6043
K	0.0886	0.0925	0.0960	0.0377	0.0491	0.0284
Na	0.1372	0.1886	0.3098	0.3109	0.3123	0.2639
Ti	0.1542	0.1323	0.1603	0.0729	0.0748	0.0645
Cr	0.0018	0.0068	--	0.0012		0.0050
Total	15.6630	15.7368	15.6955	15.3845	15.3558	15.3612
Pressure (kbar)	**2.76**	**4.92**	**3.35**	**2.07**	**2.55**	**2.14**
Al^{iv}	1.3659	1.1806	1.105	0.8173	0.8336	0.8229
Mg/Fe+Mg	0.611	0.585	0.635	0.657	0.649	0.665

Sample No.	LB18/36				
	1st point	2nd point	3rd point	4th point	5th point
SiO_2	48.708	44.019	44.767	45.674	45.519
Al_2O_3	7.204	7.328	7.240	6.830	6.727
FeO	17.368	18.077	17.856	17.470	17.801
MgO	11.225	11.164	11.413	11.821	11.618
MnO	0.480	0.455	0.505	0.473	0.461
CaO	10.528	10.706	10.772	10.763	10.981
K_2O	1.194	1.122	1.123	1.207	1.049
Na_2O	1.119	1.025	1.257	1.256	1.049
TiO_2	0.981	1.040	0.957	1.005	0.878
Cr_2O_3	---	---	---	---	---
Total	98.807	94.937	95.909	94.499	96.008
	Cations (23 Oxygen)				
Si	7.1620	6.8461	6.8801	6.9529	6.9690
Al	1.2485	1.3434	1.3116	1.2256	1.2139
Fe	2.1358	2.3512	2.6148	2.6824	2.6515
Mg	2.4604	2.5882	2.6148	2.6824	2.6515
Mn	0.0598	0.0600	0.0658	0.0610	0.0598
Ca	1.6587	1.7842	1.7739	1.7555	1.8014
K	0.2241	0.2226	0.2201	0.2345	0.2049
Na	0.3191	.03091	0.3476	0.3706	0.2849
Ti	0.1085	0.1217	0.1127	0.1150	0.1010
Cr	--	--	--	--	--
Total	15.3768	15.6264	15.6488	15.6218	15.5701
Pressure (kbar)	**2.93**	**3.39**	**3.23**	**2.82**	**2.77**
Al^{iv}	0.838	1.1539	1.1199	1.0471	1.031
Mg/Fe+Mg	0.535	0.524	0.500	0.500	0.500

Table 4.2: Pressure Calculated by Al in hornblende from the Ladakh Batholith

Samples (altitude)	Pressure Calculated (kbar)									Average Pressure (rock type)
LB 5/14 (3354m)	4.02	4.38								4.2 (diorite)
LB10/28 (5301 m)	2.88	2.98	2.64	2.55						2.21 (Granodiorite)
LB11/29 (5060 m)	2.10	1.80	2.16	2.14	2.38					2.11 (Granodiorite)
LB13/31 (4742 m)	2.60	2.76	3.54	3.47	2.45	2.74	2.69	2.81		3.27 (Granodiorite)
LB14/32 (4409 m)	3.14	2.61	3.58	2.18						2.88 (Granodiorite)
LB15/33 (4241 m)	3.52	1.97	3.90	4.28	3.78	2.74	2.76	4.92	3.35	3.69 (Granodiorite)
LB17/35 (3902 m)	2.07	2.55	2.14							2.13 (Diorite)
LB18/36 (3732 m)	2.93	3.39	3.23	2.82	2.77					3.03 (Diorite)

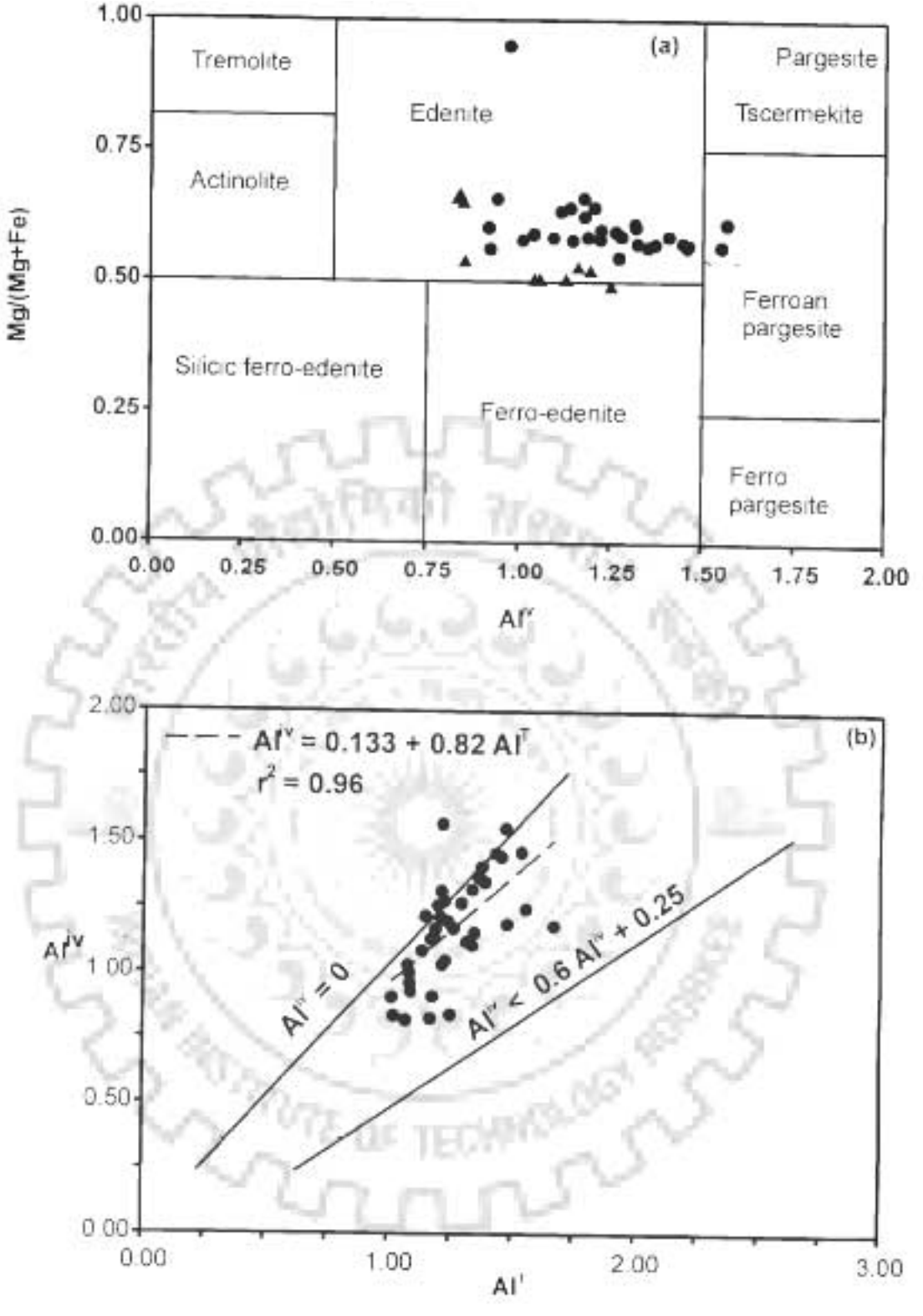

Figure 4.3: (a) Modified version of the IMA recommended plot of amphiboles (Fields after Hammertrom and Zen, 1986). Triangles denote the diorite samples and circles indicate granodiorite. (b) Plot of Al^{T} vs Al^{IV} in hornblende

The diorite sample at the lowest elevation of 3354m near Igu village (LB5/14) give an average pressure of 4.2 kbar which is the highest pressure calculated from the batholith. If the equation (4.1) is considered for depth calculation, the pressure of 4.2 kbar is equivalent to 14.27 km or when we consider the normal pressure gradient to be 3 km per kbar it is equivalent to 12.6 km (Fig. 4.4). Further, the diorite samples along the main Kharu Chang La section (LB17/35, LB18/36) from lower levels of the exposed batholith have values 2.13 kbar and 3.03 kbar averaging to be around 2.64 kbar which is equivalent to 8.97 km depth according to equation (4.1) and 7.92 km depth considering normal pressure gradient.

The granodiorite samples (LB10/28, LB11/29) from highest altitudes of 5301m and 5060m respectively indicate pressure of 2.21 kbar and 2.11 kbar averaging 2.16 kbar, which is equivalent to 7.34 km depth according to equation (4.1) and 6.4km depth considering the normal pressure gradient. However, granodiorite samples (LB13/31, LB14/32 and LB15/33) from middle level of the exposed batholith have values of 3.27 kbar, 2.88 kbar and 3.69 kbar averaging 3.28 kbar equivalent to 11.15 km depth according to equation (4.1) and 9.84 km depth considering normal pressure gradient.

Based on the pressure data it appears that the Ladakh Batholith has been crystallized at a depth between 14.27 km 7.3 km depth over a vertical section of around 2 km with diorite indicating lower crustal depth around 14.30 km and granodiorite around 7.35 km. When crustal depths are plotted against the elevation (Figure 4.4), a good correlation between crustal depths with elevation has been obtained.

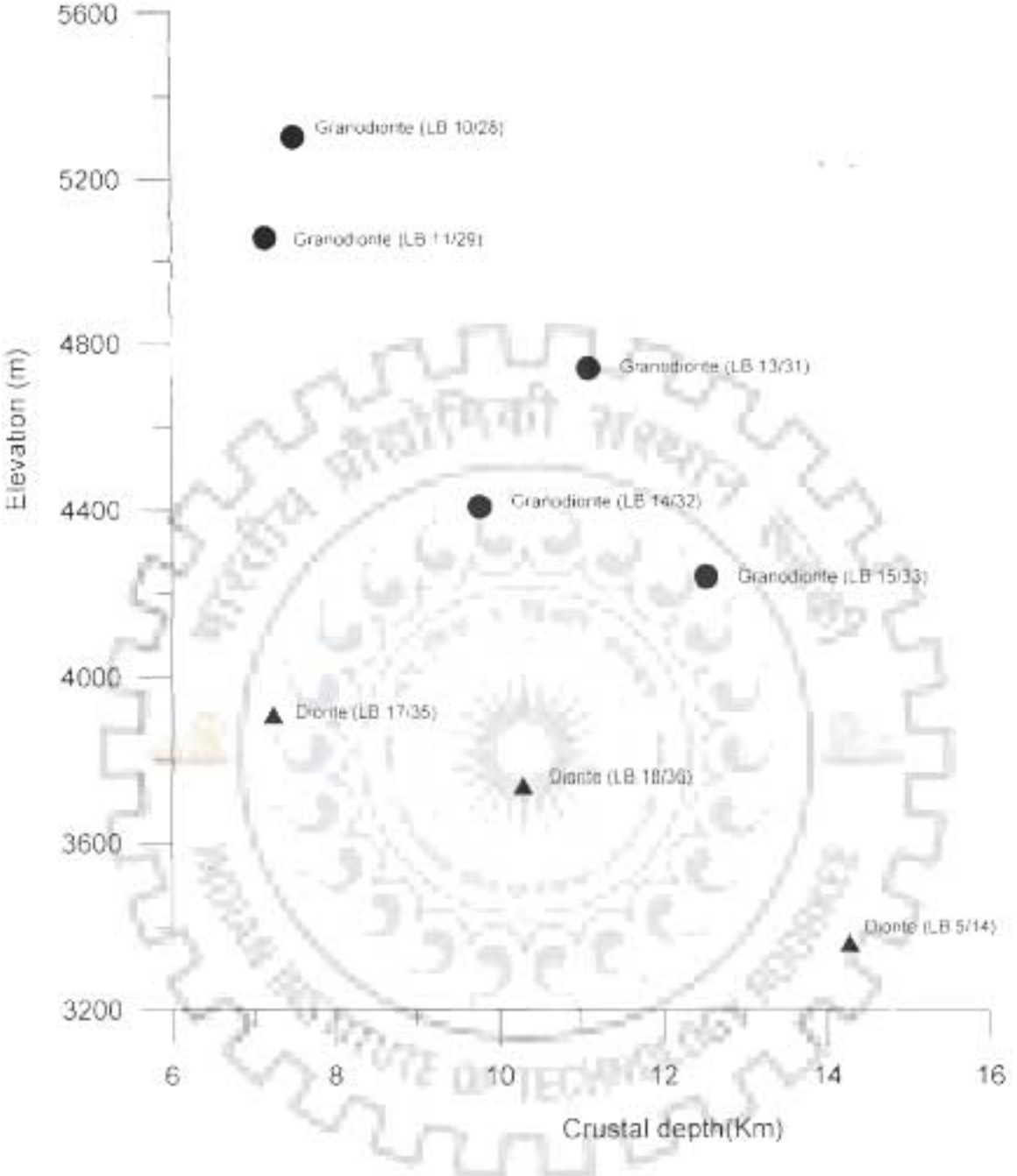

Figure 4.4: Elevation vs crustal depth plot of the Ladakh Batholith from Kharu- Chang La section.

CHAPTER–5

Rb-Sr DATING

5.1 INTRODUCTION

Isotope geology has grown over last few decades to become one of the most important fields of the Earth Sciences. It has transformed geology from a qualitative observational science to a modern quantitative one. The isotope geology has been used for understanding the petrogenesis of rocks as well as age determination of the rocks from the decay of radioactive elements. Radioactive elements have unstable nuclei which undergo spontaneous transformations, emitting matter and energy which ultimately leads to the production of stable daughter nuclei from unstable parent nuclei. Radioactive decay occurs by several different mechanisms. The most important of these in geological application are electron capture, beta decay and alpha decay. For geochronological purpose, different parent daughter pairs are in use such as Rb-Sr, Sm-Nd, K-Ar, Ar-Ar, Nd-Sr, Re-Os, U-Th-Pb etc. Each systematics has its own importance and use depending upon the rock-type and objective of the experiment, (Faure, 1977; Dikins, 1995).

The Rb-Sr systematics has been widely used for dating purposes. The Rb-Sr ratio in the mantle is much lower than the average ratio of the earth and it is much higher in the crust. Mantle derived rocks such as basalts contain low Rb-Sr ratio and because of this reason it is difficult to obtain good Rb-Sr ages on mafic and ultramafic rocks. However, igneous differentiation tends to increase the Rb-Sr ratio, because of Sr removal by fractional crystallization of plagioclase and retention of Rb in the melt, causing higher Rb-Sr ratio, thus making it a systematic suitable for the acid igneous rocks. Rb-Sr geochronometer can also be

applied to K-bearing, Rb-Sr rich minerals, because of higher Rb-Sr ratio. The whole rock isochron ages are indicative of the age of crystallization, whereas, the mineral ages are manifestation of the cooling and exhumation processes of the terrain of interest.

The main aim of the study presented in this chapter is to (a) use Rb-Sr systematic for the determination of whole rock as well as mineral ages of biotite from the Ladakh Batholith by analyzing these at the newly established Thermal Ionization Mass Spectrometer (TIMS) Laboratory IIT Roorkee, Roorkee and (b) to give the detailed procedure that is being followed at this laboratory.

5.2 PROPERTIES OF RUBIDIUM AND STRONTIUM

Both Rb and Sr are the trace elements in the earth; their concentrations are generally measured in ppm. Rb is an alkali element (Group I) with a valency of +1 and ionic radii of 1.48 Å (Table 5.1). Rubidium has two naturally occurring isotopes, ^{85}Rb and ^{87}Rb with isotopic abundance of 72.2% and 27.8% respectively. Out of these two ^{87}Rb is radioactive with a half-life of 48.8 x 10^9 years. Like other alkalies, it is generally soluble in water and hydrous fluids. Due to its bigger ionic radii of 1.48 Å makes it non acceptable to many mineral phases. Thus it is most incompatible element. The radius of Rb is similar to that of potassium (K=1.33 Å) causing its substitution in K-bearing minerals such as mica and K-feldspar.

Table 5.1: Geochemical Properties of Rubidium

Position in the periodic Table	Alkali metal (IA)
Atomic weight (a.m.u)	85.8346
Ionic radius (Å)	1.48
Isotopic Abundance (in %)	$_{37}Rb^{85}$ (72.1654±0.0132) $_{37}Rb^{87}$ (27.8346±0.00170)

Sr is an alkali earth (Group IIA) with a valency of +2 and ionic radii of 1.13 Å. The strontium has four stable, naturally occurring isotopes: ^{84}Sr, ^{86}Sr, ^{87}Sr and ^{88}Sr with isotopic abundance of 0.56%, 9.87%, 7.04% and 82.53% respectively out of which only ^{87}Sr is radiogenic; which is produced by decay of the radioactive ^{87}Rb. The ^{87}Sr in any material can be incorporated from two sources; one which formed during primordial nucleo-synthesis along with ^{84}Sr, ^{86}Sr and ^{88}Sr, and another by radioactive decay of ^{87}Rb. Sr has an atomic radius similar to that of Ca and, therefore, it substitutes for Ca in minerals. The distribution of strontium in rocks is controlled by the extent to which Sr^{+2} can substitute for Ca^{+2} in calcium-bearing minerals and the degree to which potassium feldspar can capture Sr^{+2} in place of K^{+} ions. The principal carriers of strontium in igneous rocks are plagioclase feldspar and apatite. During crystallization of magma, strontium initially enters calcic plagioclase by substitution for Ca^{+2}. As differentiation progresses and the potassium-feldspars begins to form, Sr^{+2} ions start getting from the liquid by K^{+} sites. Gradually the strontium concentration decreases with increase in degree of fractionation of the magma (Faure, 1977). The alkaline earths are also reasonably soluble in water and hydrous fluids, but not as soluble as of the alkalis. Sr is moderately mobile element as compared to Rb.

Table 5.2: Geochemical Properties of Strontium

Position in the periodic Table	Alkaline Earth (IIA)
Atomic weight (a.m.u)	87.62
Ionic radius (Å)	1.13
Isotopic Abundance (in %)	$_{38}Sr^{88}$ (82.53) $_{38}Sr^{87}$ (7.04) $_{38}Sr^{86}$ (9.87) $_{38}Sr^{84}$ (0.56)

5.3 Rb-Sr SYSTEMATICS

As indicated by Rutherford and Soddy (1902) the rate of decay of a radioactive parent to a stable daughter product is proportional to the number of atoms present at any time and the process is exponential function which is independent of chemical or physical conditions. The total number of daughter atom at any time 't' can be given as

$$D = D_0 + n(e^{\lambda t} - 1) \qquad (5.1)$$

where, D is the number of radiogenic daughter atoms, D_0 is the total number of daughter atom at time t=0, n is the number of atom, λ is the constant known as the decay constant and is expressed in the unit of reciprocal of time. This equation is the fundamental basis of geochronological dating touls (Dikins, 1995).

The Rb-Sr systematics is an example of beta decay, where ^{87}Rb transforms to ^{87}Sr. From ^{87}Rb a neutron has been converted into a proton and an electron (a beta particle β) has been expelled from the nucleus to give a ^{87}Sr atom. This can be written as:

$$^{87}Rb \rightarrow {}^{87}Sr + \beta^- + \nu + Q \qquad \text{---------} (5.2)$$

where, ν is the antineutrino and Q is the decay energy equivalent to 0.275 MeV.

The equation depicting ^{87}Sr atom in a rock which has remained in a closed system for time t years can be written as,

$$^{87}Sr = {}^{87}Sr_i + {}^{87}Rb(e^{\lambda t} - 1) \qquad \text{---------} (5.3)$$

Here ^{87}Sr is the total number of atoms of ^{87}Sr today, $^{87}Sr_i$ is the number of ^{87}Sr present when the sample first formed or system became closed, ^{87}Rb is the number of atoms of ^{87}Rb today and λ is the decay constant.

It is very difficult to measure precisely absolute isotopic abundance by mass spectrometry, whereas, the measurement of isotopic ratio is easy. Therefore, there is a need to use an isotope for normalization which is not involved in the radioactive decay process. In

case of Rb-Sr systematics ^{86}Sr is the right choice to form ratios which can be easily measured. ^{86}Sr in a sample of rock or mineral remains constant, while the number of ^{87}Sr atoms increase by decay of ^{87}Rb. Therefore, the equation (5.3) can be rewritten as

$$^{87}Sr/^{86}Sr = (^{87}Sr/^{86}Sr)_i + {}^{87}Rb/^{86}Sr\,(e^{\lambda t} - 1) \text{ ----------(5.4)}$$

where ,$^{87}Sr/^{86}Sr$=the ratio for these isotopes in the sample at the time of analysis and can be measured by mass spectrometer.

$(^{87}Sr/^{86}Sr)_i$ =the isotopic ratio at the time of formation of the rock or mineral specimen (unknown).

$^{87}Rb/^{86}Sr$=the ratio in the sample at the time of analysis.

The $^{87}Rb/^{86}Sr$ ratio of a rock or mineral can be measured using a suitable mass spectrometer, where the concentrations of Rb and Sr can be determined by various techniques individually and the $^{87}Rb/^{86}Sr$ ratio can then be calculated. Since the equation 5.4 is the equation of a straight line, the age and the intercept with Y axis can be calculated from a plot of measured $(^{87}Sr/^{86}Sr)$ vs. $(^{87}Rb/^{86}Sr)$ ratios for a suite of cogenetic samples, formed from the same parental material assuming that there has been no exchange of parent-daughter isotope other than through radioactive decay. The time 't' can be solved by the equation $t = 1/\lambda \ln$ (slope+1). This will give the age of the rock or mineral concerned provided the following conditions/assumptions are fulfilled (Faure, 1977):

1. The sample should be from homogeneous and comagmatic body.
2. The rock or mineral system neither gained nor lost either parent or daughter atoms indicating that the rock or mineral, must remain a 'closed system' with respect to the parent and the daughter isotope.
3. The value of decay constant must be known accurately and the value of the decay constant has not changed over the earth's history.

5.4 ISOCHRON & ERRORCHRON

When the $^{87}Sr/^{86}Sr$ compositions for a suite of cogenetic rock samples of the same age are plotted against their $^{87}Rb/^{86}Sr$ ratios, the points ideally define a perfect straight line called 'Isochron' (Fig 5.1).

The isotopic evolution of a suite of hypothetical minerals in the isochron diagram can be illustrated with the help of this diagram. At the time of crystallization of the rock, i.e. at t = 0, all the three samples have the same $^{87}Sr/^{86}Sr$ ratio with variable $^{87}Rb/^{86}Sr$ ratios and plot on a horizontal line. After individual sample has become a closed system, isotopic evolution starts. Due to this evolution, the points move to straight line with a slope. As ^{87}Rb decays to ^{87}Sr, $^{87}Sr/^{86}Sr$ increases and $^{87}Rb/^{86}Sr$ decreases, hence the points move along the arrow as indicated in Fig. 5.1. Each isotopic ratio remains on the isochron and its slope increases with time as long as the system remains closed.

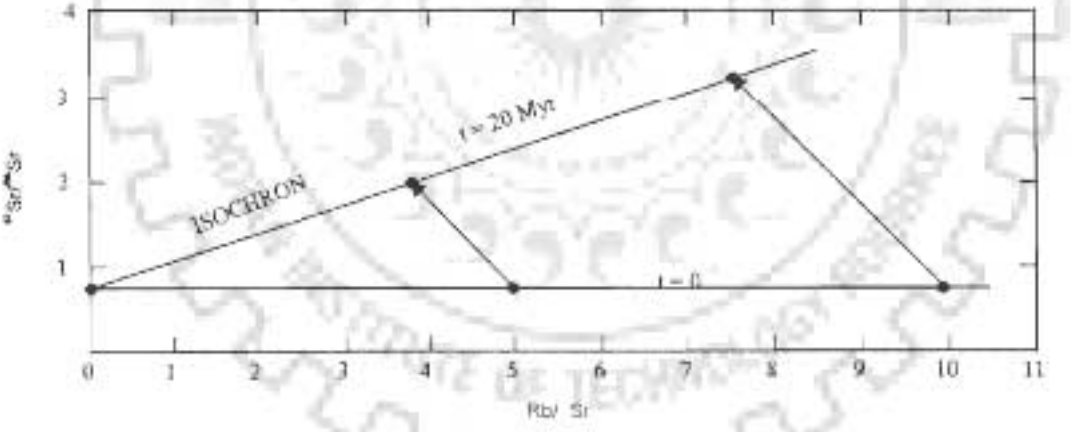

Figure 5.1: Rb-Sr isochron diagram on axes of equal magnitude showing showing production Sr as Rb is consumed in two hypothetical samples. The third sample has no Rb.

The quantities used to make an 'isochron' are measured experimentally hence experimental errors are inevitable. If a perfect straight line is not obtained, then numerous

regression methods of line fitting have been proposed and are in use (McIntyre et al., 1966; York, 1966, 1969; Brooks et al., 1972). Most of the regression methods are quite hectic and tedious with large number of mathematical calculations and need a computer to run the method.

However, a line fitted to a set of data that display a scatter about the line in excess of the experimental error is simply not an isochron (Brooks et al., 1972). McIntyre et al. (1966) proposed that Rb-Sr regression fits with excess or 'geological' scatter should be called 'errorchrons' and be treated with high degree of suspicion. This raised the problem of detecting the presence of geological scatter, bearing in mind the fact that analytical errors are only probabilities. To overcome this problem the concept of Mean Squared Weighted Deviates (MSWD) was introduced as an expression of scatter by York (1969) and Brook et al. (1968, 1972). If the scatter of data points is exactly equivalent to predicted from the analytical errors, then calculation will yield MSWD = 1. Excess scatter of data points yields MSWD >1, while less scatter than predicted from experimental errors yields MSWD <1. Since the analytical errors input into the program are only estimates of error the problem arises with the interpretation of MSWD values. To overcome this problem, Brooks et al. (1972) proposed a table of probabilities to distinguish between errorchron and isochron from MSWD values. They established a 'rule of thumb' that MSWD value < 2.5 in the data defines an isochron, otherwise it is an errorchron. Unfortunately, this thumb rule has been misused severely in past and it has become an accepted fact that MSWD must be near unity in order to have a high degree of confidence when the data represent a true isochron.

In order to date comagmatic igneous rocks by the whole rock isochron method, a suite of rocks must be collected with a wide span a range of Rb/Sr ratios if possible so that the slope of the isochron is well defined (Faure, 1977, Dickins, 1995).

5.5 CONCEPT OF CLOSURE TEMPERATURE

In order to quantify the geothermal history using mineral ages, Dodson (1973, 1979, 1981, and 1985) introduced the concept of closure temperature of a radiometric clock. He defined the closure temperature of a geochronological system as the temperature with the corresponding time of apparent age. It assumes that when the radioactive system is near to the crystallization temperature the daughter nuclide diffuses out as fast as it is produced by radioactive decay. As the system cools down, diffusion is blocked for the minerals at a certain temperature. In other words, the closure temperature of a mineral isotopic system represents a critical threshold above which the radiogenic daughter product is not retained against thermal disturbance and below which they get accumulated. Different minerals indicate different blocking temperature for different systematics. It appears that the closure is not instantaneous; rather it is transitional temperature range in which the daughter product or radiation damage is partially retained or lost.

In the Rb-Sr mineral if the systems have been opened due to thermal pulse, at the closure temperature the mineral systems will again get closed to element mobility. The dating of this mineral phase will give information about the cooling history or exhumation of terrains of interest, if the geothermal gradient of that terrain is known.

Blocking temperatures can be determined theoretically, based on calculations of the temperature-dependence of volume diffusion processes. Ideally, closure of the Rb-Sr system represents an instantaneous transition from completely mobile character to immobile character in a fast cooling terrain. In a slow cooling regional metamorphic terrain there is a continuous transition of a high-temperature regime. In this case radiogenic ^{87}Sr escapes from crystal lattice by diffusion as fast as it is formed by Rb decay. As they approach to low-temperature conditions there is negligible ^{87}Sr escape. In such a system, the apparent age of a

mineral (such as biotite) corresponds to a linear extrapolation of the low-temperature ^{87}Sr growth line back into the X-axis. If a mineral is in contact with a fluid phase, which is able to remove radiogenic Sr from its surface, then the rate of loss of ^{87}Sr depends on the rate of volume diffusion across a certain size of lattice. In the case of biotite, this diffusion will be predominantly parallel to cleavage planes rather than across them.

In the present study, closure temperature for Rb-Sr biotite system is considered to be 300±50°C (Dickin, 1995) and the decay constant used to calculate the ages has value of $1.42m \times 10^{-11}$ Yr^{-1}, as recommended by IUGC subcommission on Geochronology (Steiger and Jaegar, 1977).

5.6 MASS SPECTROMETER

A mass spectrometer is an instrument to separate the charged atoms and molecules on the basis of their masses through their motions in an electrical and/or magnetic field. Thermal ionization is a technique, which has been chiefly developed for the analysis of geological samples. The technique is used extensively for the isotope ratio measurements required for Rb-Sr, Sm-Nd, Pb-Th-U, Re-Os etc. for geochronological studies as well as the determination of rare earth elements and less frequently, other selected elements by isotope dilution analysis. Extensive chemical treatment of the sample for concentration, like ion exchange separation, is required before analysis to overcome the isobaric interferences (Faure,1977, Dickins, 1995).

A new generation modern mass spectrometer consists of three essential parts:

a. A source of positively or negatively charged mono-energetic beam of ions,

b. A magnetic analyzer, and

c. An ion collector/detector.

All the three parts of the mass spectrometer are evacuated to pressures of the order of 10^{-6} to 10^{-8} torr. The main reason of a high vacuum is to reduce collision between ions and the residue gas molecules which can cause some loss of kinetic energy from the ion. The loss of kinetic energy will reduce the appropriate flight path during deflection through the mass analyzer.

The ion source generates three types of species, uncharged molecular and atomic fragments, positively charged ions and negatively charged ions. Uncharged species cannot be used for measurement by mass spectrometry, however, positively or negatively charged ions can be measured. In a positively charged mode, uncharged and negatively charged ions collide with the walls of the instrument and are pumped away by the vacuum system, whereas positively charged particlesfions are guided through a potential gradient collimated by slits and passed into a strong magnetic field.

A positively charged ion entering a magnetic field is subjected to a force which acts to deflect the ions. This force acts in a direction mutually perpendicular to both direction of motions of the ion and the direction of magnetic field. If the magnetic field is sufficiently extensive and homogeneous, the motion of the ion would describe a circular trajectory with radius 'r'. The magnitude of this radius depends on the balance of the centrifugal force due to the kinetic energy of the ion, and magnetic centripetal force. In the absence of the field the ions would travel in the straight line. If the ion of mass 'm' has been accelerated to a potential gradient 'V' before entering the magnetic field, its kinetic energy will be given by:

$$eV = 1/2\ mv^2 \qquad \text{----------(5.5)}$$

where, e =charge on ion

v = velocity of the ion

and the centrifugal force exerted on the ion travelling in a circle of radius 'r' will be

$$\text{Centrifugal force} = mv^2/r \qquad \text{---------(5.6)}$$

The magnetic centripetal force is the force of deflection created by the magnetic field:

$$\text{Force} = HeV \qquad \text{---------(5.7)}$$

where, H = strength of the magnetic field

For these two forces in balance, it can be shown by equation (5.5), (5.6) & (5.7)

$$r = 1/H\sqrt{2}\,V(m/e) \qquad \text{---------(5.8)}$$

or $$m/e = H^2 r^2/2V \qquad \text{---------(5.9)}$$

Equation (5.8) indicates that the degree of deflection of an ion of constant mass to charge ratio increases 'r' at higher field strengths or lower acceleration potential in the ion source.

In practice, the radius of ion flight path ['r' in equation (5.9)] is normally fixed by instrument design. The specific mass-to-charge ratio observed at a fixed exit slit depends on the field strength of the magnet 'H' or the accelerating potential 'v' of the ion source. In order to scan a mass spectrum it is necessary to vary one or the other of these parameters. In most mass spectrometer design it is normal to change the magnetic field strength rather than acceleration potential. In instruments, instead of a single ion, a small solid beam of ions enters to magnetic sector. The plane of focus lie on a line, provided ion beam enter and leave the magnetic field at right angles passing through the entrance slit and the apex of the magnetic sector. In most instruments the deflected ion beam is constrained by a fixed exit slit across which the mass spectrum is scanned.

An ion detector or collector lie beyond the exit slit of the magnetic sector. Four types of devices are available for ion detector, they are; photographic plate, the electron multiplier, the daly detector and the faraday cup. The faraday cup is the simplest of the commonly used electronic detection devices. It consists of three components: a beam defining slit (the exit slit of the mass analyzer), electrode (the faraday cup or bucket) and an electron repeller plate.

Once an ion is impinging in Faraday Cup, a charged electron is deposited on the electrode. For an ion count rate of 'n' ions per second, the corresponding charge deposited on the electrode is:

$$ne = 1.602 * 10^{-19} .n \text{ coulombs sec}^{-1}$$

$$ne = 1.602 * 10^{-19} .n \text{ amperes}$$

This charge is normally leaked to earth through a resistor having very high value (in the range 10^{8} - 10^{12} ohm), the voltage dropped across the resistor are measured with the sensitive voltmeter of high input impedance. The ion count rate is proportional to this voltage drop across the resistor. There is an effect of emission of secondary electron due to impinging of ions on the electrode causing loss of signal. In order to suppress this effect, an electron repeller plate is placed in front of Faraday cup. This plate is held at negative potential (50-90 volts) with respect to the Faraday electrode, which is itself designed in the shape of a cup or bucket to further suppress this effect.

5.7 ANALYTICAL PROCEDURE

5.7.1 MECHANICAL PREPARATION: About 5-7 kg of fresh rock samples collected in situ in the field were crushed in a steel Jaw Crusher (FRIC11 model) to reduce the coarse rock powder of 1-2 mm through repeated crushing and sieving. Proper coning and quartering was performed to attain homogenization. One fraction was taken to tungsten carbide ball mill grinder (RETSCH CENTRIFUGAL BALL MILL S100) for powdering <200 mesh size and other fraction was preserved for mineral separation. From the powdered sample about 10 gm powder was taken out and manually ground to more fine powder in an agate mortar and pestle and stored in vials with neat labeling slips. For biotite separation part of the sample was crushed to size 80-150 mesh. This fraction was spread on a glossy butter paper to remove strongly magnetic particles with a covered bar magnet. A fabricated mica

vibrator was used for concentration of mica fraction. Then, Isodynamic Separator was used to separate the magnetic fraction (biotite, hornblende, etc.) from the non magnetic fraction (quartz and feldspar). The Isodynamic separator works on the theory of magnetic field and separates the fractions on the basis of magnetic properties. 0.5 ampere current with side tilt of 18^{0} was used at first and then the magnetic fraction obtained from this step was again run at 0.8 ampere current with side tilt of 22^{0} to obtain fairly concentrated biotite. After this step, the fraction was spread out on a glass slide to pick up the biotite separately by hand picking under binocular microscope (NIKON-model). During the handpicking stage, utmost care was taken to remove all the composite and altered grains. All the instruments and containers used in the processing were cleaned by high pressure air blower. Utmost care was taken to prevent any sort of cross contamination at any stage.

5.7.2 SAMPLE DISSOLUTION: Once the powder and mineral separates are ready, the samples were weighted on Sartorius Electronic Balance. Representative rock powders (~100mg) and mineral separates (~50 mg) were dissolved in 3ml HF (48%) and 1ml of highly purified HNO_3 acid. High purity (HNO_3 and HCl) acids are prepared by sub-boiling in a quartz glass distillation unit and HF into double bottle distillation unit. Sample dissolution is carried out in a tightly capped 15ml PFA teflon vessels (Savillex) first at room temperature for about 36-48 hours and then on a hotplate at about 70^{0}C for 24 hours for whole rock. The tightly capped vials were opened and the solution was evaporated to dryness at slow heat (about 70 to 80°C) and then redissolved and evaporated two times using HCl and HNO_3. For the mineral dissolution the tightly capped Savillex vials were left for 24 hours at room temperature before evaporation on hot plate at about 70 to 80^{0}C. The samples were evaporated and dried till brown cake like residue was obtained. The brown cake like residue was dissolved in 2 ml 2N HCl to get clear solution.

5.7.3 ISOTOPE DILUTION: After the dissolution is complete isotopic dilution (spiking) is done. Isotope dilution is an analytical technique by means of which the concentration of an element in a sample can be determined by use of Mass Spectrometer. Isotope Dilution Mass Spectrometry is abbreviated as ID(TIMS). The isotope dilution method is based on the estimation of the quantity of an element from the change induced in its isotopic composition by the addition of a known quantity of spike of that element contributed from the spike and the unknown amount of element contributed from the sample. The isotope dilution technique can be applied to any element that exists as two or more naturally occurring isotopes, provided a spike is enriched in one of the isotopes of that element is available (Blichert, 1993). Vial along with the sample and 2N acid, which was last added, was weighted, readings are noted and then ^{84}Sr spike (~30mg) was added to it. After spike is added from first bottle it was also weighted and reading noted down. After this ^{87}Rb spike was added to it and readings for both vial and spike bottle were taken. This is done to cross check the exact amount of spike that was added. A spike is a solution that contains a known concentration of a particular element in which natural isotopic composition has been altered by the enrichment of one of its naturally occurring isotopes. The exact concentration and isotopic composition of the spike element are verified separately by calibration using standard solutions of well-known concentrations.

In case of whole rock samples, the ^{84}Sr spike amount that has been added is ~30 mg and ^{87}Rb spike is ~150 mg. In case of biotite samples the ^{84}Sr spike amount that has been added is ~30 mg and ^{87}Rb spike is ~100 mg. The amount of spike that has been added in case of whole rock is higher because the Rb content in the rock is already high whereas in case of biotite samples the Rb content is less as it has higher mobility and must have escaped from the mineral to the rock.

Quantitative dissolution of finely powdered rocks has been checked by multiple measurements of Rb concentrations by isotope dilution on the same rock-powder. The agreement was found to be very good (typically within 1%) over a range of Rb concentrations in felsic rocks. After dissolution, small amounts (typically 0.3 to 0.2 g) of ^{87}Rb and ^{84}Sr spikes of high isotopic purity are added to the solution and evaporated. After evaporation the residue left in the vial was dissolved in 1.2ml 2N HCl and transferred in centrifuge tube with the help of micropipette. The sample spiking procedure was the same for the whole rock as well as the mineral separates.

5.7.4 ION EXCHANGE CHROMATOGRAPHY: Ion exchange chromatography refers to any exchange method invoiving the distribution of components between a fixed (stationary) and a moving (mobile) phase. The later is also called the eluent. Separation of individual components towards the stationary and mobile phases causes different components to move at different rates along a column. This process, by which an eluent makes a compound move along a column, is called elution (Blichert, 1993).

Ion exchange chromatography involves the reversible exchange of ions between a solid phase (the resin itself) and a mobile phase (a solution of the ions). The resin is normally packed in a suitable glass tube, the column held vertically, and the sample solution is poured (loaded) on the top of the column. The sample is then eluted by washing its ionic components through the columns using a suitable solvent at a controlled rate. Ions are separated from one another due to differences in their affinity towards the ion exchange resin. The more strongly an ion is attracted to the resin, the larger the volume of the eluent required to wash that ion out of the ion exchange column.

In the dry resin each fixed functional group ($-SO_3^-$) is attached with a counter ion (H^+) to maintain electrical neutrality. However on being mixed with water, the counter ions

become mobile and some diffuse out of the resin into the bulk solution. This causes an uncompensated negative charge in the resin, which makes it more and more difficult for further counter ions to leave the resin. A dynamic equilibrium is readily set up so that the number of counter ions diffusing out of the resin equals the number of ions diffusing back. A small electrical potential is thus set up at the resin boundary called the Donnan potential. Due to it, ions other than the original counter ions may also diffuse in to the resin and associate with a functional group. The proportion of such ions participate in this ion exchange process depends on their affinity for the functional group compared with original counter ions (Blichert, 1993).

The theory of ion migration down a column is based on the principal that when a solution is loaded on column, a dynamic equilibrium is rapidly established such that ions in solution partition themselves between the stationary phase (ion exchange resin) and the mobile phase (the eluent) according to distribution law

$$D = C_{solute,\ resin} / C_{solute,\ resin}$$

where D is the distribution coefficient for a given ionic species between the resin and the eluent, and C is the concentration of the ionic species (solute) in the resin and eluent.

When D is minimum, the most ions are in the eluent, whereas when D is maximum, most ions are in the resin. D decreases with the increasing normality of the eluent for cation exchange resins, and decreases with decreasing normality of the eluent for anion exchange resins. A strong eluent is required for the cleaning of a cation exchange resin, whereas a dilute eluent or H_2O suffice for the cleaning of anion exchange resins. For our work we are using a cation exchange column.

The distribution coefficients of most ions also depends on the concentration of solute ions present in a given resin volume, i.e. how much material is loaded on the column. D becomes smaller as the loading is increased. The more dilute the solution, the more strongly

an ion will be held by the resin, and vice versa. Ion exchange is therefore best performed under conditions where loading is low (a conservative estimate recommends the use of no more than 10% of the total resin capacity but here we are using the loading capacity of 30%) and D thereby nearly constant. Overloading a column will lead to incomplete separation and partial loss of elements (Blichert, 1993).

A total resin capacity is defined as the number of exchange site equivalents per unit weight or volume of the ion exchange resins is usually about 5 meq/g of dry hydrogen from resin or 1.8 meq/ml (or cm^3) of wet resins bed. The capacity of quaternary ammonium types of anions exchange resin is about 3 meq/g of dry chloride from resin or 1.2 meq/ml (or cm^3) of wet resin bed.

The separation factor, α, is the ratio of the distribution ratios of two sample components, A and B, and is written as

$$\alpha = D_B / D_A$$

α is the measure of the separation that can be achieved by parting two components after a single equilibration with the resin. The degree of separation increases as α deviates from unity. Two solutes are completely separated only if all of solute A is in one phase and all of solute B in the other.

The ion exchange reaction that takes place between an ion exchange resin and a surrounding ionic solution can be illustrated by the following cation exchange reaction

$$RSO_3^- H^+ + A_{aq}^+ = RSO_3^- A^+ + H_{aq}^+$$

Since exchange take place equivalents for equivalent, for divalent ions:

$$2RSO_3^- H^+ + B^{2+} = 2H_{aq}^+$$

In the equilibrium position these reaction depends upon the relative concentrations of the counter ions H^+, A^+, and B^{2+} in the solution and in the resin, respectively, assuming that the ions have equal affinities for the resin.

The relative preferences of a given series of ions are determined primarily by the properties (acidity- basicity) of the fixed functional groups of the resin. The selectivity increases with increasing ionic size, for example, for the calc-alkaline elements; Ca will be eluted prior to Sr, which will be eluted prior to Ba (rBa>rSr>rCa). Among a group of ions with different valences, ions higher charges are usually more strongly selected by a resin and bounded to it more tightly than divalent ions. Additional factors affecting the selectively of ion exchange resins are the pore size of a resin. The degree of cross linkage, which affects the degree of swelling and thereby pore sizes and temperature, pressure, ionic strength of solutions.

5.7.5 ELUTION PROCESS: Sample is loaded into the column on the resin bed. As the sample moves through the column all the ions in the samples are adsorbed on the surface of the resin. Elution is done with 2N HCl. Many experiments have been conducted and it is shown by these experiments that 2N mode is the best for the elution of Rb and Sr and the range for collecting Rb and Sr fraction have been calibrated (Table 5.3). Rb and Sr are both cation and they attach themselves to the sulphonate group of the resin. As we add more and more HCl to the column the H^+ ions keep on attaching themselves to the resin. Soon the resin becomes loaded with H^+ ions and due to this the Rb starts detaching from the resin. Later on Sr follows the same process. The reason for elution of Rb before Sr is that Rb has positive charge of one and Sr has positive charge of two, so the Sr is more strongly bonded to the resin than the Rb. After elution of Rb and Sr, regeneration is done. This is done with help of 6N HCl. 6N is used so that all other ions which are left in the column are removed from the column. We can use acids of higher strength also but due to presence of more water in 6N this is used. Water acts as a catalyst thereby increasing the rate of the reaction and this will thereby reduces the time of regeneration. Acids of higher strength i.e. more concentrated will

reduce the rate of the reaction and hence increasing the time of elution and may also harm the resin. Acids of lower strengths than 6N may not be able to elute all the left over ions from the column. The total procedural blank is less than 8 ng. Rb and Sr fractions collected in separate Savillex vails were evaporated to dryness in and stored for loading.

Table 5.3: Elution Process for Rb-Sr Separation Procedure

Sample Type: Date:

Sample Number: Sample Location:

The following steps are to be followed for the elution:

Column No./Steps	A	B	C	D
Load 1 ml sample in 2N HCl, collect and discard.	□	□	□	□
Load 1 ml 2N HCl, collect and discard.	□	□	□	□
Load 1 ml 2N HCl, collect and discard.	□	□	□	□
Load 1 ml 2N HCl, collect and discard.	□	□	□	□
Load 1 ml 2N HCl, collect and discard.	□	□	□	□
Load 6 ml 2N HCl, collect and discard	□	□	□	□
Load 7 ml 2N HCl (collect Rb in vial)	□	□	□	□
Load 11 ml 2N HCl, collect and discard.	□	□	□	□
Load 13 ml 2N HCl (collect in savillex vial for Sr.)	□	□	□	□
Load 20 ml 6N HCl for regeneration	□	□	□	□
Load 20 ml 6N HCl for regeneration	□	□	□	□
Load 20 ml 6N HCl for regeneration	□	□	□	□
Conditioning the column for next separation of Rb-Sr.				
Load 20 ml 2N HCl, collect and discard.	□	□	□	□
Load 20 ml 2N HCl, collect and discard.	□	□	□	□

5.7.6. SAMPLE LOADING: Prior to sample loading on filament, the filaments have been treated in a separate degassing unit to remove all the gases present so that they do not intertere with the ionization process. These degassed filaments are then put in the socket of the heating instrument. All these filaments are to be handled with the help of forceps and

no use of hand should be there to prevent any contamination and grease. Contamination will hamper the analysis and grease will reduce the vaccum. One microlitre of H_3PO_4 is put on the Ta-filament or one microlitre of TaF_5on the W-filament in the centre with the help of one microlitre pipettman. The H_3PO_4 or TaF_5 is used for base which provides adhesive surface for sample and it also removes the organic impurities from the sample.

Gradually the current was increased up to 0.8 ampere to heat the filament so that H_3PO_4 or TaF_5 becomes viscous and forms a uniform layer over the filament. As the H_3PO_4 or TaF_5 becomes viscous we slowly reduce the current to zero. After this 2 µlitre of MQ wateris put into the vail containing sample, which is in the nitrate form [for Sr it is Sr $(NO_3)_2$]. In this form it is easily dissolved in water. Then one µ litre of the sample is taken in the pipette and the sample is loaded on the filament at the centre on viscous H_3PO_4 or TaF_5. We slowly increase the current up to 0.8 ampere and maintain this for some time till it become dry. Now the current is increased till the fume of H_3PO_4 or TaF_5 start coming. This current is maintained for some more duration till the fumes stop emerging. The temperature is again increased in a flashed manner till the red glow appears on the filament. This current is then reduced to zero after a flash. Now the sample is ready for putting up in the TIMS. This process has been followed for all the samples but the micropipette-tip has to be changed for each sample. The following precautions are necessary during sample loading:

1. Micropipette-tip should be changed for each and every sample for loading and care should be taken so that same tip is not repeated for the other sample.
2. Current should be increased very slowly otherwise it could lead to:

   loss of sample and

   burning of filament.

3. After loading the sample the current should be maintained for some time till the fumes stop coming. This is done so that the fumes of phosphoric acid or TaF_5 do not enter the source chamber during ionization process causing bad vaccum.

Before loading proper catalogue maintenance is a necessary step so that the sample identification can be done after the analysis. A turret is circular wheel like part of mass spectrometer on which the filaments are loaded on 21 notches. These notches are numbered from 1 to 21. Each filament is put on the turret with proper numbers. After this step the turret is placed in the source chamber. Before placing the turret in the source chamber it has to be checked if high voltage

HV is off and

analyzer gate is closed.

Then the vacuum in source chamber is broken by inserting the key. The latch on the source chamber gate is loosened when the pressure is released from the source chamber the nitrogen gas has to be leaked into source chamber at low (0.5 bar) and constant pressure from the nitrogen cylinder. Gradually pressure increases in the source chamber and when it reaches equal to the atmospheric pressure the gate opens. The turret is then loaded into the source chamber. After it the gate of the source chamber is shut down and vacuum creation starts by switching back the key. When the pressure decreases to $2.3*10^{-7}$ bars, the samples are ready for data acquisition.

The sample is atomized and ionized by gradually heating the filament to the required temperature by passing an electric current through it. Ions are extracted into the analyzer by applying a potential of several kilovolts (positive) to the filament relative to an anode plate. After this, the data acquisition is carried out by using the software provided by Finnigan.

5.8 LABORATORY SPECIFICATION

Both Rb and Sr concentrations are measured by isotope dilution. The ^{84}Sr (82.5%) tracer solution has been calibrated using gravimetric solutions prepared from NIST SRM 987 $SrCO_3$. The isotopic compositions of these have been determined in the laboratory with appropriate mass fractionation corrections determined by running NIST standards under identical loading and running conditions. Gravimetric solutions prepared from NIST SRM 984 RbCl standard has been used for calibration of ^{87}Rb tracer. The Rb tracer has been prepared from enriched salts of ^{87}Rb (98%).Tracer solutions are stored in tightly capped FEP bottles that are weighed each time the spike is added to a sample to monitor the evaporation loss. Both Rb-Sr isotopic composition and isotopic dilution measurements are done on a single dissolution. With these procedures the uncertainties are about 0.1% for Sr and about 0.5% for Rb. Rb and Sr concentrations in sample are calculated off line after correcting for fractionation and the $^{87}Sr/^{86}Sr$ ratio is calculated after deducting the spike contribution according to the double spike correction method (Boelrijk, 1968). The reproducibility of this method has been checked by spiking the NIST SRM 987 several times. The obtained value for $^{87}Sr/^{86}Sr$ of SRM 987 agreed each time with the recommended value within the precision of the mass spectrometer (about 5 ppm). The method has been programmed on a Microsoft EXCEL spreadsheet and saves the trouble of separate dissolution for IC and ID.

Isotopic measurements are performed on the Thermo Electron TRITON TI fully automatic variable collector mass spectrometer (Fig 2). Typical sample loads are less then 500 ng of Sr and ~ 200 ng of Rb on a single degassed W filament with 1µl of TaF_5 solution having 1% Ta in the solution (Birck, 1986). TRITON of this laboratory has 9 Faraday collectors and one electron multiplier permitting measurement of all the isotopes plus interfering isotopes for the element of concern in a single static integration. During a static

Figure 5.2: Triton T1 Thermal Ionization Mass Spectrometer housed at Institute Instrumentation Center (IIC), Indian Institute of Technology Roorkee Roorkee, India

multi-collection (except for Rb) data acquisition is done in 9 Blocks of 40 cycles each giving a total of 360 measurements for each isotope. The amplifiers are rotated among the Faraday cups between the blocks. Thus each of the 9 amplifiers get sequentially connected once to each Faraday cup during the data acquisition. In general 4s integration time and 3s of settling time is allowed using TRITON software supplied by the company. This makes the data acquisition fast and eliminates the amplifier gain differences as well as the possible cup biases. Isotope dilution measurement of Rb consists of 100 ratios in 5 blocks of 20 ratios each without amplifier rotation. The beam intensity for Sr is kept at $5X10^{-11}$ amp of ^{88}Sr. Normally within run 1 s.e mean is much less than 10 ppm (often about 5 ppm) for normalized $^{87}Sr/^{86}Sr$. The measured ratios for isotopic composition are normalized to $^{86}Sr/^{88}Sr = 0.1194$ using Rayleigh Law. Isotopic ratio measurement of international laboratory standards have been done in both static and dynamic multi collection modes using the following cup configuration for dynamic mode as given in the TRITON software:

Triple collector measurement of Sr:

	L_1	C	H_1
1.	^{85}Rb	^{86}Sr	^{87}Sr
2.	^{88}Sr	^{87}Sr	^{85}Sr
3.	^{87}Sr	^{88}Sr	-

True $^{87}Sr/^{86}Sr$ ratio is calculated online by the software by taking appropriate ratios in each line with the assumption that the fractionation remains the same in each line and also the cup efficiency is constant.

The internal precision of Sr standards obtained by using the static and dynamic multi-collection data acquisition modes were found indistinguishable from the respective static multi-collection runs. External precision of several runs of Sr standards taken over the past

one year is also similar to the internal precision (within 10 ppm - Fig 5.3). The data obtained in the lab on NIST SRM 987 has a mean value of $^{87}Sr/^{86}Sr = 0.710248 \pm 10$ (1σ) against the quoted value of 0.710245 (Choudhary et al., 2004).

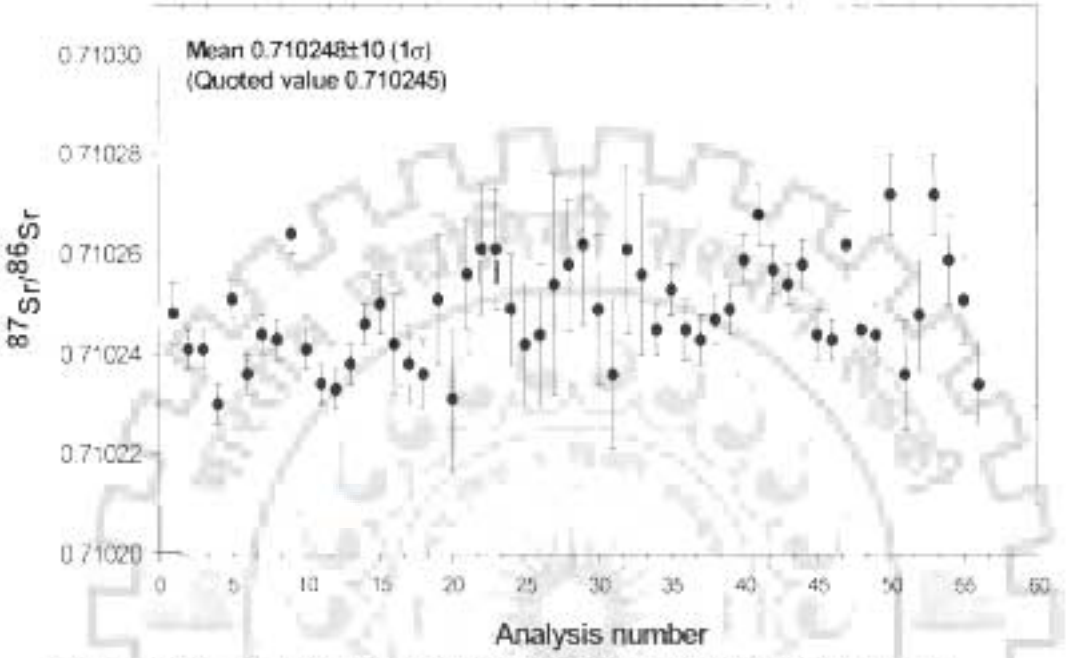

Figure 5.3: External precision of several runs of Sr standards (NIST 987) taken over the past one year

5.9 RESULTS

New Rb-Sr isotopic and abundance data for 21 whole rock samples and 7 biotite fractions separated from some of these selected samples have been generated for this study. The whole rock samples are from all the three sections (a) the Kharu-Chang La, (b) the Leh-Khardung La and (c) the Lyoma-Hanle sections. The location of the samples is shown in Figure 5. 4). From the whole rock Rb-Sr data, the primary crystallization age has been tried while mineral age data have been used to infer the cooling and exhumation history of the

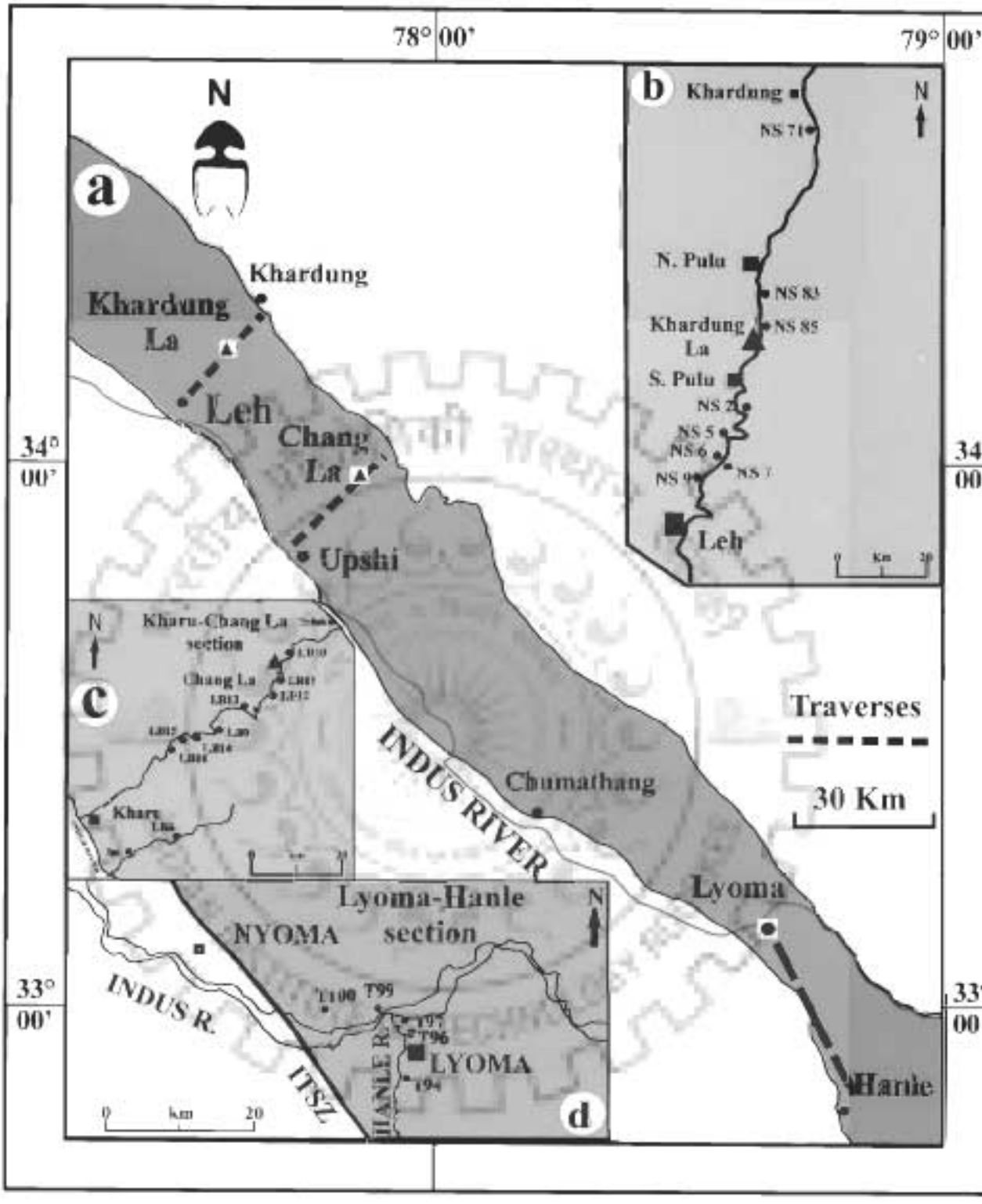

Figure 5.4: Location map of samples from the Ladakh Batholith for Rb-Sr Geochrono
(a) Map of the Ladakh Batholith. (b) Leh-Khardung La section. (c) Kh
Chang La section. (D) Lyoma-Hanle section.

Ladakh Batholith in combination with the Fission track zircon and apatite ages which is discussed in the chapter 7. Table 5.4 shows the whole rock data whereas the Table 5.5 shows the data of the biotite analyzed reduced by using Isoplot 3.1 programme (Ludwing, 2003).

The whole rock $^{87}Rb/^{86}Sr$ and $^{87}Sr/^{86}Sr$ ratios do not give any distinct pattern (Fig 5.5) Most of the points are clustered with very little Y axis spread but there is some spread in the X axis. The $^{87}Rb/^{86}Sr$ value shows a wide variation from 0.20460 to 28.21580 and $^{87}Sr/^{86}Sr$ ratio on Y axis shows a variation from 0.704000 to 0.763413. Due to incosistent spread in the ratios it is not possible to plot an isochron and infer the absolute age of the body if all the analyzed samples taken into consideration at a time. As the Rb-Sr whole rock data departs significantly from a strict linear pattern, an isochron and hence age determination is quite difficult for the set of data generated. However, if the samples of separate sections are taken into consideration then we get a perfect 4-point isochron on the samples LB8/23, LB12/30, LB14/32, and LB15/33 from the Kharu-Chang La section (Fig 5.6). This isochron gives the crystallization age of 61.59±0.05 Ma with initial $^{86}Sr/^{87}Sr$ ratio of 0.70417±0.000006. The MSWD value of 0.92 for this isochron depicts the good quality of fit. This age is in conjunction with the reported SHRIMP II U-Pb age of 60.1±0.9 Ma (Singh et al. 2003; Jain et al. 2003, 2004). When isochron plots for individual sections are considered, no distinct pattern emerges from Leh-Kardung La (Figure. 5.7), Kharu-Chang La section (all samples, Figure 5.8) and Lyoma-Hanle section (Figure 5.9). This pattern is consistent with the previous studies by Honneger et al. (1982), Scharer et al. (1984) and Sorkhabi et al. (1994), who also observed such heterogeneities from the Ladakh Batholith.

Seven biotite mineral fractions were separated from the whole rock samples and analyzed in the same way as the whole rock. The biotite ages obtained from the analysis give a wide range of ages from 36.71±0.05 to 52.48±0.05 Ma. These ages represent that the

Table 5.4: Rb-Sr data for whole rock analysis of granodiorites from the Ladakh Batholith

Serial No.	Sample No.	^{87}Rb	^{86}Sr	Sr(ppm)	Rb(ppm)	$^{87}Rb/^{86}Sr$	$^{87}Sr/^{86}Sr$
			Leh-Khardung La Section				
1	NS 2/3	0.2101	0.0140	121.4	64.30	1.5335	0.706051
2	NS 5/12	0.02194	0.019	140.6	57.0	1.1718	0.703085
3	NS 6/14	0.03499	0.006	53.1	104.3	5.6812	0.708774
4	NS 7/19	0.04822	0.002	14.5	141.9	28.2158	0.726958
5	NS 9/20	0.01288	0.050	276.9	40.5	0.4225	0.704880
6	NS 21/26	0.01980	0.020	380.3	46.3	0.6681	0.705015
7	NS 83/157	0.02291	0.025	213.9	67.8	0.9168	0.705337
8	NS 85/161	0.02885	0.013	111.8	93.6	2.3708	0.705927
			Kharu-Chang la section				
9	LB 8/23	0.01280	0.03742	358.40	42.3689	0.3419	0.704478
10	LB 9/27	0.00041	0.07309	408.50	1.2205	0.2046	0.707771
11	LB 10/28	0.02291	0.01506	70.00	73.0077	1.5363	0.699053
12	LB 11/29	0.00507	0.02611	223.90	26.9	0.3473	0.705487
13	LB 12/30	0.10695	0.03167	327.28	38.1997	0.3376	0.704431
14	LB 13/31	0.00936	0.01030	90.20	28.3128	0.9112	0.706018
15	LB 14/32	0.01833	0.01901	178.43	59.4864	0.9645	0.704993
16	LB 15/33	0.02222	0.01232	111.98	70.3209	1.8177	0.705421
			Lyoma-Hanle section				
17	T 94/335	0.03074	0.02639	222.12	59.70	1.1671	0.7075534
18	T 97/343	0.04062	0.02409	209.83	91.90	1.2703	0.7140884
19	T 99/346	0.04181	0.02515	222.10	127.90	1.6643	0.705705
20	T 100/350	0.05075	0.00292	25.60	153.29	17.3808	0.728412
21	T 96/341	0.07172	0.02240	195.43	215.07	3.2019	0.763888

Table 5.5: Rb-Sr data for biotite analysis from the Ladakh Batholith

Sl. No.	Sample No.	^{87}Rb	^{86}Sr	Sr_{total} (ppm)	Rb_{total} (ppm)	$^{87}Rb/^{86}Sr$	$^{87}Sr/^{86}Sr$	Age (Ma) (WR-Bio pair)
1	LB 11/29	0.04837	0.00309	46.20	241.80	15.12	0.714373	45.55±0.06
2	LB 9/23	0.07677	0.00158	29.40	491.1	48.5107	0.743672	52.37±0.05
3	LB 15/33	0.08556	0.00177	29.30	514.60	51.0815	0.742425	52.48±0.05
4	LB 8/23	0.04021	0.00271	53.10	271.30	14.7967	0.71500	51.25±0.07
5	LB 14/32	0.05543	0.00250	40.50	309.60	22.0952	0.716034	36.71±0.05
6	LB 10/28	0.16930	0.00038	6.54	633.31	280.53	0.885223	46.67±0.05
7	NS 5/12	0.06401	0.00187	36.56	430.45	34.2799	0.733890	44.92±0.05

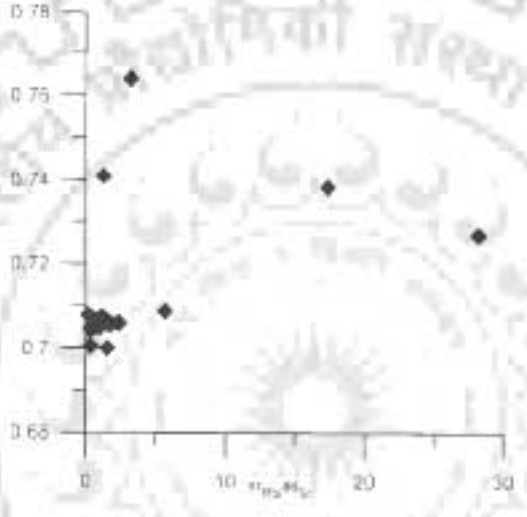

Figure 5.5. Plot of the whole rock $^{87}Rb/^{86}Sr$ and $^{87}Sr/^{86}Sr$ ratios of samples anlysed from the Ladakh Batholith

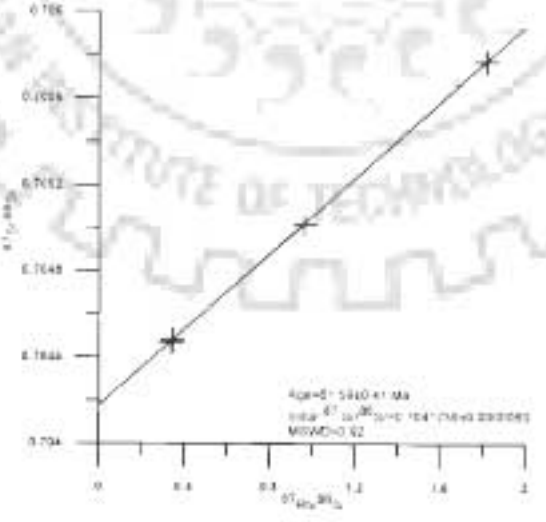

Figure 5.6. Plot of 4 point isochron from Kharu-Chang La section, Ladakh Batholith

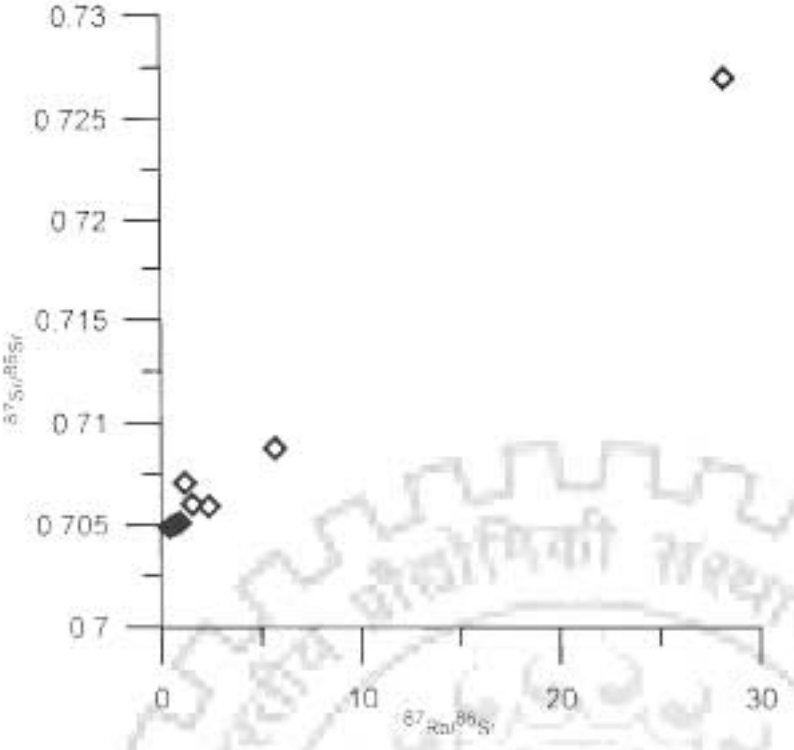

Figure 5.7 Plot of the whole rock $^{87}Rb/^{86}Sr$ and $^{87}Sr/^{86}Sr$ ratios of samples from the Leh-Khardung La section, Ladakh Batholith.

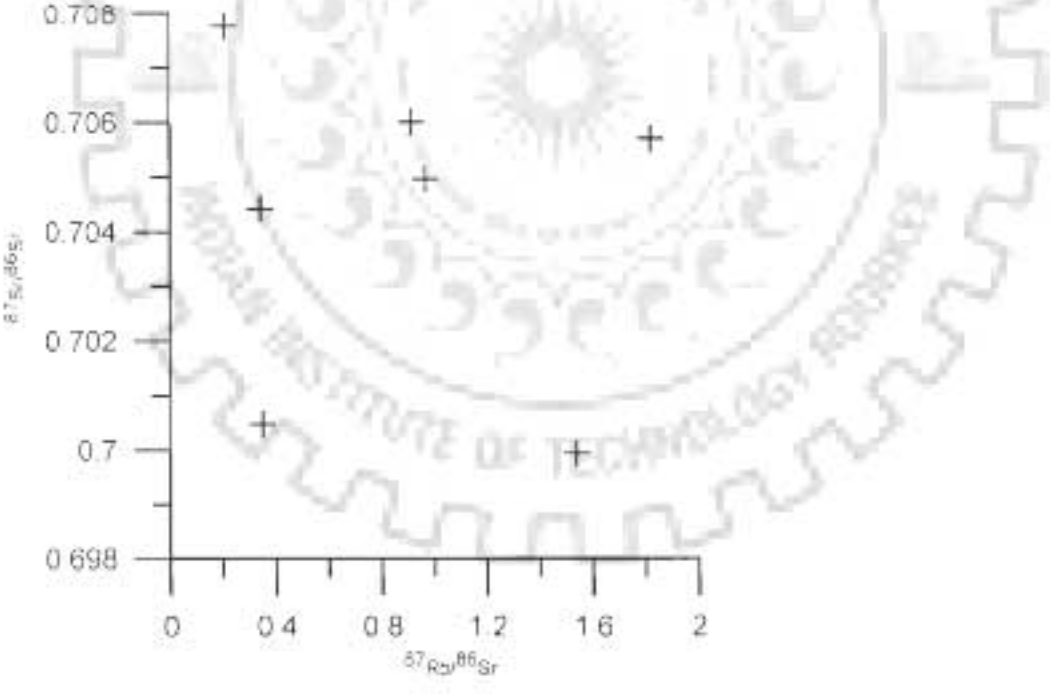

Figure 5.8 Plot of whole rock $^{87}Rb/^{86}Sr$ and $^{87}Sr/^{86}Sr$ ratios samples from Kharu-Chang La section, Ladakh Batholith.

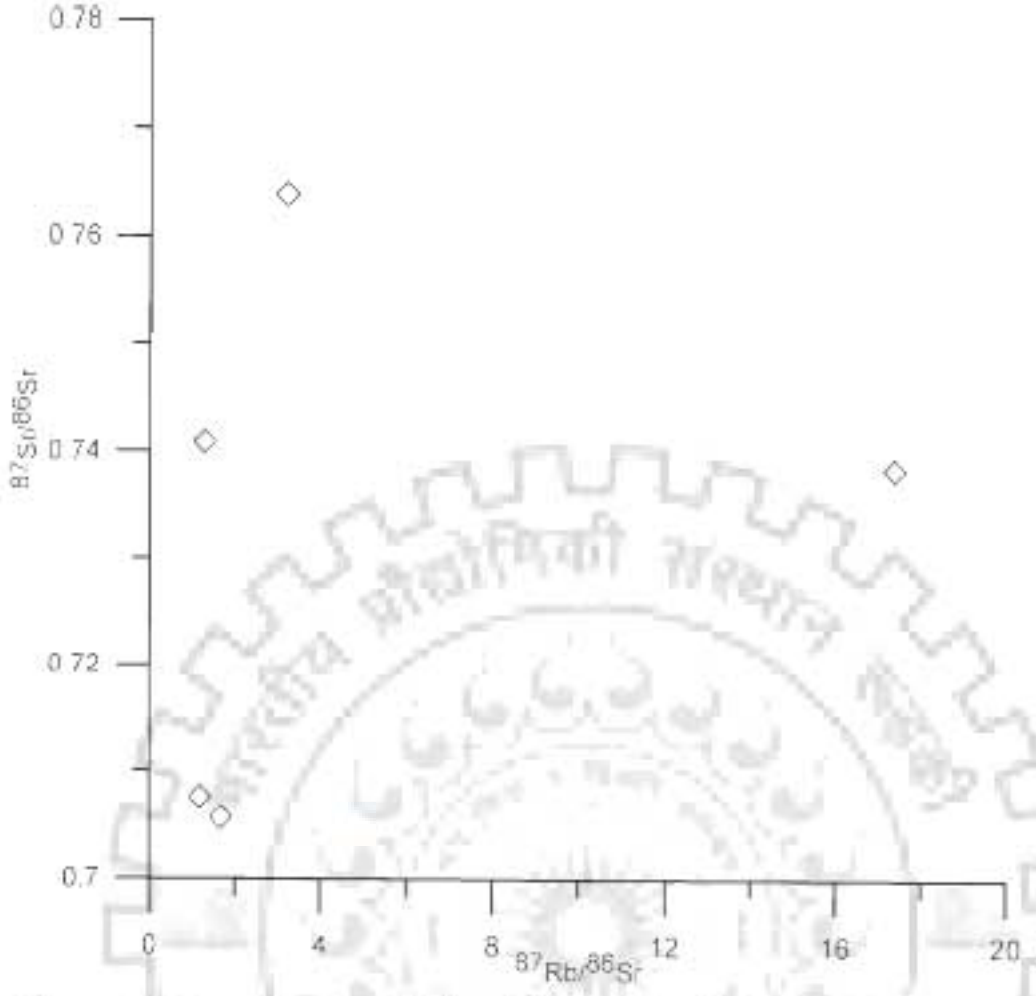

Figure 5.9 Plot of whole rock $^{87}Rb/^{86}Sr$ and $^{87}Sr/^{86}Sr$ ratios of samples from Lyoma-Hanle section, Ladakh Batholith.

body crossed the 300±50°C geotherm during this time span. Two biotite ages from the batholith, one by K-Ar method (Honegger et al., 1982) and the other by $^{40}Ar/^{39}Ar$ method (Schlup et al., 2003) are 48.7±1.6 Ma and 32.6±2 Ma, respectively. Honneger et al. (1982), have also reported Rb-Sr biotite age of 45 Ma from the Shey granite body of the Ladakh Batholith. All these ages have been used to interpret the cooling and exhumation pattern of the batholith since its crystallization and are discussed in detail in Chapter 7.

CHAPTER–6

FISSION TRACK DATING

6.1 INTRODUCTION

In order to unravel the complex history of the Himalayan Mountain resulting from the collision of the Indian and Eurasian Plates and ensuing crustal shortening, polyphase deformation, regional metamorphism and uplift, it is essential to establish a temporal framework for some of these events. Radiometric dating clocks, in general, provide time and temperature coordinates to determine the cooling and uplift rates and styles in the thermal history of rocks. The potential of Fission Track (FT) zircon and apatite clocks is to provide time data for low-temperature history of a rock and has promoted widespread use of the method in many active mountain belts such as Rockies (Naeser, 1979), the Andes (Kohn et al. 1984), the Transantarctic mountains (Fitzgerald et al., 1986) and the Alps (Wagner et al., 1977; Hurford et al., 1991). The technique has also been applied in the Himalaya (Zeitler, 1985; Kumar et al., 1995; Sorkhabi et al., 1994, 1996, 1997; Lal et al., 1999; Jain et al., 2000). Keeping in view the size and complex tectonic evolutionary history of the Himalaya, age data are required from different sectors.

This chapter provides the FT age data on 30 samples from the following three sections across the Ladakh Batholith (Fig. 6.1a) with the distribution of the samples as given against each section.

(a) Leh-Khardung La section across the batholith (Fig. 6.1b; 9 samples),

(b) Kharu-Chang La section across the batholith (Fig. 6.1c; 11samples), and

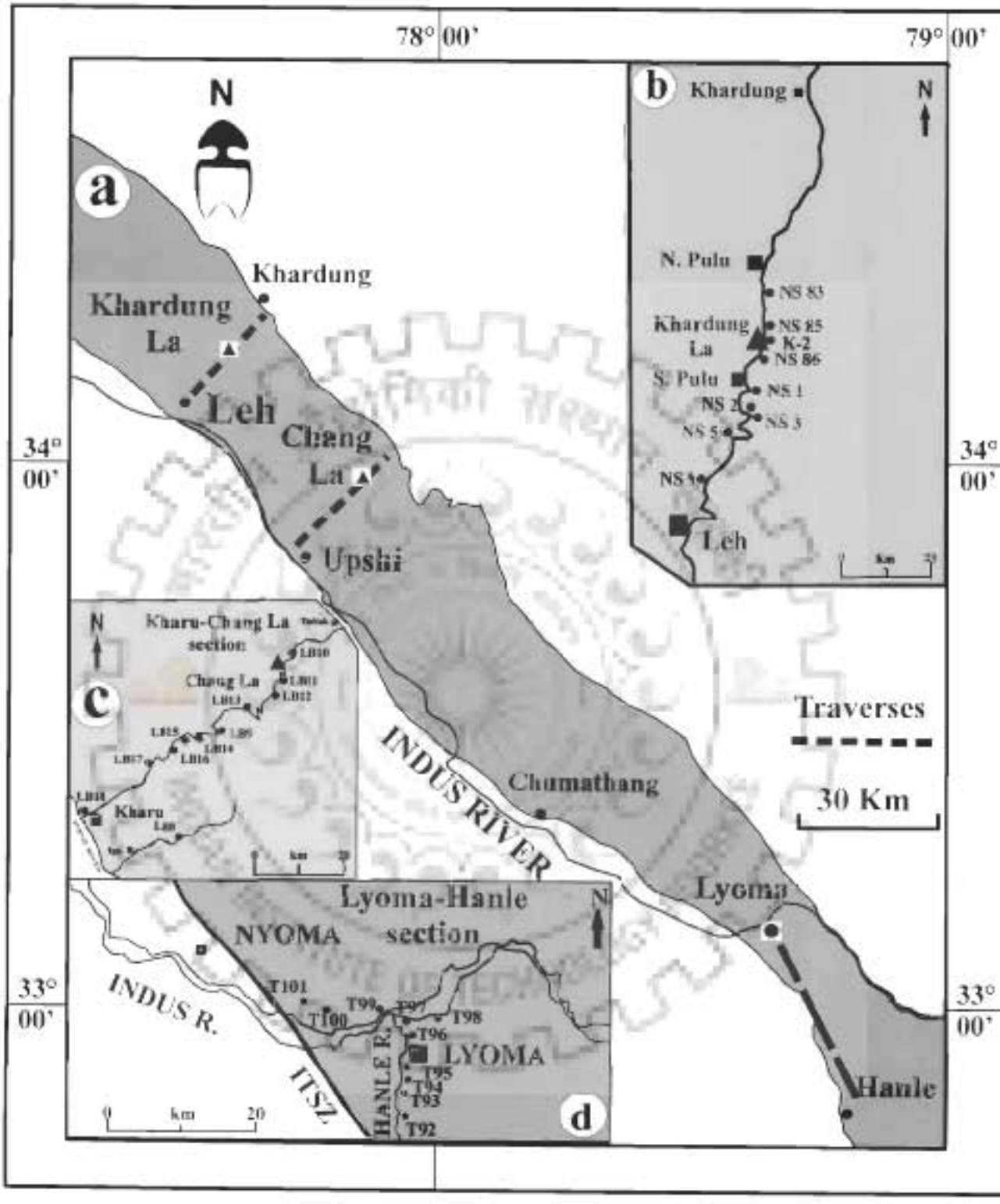

Figure 6.1: Location map of samples from the Ladakh Batholith for Fission Track Dating (a) Map of the Ladakh Batholith. (b) Leh-Khardung La section. (c) Kharu-Chang La secti (d) Lyoma-Hanle section.

(c) Lyoma-Hanle section along the southern margin of the batholith (Fig. 6.1d; 10 samples)

Fission track geochronology is a radiogenic method of age estimation of damage trails left by nuclei that are expelled during fission decays of the uranium isotope ^{238}U (e.g., Fleischer and others, 1975 and references therein). The primary mode of decay of ^{238}U is by alpha particle emission, one of the decay paths exploited in U- Pb systematic. However, about one time in two millions, a ^{238}U nucleus will instead decay by fission. In this mode, the nucleus spontaneously splits into two nuclei with mass numbers ~85 to 105 and ~130 to 150. These two nuclei are highly charged and so mutually repel and travel directly away from each other in a straight line, dissipating their kinetic energy to the host crystal lattice they travel. This creates a single linear damage through the lattice (Fig 6.2). Because tracks are so narrow, they are essentially undetectable in natural state with light in the visible region. However the damaged lattices in the track are chemically reactive and may be widened with laboratory etchants to microns or so and are readily observable under high power objective in an optical microscope. The major difference between fission track dating and other conventional isotopic dating techniques is that the daughter product is physical damage to the crystal lattice, rather than another isotope.

Fission Track Dating (**FTD**) technique made its advent in the arena of isotope geochronology towards the end of sixties and now has acquired the status of a routine dating method. Now a-days there are several laboratories, especially in Europe, USA, Australia and Japan where FTD technique is being routinely used with other dating methods. FTD is just one facet of a technique popularly known as Solid State Nuclear Track Detector (SSNTD) technique (Fleischer et al., 1975). The early development work on the SSNTD was done by three

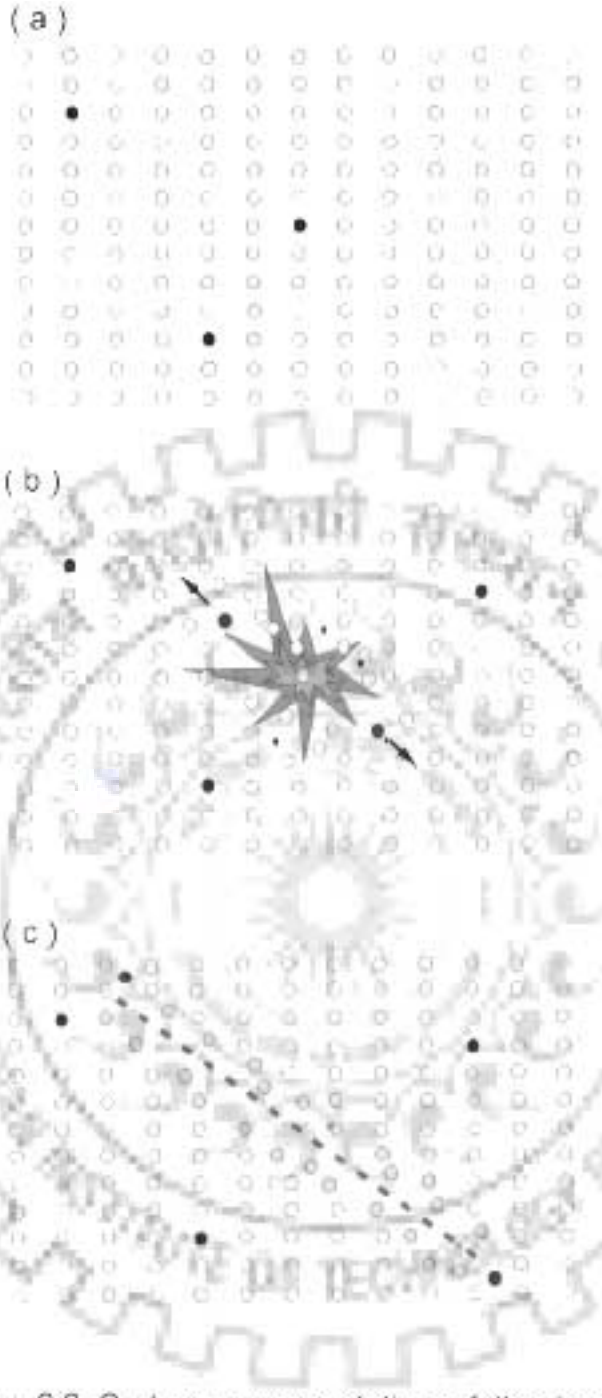

Fig: 6.2 Cartoon representation of the ion spike explosion model and the formation of fission track in a mineral. (a) Trace amount of radioactive ^{235}U are present in the crustal lattice (dark dots). (b) Spontaneous fission of ^{238}U produces two highly charged heavy particles. (c) damage trail or fission track left by the highly charged heavy particles.

Solid State Nuclear Track Detectors (SSNTD's) are essentially the materials that are damaged by the energetic particles in such a way that the particle tracks can be developed by subsequent etching and observed microscopically. These materials include most of the insulating solids, such as minerals, glasses and polymers in the order of increasing sensitivity. A comprehensive review of this subject is available in various publications (Fleischer et al., 1975; Durani and Bull, 1987; Lal, 1991, 1992 a, 1992 b).

The passage of heavily ionizing particles through dielectrics creates narrow paths of intense damage primarily through coulomb interaction with the orbital electrons of the target materials atoms. The salient features of these damages are:

(i) The extent of these damages is less than 100 Å and that it is the damage within 50 Å of the particle trajectory, which is significant.

(ii) Tracks have been found to be consisting of atomic defects.

(iii) Latent tracks though stable at ambient conditions fade at elevated temperatures. The activation energies associated with the repair of damage trails are several electron volts. These energy values are typical of those involved in atomic diffusion and thus provide further evidence of the atomic nature of the defects.

(iv) TEM observations of tracks in diffraction contrast mode reveal that tracks are centers of strain.

(v) In the last few microns of the range of charged particle, the track is not revealed. This is called range deficit.

(vi) Metals and most semiconductors do not record tracks.

The track formation model, which is consistent with all the above experimental features of tracks in inorganic crystals, is known as **Ion Explosion Spike Model.** According to this model, tracks are the result of the defects created by the removal of electrons by the ionizing particle (Fleischer et al., 1965 a). A narrow cylindrical region of positively ionized

atoms ~1 nm in diameter is produced behind the ion trajectory. These positive ions strongly repel one another and are ejected into interstitial positions surrounding a new-depleted core region. The repulsion will take place if and only if the electrostatic stress is greater than the mechanical strength. Subsequent processes include neutralization of the positive ions and relaxation of the surrounding lattice that produces long range strain fields. This model explains all the experimental features of the tracks in minerals and glasses.

6.2 CHEMICAL ETCHING PROCESS

Chemical etching of radiation damages is the backbone of SSNTD technique in having its widespread applications. The chemical etching transforms the latent track into an interasable structure by supplying the required amount of energy for the enlargement process. The sensitivity of this chemical amplifier is comparable to very sensitive electronic amplifier (e.g. etched track of 100 μm diameter has a volume which is 10^9 times larger than the volume of the latent track).

Etching takes place via rapid dissolution of the damaged region of the track core than the undamaged bulk material. The preferential chemical attack velocity V_t and bulk attack velocity V_g determine the size and shape of the resultant etched track. Each detector has an etching efficiency which is defined as the ratio of the number of observed etched tracks to the number of latent damage trails crossing a unit area of the original surface of the detector. Its value depends on V_t and V_g of the detector.

6.3 FISSION TRACK AGE EQUATION

Uranium is fairly ubiquitous trace element at ppb to ppb level in minerals and glasses. In the span of geologic time, ^{238}U is transformed in two different ways namely alpha decay and fission. Alpha particles are not sufficiently massive or energetic to make tracks in

common minerals. About one out of every two million transformations in ^{238}U is by fission. As a result of fission, the nucleus breaks up into two nuclei, one averaging about 90 am and the other about 135 am, with the liberation of about 200 MeV of energy. These two fission fragments recoil in opposite directions, and damage the crystal lattice along its path. The result is a zone of damage defining the **fission track** which is tens of angstroms in diameter and 10-20 μm in length. Tracks formed in the low-density minerals are longer than those formed in dense minerals. In terrestrial materials although other fissioning elements such as ^{235}U and ^{232}Th are also present, ^{238}U is the only significant producer of tracks due to its high rate of fission.

The number of fission tracks depends not only on the time during which they have been accumulating, but also on the uranium content of the material; the greater the uranium content, the greater the number of tracks.

The total number of decay of ^{238}U, in a given volume of mineral containing uranium atoms distributed evenly throughout its volume, during time T is

$$D_t = N_{238}(e^{\lambda_d T} - 1) \quad \ldots 1$$

Where D_t and N_{238} are the number of decay events/cc and the number of uranium-238 atoms/cc (at present) in the mineral sample respectively, λ_d is the total decay constant of ^{238}U.

Most of these decay events correspond to α-emission. The fraction of ^{238}U decays that are due to spontaneous fission, is λ_f/λ_d, and so the number of fission events F_s per unit volume is given by

$$F_s = \lambda_f/\lambda_d \, N_{238}(e^{\lambda_d T} - 1) \quad \ldots 2$$

The number density, ρ_s, of spontaneous fission tracks crossing a unit internal surface of the sample after etching is related to the volume density F_s by

$$\rho_s = \eta \, R \, F_s \quad \ldots 3$$

Where R is the range of a single fission fragment, and η is the etching efficiency of the material.

Combining equations 2 and 3, we obtain

$$\rho_s=\lambda_f/\lambda_d N_{238} \eta R (e^{\lambda dT} -1) \quad \ldots\ldots 4$$

The determination of age T thus requires the measurement of ^{238}U concentration in the sample. Rather than measuring the ^{238}U content directly, it is more convenient to measure the ^{235}U content of the sample and to assume (as is always the case) that this stands in a constant ratio to the ^{238}U. The determination of ^{235}U content by fast-neutron fission is avoided as these neutrons would produce fission, also in the thorium content of the sample. If the sample is irradiated with a known fluence ϕ of thermal neutrons, then the number of induced fissions per unit volume is

$$F=N_{235} \sigma\phi \quad \ldots\ldots 5$$

Where σ is the thermal-fission cross-section of ^{235}U, and N_{235} is the number of ^{238}U atoms per unit volume. If we assume that the range and etching efficiency for spontaneous and induced fission tracks are the same, then the number of induced fission tracks per unit area is

$$\rho_i=R F_i \eta=\eta R N_{235} \sigma \phi \quad \ldots\ldots 6$$

Dividing equation 4 by 6 and re-arranging the terms we get

$$T=1/\lambda_d \ln [1 + (\lambda_d \sigma I \phi \rho_s) / \lambda_f \rho_i] \quad \ldots\ldots 7$$

as the fundamental age equation of fission track method.

The measurement of FT age is now reduced to determination of the ratio of a spontaneous to an induced track density (ρ_s/ρ_i), thermal neutron fluence (ϕ) and fission decay constant λ_f. In principal, since the values of the constants λ_d, σ, and I are well established, it remains only to determine the track density ratio to measure the neutron fluence and insert a value for the fission decay constant λ_f in order to determine a FT age. Unfortunately there is a 20% value difference in the published values of λ_f by two groups (Thiel and Herr, 1976;

Hipazzi, 1981). The values obtained by the groups experimentally lie around either 8.46×10^{-17} a^{-1} or 7.00×10^{-17} a^{-1}. The lower value is supported by track accumulation experiments and the dating of minerals and natural glasses of independently known age, the higher value by measurements made using rotating bubble chambers, ionization chambers, radiochemical measurements and by the dating of man-made glasses of known date of manufacture. These are the two values of λ_f that are commonly used. In addition, the determination of absolute values for the neutron fluence, used to induce fission of ^{235}U in the sample, can be very complex. Also, the identification criteria of tracks in the mineral grains as well as the external detector may not only vary from one individual to another but also with the microscope conditions (dry or oil immersion objective and magnification). All these factors can lead to great variation in the calculated ages obtained from the ρ_s/ρ_i track density ratio counted for a sample thus making the interlaboratory comparison of FT data very difficult.

In order to make interlaboratory comparison and thus establish the reliability and reproducibility of FT ages, IUGS Subcommission on Geochronology recommended that a calibration factor, zeta (ζ) be substituted into the age equation for λ_f, I, σ and B (where $\phi = B\rho_d$, ρ_d being the track density in the external detector placed in contact with the uranium dosimeter glass, B is constant for given glass and is very difficult to evaluate) to modify the age equation as

$$T = (1/\lambda_d) \ln [1 + \lambda_d \zeta G (\rho_s/\rho_i) \rho_d] \quad \text{-------- 8}$$

Zeta represents a calibration baseline for the specific dosimeter in which ρ_d is counted and can be evaluated from a series if internationally accepted age standards. ρ_s and ρ_i are assumed to be counted on surfaces of similar registration geometry, or else, modified by a suitable geometry factor. Such a system calibration should be based on a series of age standards, not on a single measurement that is far from precise. The etching and track identification criteria play vital role in the determination of FT ages. In the present FT work,

the etching and track identification criteria as well as the microscope conditions were the same as adopted by Prof. Nand Lal, In-Charge of only working FT Laboratory, Department of Earth Sciences, Kurukshetra University, Kurukshetra, India and time to time reported from the same laboratory by Thakur and Lal (1993) and Kumar (1999). Hence the ages of apatites and zircons were calculated by using the value of zeta determined by them. The values of ζ=296.98±8.18 in the present study, was obtained from values of zeta determination for zircon and apatite by Kumar, 1999 (Unpublished Ph.D. thesis) on the Standard Glass Corning 5 (CN5) prepared by Dr. J. W.H. Schreurs at Corning Glass Works, Corning, New York, USA.

Essentially FT dating requires the determination of the ratio of the densities of spontaneous to induced tracks which is directly analogous to measuring the ratio of daughter to parent isotopic abundances in other radiometric dating methods, such as K-Ar, Rb-Sr etc.

One of the important assumptions in calculating the ages using equation 7 is that the material being dated has been a closed system with respect to fission tracks and uranium since its formation. This means that the only alteration in the ratio ρ_s/ρ_i is due to radioactive decay. Two aspects of this assumption need to be considered. Firstly, the fission tracks once formed must be stable over the lifetime of the material recording them. Secondly, there must be no migration of uranium.

6.4 DATING PROCEDURES

Different types of practical procedures are possible in FTD and for each there is specific advantages and limitations. The most favorable procedures in any specific instance depend on the type of material used, its uranium content and its homogeneity, age and grain-size. The techniques used in this work have been aimed at achieving a high degree of

reproducibility in the results and speed of handling. This has been accomplished by the standardization of procedures and refining of laboratory techniques.

There are several well established methodologies described and being adopted in the well known laboratories throughout the globe. All of them can be classified into two sub-groups:

1. **Multi-grain methods**
   - (a) Population Method (PM)
   - (b) Subtraction Method
2. **Single-grain methods**
   - (a) Re-polish method
   - (b) Re-etch method
   - (c) External Detector Method (EDM)

In all the methods mentioned above the basic feature is the use of surfaces for track registration for measurement of ρ_s and ρ_i. All the methods have almost the same procedure for estimation of ρ_s, but different measurement procedure for ρ_i. As for example in the PM the ρ_s and ρ_i are measured on different surfaces with different U-contents which are statistically equivalent to one another. In contrast, the EDM looks at induced tracks produced from exactly the same surface on which the spontaneous tracks are etched. The external detector used to record induced tracks has different track registration characteristics, which must be calibrated.

Out of the different methods, EDM has got an upper hand due to its advantages and simplicity of handling required after irradiation. In particular, no grinding and polishing of radioactive materials is required which is an important safety consideration. Also, with this method useful ages can be obtained on individual crystals, even when these are very small.

With the EDM, spontaneous tracks are counted in the etched mineral, whilst the induced tracks are counted in an external detector of negligible uranium content muscovite held against the mineral during irradiation and subsequently etched. Spontaneous and induced tracks are measured in exactly matching areas from the same planar surface of an individual crystal. Thus uranium in homogeneity, if at all present, both within and between crystals, is of negligible consequence. The method also permits careful selection of crystals, avoiding those badly etched, wrongly oriented or containing dislocations. In this method spontaneous tracks result from the passage of fission fragments across the internal surface, from both above and below, producing 4π geometry. Induced tracks result from one way passage of fission fragments from the mineral into the external mica detector giving 2π geometry. In order to account for the different geometries of spontaneous and induced track, a factor G is introduced in to the equation 8. The assumption of a correction factor of 0.5 to correct for the difference in geometry of the two surfaces has been shown to be valid only when the etching efficiencies of the two surfaces are virtually identical, (i.e. 100%) and both spontaneous and induced tracks have been fully revealed (Gleadow, 1978; Naeser et al, 1980). Greatest care is therefore required in both the control of etching and selection of appropriate crystals, as detailed above.

Considering the reliability and usefulness as well as the advantages EDM (Tagami et al., 1988) has been used in the present study.

6.5 METHODOLOGY

6.5.1 Mineral separation: For the separation of the minerals from the rock specimen it is essential to study the thin section of each rock specimen to examine the presence and abundance of suitable sized (~100 μm) grains of either apatite and/or zircon. This step also helps in assessing the quantity of the crop of apatite and/or zircon so as to get

an idea of the amount of the rock specimen to be taken for processing. The flow chart showing all the steps involved in mineral separation is given in Figure 6.3.

6.5.2 Hand picking and mounting: In order to identify the mineral grains and corresponding replica in the external detector precisely, mineral grains were arranged in an array and mounted to facilitate the steps of pre-grinding and description procedure. The size of the array was adjusted according to the requirements. The mounting of apatite and zircon was made in different materials because of their different track etching and fading conditions. The hand picking and mounting procedures are described below.

6.5.2.1 Zircon: Small fraction of the zircon grains were spread on a silica glass of size 5 cm x 5 cm. Using a sharp tipped needle the grains were picked one by one and arranged in a small place on the glass slide in such a manner that c-axis of all the grains was in one direction. In selecting the zircon grains, care was taken so as to hand pick large transparent euhedral crystals having well defined c-axis, and crystals of approximately same size for a single mount. One of the corner grains was slightly displaced from the regular array. The usefulness of arranging the grains along their c-axis and the slight displacement of one grain helps during grinding/polishing, etching of zircon and track counting in mica detector, respectively. The remaining grains were removed from the glass slide and stored in the vial. The silica glass slide was then shifted on to a hot plate having good temperature control. Zircon grains are mounted in PFA (Copolymer of tetrafluoroethylene perfluoro alkoxyethylene) teflon pieces (each of size 1.5 cm x 1.5cm x 0.5 mm), because of its stability against the etching of zircon. The temperature of the hot plate was maintained at 320°C. The teflon mount was then slightly cut asymmetrically at its right top corner. This asymmetric cutting makes it convenient to recognize the grain side of the teflon sheet by naked eyes. The sample code was written with a needle pen on the backside of the teflon mount.

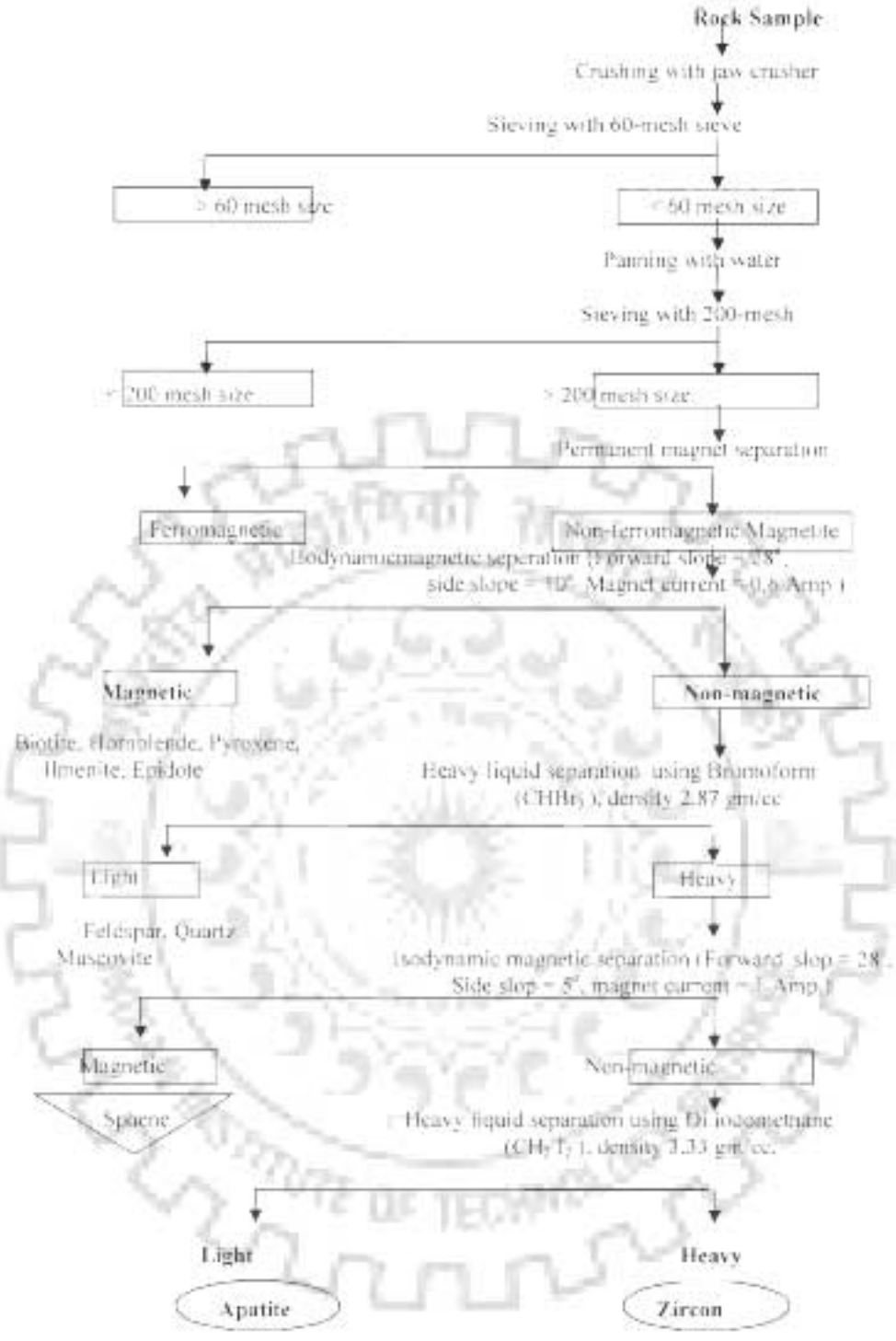

Figure 6.3: Flow chart for mineral separation

6.5.2.2 Apatite: Since fission tracks in apatite are very sensitive to thermal effects, its mounting in teflon is not possible. An alternative procedure, which does not involve high temperature treatment, was adopted. Epoxy is the best material for this purpose, as it gets

solidified at room temperature. Resin and hardener were mixed in the ratio of 10:1 by volume, respectively. The epoxy resin mount after drying can not be detached from the glass slide but can easily be removed from the teflon slide, which is, therefore, very useful for apatite mounting. The teflon slide was attached on the glass slide of the same size by means of bifacial tape (henceforth this combination of Teflon and glass sheet will be called TG slide). TG slide is cleaned with alcohol and a little petroleum jelly was applied on the teflon side of the TG slide so that the apatite grains would stick to it. In the absence of the jelly the electrostatic effect could disturb the grain arrangement during hand picking. The hand picking of apatite grains was done similar to that of zircon but without any directional alignment of the grains.

All the TG slides containing apatite grains were arranged on a horizontal surface. On each slide, two small glass pieces of thickness 15 mm were placed as spacers. The epoxy resin of fixed amount was then poured on the grains carefully so that the grain arrangement did not get disturbed during pouring of epoxy resin. The amount of the epoxy resin was adjusted in such a manner that when another TG slide was put on the glass spacers, the poured resin was made a flattened cylindrical form whose diameter was about 15 mm.

This arrangement was kept for about 24 hours at room temperature to allow the epoxy resin to solidify. After removing the mount from the TG slide, sample code was written with a needle pen parallel to one of the four sides of the grain arrangement on backside of the mount.

6.5.3 Grinding and polishing: In order to expose the internal surface of crystals for measuring spontaneous track density, mineral grains were exposed by grinding and polishing. For using internal surfaces of the minerals, it is essential to remove a certain thickness to expose the 4π geometry. This thickness corresponds to half of an etchable track length, which varies from one mineral to another i.e., 6 μm for zircon (Krishnaswami et al.,

1974), 8μm for apatite (Gleadow et al., 1986) and 7 μm for sphene (Gleadow and Lovering, 1975). If all the mineral grains are mounted so that the exposed crystal surface is equally flat, then the grains will be ground almost uniformly and the removal of the thickness, which satisfies the 4π geometry, will be quite easy. However, in case mineral grains are inclined, eroded or have irregular shape or caves, all the surface area of each grain will not be ground equally, and hence the measurement of the removed thickness for the 4π geometry condition will not be possible from the first grinding. In such a case, grinding should be continued till maximum possible area is exposed before measuring the thickness. This step is called the "pre-grinding" stage.

After pre-grinding, a brief description about the suitability of each grain is necessary. As discussed above, some part of the crystal might not have been exposed during pre-grinding and will not satisfy the condition of the 4π geometry. As it is impossible to judge such non-exposed area after finishing the grinding, all these areas were recorded at this stage in a notebook by labeling individual grain.

The next step was to grind the mount and remove a certain thickness peculiar to each mineral for exposing the 4π geometry. After description, the mount was ground perpendicular to the direction of the pre-grinding (using 25 μm diamond paste) till all the preceding grinding scratches disappeared. Next step of grinding was carried out, using 14 μm diamond pastes, again perpendicular to the direction of the previous grinding scratches and new scratches on all surface area were checked. This alternate grinding with 25 μm and 14 μm diamond paste resulted in the removal of 1.75 μm thickness. While shifting from one grade of diamond paste to another, mount was washed with water using ultrasonic cleaner for about 8-10 minutes. This process was repeated until the removed thickness reached half of etchable track length for each mineral. To be on the safe side, however, the thickness of the removed surface was kept more than 3/2 of the minimum depth for exposing the 4π geometry. Thus,

above step of grinding was repeated, in our routine, 5 times for zircon, and 7 times for apatite.

In case of zircon, grinding procedure was slightly different from those of apatite. It is not advisable to grind zircon crystals along their crystallographic c-axis because it often produces deep cracks or damages on the surface. The cracks or damages are enlarged during chemical etching and sometimes disturb the track counting. Hence, the pre-grinding and grinding of zircon mounts should be carried out perpendicular to c-axis only, for which the arrangement of zircon crystals along c-axis is desired. After each step of grinding, all grinding scratches were erased by 8 μm diamond paste polishing parallel to c-axis so that next grinding scratches could be easily observed.

After grinding, the mount was polished successively with 8 μm, 3 μm, 1 μm, 0.25μm diamond paste. At every step of polishing, the direction of polishing is changed by 90° from that of preceding polishing. The alternately changing of polishing direction made it easy to distinguish the disappearance of the preceding polishing scratches, thereby, ensuring the completion of each polishing step. Before switching from one diamond paste to another the samples were washed under running water and ultrasonic cleaner to make them clean of the preceding grade diamond paste.

6.5.4 Etching of tracks: *6.5.4.1 Zircon:* The determination of conditions for optimum etching in zircon requires a special care. It is quite necessary because zircon show anisotropic etching behavior of fission tracks and all the tracks in various crystallographic directions do not have same etching rate (Gleadow, 1981). Therefore, it is necessary to continue the etching until the tracks in all directions become visible. In case of zircon, isotropic distribution of etched tracks is characterized by the complete revelation of thin tracks parallel to c-axis.

For etching a large number of zircon mounts together with a specially designed etching bath with temperature controller is used.

After obtaining the desired temperature (230°C) of heater, teflon beaker/beakers containing the eutectic mixture of NaOH: KOH etchant (Gleadow et al., 1976) was kept in the heater for 12 hours before putting the sample mounts in the beaker. In doing so, no air bubbles were left in the etchant. The mount after etching for a desired time was put in 5% HCl solution in an ultrasonic cleaner for 15-20 minutes and subsequently in water for 5-10 minutes using ultrasonic cleaner to remove the traces of the etchant sticking to the mount. The etching time for zircons varies with the track density. Most zircons etch within a period of 12-96 hours.

6.5.4.2 Apatite: The tracks in apatite were etched in 0.6% HNO_3 (by volume) at 30°C for 70 seconds.

6.5.5 Packing and irradiation: Before irradiating the samples in reactor with thermal neutrons, uranium-free fission track detectors were fixed firmly in contact with the mineral mounts. The Brazilian muscovite, which is almost free from uranium impurities, was used in the present study. It was cut into square pieces of size slightly larger than the area of the mounted grains and of suitable thickness (~0.1 mm).

The sample code was written with a sharp needle on the back of the muscovite. To distinguish the surface fixed against mineral grains, one corner of it was cut asymmetrically such that when fixed against the grain arrangement in the teflon sheet, the cuts of both were in the same direction. For epoxy resin mounts, the corner cut of muscovite detector was made in the same manner before putting detectors. All the mineral mounts were thoroughly washed with alcohol using ultrasonic cleaner. After keeping the mica detector on the grains, it was covered with a clean plastic sheet (thickness 0.5-mm) of size slightly larger than the muscovite. The purpose of this plastic sheet was to avoid the sticking of the tape to the mica

detector. The entire arrangement was then wrapped up firmly with scotch magic tape and the sample code written on the tape. The sample was thus ready for irradiation

6.5.6 Thermal neutron irradiation: IC2 thermal column of the CIRUS reactor at Bhabha Atomic Research Centre, Trombay, Mumbai was used in the present study for thermal neutron irradiation. The dimensions of the aluminium capsule for sample irradiation in this reactor are 3.5 cm in length and 1.5 cm diameter. After fixing the muscovite detectors on mounts, the samples were stacked vertically and packed in the capsule. In order to measure thermal neutron fluence and to take into account dose gradient along the capsule, two uranium standard glasses (one on the top and another at the bottom of the capsule) were also packed along with the samples. Each dosimeter mount was made using standard glass, namely Corning 5 (CN5) prepared by Dr. J.W. H. Schreurs at Corning Glass Works Corning, New York, USA. The mounting, polishing and packing of these standard glasses was done in similar way to that of apatites. The muscovite detectors attached to these standard glass mounts were used for counting of the tracks. The track density ρ_d was calculated by taking mean of the counts of two dosimeter glasses. The Corning glass CN5 contains ~12 ppm undepleted uranium of natural isotopic abundance ($^{235}U/^{238}U$=0.7262%) and ~0.4 ppm thorium without any interfering trace elements.

Counting of tracks in apatite and zircon, both spontaneous as well as the induced on mica detector was carried out on the samples from the Ladakh Batholith after irradiation on the Nikon Optiphot Microscope under 100X dry objective.

6.6 RESULTS

6.6.1 Chemical composition of apatite: The rate of thermal annealing in apatite is also dependent on the chemical composition of the host apatite crystal, specifically on the ratio of Cl/Cl + F (Green et al., 1989), with higher rates of annealing for fluorine-rich

apatite relative to chlorine-rich apatite at a given temperature. This compositional effect implies that individual apatite grains from the same sample can display different degrees of thermal annealing even though they have experienced the same thermal history. This effect is commonly observed in the samples from sedimentary terrains having variegated provenance and thus also display a range in apatite composition. This variation in thermal annealing behavior between single apatite grains thus provide important information about the maximum temperatures experienced by a sample.

To investigate the effects of chlorine and fluorine contents on the ages of apatite, chemical composition of seven apatite samples from all the three sections was determined. These measurements were made using JEOL JXA-8600M EPMA (Electron Probe Micro Analyzer) with a 15 kV accelerating voltage and 2×10^{-8} A sample current, having a beam size of 1 μm. Natural mineral standards (SPI Standard, Canada) were used for the analysis. ZAF corrections were applied to the data. In each sample, 4-5 apatite grains were analyzed to calculate the mean values. The separates from the samples were mounted and polished in the same way as they were mounted for irradiation. Then the samples were taken for EPMA analysis. The compositional variation of apatite grains from the selected samples are shown in Table 6.

Cl content in samples was found to be much less than the F content. These values fall between end member flourapatite and Cl content Durango apatite (Mexico), and are much less than the 0.04 wt % of Cl content of the latter. Cl/Cl + F ratio varies from 0.008 to 0.339; hence the chemical composition of apatite appears to have no effects on the annealing properties of fission track, and consequently the FT ages.

6.6.2 FT ages: A measured FT age is merely a physical quantity of dimension 'time', which equals in the first approximation the period of FT accumulation in the sample. This quantity may or may not bear geological information. Its association with a geologically

meaningful event is the aim of the geological interpretation. It is by this procedure that the measured age becomes the age of a geological event.

The fission track (FT) ages have been determined by the External Detector Method, and the ages were calculated following the Zeta calibration approach. The value of zeta, used in the present study, is 296±8.18 and was obtained for zircon and apatite by Kumar, 1999 (unpublished Ph.D. thesis) on the Standard Glass Corning 5 (CN5) prepared by Dr. J.W.H. Schreurs at Corning Glass Works, Corning, New York.

Tables 6.2 and 6.3 present the results of FT age data on apatite and zircon from the Ladakh Batholith from three important sections, respectively. The statistical uncertainties quoted with the FT ages have been calculated using the procedure described by Galbraith (1981) and Green (1981), and are quoted as $\pm 1\sigma$ (σ = standard deviation) throughout unless otherwise specified. As the individual (ρ_s / ρ_i) ratios are independent of uranium variation between grains, only random variations governed by Poisson's statistics are expected to be associated with these ratios. However, the experimental data generally show a supplementary variation between (ρ_s/ρ_i) ratios. A χ^2 test allows detection of these supplementary variations. If the track count satisfies the χ^2 test, i.e. P (χ^2) is $\geq$ 5% the errors are calculated using conventional approach. On the other hand, if the sample fails to satisfy the χ^2 test i.e. P (χ^2) is <5%, real differences in the FT ages are considered to exist between individual grains. It may be either due to the inherited effects different provenance regions or variation in the rate of track length reduction during extreme partial annealing because of compositional differences. In such cases, calculation of a pooled FT age is not strictly valid and instead a mean age is calculated with an uncertainty taken as the standard deviation of the individual grain ages. Subjectivity in selecting grains was avoided by counting all grains with sharp polishing scratches. In the present analysis, only one sample i.e. NS86/163 failed the χ^2 test and is thus associated with large statistical error.

Table 6.1: Analysis of Apatite at oxygen base 12.

NS1/1 (Leh-Khardung section)

	Gr1/1	Gr1/2	Gr1/3	Gr2/1	Gr2/2	Gr2/3
FeO	0.001	0.011	0.019	0.003	0.011	0.001
MnO	0.151	0.078	0.086	0.065	0.078	0.071
MgO	0.000	0.000	0.000	0.000	0.074	0.100
CaO	51.777	51.595	51.230	52.058	52.084	50.609
Na_2O	0.000	0.000	0.000	0.000	0.000	0.000
P_2O_5	41.591	42.115	41.827	42.141	42.524	42.000
F	5.724	7.410	6.438	5.927	5.032	6.835
Cl	0.068	0.088	0.079	0.064	0.042	0.060
Total	96.687	98.157	96.950	97.746	97.817	96.785
Cation (12 oxygen Base)						
Fe	0.0001	0.0007	0.0013	0.0002	0.0007	0.0001
Mn	0.0107	0.0055	0.0061	0.0045	0.0055	0.0050
Mg	0.0000	0.0000	0.0000	0.0000	0.0091	0.0125
Ca	4.6483	4.5909	4.5898	4.6151	4.5868	4.5347
Na	0.0000	0.0000	0.0000	0.0000	0.0000	0.0000
P	2.9363	2.9611	2.9611	2.9521	2.9592	2.9771
F	1.5162	1.9461	1.7024	1.5508	1.3081	1.8097
Cl	0.0096	0.0124	0.0118	0.0086	0.0059	0.0086
Total	9.1219	9.5167	9.2720	9.1312	8.8752	9.3526
Cl/Cl+F	0.0117	0.0147	0.0121	0.0101	0.0082	0.0087

NS 86/163 (Leh-Khardung section)

	Gr1/1	Gr1/2	Gr1/3	Gr2/1	Gr2/2	Gr2/3
FeO	0.032	0.000	0.045	0.052	0.035	0.009
MnO	0.140	0.118	0.106	0.115	0.108	0.142
MgO	0.008	0.000	0.000	0.000	0.080	0.000
CaO	54.382	53.618	54.119	53.981	55.097	55.406
Na_2O	0.000	0.000	0.000	0.000	0.000	0.000
P_2O_5	42.464	43.311	43.371	41.785	42.659	42.081
F	4.458	4.892	5.317	7.290	6.202	8.348
Cl	0.083	0.083	0.103	0.256	0.125	0.112
Total	99.672	99.942	100.799	100.352	101.646	102.859
Cations(12 oxygen base)						
Fe	0.0022	0.0000	0.0030	0.0035	0.0010	0.0006
Mn	0.0096	0.0080	0.0072	0.0080	0.0074	0.0098
Mg	0.0010	0.0000	0.0000	0.0000	0.0096	0.0000
Ca	4.7147	4.6199	4.6416	4.7401	4.7369	4.7951
Na	0.0000	0.0000	0.0000	0.0000	0.0000	0.0000
P	2.9090	2.9488	2.9393	2.8994	2.8981	2.8778
F	1.1408	1.2442	1.3459	1.8894	1.5737	2.1325
Cl	0.0384	0.0381	0.0140	0.0355	0.0169	0.0153
Total	8.7887	8.8421	8.9510	9.5758	9.2436	9.8311
Cl/Cl+F	**0.0183**	**0.0165**	**0.0190**	**0.0339**	**0.0198**	**0.0132**

NS 9/20 (Leh-Khardung section)

	Gr1/1	Gr1/2	Gr1/3	Gr2/1	Gr2/2	Gr2/3
FeO	0.013	0.008	0.026	0.000	0.000	0.003
MnO	0.083	0.124	0.101	0.142	0.102	0.090
MgO	0.000	0.009	0.000	0.024	0.000	0.022
CaO	52.063	51.927	50.515	52.302	51.520	52.568
Na2O	0.000	0.000	0.000	0.000	0.000	0.000
P2O5	41.159	41.835	40.972	42.395	42.347	42.210
F	4.759	6.220	5.546	9.426	9.001	8.662
Cl	0.085	0.088	0.071	0.014	0.028	0.036
Total	98.140	97.902	94.880	100.333	99.402	99.935
Cation(12 oxygen base)						
Fe	0.0009	0.0006	0.0019	0.0000	0.0000	0.0002
Mn	0.0059	0.0087	0.0073	0.0099	0.0072	0.0063
Mg	0.0000	0.0012	0.0000	0.0029	0.0000	0.0028
Ca	4.6816	4.6237	4.6078	4.6081	4.5575	4.6364
Na	0.0000	0.0000	0.0000	0.0000	0.0000	0.000
P	2.9246	2.9463	2.9532	2.9517	2.9741	2.9418
F	1.2632	1.7661	1.4931	2.4513	2.3503	2.2549
Cl	0.0121	0.0125	0.0102	0.0019	0.0039	0.0050
Total	8.8884	9.3589	9.0735	10.0258	9.8431	9.8473
Cl/Cl+F	**0.0176**	**0.0129**	**0.0126**	**0.0015**	**0.0031**	**0.0041**

K-2 (Leh _Khardung La section)

	Gr1/1	Gr1/2	Gr1/3	Gr2/1	Gr2/2	Gr2/3
FeO	0.081	0.000	0.032	0.085	0.049	0.072
MnO	0.033	0.080	0.106	0.084	0.047	0.065
MgO	0.087	0.079	0.002	0.000	0.038	0.000
CaO	50.664	50.309	50.647	53.028	51.319	51.734
Na2O	0.000	0.000	0.000	0.000	0.000	0.000
P2O5	42.059	40.530	40.943	41.144	41.686	41.243
F	3.578	7.193	1.796	5.195	5.454	6.648
Cl	0.261	0.303	0.317	0.243	0.290	0.306
Total	95.198	95.398	93.046	97.536	96.521	97.198
	Cation (12 oxygen base)					
Fe	0.0057	0.0000	0.0023	0.0059	0.0034	0.0050
Mn	0.0024	0.0058	0.0076	0.0060	0.0033	0.0046
Mg	0.0108	0.0101	0.0003	0.0000	0.0047	0.0000
Ca	4.5384	4.6244	4.6168	4.7333	4.6024	4.6567
Na	0.0000	0.0000	0.0000	0.0000	0.0000	0.0000
P	2.9771	2.9439	2.9492	2.9019	2.9543	2.9335
F	0.9460	1.9522	0.4832	1.3686	1.4439	1.7658
Cl	0.0370	0.0440	0.0458	0.0343	0.0412	0.0435
Total	8.5173	9.5804	8.1052	9.0499	9.0536	9.4090
Cl/Cl+F	**0.0680**	**0.0404**	**0.1500**	**0.0447**	**0.0505**	**0.0440**

LB10/28 (Kharu-Chang La section)

	Gr1/1	Gr1/2	Gr1/3	Gr2/1	Gr2/2	Gr2/3
FeO	0.011	0.029	0.000	0.000	0.004	0.003
MnO	0.059	0.095	0.104	0.068	0.069	0.071
MgO	0.000	0.000	0.000	0.000	0.000	0.000
CaO	50.837	41.813	41.717	51.443	52.172	52.005
Na_2O	0.000	0.000	0.000	0.000	0.000	0.000
P_2O_5	41.572	41.813	41.717	41.557	42.306	42.172
F	3.858	3.753	4.875	7.368	5.356	4.734
Cl	0.242	0.089	0.231	0.069	0.084	0.060
Total	95.204	96.146	96.222	97.387	97.701	97.038
Cation (12 oxygen base)						
Fe	0.0007	0.0002	0.0000	0.0000	0.0003	0.0002
Mn	0.0042	0.0067	0.0074	0.0048	0.0048	0.0050
Mg	0.0000	0.0000	0.0000	0.0000	0.0000	0.0000
Ca	4.5656	4.6307	4.6066	4.6209	4.6100	4.6099
Na	0.0000	0.0000	0.0000	0.0000	0.0000	0.0000
P	2.9718	2.9442	2.9544	2.9497	2.9530	2.9540
F	1.0226	0.9874	1.2895	1.9534	1.3969	1.2385
Cl	0.0344	0.0126	0.0327	0.0098	0.0089	0.0084
Total	8.5993	8.5833	8.8906	9.5387	8.9748	8.8160
Cl/Cl+F	**0.0500**	**0.0252**	**0.0152**	**0.0093**	**0.0118**	**0.0125**

LB8/23 (Kharu-Chang La section)

	Gr1/1	Gr1/2	Gr1/3
FeO	0.065	0.122	0.032
MnO	0.091	0.009	0.080
MgO	0.000	0.047	0.000
CaO	43.981	47.181	47.992
Na_2O	0.000	0.000	0.000
P_2O_5	37.813	39.689	37.726
F	2.184	3.172	2.818
Cl	0.205	0.203	0.180
Total	83.374	89.042	87.632
Cation (12 oxygen base)			
Fe	0.0051	0.0091	0.0024
Mn	0.0073	0.0007	0.0062
Mg	0.0000	0.0062	0.0000
Ca	4.4425	4.5022	4.6948
Na	0.0000	0.0000	0.0000
P	3.0181	2.9927	2.9186
F	0.6511	0.8935	0.8137
Cl	0.0306	0.0306	0.0279
Total	8.1568	8.4350	8.4637
Cl/Cl+F	**0.0858**	**0.0601**	**0.0600**

T96/341 (Lyoma-Hanle section)

	Gr1/1	Gr1/2	Gr1/3	Gr2/1	Gr2/2	Gr2/3
FeO	0.027	0.064	0.034	0.054	0.023	0.019
MnO	0.020	0.011	0.023	0.000	0.000	0.000
MgO	0.076	0.162	0.000	0.061	0.000	0.000
CaO	50.334	50.401	51.018	53.206	53.115	51.212
Na_2O	0.000	0.000	0.000	0.000	0.000	0.000
P_2O_5	41.382	42.375	42.741	43.625	44.135	42.470
F	9.608	7.148	9.866	7.214	8.888	9.420
Cl	0.199	0.045	0.014	0.106	0.094	0.095
Total	97.498	97.301	99.539	101.205	102.491	99.228
Cation (12 oxygen base)						
Fe	0.0019	0.0044	0.0024	0.0036	0.0015	0.0013
Mn	0.0014	0.0007	0.0016	0.0000	0.0000	0.0000
Mg	0.0096	0.0201	0.0000	0.0073	0.0000	0.0000
Ca	4.5677	4.5003	4.5183	4.5763	4.5423	4.5479
Na	0.0000	0.0000	0.0000	0.0000	0.0000	0.0000
P	2.9678	2.9898	2.9914	2.9651	2.9825	2.9803
F	2.5735	1.9365	2.5789	1.8315	2.2434	2.4695
Cl	0.0171	0.0068	0.0020	0.0145	0.0123	0.0133
Total	10.1389	9.4581	10.0942	9.3981	9.7825	10.0121
Cl/Cl+F	**0.0203**	**0.0061**	**0.0014**	**0.0145**	**0.0104**	**0.0100**

FT apatite ages range from a maximum of 25.35±2.57 Ma to a minimum value of 9.21±0.87 Ma over the entire length of the Ladakh Batholith under investigation. The oldest fission track apatite ages in the present study have been encountered from the highest uplifted

locations in the Ladakh Batholith. These ages are 23.07±1.10 Ma and 25.35±2.57 Ma for the Khardung La (K-2, 5440m) and Chang La top (LB10/28, 5301m), respectively. The apatite ages are showing good correlation with the elevation and show lower cooling ages with decreasing elevation (Figs. 6.4, 6.5). These ages are 11.79±1.10 Ma at Ma at the lowest elevation (NS9/20, 4038m) in the Khardung La section and 9.21±0.87 Ma in the Chang La section near Kharu (LB18/36, 3732m). The overall weighted mean AFT age for the Khardung La section comes out to be 17.38±0.33 Ma, whereas the same for the Chang La section is 14.93±0.32 Ma. In the third section, when the sample (198/3451 yielding much higher age of 23±2.40 Ma is left out, FT apatite ages range from 12.10±0.88 Ma to 18.50±1.42 Ma with the weighted mean of 15.23±0.40 Ma for samples lying between 4160m 4225m.

Table 6.2: Apatite Fission Track Data of the Ladakh Batholith

Sl. No.	Sample Code	Lab Code	Number of Crystals	Track Densities		P (χ^2) %age	Glass Dosimeter ρ_d (N_d)	Elevation (m)	Age (Ma)
				Spontaneous ρ_s(N_s)	Induced ρ_i(N_i)				
A. Leh-Khardung La section									
1	NS 1/1	KA1*	52	0.3605 (451)	3.2173(4150)	85	0.7777 (3511)	4645	12.53±0.66
2	NS 2/3	KA2	47	0.3406 (345)	2.0583(2085)	30	0.7777 (3511)	4600	19.08±1.16
3	NS 3/7	KA3	54	0.4225 (545)	3.4721(4479)	80	0.7777 (3511)	4427	14.03±0.68
4	NS 5/12	KA4	24	0.4508 (288)	3.4484(2207)	30	0.7777 (3511)	4401	15.05±0.98
5	NS 9/20	KA5*	59	0.2989 (584)	2.9253(2279)	80	0.7777 (3511)	4038	11.79±0.76
6	K-2	KA6*	50	0.5837 (610)	2.9167(3048)	70	0.7777 (3511)	5440	23.07±1.10
7	NS83/157	KA7	41	0.3854 (451)	2.2701(2656)	90	0.7777 (3511)	5071	19.58±1.05
8	NS 5/162	KA9	17	0.3312 (156)	1.7303 (815)	10	0.7777 (3511)	5375	22.06±1.96
9	NS86/163	KA10	26	0.5241(294)	2.9340(1646)	<10	0.7777 (3511)	5305	20.59±1.35
B. Kharu-Chang La section									
10	LB 8/25	8/23A	18	0.5225 (209)	3.885(1554)	30	0.5025 (2010)	3572	10.02±0.77
11	LB 9/27	AP4	15	0.6000 (219)	3.1096(1135)	80	0.5025 (2010)	4572	14.38±1.30
12	LB 10/28	AP22*	7	0.8915 (115)	5.6279(726)	80	1.0800 (4320)	5301	25.35±2.57

13	LB-11/29	11/29A	23	0.5391 (252)	3.0102(1463)	20	0.7777 (3111)	5060	20.06±1.40
14	LB-12/30	12/30A	23	0.5391 (262)	3.8786(1399)	90	0.7777 (3111)	4893	21.59±1.50
15	LB 13/31	AP14	9	0.4933 (111)	2.1467(483)	>95	0.5025 (2010)	4742	17.12±1.84
16	LB 14/32	14/32A*	31	0.6327 (449)	6.3925(4609)	80	1.0800 (4320)	4409	15.60±0.80
17	LB 15/33	AP11	28	0.5039 (325)	5.6356(3635)	30	0.9867 (3947)	4241	13.08±0.78
18	LB 16/34	16/34A	21	0.5436 (280)	8.1126(4178)	30	1.0800 (4320)	4072	10.74±0.68
19	LB 17/35	AP9	11	0.6509 (166)	6.0471(1542)	80	0.6097 (2439)	3902	9.73±0.81
20	LB 18/36	AP13	10	0.5522 (127)	5.4217(1247)	75	0.6097 (2439)	3732	9.21±0.87
C. Lyoma-Hanle section									
21	T 92/333	AP16	16	0.5508 (195)	4.7684(1688)	65	1.0800 (4320)	4225	18.50±1.42
22	T 93/334	AP18*	17	0.6962 (275)	3.9826(1494)	30	0.5036 (2000)	4200	13.71±0.95
23	T 94/335	AP7	9	0.6533 (237)	6.4889(1460)	30	0.5025 (2010)	4200	12.10±0.88
24	T 95/339	AP5	3	0.9077 (59)	10.8614(706)	10	1.0800 (4320)	4200	13.39±1.82
25	T 96/341	AP20	8	0.9804 (150)	10.908(1669)	95	1.0800 (4320)	4200	14.40±1.24
26	T 97/343	AP21*	6	0.6933 (104)	7.693(1154)	90	1.0800 (4320)	4160	14.44±1.49
27	T 98/345	AP3	7	0.6750 (108)	4.6812(749)	60	1.0800 (4320)	4160	23.08±2.40
28	T 99/346	AP1	11	0.8387 (260)	8.4419(2617)	75	1.0800 (4320)	4200	15.91±1.06
29	T 100/350	AP19*	16	0.5825 (273)	3.0325(1213)	>95	0.6097 (2439)	4160	17.27±1.29
30	T 101/351	AP2	12	0.7615 (198)	4.2346(1127)	10	0.6097 (2439)	4160	15.88±1.26

1. Track densities ρ's are measured and are 10^3 tr/cm^2.
2. N is the number of tracks counted.
3. P (χ^2) is the probability of obtaining χ^2 values of α degrees of freedom.
4. where α = (no. of crystals - 1).
5. *Track Length Measurement done on these samples
6. The ages were calculated by using the following relation (Hurford, 1990):

$$T = 1/\lambda_d \ln[1 + G\zeta\lambda_d(\rho_s/\rho_i)]$$

where,

λ_d =Total decay constant of U^{238}

G =geometry factor (=0.5, as the spontaneous tracks were counted under 4π conditions)

ρ_s=Spontaneous track density

ρ_i& ρ_d =Induced track density in mica detector placed against the mineral sample and glass dosimeter respectively.

ζ=Zeta calibration factor.

Table 6.3: Zircon Fission Track Data of the Ladakh Batholith

Sr. No.	Sample Code	Lab Code	Elevation (m)	Number of Crystals	Track Densities		P (χ^2) %age	Glass Dosimeter ρ_d (N_d)	Age (Ma)
					Spontaneous ρ_s (N_s)	Induced ρ_i (N_i)			
1	LB10/28	Zr14	5301	09	9.5614 (545)	22.491(1282)	50	0.6632 (2653)	41.73±2.28
2	LB12/30	12/30z	4893	04	9.2609 (215)	20.9565(482)	50	0.6632 (2653)	43.37±3.66
3	T100/250	Zr15	4160	02	4.875(195)	15.1000(n04)	50	0.6632 (2653)	31.71±2.68

Track densities ρ's are measured and are 10^6 tr/cm^2, N is the number of tracks counted.
P (χ^2) is the probability of obtaining χ^2 values of n degrees of freedom,
where n = (no. of crystals - 1).

The values of ζ = 296.98±8.18 in the present study, was obtained from values of zeta determination for zircon and apatite by Kumar,1999 (Unpublished Ph.D. thesis) on the Standard Glass Corning 3 (CN5) prepared by Dr. J. W.H. Schreurs at Corning Glass Works, Corning, New York, USA.

6.6.2 Apatite Track length measurements: An additional tool for the interpretation of FT data is the distribution of track length in apatite, which is diagnostic of the style of cooling and will reveal more complex thermal histories (Gleadow et al., 1986). The length data are generally collected from only on a specific type of track called a horizontal confined track. Confined tracks are completely contained within the host mineral grain and have etched through the etchant penetrating along contiguous cracks or other tracks that intersect the polished surface. Although biased against sampling short tracks (Laslett et al., 1982, 1984; Green, 1988), this method provides the most direct and reproducible estimate of the true distribution of track lengths within a sample (Gleadow et al., 1986; Green et al., 1989). As new fission tracks are formed continually in the host crystal by radioactive decay each track experiences a different portion of the total thermal history of the sample. The final distribution of the track lengths and measured apparent fission track age of a sample therefore represent an integrated record of its total thermal history over a temperature range within which fission tracks are preserved. It is therefore, essential to have information about the distribution of track lengths within a sample in order to meaningfully interpret measured apparent fission track ages (Gleadow et al., 1986).This approach was also undertaken on the

apatite grains in the present study. The track length measurement was performed on Macintosh TM-controlled microscope stage and digitizing tablet system for Fission Track Stage and Digitizing. The assembly comprises of high quality Kinetek TM automated scanning stage.

Apart from the cooling ages on apatite grains, the track length measurements were also performed on three samples from each section (Total 9 samples, Table 6.4, Fig.6.6). To observe the elevation effect on the track length distribution, samples from highest, intermediate and lowest elevations were selected (Fig.6.7). In the Chang La section, the mean track length varies from 12.55±0.24 μm with standard deviation of 1.72 μm to 9.95±0.21 μm with standard deviation of 1.59 μm (Fig.6.7a). Similarly, in the Khardung La section, the highest point yielded a mean track length of 12.43±0.16 μm with standard deviation of 1.45 μm, and the sample from lowest elevation has a mean track length of 10.70±0.19 μm with standard deviation of 1.38 μm and the intermediate point sample has mean track length of 11.48±0.19 μm with standard deviation of 1.141 μm (Fig.6.7b). Therefore one observes is a remarkable contraction in track lengths with decreasing elevation.

The most striking feature of the track length distribution data is the standard deviations of the lengths are quite high (Fig.6.6 and Table 6.4). According to Gleadow et. al. (1986), confined track length distribution of similar mean length and standard deviation are typical of slow and simple cooling history.

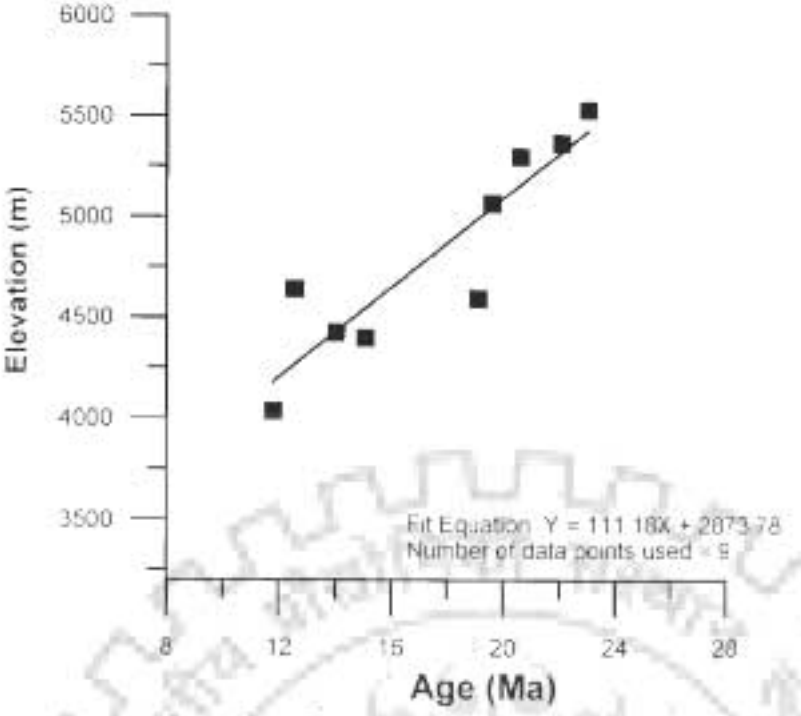

Figure 6.4 Elevation vs age plot for Ladakh Batholith in Leh Khardung La Section

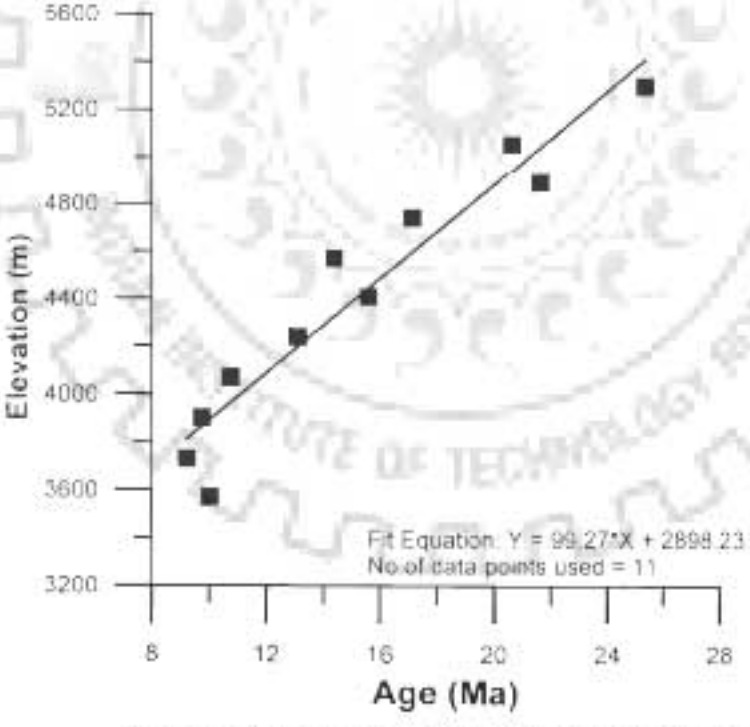

Figure 6.5: Elevation vs age plot for Ladakh Batholith in Kharu - Chang La Section

Table 6.4: Apatite mean track length data of the Ladakh Batholith

Sr. No.	Sample Code	Lab Code	Elevation (m)	Mean Track Length (μm)	Standard Deviation (μm)	No. of tracks measured
1	NS1/1	KA1	4645	11.48±0.15	1.14	61
2	NS9/20	KA5	4038	10.70±0.19	1.38	51
3	K-2	KA6	5440	12.43±0.16	1.45	83
4	LB 30/28	AP22	5301	12.55±0.24	1.72	50
5	LB14/32	14/32A	4409	10.20±0.26	1.89	50
6	LB18/36	AP13	3732	9.95±0.21	1.52	51
7	T93/354	AP18	4200	10.18±0.26	1.83	51
8	T97/345	AP21	4160	9.80±0.24	1.69	51
9	T100/350	AP19	4160	10.50±0.19	1.85	51

6.7 DISCUSSIONS

Before discussing the results it will be apposite to give a brief discussion about the thermal annealing and closure temperature of the FT apatite and zircon clocks.

6.7.1 Thermal annealing and closure temperature of apatite: In fission track dating, the term 'annealing' is used for the partial to complete erasure of tracks (Fleischer et al., 1965b). The fading occurs when some of the ions that were displaced during formation of the track, diffuse back into the track and heal some of the broken bonds. The annealing process appears to slow the etching rate, and so the etchant takes longer time to etch out the track. After a certain amount of annealing, the track has been broken by diffusion so many times that it etches at the same rate as the crystal and therefore cannot be seen.

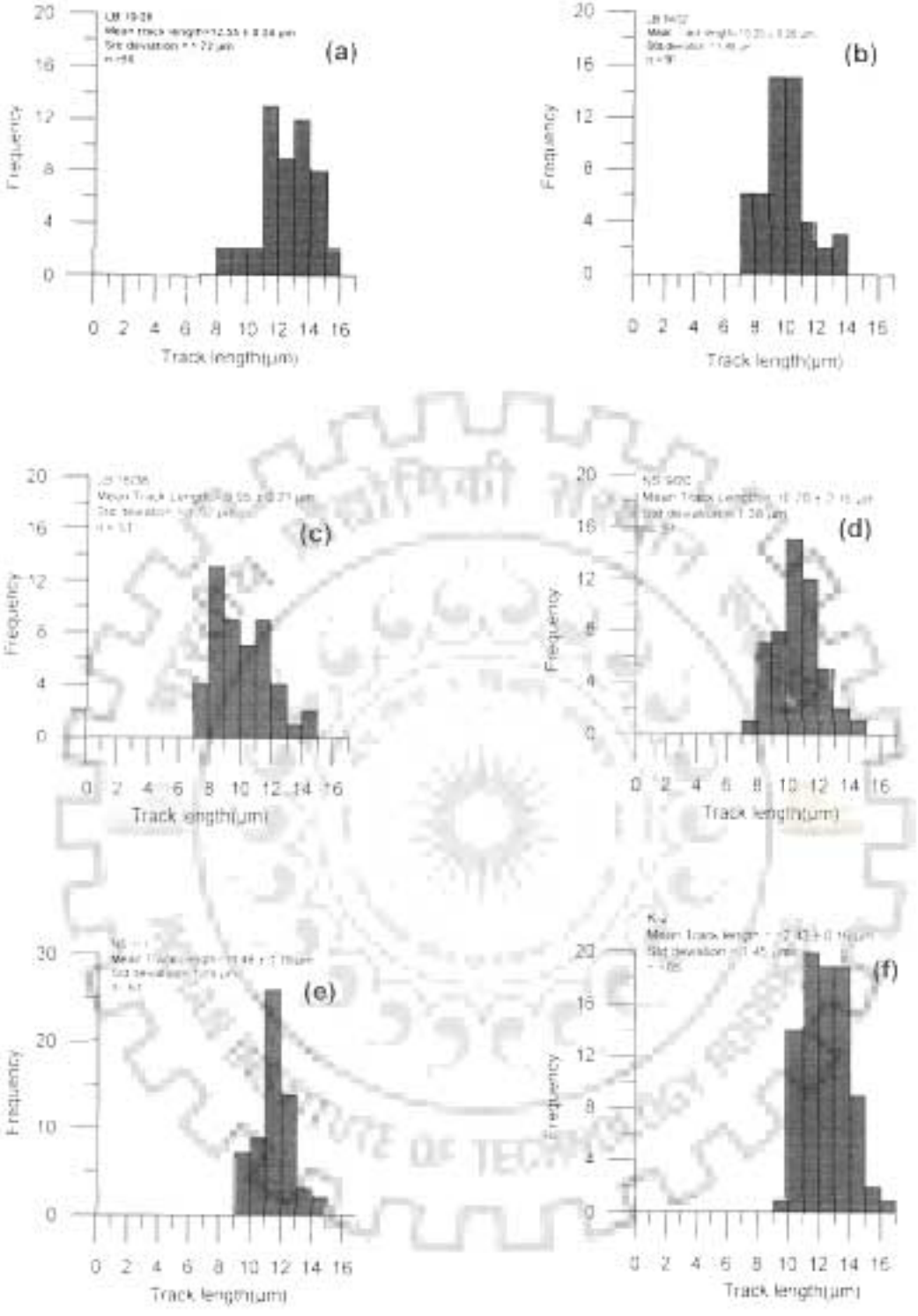
(a)
(b)
(c)
(d)
(e)
(f)
Frequency
Track length(μm)

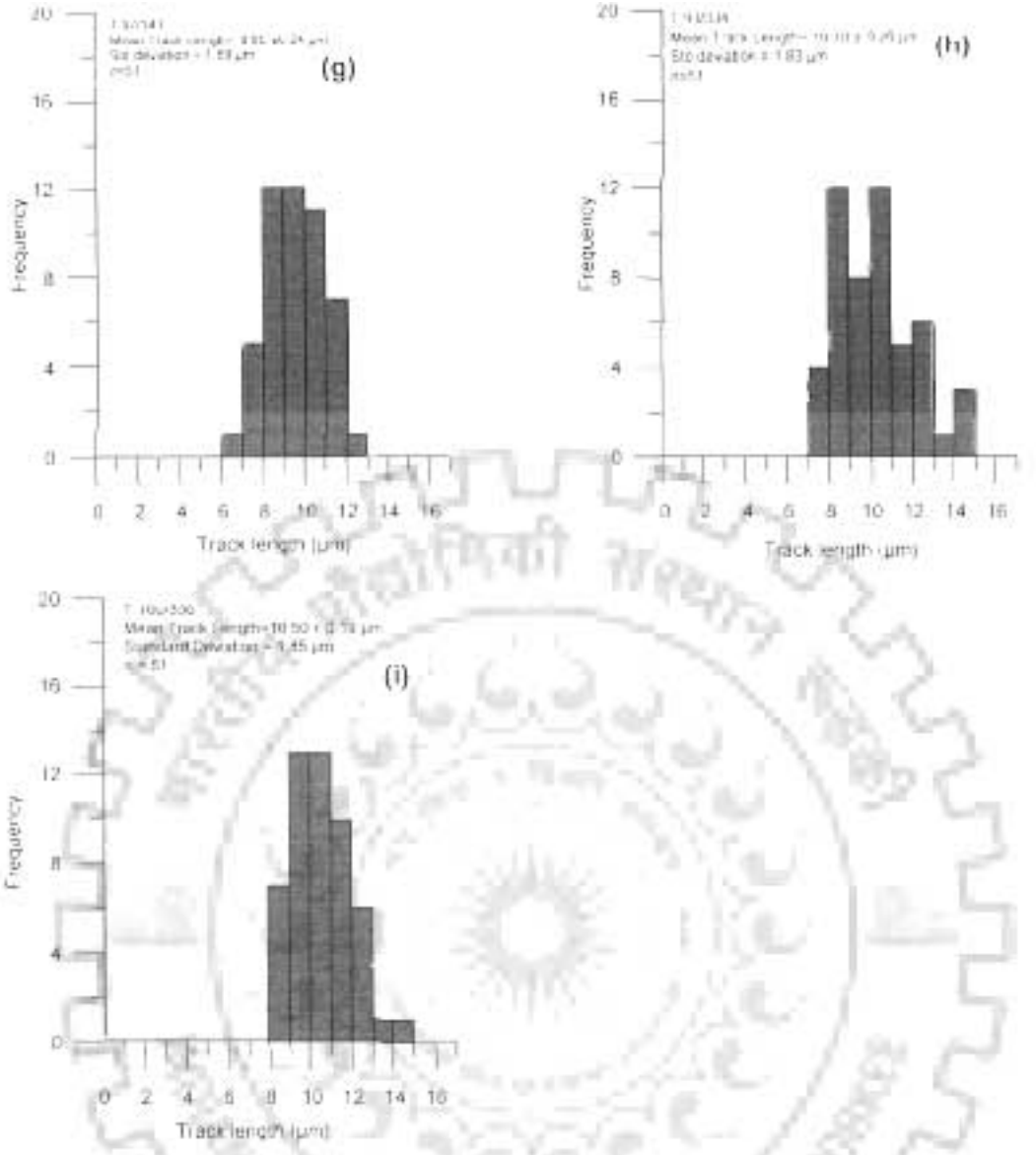

Figure 6.6: Track length measurements on apatite from Ladakh Batholith. (a), (b), (c) Kharu-Chang La section. (d), (e), (f) Leh-Khardung La section. (g), (h), (i) Lyoma Hanle section. X-axis denotes the track length (μm) and Y-axis denotes the frequency of track lengths.

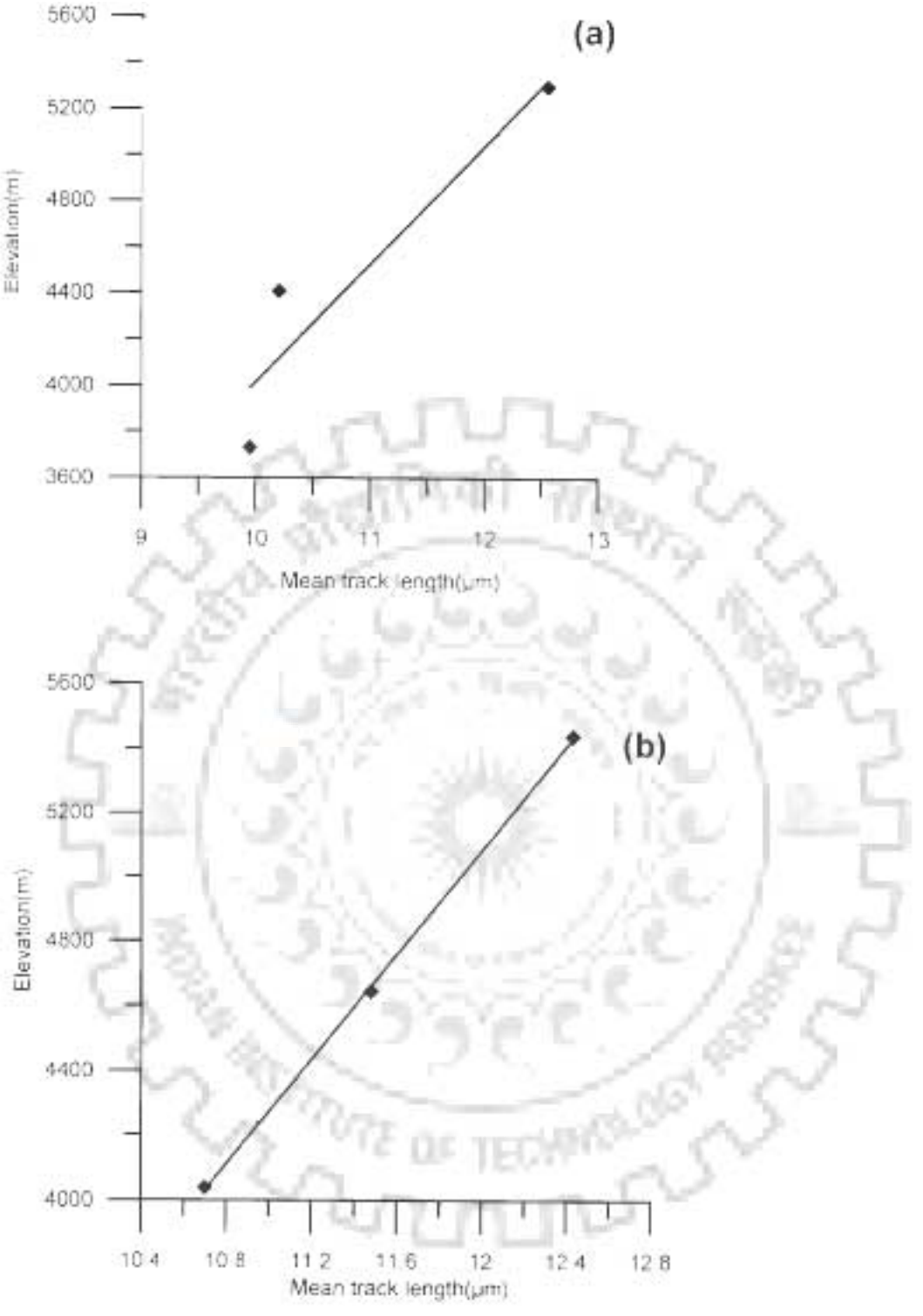

Figure 6.7 Variation of average apatite track length with elevation
(a) Kharu- Chang La section (b) Khardung La section

The studies of the effects of various environmental parameters on track stability in different mineral and glasses (Fleischer et al., 1965b; Wagner and Van Den Haute, 1992)

indicate that ordinarily it is the temperature that has the predominant effect. Under geological condition, fading of fission tracks is a common phenomenon and the resulting loss of fission tracks tends to lower the apparent FT age. In that case, the time at which the FT clock was turned on and the time that is given by the clock is no longer the same. The apparent FT mineral ages lowered by partial or complete track fading have resulted in understanding the insights of the thermal history of the host rock.

Track fading is a time and temperature dependent process (Fleischer et al., 1965b) and equivalent effects can be achieved by heating at low temperatures for prolonged periods and vice-versa. Uranium fission tracks in apatite and zircon are metastable, because recombination of defects causes the tracks to fade and anneal at elevated temperature. The annealing behavior of fission tracks in apatite and closure temperatures for retention of tracks therein have been estimated by both extrapolation of laboratory annealing data to geological time (Naeser and Faul, 1969; Wagner, 1969; Nagpaul et al., 1974; Naeser, 1979), as well as from the bore hole samples of reasonably well-known thermal history, where increase in depth and temperature produces a decrease in age (Gleadow and Duddy, 1981; Fleischer et al., 1965b). Over the geological time between 1 and 100 Ma, tracks in apatite begin to anneal around 70°C with complete track loss over a range of ~105-150°C. These low-closure temperatures are sensitive to the time spent in the track annealing zone, and thus, to the rate of cooling. These have been found to range from 90°C at relatively low cooling rates to 140°C at fast cooling rates (Wagner and Van den haute, 1992 and references therein). The assumed closure temperatures of FT apatite system for the samples from the Ladakh Batholith has been considered to be 110°±10° C in the present study.

6.7.2 Thermal annealing and closure temperature of zircon: The annealing behavior of the zircon fission tracks is comparatively less well known. Although it is well established that FT retention is higher in zircon than in apatite, various estimates for

closure temperatures in zircon range widely from about 175°C (Harrison et al., 1979) to 300°C (Krishnaswami et al., 1974). The earliest laboratory studies on FT annealing of zircon made with induced tracks suggested anomalous high stability temperatures (Fleschier et al., 1965b; Krishnaswami et al., 1974, Bal et al., 1983). These results are clearly at variance with the estimated closure temperatures determined from field studies using several radioactivity-based geothermochronometers or from analysis of deep drill hole samples. These temperatures fall in the range of 175-240°C (Harrison et al., 1979; Hurford, 1985, 1986, Zaun and Wagner, 1985). The potential difficulty in understanding the annealing behavior of FT zircon appears to be the role of accumulated radiation damage from α-decay of uranium and thorium. The concentration of uranium and thorium and thus the extent of radiation damage due to α-decay in zircon is much larger than that in apatite. As a result of these damages it is possible that annealing behavior of spontaneous fission tracks in zircon might be different from that of induced fission tracks giving rise to high closure temperatures of zircon deduced from the later type of tracks. No such significant difference is reported in apatite possibly due to low extent of α-damage. But still there is a difference of opinion about the role of α-damage in annealing behaviour. According to Kasuya and Naeser (1988), the thermal stability of FT in zircon is inversely proportional to the density of accumulated alpha recoil damage within the zircon grains. On the other hand, Carter (1990) found no real correlation between uranium concentration and zircon fission track ages and suggested the differential annealing of FT in zircon might be rather a function of mineral chemistry similar to the one observed in apatite (Green et al., 1989), where the annealing kinetics are found to be strongly dependent on the Cl/F ratio of the apatite grains.

From the above discussion it is obvious that if an appropriate FT closure temperature is to be assigned to zircon, it is essential that only spontaneous fission tracks are to be used (Brandon and Vance, 1992 and Tagami et al., 1990). Tagami et al. (1990) have reported the

degree of annealing of spontaneous fission tracks as a function of temperature as determined in a series of 1 hour annealing experiments. Zaun and Wagner (1985) have employed naturally annealed samples from deep borehole with a well constrained thermal history to determine the thermal stability over a time span of 100 Ma.

Using the approach suggested by Dodson (1973) and data of Zaun and Wagner (1985) and Tagami et al., (1990), Brandon and Vance (1992) calculated closure temperature of zircon. The values range from 210°C to 260°C for different cooling rates ranging from 1°C/Ma to 100°C/Ma. Hurford's (1986) estimate of T_{cc} = 240±50°C for a cooling rate of 15°C/Ma from cooling history of Lepontine Alps based on a variety of isotopic data, is in good agreement with those predicted by Brandon and Vance (1992). In the present study the closure temperatures of FT zircon system is assumed to be 220±25°C.

6.7.3 Exhumation rates: For the purpose of calculating the exhumation rates in the present work, the geothermal gradient of 30°C/km has been used. This value has also been used by Zeitler (1985) in the NW Himalaya in Pakistan. In order to calculate the cooling rate and corresponding exhumation rates from apatite age to present, a mean annual surface temperature of 10±5°C (already assumed by several workers e.g. Zeitler, 1985; Shusheng and Feng, 1988 in Himalaya and Wagner et al., 1977; Hurford, 1986 in Alps) has been assumed. Uncertainties in the exhumation rates will include the uncertainties in age and in closure temperature and as a result, may become relatively large in some cases.

FT ages from a young orogenic terrain can have varied geological significance. The concept of *blocking or closure temperature* represents the keystone for discussion of radiometric data and thermal history. The meaning of FT ages to specific geological processes can be linked in two basic ways. If the isotopic mineral ages of cogenetic minerals are available in the area, then from the sequence of mineral ages and their corresponding closure temperatures, it is possible to infer whether the FT ages are cooling ages or not. In the

absence of isotopic mineral ages, it is the geologic context of the samples such as grade of metamorphism and/or P-T conditions, which help in assigning the meaning of the FT ages. Once it is established that it represents a cooling age, it can be combined with other radiogenic thermochronometers to study the thermal history of rock from temperatures as high as 500°C to temperatures as low as about 100°C. From such cooling curves, exhumation rate can be calculated using the relation

Exhumation Rate = Cooling Rate/ Thermal Gradient

An alternative approach uses the apatite/zircon FT data to yield exhumation rates without any assumptions for values of geothermal gradient and closure temperature of the mineral. For a given intrusive or basement body, apatite and/or zircon age invariably increases with altitude due to the earlier passage of the upper sample below the closure temperature for the retention of tracks. Thus for limited lateral distance, the difference in elevation divided by the difference in age provides a direct measurement of exhumation rate (Wagner et al., 1977; Zeitler, 1985; Schlup et al., 2003). Such values are free from large errors of closure temperatures. This approach is widely in use and has also been employed in granitic terrains of Eastern Cordillera of Peru by Lauhachaer and Naeser (1994).

Approximations of exhumation rate provided by these procedures are dependent upon critical isotherms remaining horizontal and not influenced by surface topography or variable thermal conductivity (Parrish, 1983, 1985). Isotherms should also remain at constant depth relative to the surface. This requires that the isotherms should not relax and sink, for example, following tectonism, and that the rates for the Coast Mountains in British Columbia shows agreement within error of model and measured values where uplift is 0.3 mm/a or less, but that where rates are greater than 0.5 mm/a, uplift has a significant effect upon the movement of geotherms and geothermal gradient.

Considering the Apatite Fission Track (AFT) ages and the age vs. elevation plot in the two sections, the slope of the line gives the exhumation rate. The exhumation rates are very low for the Khardung La and Chang La sections and varies from 0.11mm/a during the time span of 23.01 Ma to 11.79 Ma to 0.09 mm/a during 25.35 Ma to 9.21 Ma in these sections, respectively. The Lyoma section which has got no significant elevation difference, the ages are tightly clustered and vary from 17.37 Ma to 12.01 Ma except one sample which gives an age of 23.08 Ma.

The zircon yield in the samples was of quite poor quality and hence not worth dating. Despite the best efforts, only three samples LB 10/28, LB 12/30 from the Chang La section and T100/350 from the Lyoma-Hanle section produced some datable cogenetic zircons. However, statistical quality of the data is not very good due to nonavailability of large number of crystals. Their ages came out to be 41.73±2.28 Ma, 43.32±3.36 Ma and 31.71±2.68 Ma from two sections from west to the east, respectively. These samples are located at 5301m, 4893m and 4160 m respectively. Considerable younging of the FT zircon ages is noticeable towards east, though it could not be confirmed due to lack of data set. Considering these ages, the exhumation rates for the respective samples are 0.24 mm/a, 0.18 mm/a and 0.28 mm/a, respectively with a mean exhumation rate of 0.23 mm/a between 41.73 and 25.35 Ma. The temporal variations of exhumation rates are illustrated in Table 6.5 and Fig. 6.8.

In comparison to the FT data set from the Ladakh Batholith generated for in this work, Schlup et al. (2003) obtained only one FT apatite age of 5±1 Ma from Chumathang with mean track length of 14.73±0.14 μm and interpreted it diagnostic of rapid cooling through Partial Annealing Zone of 60–110°C due to longer residence period of the batholith at greater depth as a result of its local overthrusting by the Indus molasses deposits during Late Eocene.

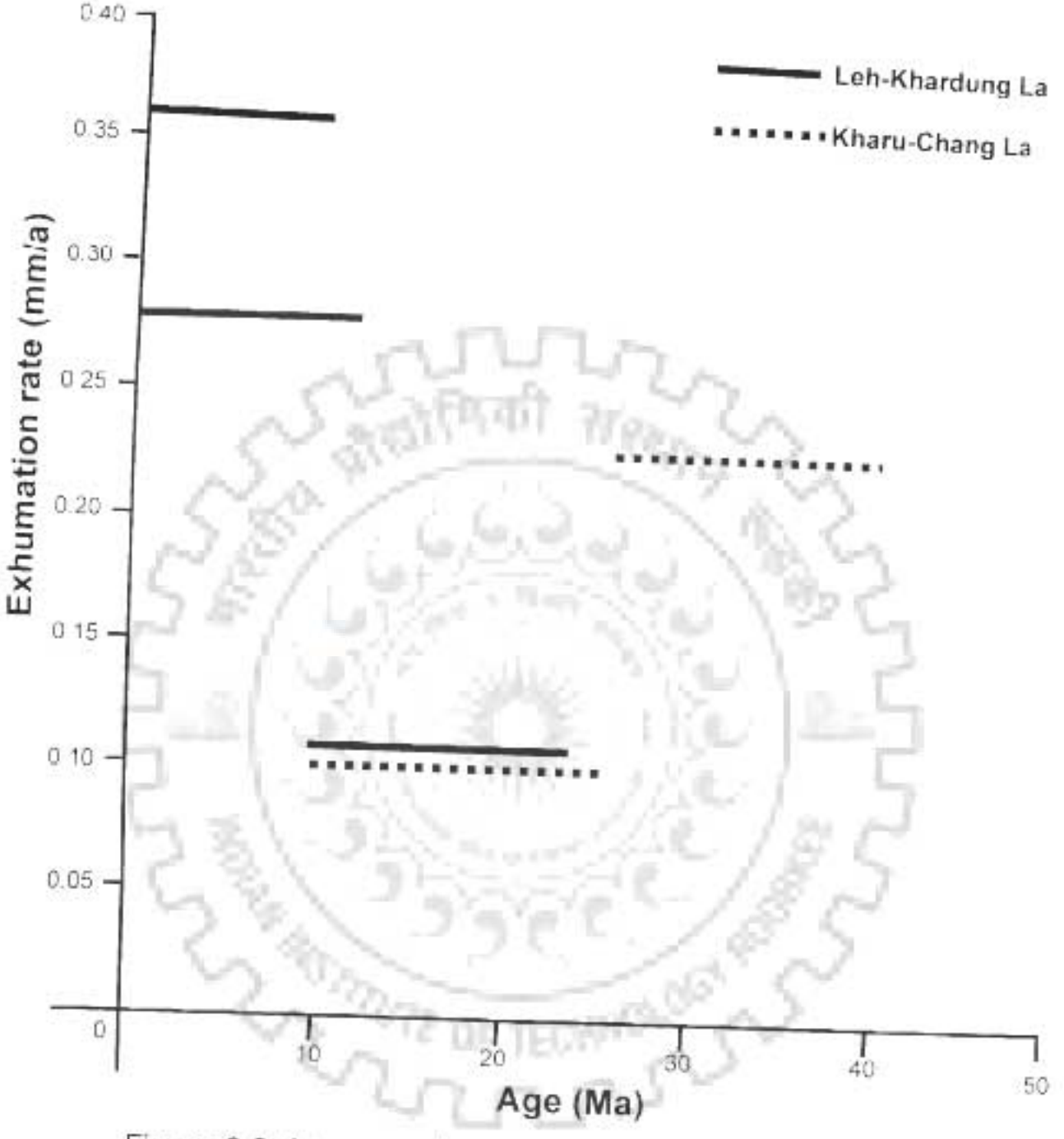

Figure 6.8: Age vs. exhumation plot of the Ladakh Batholith

Table 6.5: Exhumation rates of the Ladakh Batholith for various time spans

Section	Time span	Exhumation rates
Leh-Khardung La	23.01 to 11.79 Ma	0.11 mm/a (From age vs. elevation plot)
	11.79 to Present	0.28 mm/a (From Ap to Present)
Kharu- Chang La	41.73 to 25.35 Ma	0.23 mm/a (From Zr to Ap cooling age)
	25.35 to 9.21 Ma	0.099 mm/a (From age vs. elevation plot)
	9.21 Ma to Present	0.36 mm/a (From Ap to Present)

In comparison to the FT data set from the Ladakh Batholith generated for in this work, Schlup et al. (2003) obtained only one FT apatite age of 5±1 Ma from Chumathang with mean track length of 14.73±0.14 μm and interpreted it diagnostic of rapid cooling through Partial Annealing Zone of 60–110°C due to longer residence period of the batholith at greater depth as a result of its local overthrusting by the Indus molasses deposits during Late Eocene.

However, Sinclair and Jaffey (2001) obtained much older FT apatite age of 28±3 Ma and 29±2 Ma as the cooling ages of the Ladakh Batholith from Upshi. These ages are much older to 10.02±0.77 Ma, obtained in this work around Kharu, which is nearest to this locality. They also calculated the FT apatite ages from 2 sedimentary sequences in immediate vicinity of the Ladakh Batholith, i.e. the Nimmu Formation as 14±3 Ma and from a boulder in Choksti conglomerate from Zanskar gorge as 12 Ma. From these ages and extrapolation with the illite crystallinity, they deciphered the termination of sediment accumulation in the Indus Valley in early Miocene, and the earliest possible time for the initiation of a paleo–Indus River in this area in early Miocene (< 26 Ma). Interestingly, considering that the samples at the highest elevations of 5300 to 5400 m from the Ladakh Batholith had crossed the 110±10° C geotherm (~3.5 km depth) between 23–25 Ma, one would expect that the overlying

batholith column at the surface available for the erosion would have shown FT apatite age of ~ 24–26 Ma, considering the average exhumation rate of 0.10 mm/yr. It is, therefore, evident from our data as well that the Ladakh Batholith possibly was first exposed to the surface between 24–26 Ma and was drained off by the paleo–Indus River around that time on its southern slopes, as has been deciphered by Sinclair and Jaffey (2001).

Schlup et al. (2003) determined zircon FT age of 40.5±2.1 Ma from a sandstone of the Chultze Molasse and indicated that these zircons were derived from a single source as erosional product, probably from the emplaced North Himalayan nappe stack much to the south. Instead, our zircon FT data clearly reveals that part of the Ladakh Batholith crossed the 220±25° C isotherm between 45 and 30 Ma in the region between Upshi and Lyoma, thus becoming a strong provenance for the Indus sediments during Oligocene.

The whole of the batholith inherits a slow cooling and exhumation history as shown from the elevation vs. age plots (Figs 6.4, 6.5). Yet close observation from the exhumation vs. time plot indicates a slight change in the rates of exhumation. Initially, the exhumation was a slightly faster, as indicated by the zircon cooling ages which yielded average exhumation rate of 0.21 mm/a. Then, elevation vs. plots from the FT apatite ages give an average exhumation rate of 0.10 mm/a. After the minimum FT apatite age of the dated sample at 9.21 Ma to the Present, the batholith again cooled and exhumed somewhat rapidly with a rate of 0.31 mm/a, which is almost three times than the exhumation from 25.35 Ma to 9.21 Ma (Fig. 6.5).

CHAPTER–7

DISCUSSIONS AND CONCLUSIONS

7.1 GEOLOGICAL FRAMEWORK

The Himalaya marks the youngest orogeny on the Earth and has drawn global attention from a large number of geoscientists because of its past records of the collision tectonics. The Himalaya is one of the best belt to study the intricacies of plate tectonic theory, starting from subduction-related (Andean-type) processes to continent-continent collision. The Ladakh Batholith, a part of the Trans-Himalayan complex, is a result of north dipping subduction of the Tethyan crust beneath Eurasia. As a result, the batholith has intruded into the Dras Volcanics giving rise to Andean-type active arc setup after its accretion and prior to collision and reveals a unique three-dimensional exposure due to high relief (Honegger et al., 1982; Dietrich et al., 1983; Raz and Honegger, 1989).

The Ladakh Batholith have been referred as "Ladakh Granite" by Tewari (1964), "Ladakh Intrusives" by Frank et al. (1977), "Ladakh-Deosai Batholith" (Brookfield and Reynolds, 1981) and "Ladakh Batholith" by Rai (1983). The body has been described in detailed in field by earlier workers (Sharma and Gupta, 1978; Thakur and Virdi, 1979; Thakur, 1981; Raz and Honegger, 1989; Singh, 1993). Sharma and Gupta (1978) observed that the body reveals a zoned nature with more basic variety outside close to the Indus Molasse and the Indus Flysch and more acidic varieties within the core, and attributed this zoning to magmatic differentiation. Thakur (1981) described it as the Ladakh magmatic arc with distinct three phases of magmatic activity. (a) tholeiilites and calc-alkaline volcanics of Dras and Luzamu Formation, (b) the calc-alkaline intrusives of the Ladakh plutonic

complex, and (c) the acid volcanics of the Khardung Formation. However, Singh (1993) carried out a detailed mapping of the whole batholith and divided it into five different zones on the basis different rock types.

7.2 PETROGRAPHY AND GEOCHEMISTRY

The batholith has been studied further petrographically and geochemically (Rai, 1977, 1980, 1983, 1986; Rai and Pande, 1978; Sharma et al., 1978, 1983; Honegger et al., 1982; Pande and Rai, 1982; Sharma, 1983 Sharma and Choubey, 1983; Singh, 1993, Ahmad et al. 1998). Available petrological and geochemical data from the Ladakh Batholith suggest that the majority of the rocks range in composition from diorite to granite with occasional occurrence of more basic varieties like norite and gabbro in the Kargil area. The geochemical affinity indicates that it has evolved as an Andean-Type active margin.

In the present study, systematic work has been carried out for temporal and lateral variations of petrography and geochemistry, along three sections of the Ladakh Batholith, viz. Leh-Khardung La, Kharu-Chang La and Lyoma-Hanle. For this purpose 53 samples have been selected from these three sections (Leh- Khardung La: 30 samples; Kharu-Chang La: 13 samples and Lyoma-Hanle: 10 samples). The petrographic studies (Chapter 3) clearly indicate three main types of rocks-diorite (16 samples), granodiorite (27 samples) and granite (10 samples). Similar picture has emerged from the Quartz-Alkali Feldspar-Plagioclase (Q-A-P) normative calculation plot of Streicksen (1976). The major oxide plots, in particular the SiO_2 vs (K_2O+Na_2O) plot indicates its sub-alkaline, SiO_2 vs K_2O plot indicates medium to high K-bearing rocks and AFM plot indicates its calc-alkaline character. In the discrimination Rb vs (Y+Nb) and Rb vs (Yb+Ta) plots of Pearce et al. (1984) the batholith falls in the Volcanic Arc Granite (VAG) field. The normalized spiderplots and REE plots show enrichment of LREE-LILE and depletion of HFSE which are characteristic of subduction-related

magmatism (Saunders et al., 1980; Holm, 1985). Typical signature of negative Nb anomaly for subduction zone environment (Wood et al., 1979) is also characterized by the spiderplot of the samples from the Ladakh Batholith. Similar character of REE pattern has been reported by Honneger et al. (1982), Dietrich et al. (1983), and Ahmad et al. (1998) from the study of the Ladakh Batholith from different sections.

7.3 GEOCHRONOLOGY AND CRYSTALLIZATION AGE

For obtaining the crystallization age as well as biotite cooling ages, Rb-Sr systematics on 21 whole rock and 7 whole rock-biotite pairs from the Ladakh Batholith have been attempted. All $^{87}Rb/^{86}Sr$ and $^{87}Sr/^{86}Sr$ values have been determined in newly- established TIMS Laboratory at IIT Roorkee (Chapter 5). The data generated shows a good spread in the $^{87}Rb/^{86}Sr$ ratios but no proper isochron could be drawn. However, four samples LB8/23, LB12/30, LB 14/32 and LB15/33, from the Kharu-Chang La section give a very good isochron age of 61.59±0.41 Ma with an initial $^{87}Sr/^{86}Sr$ ratio of 0.7041759±0.0000060 with MSWD .92. This age has been considered to be the age of crystallization of the Ladakh Batholith and is similar to SHRIMP II U-Pb zircon age of 60±0.09 Ma from the same section. (Singh et al., 2003; Jain et al., 2003, 2004). Initial Sr isotopic ratios from the Ladakh Batholith range between 0.704000 to 0.763413 and, when considered with the already published values between 0.7034 to 0.7048 (cf Honneger at al., 1982), these point to oceanic crust and mantle origin of the magmas.

The problem of getting a good isochron on the samples of Ladakh Batholith is quite old. This was first encountered by Honneger et al. (1982), who could generate only a three - point isochron age of 60±10 Ma from the Shey granite body near Leh. Schrarer et al. (1984) and Sorkhabi et al. (1994) have also made efforts to date the body by Rb-Sr systematics but failed to generate any isochron. The lack of good isochron can be attributed to non-

equilibrium of the Sr isotopes and their inhomogeneity within the body. It may reflect the limited time span of generation and emplacement of local melts (Honneger et al. 1982). It can also be attributed to real age differences in the rocks due to multiple phases of emplacement on relatively small scale which is evident from the fact that the batholith consists of phases of about 103-102 Ma in Kargil area to about 60 Ma near Leh and later with later on pulses of magmatic activity at around 46 Ma. These pulses themselves reflect the heterogeneity of parent material. The other explanation can be that the system has become open with respect to the Rb-Sr Systematics due to some later activity. So far, when ages obtained by zircon dating by SHRIMP U-Pb and conventional U-Pb method, and Rb-Sr whole rock dating techniques are clubbed together, an overall weighted mean age of 60.05± 0.24 Ma has been obtained and considered as the crystallization age.

7.4 FISSION TRACK AGES AND EXHUMATION RATES

Fission track dating of the Ladakh Batholith on 30 apatite and 3 zircon samples from three sections (Chapter 6) show a good correlation of FT-apatite age with elevation except in Lyoma-Hanle section and provide invaluable data on the exhumation rate of the batholith. The ages range from 9.21 Ma to 25.35 Ma. However, FT zircon ages are 41.73Ma, 43.37 Ma and 31.71 Ma from west to east and show younging towards east. FT apatite data on 7 samples from Kargil plutonic complex by Sorkhabi et al. (1994) from the western sector range from 13.5±1.8 Ma to 25.6±4.0 Ma while 2 zircon ages are age 41.4±2.2Ma and 45.2±3.5 Ma and fall within the age ranges obtained in this work (Table 7.1).

Two $^{40}Ar/^{39}Ar$ hornblende ages, viz. 45.7±0.8 Ma (Weinberg and Dunlap, 2000) and 44.7±0.3 Ma (Schlup et al., 2003) from the Ladakh Batholith are currently available and reveal that this batholith has crossed the 500±50° C geotherm (cf. McDougall and Harrison, 1988) at ~ 44.83 Ma (overall weighted mean). However, Schlup et al. (2003) have interpreted

Table 7.1 : Geochronological data from the Trans-Himalayan Ladakh Batholith

S.No.	Age (Reference)	Overall Weighted Mean (OWM)	Temp. (°C)	Time span	Cooling (°C/Ma) & exhumation (mm/a) rates
A. Crystallization age					
1	61.5±2, 58.4±1.49.8±0.8 Ma (U-Pb SHRIMP zircon) (Weinberg and Dunlap, 2000)	60.05±0.74 Ma	750±50	60.05 to 44.8 Ma	16.42 °C/Ma 0.35 mm/yr
2	60.7±0.4 Ma (U-Pb zircon) (Schaier et al., 1984)				
3	58.4±1, 60.1±0.9 Ma (U-Pb SHRIMP zircon) (Singh et al., 2003)				
4.	60±10 Ma (Rb-Sr Whole rock) (Honneger et al., 1982)				
5.	61.59±0.4 Ma (Rb-Sr Whole rock) **Present work**				
B. Mineral Ages					
6	45.7±0.8 Ma (Ar-Ar Hbl) (Weinberg and Dunlap, 2000) 44.7±0.03 Ma (Ar-Ar Hbl) (Schlup et al., 2003)	44.83±0.25 Ma	500±50	Between 45.6 to 44.8 Ma	200 °C/Ma
7	45 Ma (Rb-Sr Biotite) (Honneger et al., 1982) 52.48±0.05, 52.37±0.05, 51.25±0.07, 46.62±0.05, 44.92±0.05, 36.71±0.05, 45.53±0.06 Ma (Rb-Sr Biotite) **Present work**	45.65±0.06 Ma	300±50		
8.	41.73±3.36, 43.37±3.66, 31.71±2.68 (FT Zircon) **Present work** 41.4±2.2, 45.2±3.1 Ma (FT Zircon) (Sorkhabi et al., 1994) (The sample yielding 31.71±2.68 Ma is left out in OWM calculation)	42.72±1.45 Ma	250±25	45.6 to 42.7 Ma	27.3 °C/Ma 0.35 mm/yr
9.	36±0.05 Ma (Ar-Ar K Feldspar) (Dunlap et al., 1998)	36 Ma	150±25	42.7 to 36.0 Ma	10.4 °C/Ma 0.35 mm/yr
10.	25.35 Ma to 9.21 Ma on 30 samples (FT apatite ages). **Present work** 13.2±2.4 Ma to 25.6±4Ma on 7 samples (FT apatite ages) Sorkhabi et al. (1994)	16.48±0.29 Ma	110±10	36.0 to 16.5 Ma	2.05 °C/Ma 0.07 mm/yr

the 44.7±0.3 Ma hornblende age representing a time near its crystallization and broadly coeval with the magmatic activity of the Ladakh Batholith, based on youngest magmatic SHRIMP U-Pb zircon age of 49.8±0.8 Ma. In this work, $^{40}Ar/^{39}Ar$ hornblende age of 44.83 Ma has been considered as the cooling age of the Ladakh Batholith through 500±50° C from its crystallization temperature of ~750±50° C at 60.05 Ma. It indicates that the Ladakh Batholith has cooled @ 16.42°C/Ma and exhumed @ 0.55mm/yr during 60-45 Ma in the central parts of the pluton around Leh.

Seven Rb-Sr biotite ages, obtained in this work, show a wide range from 36.71±0.05 Ma to 52.38±0.05 Ma and, when the age obtained by Honnegger et al. (1982) is considered together, an overall weighted mean average age of 45.65±0.09 Ma has been obtained. Considering the ages, obtained in this work on Rb-Sr biotite, the batholith appears to have crossed the 300±50°C geotherm at ~45.6 Ma. When this Rb-Sr biotite age is considered with rather scanty $^{40}Ar/^{39}Ar$ hornblebnde ages ~ 44.8 Ma, there appears to be an anamoly in the cooling ages with respect to blocking temperature of hornblende and biotite: hornblende having a higher blocking temperature of 500±50°C has an 'apparent' younger age of ~ 44.8 Ma than biotite of 45.6 Ma with 300±50°C blocking temperature with ~ 45.6 Ma age. Either available hornblende ages are very scanty (only 2 in numbers) and thus giving an 'apparent' cooling age or some of the biotites in this work reveal higher Rb-Sr ages. An 'apparent' cooling of 200°C is, therefore, inferred at approximately 44-45 Ma.

Two more biotite ages from the Ladakh Batholith, one by K-Ar method (Honegger et al., 1982) and the other by $^{40}Ar/^{39}Ar$ method (Schlup et al., 2003) are 48.7±1.6 Ma and 32.6±2 Ma, respectively. When plotted in the exhumation path diagram, the former is older to $^{40}Ar/^{39}Ar$ hornblende weighted mean age, though indicating a cooling temperature of 300±50° C. Like many other terrains, it appears to be due to retention of excess argon in

biotite. On the other hand, biotite age of 32.6±0.2 Ma is much younger to the FT zircon ages, obtained in the present work from the Kharu-Chang La section, and appears to be anamolous again, possibly due to subsequent tectonics around Chumathang. Both these ages have, therefore, not been considered in the calculation of exhumation rates. Hence, $^{40}Ar/^{39}Ar$ hornblende age of ~ 44.8 Ma and the FT zircon age with an overall weighted mean of 42.72±1.45 Ma [3 samples from this work and 2 from Sorkhabi et al., (1994)] provide an estimated extremely fast cooling of 133° C/Ma through 500±50° C and 220±25° C, and therefore, an unexpectedly fast exhumation rate of 4.42 mm/yr.

Cooling rate of the Ladakh Batholith from Rb-Sr biotite to FT Zircon during the time span from 45.6 to 42.7 Ma comes out to be 27.30°C/ Ma with an exhumation rate of 0.35 mm/a indicating a sudden slow down in its exhumation.

It appears that subsequent cooling history of the Ladakh Batholith has been very slow, as it is apparent from a single modeled $^{40}Ar/^{39}Ar$ K-feldspar age of ~36 Ma (Dunlap et al., 1998). Cooling rates between FT zircon annealing temperature of ~220° C and Ar retention temperature in feldspars ~150° C have, therefore, been considerably fallen to 10.42°C/Ma, and amounts to an exhumation rate of 0.35 mm/yr between 42.7 and 36 Ma. There is further decrease in cooling and exhumation rates when $^{40}Ar/^{39}Ar$ K-feldspar age of ~36 Ma and apatite age of 16.48±0.2 Ma have been considered for the calculation of cooling and exhumation rates during this time span when the batholith has further cooled down by another 40°C to 110°C. Cooling rates appear to have slowed down to as low as 2.05°C/Ma with an exhumation rate of 0.07 mm/yr.

Elevation profiles of apatite ages along the Leh-Khardung La and the Kharu-Chang La sections also provide an insight into the exhumation rates of the Ladakh Batholith. Elevation vs. age profiles (Fig 6.3 and 6.4) along these two sections yield exhumation rates of

0.11 mm/yr between 23.01 and 11.79 Ma for the former section and a rate of 0.09 mm/yr between 25.35 and 9.21 Ma for the latter. Therefore, it is evident that the Ladakh Batholith has exhumed at a very slow rate somewhere between 0.07 mm/yr to 0.11 mm/yr since it has crossed ~150° C geotherm for the retention of Ar in feldspar at ~36 Ma and ~9 Ma-the youngest apatite FT ages from the batholith.

Considering the the weighted mean ages of FT apatite geochronometer from the Leh- Khardung La, the Kharu-Chang La and the Lyoma-Hanle sections, the exhumation rates of 0.19 mm/yr, 0.21 mm/yr and 0.22 mm/yr since 17.38 Ma, 15.93 Ma and 15.23 Ma to the present for these sections, respectively. Figure 7.1a presents the exhumation path of the Ladakh batholith on the basis of the available data.

7.5 COMPARISON WITH OTHER WORKS

About 250 km to the west from Leh, detailed study of FT zircon and apatite ages from the Kargil pluton which intrudes the Dras Volcanics, has revealed that zircon ranges from 41.4±2.2 Ma and 45.2±3.1 Ma from 2 samples, while cogenetic apatite yields ages of 19.3±2.0 Ma and 24.7±2.5 Ma, respectively (Sorkhabi et al., 1994). Therefore, cooling rates have varied between 5.4±1.4° C/Ma to 5.8±1.7° C/Ma for a period between 41–45 Ma to 19–25 Ma and consequently the exhumation rates as 0.18–0.19 mm/yr. These have almost remained the same around 0.15 mm/yr since 20 Ma till present. It is interesting to note that the Ladakh Batholith has exhumed almost at the same rate since 41–45 Ma over a distance of more than 500 km, as is evident from the FT zircon–apatite studies from Kargil, Leh–Khardung La, Kharu–Chang La, and Lyoma–Hanle sections. Older exhumation history of the Kargil body appears to be more complex since its crystallization ~102 Ma. Two granodiorites from Kargil yield U–Pb zircon concordia ages of 103±3 Ma (Honegger et al., 1982) and 102±2 Ma (Scharer et al., 1984). K–Ar and $^{40}Ar/^{39}Ar$ hornblende ages from the

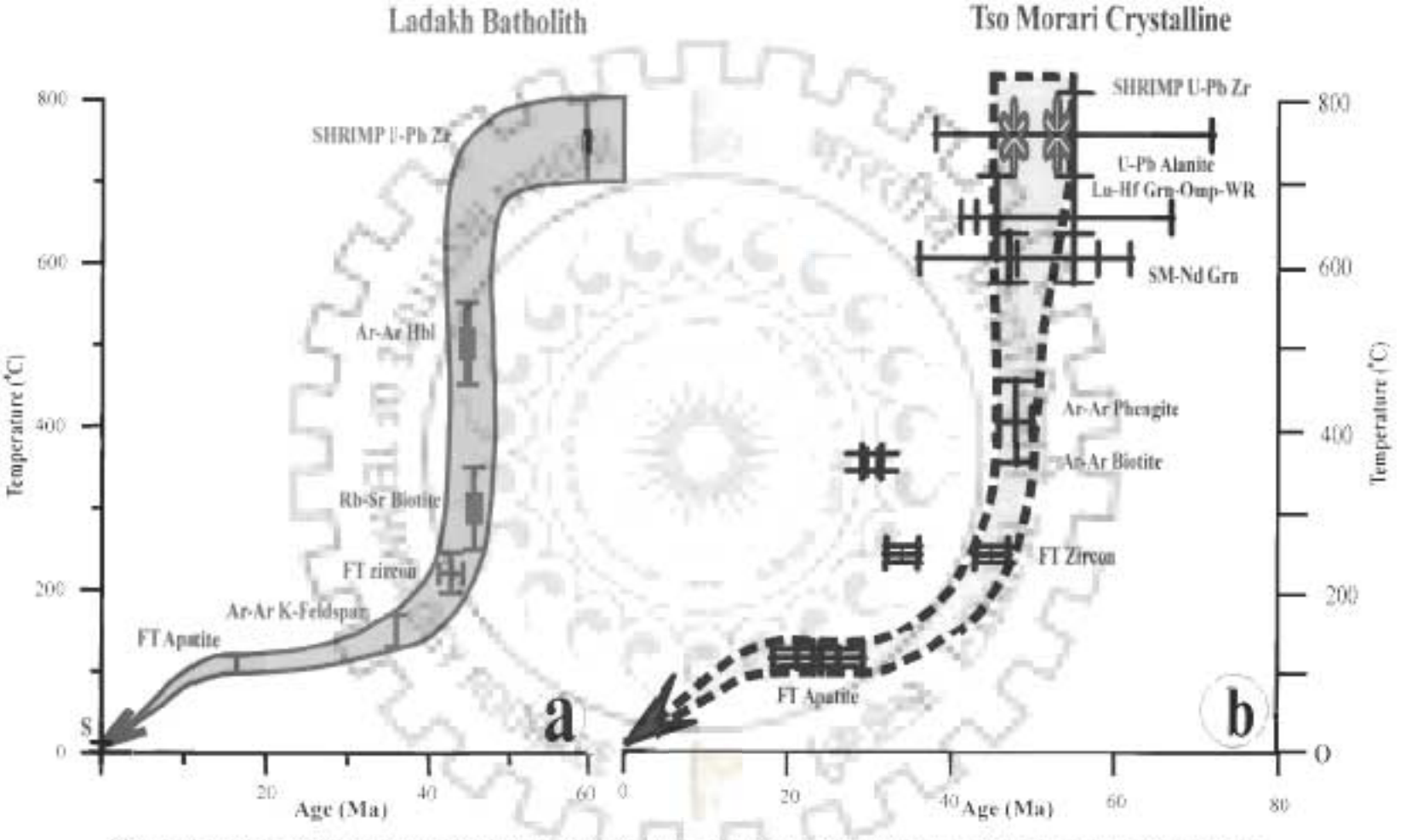

Figure 7.1: Exhumation paths of the (a) Trans-Himalayan Ladakh Batholith and (b) Tso Morari Crystallines. Note their almost parallel trend. Based on published data, and Rb-Sr biotite and FT zircon data of this work.

Kargil range from 90±2 Ma (Sorkhabi et al., 1994) to 82±6 Ma from a syenite (Brookfield and Reynolds, 1981), and 80.7±3.2 Ma and 82.6±2.5 Ma from the contact zone with the Dras Volcanics (Frost et al., 1984). All these ages average ~85 Ma when the Kargil body cooled through 500±50° C geotherm @ 14.7° C/Ma and exhumed @ 0.49 mm/yr since its crystallization. Though much older in age to the main body of the Ladakh Batholith it reveals almost similar exhumation rates.

The FT results obtained in this work on 30 apatite and 3 zircon samples from the Ladakh batholith are not in agreement with isolated ages obtained by Sinclair and Jaffey (2001), who determined the FT apatite ages on 2 samples from Upshi as 28±3 and 29±2 Ma. These ages are much older to 10.02±0.77 Ma, obtained in the present work around Kharu, which is about 10 Km from Upshi. They also calculated the FT apatite ages from 2 sedimentary sequences in immediate vicinity of the Ladakh Batholith i.e. the Nimmu Formation as 14±3 Ma and from a boulder in the Choksti conglomerate from the Zanskar gorge as 12 Ma. From these ages and extrapolation with the illite crystallinity they deciphered the termination of sediment accumulation in the Indus Valley and earliest possible time for the initiation of a paleo-Indus River in this area in the early Miocene (<26 Ma). Interestingly, considering that the samples at the highest elevations of 5300 to 5400 m from the Ladakh Batholith had crossed the 110±10°C geotherm, i.e. ~3.5 km depth between 23–25 Ma, one would expect that the overlying batholith column at the surface available for the erosion would have shown FT apatite age of ~24–26 Ma, considering the average exhumation rate of 0.10mm/yr. It is, therefore, evident from the data generated in this work that the Ladakh Batholith possibly was first exposed to the surface between 24–26 Ma and was drained off by the paleo-Indus River around that time on its southern slopes, as has been deciphered by Sinclair and Jaffey (2001).

7.6 TECTONIC IMPLICATIONS

From the foregoing discussions, it is evident that the subduction of the Neo – Tethyan oceanic lithosphere beneath the southern margin of Eurasia along the Indus Tsangpo Suture Zone (ITSZ) and partial melting of the mantle has produced large volumes of calc-alkaline plutons in pulses starting from 103 Ma till 50 Ma. These bodies range from gabbro-norite near Kargil of 103 to 101 Ma – a concordant U-Pb zircon age (Honegger et al., 1982; Scharer et al., 1984), granodiorite to diorite of 60.1±0.9 Ma across Chang La and 58.4±1 Ma at Kharu (SHRIMP U-Pb zircon age, Singh et al., 2003; Jain et al., 2004), granodiorite to granite of 60±3 Ma (Rb-Sr whole rock age of Shey-granite-Honegger et al., 1982), 61.59±0.41 Ma (Rb-Sr whole rock isochron age on granodiorite from Kharu-Chang La section) and possibly a younger quartz diorite intrusion of 49.8±0.8 Ma (SHRIMP U-Pb zircon age of Leh granodiorite-Weinberg and Dunlap, 2000). Initial manifestation of the Andean-type margin appeared only after the closure of the vast Tethyan ocean along the ITSZ when the oceanic lithosphere underwent extensive partial melting to produce enormous quantities of granodiorite-diorite plutons, which were emplaced and crystallized at an approximate depth of about 15-20 km.

$^{40}Ar/^{39}Ar$ hornblende ages of ~45 Ma from the Ladakh Batholith clearly reveal that this pluton has undergone cooling and exhumation since its emplacement ~60 Ma @ 16.42°C/Ma and 0.55mm/yr, respectively assuming a constant geothermal gradient of ~30°C/km. At this stage, it appears likely that the Indian continental lithosphere detached itself almost completely from the oceanic lithosphere and has underwent deep subduction to a depth of ~100 km to produce UHP coesite-bearing rocks in immediate vicinity to the south de Sigoyer et al. (2000) determined the age of this ultrahigh pressure the (UHP) metamorphism ~55 Ma in the Tso Morari by Sm±Nd method on gr-gln-whole rock (55±7

Ma), Lu-Hf age on grt-pyx-whole rock (55±12 Ma) and U-Pb allanite (55±17 Ma). SHRIMP U-Pb zircon ages obtained by Leach et al., 2003 (in review) have indicated metamorphic zircon growth at 53±0.5 Ma during the UHP metamorphism and provide more precise age for this important event on the subducting Indian lithosphere (Fig. 7.1b). Therefore, initial exhumation of the Ladakh Batholith appears to be controlled by the subducting Indian continental lithosphere prior to its attaining the UHP metamorphism ~53 Ma.. It is a remarkable similarity that subsequent superposed amphibolite facies metamorphism during the isothermal decompression has been dated between 48 Ma and 45 Ma by $^{40}Ar/^{39}Ar$ phengite (48±2 Ma), Sm/Nd grt-hb whole rock (47±1 Ma) and Rb-Sr phengite-apatite-whole rock (45±4 Ma) (de Sigoyer et al., 2000). In the Ladakh Batholith, this event coincides with $^{40}Ar/^{39}Ar$ hornblende age of ~45 Ma and gives an exhumation rate of 0.55 mm/yr. As the Indian continental lithosphere undergoes exhumation and retrogression of the UHP assemblage in the amphibolite facies ~47-43 Ma @5mm/yr (de Sigoyer et al., 2000), the Ladakh Batholith also exhumed at accelerated speed of 4.42 mm/yr between 44.83 and 42.55 Ma on top of the dismembered segment of the Indian lithosphere along the ITSZ (Fig. 7.1b).

7.7 CONCLUSIONS

The work undertaken in the present thesis is an integration of field data with petrography, geochemistry, geochronology (Rb-Sr dating) along with cooling and exhumation history by FT dating of the Trans-Himalayan Ladakh Batholith. The main conclusions of this work are as follows:

1. The Ladakh batholith is located between two Himalayan suture zones, the Indus Tsangpo Suture Zone (ITSZ) and the Shyok Suture Zone as a WNW-ESE trending linear belt of about 600 km land 30-80 km in width. The batholith is dominated by

granodiorite, though minor amount of more basic varieties like norite and gabbro also occur in Kargil area. Geochemically, the body shows, Calc-alkaline, high to medium k bearing rocks with sub alkaline character. The normalized trace elment spider plot and REE pattern shows signatures of subduction related magmatism due to partial melting of oceanic lithosphere.

2. Based on the Al-content in hornblende geobarometer, the batholith appears to have been crystallized at depth between 14.27 and 7.3 km over a vertical section of around 2 km with diorite indicating lower crustal depth around 14.30 km and granodiorite around 7.35 km. When the crustal depths are plotted against the elevation, a good correlation between crustal depths with elevation has been obtained indicating that the diorites at lower elevation have crystallized first. Also, if the total depth difference is considered, it comes out be~7 km whereas the elevation difference is ~ 2 km. It can be inferred that this body has undergone either magmatic compression or tectonic removal within this section.

3. The Trans-Himalayan calc-alkaline Ladakh Batholith pluton has developed due to partial melting of the leading edge of the subducting Neo- Tethyan oceanic lithosphere and was emplaced along the southern margin of the Eurasian Plate between 61.59±0.41 Ma and 58.4±1 Ma, as is indicated by the Rb-Sr whole rock ages and SHRIMP U–Pb zircon ages. These ages, when considered with the already available Rb–Sr whole rock isochron ages of the Shey granite and the U–Pb zircon concordia ages from Leh, reveal an extensive and widespread plutonism in the Ladakh Range around 60 Ma, which was subsequently affected by minor intrusive plutons and dolerite dykes.

4. FT zircon and apatite ages from 3 widespread sections through the Ladakh Batholith

reveal its exhumation history through low temperature geotherms of 220±25°C and 110+10°C around 43.37+3.66 Ma and 25.35±2.57 Ma, as is evident from the oldest FT zircon and apatite ages. Extremely good correlations have been established between the elevation and age for FT apatite in two profiles of the Ladakh Batholith and provide a very slow average exhumation rates of 0.11 mm/yr between 25.35 Ma and 9.21 Ma, irrespective of any assumed values for geothermal gradient, annealing temperatures and present-day temperatures.

5. Comparison of exhumation history of the continental lithosphere of the UHP Tso Morari terrain in the south, which has subducted to a depth of about 100 km around 53 Ma with the part of the Ladakh Batholith reveals that the later has exhumed as a piggy back sequence along north dipping ITSZ. Since its emplacement around 60 Ma till 43 Ma exhumation has been calculated at a rate between 0.55mm/yr in the initial stages to 4.42 mm/yr subsequently. The Ladakh Batholith has crossed 220±25°C geotherm at ~ 43 Ma, as is indicated by average FT zircon age and 110±10°C at around ~25 Ma –the oldest apatite age from the batholith. In comparison to the available FT zircon and apatite ages from any other tectonic units of the Himalaya, the Ladakh Batholith reveals an almost uniform and slow exhumation pattern between ~25 to 9 Ma at an average rate of about 0.11mm/a. Exhumation paths of the Tso Morari and the Ladakh Batholith are almost identical since ~ 53 Ma and older when compared to the exhumation of the Higher Himalayan Crystallines further south.

REFERENCES

Ahmad, T., Thakur, V. C., Islam, R., Khanna, P. P. and Mukherjee, P. K. (1998). Geochemistry and geodynamic implications of magmatic rocks from the Trans-Himalayan arc. Geochem. Jour., v. 32, pp. 383-404.

Allegre, C.J. and Othman, D.B. (1980). Nd-Sr isotopic relationship in granitoid rocks and continental crust development: a chemical approach to orogenesis. Nature, v. 286, pp. 335-342.

Auden, J.B. (1935). Traverses in the Himalaya. Rec. Geol. Surv. India, v. 69, pp. 123-167.

Bal, K.D., Lal, N. and Nagpaul, K.K. (1983). Zircon and sphene as fission track geochronometer and geothermometer, a reappraisal. Contrib. Mineral Petrol., v. 83, pp. 199-201.

Balaram, V., Ramesh, S.L., and Anjaniah, K.V. (1995). Comparative study of sample decomposition procedure in the determination of trace and rare earth elements in anorthosites and related rocks by ICP- MS. Fresenius J. Anal. Chem., v. 353, pp. 176-182.

Balaram, V., Ramesh, S.L., and Anjaniah, K.V. (1996). New trace elements and REE data in thirteen GSF reference samples by ICP-MS. Geostand. Newslett., v. 20, pp. 71-78.

Berthelsen, A. (1953). On the geology of Rupshu dist., Northwest Himalaya. Medd. Fra. Danks geologisk Forening, v. 12 (30), pp. 351-414.

Bigazzi, G. (1981). The problem of the decay constant λ_f of ^{238}U. Nucl. Tracks, v. 5, pp. 35-44.

Blichert, J. S. (1993). Manual for Sr and Nd Isotope Geochemistry. Copenhagen. Unpublished manual, 121p.

Brandon, M. T. and Vance, J. A. (1992). Tectonic evolution of the Cenozoic Olympic subduction complex, Washington State, as deduced from fission track ages for detrital zircons. Am. J. Sci., v. 292, p. 565-636.

Brookfield, M.E. and Reynolds, P.H. (1981). Late Cretaceous emplacement of the Indus Suture Zone ophiolitic mélanges and an Eocene–Oligocene magmatic arc on the northern edge of the Indian Plate. Earth. Planet. Sci. Lett., v. 55, pp. 157-162.

Brookfield, M.E. and Reynolds, P.H. (1990). Miocene 40Ar/39Ar ages from the Karakoram Batholith and Shyok mélange, northern Pakistan, indicate late Tertiary uplift and southward displacement. Tectonophysics, v. 172, pp. 155-168.

Brooks, C., Hart, S.R., Wendt, I. (1972). Realistic use of two-error regression treatment as applied to rubidium-strontium data. Rev. Geophys. Space Phys., v. 10, pp. 551.

Brooks, C., Wendt, I. and Harre, W. (1968). A two-error regression treatment and its application to Rb-Sr and initial $^{87}Sr/^{86}Sr$ ratios of younger variscan granitic rocks from the Schwarzwald Massif, south-west Germany. J. Geophys. Res., v. 73, pp. 6071.

Brown, L. D., Zhao, W., Nelson, K.D., Hauck, M. and Alsdorf, D. (1996). Bright spots, structure and magmatism in southern Tibet from seismic reflection profiling. Science, v. 274, pp.1688-1691.

Burg, J.P. and Chen, G.M. (1984). Tectonics and structural zonation of southern Tibet. Nature, v. 311, pp. 219-223.

Carter, A. (1990). The thermal history and annealing effects in zircons from the Ordovician of North Wales. Nucl. Tracks Rad. Meas., v. 17, pp. 309-311.

Chandra, R., Upadhyay, R. and Sinha, A.K. (1999). Subduction and collision related magmatism in the Shyok Suture and eastern Karakoram. Paleobotanist, v. 48, pp. 183-209.

Chappel B.W. and White, A. J.R. (1974). Two contrasting granite types, Pacific Geol., v. 8, pp. 173-174.

Choudhary, A.K., Manickavasagam, R.M., Jain, A.K., Singh, S. and Chandra, K., 2004. National Facility on Geochronology and Isotope Geology at IIT, Roorkee- New data on Southern Granulite Massif. In: S.K. Aggarwal and P.G. Jaison (eds.), Eleventh ISMAS Workshop on Mass Spectrometry, October 7-12, Shilan Bagh, Shimla, Indian Society for Mass Spectrometry, pp. 51-58.

Choudhary, B.K. (1983). Structure, metamorphism and deformational history of the Pangong Tso area, Eastern Ladakh In: Geology of Indus Suture Zone of Ladakh (V.C. Thakur and K.K. Sharma eds.), Wadia Institute of Himalayan Geology, Dehradun, pp. 107-116.

Clarke, D. B. (1992). Granitoid rocks. Chapman and Hall, India, 283p.

Coryell, C.G., Chase, J. W. and Winchester, J.W. (1963). A procedure for geochemical interpretation of terrestrial rare earth abundance patterns, J. Geophys. Res., v. 68, pp. 559-566.

Coward, M.P., Jan, M.Q., Rex, D., Tarney, J., Thirlwall, M. and Windley, B.F. (1982) Geotectonic framework of the Himalaya of North Pakistan. J. Geol. Soc. London, v. 139, pp. 299-308.

Dainelli, G. (1933-34). La Serdei Terrani. Spoedizione Italina De Fellipi 1913-14, Ser. 2(2), Bologne.

de Sigoyer J., Chavagnac V., Blichert-Toft J., Villa I., Luais B., Guillot S., Mascle G. and Cosca M. (2000). Dating continental subduction and collisional thickening in NW Himalaya: Multichronometry of the Tso Morari eclogites. Geology, v. 28 (6), pp. 487-490.

De Terra, H. (1935). Geological studies in northwest Himalaya between Kashmir and the Indus valley, Mem. Connecticut. Acad. Arts. Sci., v. 8 (2), pp. 18-76.

Desio, A. (1977). On the geology of Deosai plateau, Kashmir. Mem. Acad. Naz. Lincei., v. 15, pp. 1-19.

Dewey, J.F. and Bird, J.M. (1970). Mountain belts and its new global tectonics. J.Geophys. Res., v. 75, pp. 2625-2647.

Dewey, J.F. and Burke, K. (1973). Tibetan, Variscan and Precambrian basement reactivation: products of continental collision. Jour. Geol., v. 81(6), pp. 683-692.

Dickin, A.P., 1995. Radiogenic Isotope Geology. Cambridge University Press. 1-452p.

Dodson, M.H. (1973): Closure temperature in cooling geochronological and petrological systems. Contrib. Mineral. Petrol., v. 40, pp.259-274.

Dodson, M.H. (1979): Theory of cooling ages. In: Jagert, E. and Hunziker, J.C. (eds). Lectures in Isotope Geology, pp. 194-202.

Dodson, M.H. (1981): Thermochronometry. Nature, v. 293, p. 606.

Dodson, M.H. (1985): Isotopic and palaeomagnetic evidence for rates of cooling, uplift and erosion. In: The Chronology of the Geological Record, Snelling, N.J. (ed.), Mem. Geol. Soc. Lond. Mem., pp.315-325.

Drew, F. (1857). The Jummoo and Kashmir Territories, London.

Dunlap, W.J. and Wysoczanski, R. (2002). Thermal evidence for early Cretaceous metamorphism in Shyok suture zone and age of the Khardung volcanic rocks, Ladakh, India. Jour. Asian Earth Sc., v.20, pp. 481-490.

Durani, I.R. and Bull, R.K. (1987). Solid State Nuclear Track Detection (Principles, Methods, and Applications), Pergamon Press, Oxford., 304p.

Faure, G. (1977). Principles of Isotope Geology, John Wiley, New York, pp. 1-589.

Fitzgerald, P.G., Sandiford, M., Barrett, P.J. and Gleadow, A.J.W. (1986). Asymmetric extension associated with uplift and subsidence in the Trans-Antarctic Mountains and Ross Embayment. Earth Planet. Sci. Lett., v. 81, p.67-71.

Fleischer, R.L., Price, P.B. and Walker, R.M. (1965a). The ion explosion spike and mechanism for formation of charged particle tracks. J. Appl. Phys., v. 36, pp. 3645-3652.

Fleischer, R.L., Price, P.B. and Walker, R.M. (1965b). Effects of temperature, pressure and ionization on the formation and stability of fission tracks in minerals and glasses. Jour. Geophy. Res., v.70, pp. 1497-1502.

Fleischer, R.L., Price, P.B. and Walker, R.M. (1975). Nuclear tracks in solids: Principle and applications. University of California press, Berkley, 605p.,

Flood, R. H. and Vernon, R. H. (1988). Microstructural evidence of orders of crystallization in granitoid rocks. Lithos, v. 21, pp. 237-245.

Frank., W., Thoni, M., Purtscheller., F., 1977. Geology and petrography of Kulu-south Lahul area. Colloq. Int CNRS Himalaya, v. 268, pp. 147-160.

Gaetani, M. and Garzanti, E. (1991). Multicyclic history of the northern India continental margin (Nortwestern Himalaya). Am. Assoc. Petrol. Geol. Bull., v. 75, pp. 1427-1446.

Galbraith, R. F. (1981). On statistical models for fission track counts. Math. Geol., v.13. pp. 471-488.

Gansser, A. (1964). Geology of the Himalayas, Wiley-Interscience, London. 289p.

Gansser, A. (1977). The great suture zone between Himalaya and Tibet: a preliminary account. Coll. Int. Cent. Nat. Res. Sci., v. 33. pp. 181-192.

Gansser, A. (1980). The significance of the Himalayan suture zone, Tectonophysics, v. 62, pp. 37-52.

Gleadow, A., J.W. and Duddy, I.R. (1981). A natural long track annealing experiment for apatite, Nucl. Tracks, v. 5, pp. 169-174.

Gleadow, A.J.W. (1978). Comparison of fission dating methods: effects of anisotropic etching and accumulated alpha damage. U. S. Geol. Surv. Open File Report, pp. 78-701 and pp. 143-145.

Gleadow, A.J.W. (1981). Fission Track dating methods: What are the real alternatives? Nucl. Tracks, v. 5, pp. 3-14.

Gleadow, A.J.W. and Lovering, J.F. (1975). Fission Track dating methods. Dept. Geol. Sch. Earth Sci., Uni. Melbourne, Publ. 3, 93p.

Gleadow, A.J.W., Duddy, I.R., Green, P.F., and Lovering, J.F. (1986). Confined fission track lengths in apatite: a diagnostic tool for thermal history analysis. Contrib. Mineral. Petrol., v. 94, pp. 405-415

Gleadow, A.J.W., Hufford, A.J. and Quafie, R.D. (1976). Fission track dating of zircon: improved etching techniques. Earth Planet. Sci. Lett., v. 33, pp.273-276.

Govindraju, K. (1989). Compilation of working values and sample description for 272 geostandards. Geostandards newsletter, vol. XIII, page 15 of Appendix I.

Green P. F. (1981). A new look at statistics in the fission track dating, Nucl. Tracks, v. 5, pp. 77-86.

Green, P.F. (1988). The relation between track shortening and fission track reduction in apatite: Combined influence of influence of inherent instability, annealing anisotropy, length bias and system calibration. Earth and Planet. Sci. Lett, v. 89, pp. 335-352.

Green, P.F., Duddy, I.R., Gleadow, A.J.W. and Lovering, J.F. (1989). Apatite fission track analysis as a paleotemperature indicator for hydrocarbon exploration. In N. D. Naeser and Th. McCullon (eds.), Thermal History of sedimentary Basins. Springer- verlag, New York, pp. 181-195.

Guillot, S., Garzanti, E., Baratoux, D., Marquer, D., Maheo, G., de Sigoyer, J. (2003). Reconstructing the total shortening history of the NW Himalaya. Geochem. Geophy Geosystems, v. 4 (7), pp. 1-22.

Hall, A. (1987). Igneous Petrology, Longman, London, 354p.

Hammerstrom, J., and Zen, E. An (1986): Aluminium in Hornblende: an empirical igneous geobarometer. American Mineralogist, v.71, pp. 1297-1313.

Hanson, G.N. (1989). An approach to trace element modeling using a simple igneous system as an example. In: The Geology and Geochemistry of Rare Earth Elements (Lipin and McKay – eds). Reviews in Mineralogy, v. 21, pp. 79-97.

Harrison T.M., Armstrong, R.L., Naeser, C.W., and Harakal, J.E. (1979). Geochronology and thermal history of the Coast plutonic complex near Prince Rupert, British Columbia, Canada. J. Earth Sc. v. 16, pp. 400-410.

Hawthorne, F.C. (1983). The crystal chemistry of the amphiboles. Canadian Mineralogists, v. 21, pp.173-480.

Hayden, H.H. (1907). The geology of the provinces of Tsang and U in central Tibet, Mem. Geol. Surv. Ind., v. 36 (2), pp. 121-203.

Heim, A. and Gansser, A. (1939). Central Himalaya- Geological observations of Swiss Expedition 1936. Mem. Soc. Helve. Sci. Nat., v. pp.73, 245.

Helz, R.T. (1982). Phase relations and compositions of amphiboles produced in studies of the melting behaviour of rocks. Mineralogical Soc. America, Reviews in Mineralogy, V 9B, pp. 279-346.

Herren, E. (1987). Zanskar Shear Zone: Northeast-southwest extension within the Higher Himalaya (Ladakh, India). Geology, v. 15, pp. 409-413.

Hodges, K.V. (2000). Tectonics of the Himalaya and southern Tibet from two decades perspectives. Geol. Soc. Amer. Bull., v. 112, pp. 324-350.

Hodges, K.V., Parrish, R.R., and Searle, M.P. (1996) Tectonic evolution of the central Annapurna Range, Nepalese Himalayas. Tectonics v. 15, pp. 1264-1291.

Honegger, K., Dietrich, V., Frank, W., Gansser, A., Thoni, M. and Trommsdorff, V. (1982). Magmatism and metamorphism in the Ladakh Himalaya (the Indus-Tsangpo suture zone). Earth Planet. Sci. Lett., v. 60, pp. 253-292.

Hurford, A.J. (1985). On the closure temperature for fission tracks in zircon. Nucl. Tracks Rad. Meas., v. 10, pp. 415-421.

Hurford, A.J. (1986). Cooling and uplift patterns in Leptonite Alps South Central Switzerland and age of vertical movement on the Insubric fault line. Contrib. Mineral. Petrol., v. 92, pp. 413-427.

Hyden, H.H. (1907). The geology of the provinces of Tsang and U in central Tibet, Mem. Geol. Surv. Ind., v. 36 (2), pp. 121 - 203.

Irvine, T. N. and Baragar, W.R.A. (1971). A guide to the chemical classification of the common volcanic rocks. Can. J. Earth Sci., v. 8, pp. 523-548.

Jain, A.K. and Anand, A., (1988). Deformational and strain patterns of an intracontinental collision ductile shear zone - an example from the Higher Garhwal Himalaya. J. Struct. Geol. v. 10 (7), pp. 717 734.

Jain, A.K. and Manickavasagam, R.M. (1993). Inverted metamorphism in the intracontinental ductile shear zone during Himalayan collision tectonics. Geology, v. 21, pp. 407-410.

Jain, A.K., Kumar, D., Singh, S. Kumar, A and Lal, N. (2000). Timing, quantification and tectonic modeling of Pliocene Quaternary movements in the NW Himalaya: evidences from fission track dating. Earth Planet. Sci. Lett., v. 179, pp. 437-451.

Jain, A.K., Manickavasagam, R.M., and Singh, S. (2002). Himalayan Collision Tectonics. Gondwana Research Group Memoir no. 7, 114 p.

Jain, A.K., Singh, S., Manickavasagam, R.M., Joshi, M. and Verma, P.K. (2003). HIMPRORF Programme: Integrated Studies on Geology, Petrology, Geochronology and Geophysics of the Trans- Himalaya and Karakoram. Mem. Geol. Soc. Ind., No. 53, pp. 1-56.

Johnson, M.C. and Rutherford, M.J. (1989). Experimental calibration of the aluminium in hornblende geobarometer with application to Long valley Caldera (California) volcanic rocks. Geology, v. 17, pp. 837-841.

Kasuya, M. and Naeser, C.W. (1988). The effects of a damageon fission track annealing in zircon. Nucl. Tracks Radiat. Meas., v. 14, pp. 477-480.

Klootwijk, C.T., Gee, J.S., Peirce, J.W., Smith, G. M. and McFadden, P.L. (1992). An early India-Asia contact: Paleomagnetic constraints from Ninetyeast Ridge., ODP Leg 121. Geology, v. 20, pp. 395-398.

Kohn B.P., Shagam, R., Banks, P.O. and Burkley, E.A. (1984): Mesozoic-Pleistocene fission track ages on rocks of the Venenzuelan Andes and their tectonic implications. Mem. Geol. Soc. Amer., v. 162, pp. 365-384.

Krishnaswami, S., Lal, D., Prabhu, N. and Mc-Dougall, D. (1974). Characteristics of fission tracks in zircons: applications to geochronology and cosmology. Earth Planet. Sci. Lett., v. 22, p.51.

Kumar, A., Lal, N. Jain, A.K. and Sorkhabi, R.B. (1995). Late Cenozoic- Quaternary Thermo- Tectonic history of Higher Himalayan Crystallines (HHC) in Kishtwar- Padar-Zanskar region, NW Himalaya: Evidences from fission track ages. J. Geol. Soc. Ind., v. 45, p.375.

Kumar, D. (1999). Fission track Zircon-apatite ages and exhumation of the Himalayan Metamorphic Belt (HMB) along Beas- Sutlej Valleys, Himachal Pradesh. Unpublished Ph.D. thesis. Kurukshetra University, Kurukshetra, India. p. 34.

Laird, J. and Albee, A.L. (1981). Pressure, temperature and time indicators in mafic schists: their application to redonstructing the polymetamorphic history of Vermont. American Jour. Sci., v. 281, pp. 127-175.

Lal, N. (1991). Solid state nuclear track detector -I: Track characteristics and formation mechanisms. Phy. Edu., v. 7 (4), pp. 289-299.

Lal, N. (1992a). Solid state nuclear track detector -II: Various subfields. Phy. Edu., v. 8 (3), pp. 311-319.

Lal, N. (1992b). Solid state nuclear track detector -III: Application in science and technology. Phy. Edu., v. 8, No. 4, pp. 359-366.

Lal, N., Mehta, Y. P., Kumar, D., Kumar, A., and Jain A.K. (1999). Cooling and exhumation history of the Mandi Granite and adjoining tectonic units, Himachal Pradesh, and estimation of closure temperature from external surface of zircon. In: Jain, A.K. and Manickavasgam, R.M. (Ed.) Geodynamics of the NW Himalayas. Gondwana Research Group, Mem. No. 6, pp. 207-216.

Laslett, G.M., Gleadow, A.J.W. and Duddy, I.R. (1984). The relationship between fission track length and track density in apatite. Nuclear Tracks, v. 9, pp. 29-38.

Laslett, G.M., Gleadow, A.J.W. and Duddy, I.R. (1984). The relationship between fission track length and track density in apatite. Nuclear Tracks, v. 9, pp. 29-38.

Laslett, G.M., Kendall, W.S., Gleadow, A.J.W. and Duddy, I. R. (1982). Bias in measurement of fission track length distributions. Nuclear Tracks, v. 6, pp. 79-85.

Laubacher, G., and Naeser, C.W. (1994). Fission- track dating of granitic rocks from the Eastern Cordillera of Peru: evidences for Late Jurassic and Cenozoic cooling. Jour. Geol. Soc. London, v. 151, pp. 473-483.

Le Fort, P. (1975). Himalayas: The collided range. Present knowledge of the continental arc. Amer. J. Sci., v. 275, pp. 1-44.

Le Fort, P. (1986). Metamorphism and magmatism during the Himalayan collision. In: Cowards, M.P. and Ries, A.C. (Eds.) Collision Tectonics. Geol. Soc. London., Spec. Publ. No. 19, pp. 159-172.

Le Fort, P. (1989). The Himalayan orogenic segment. In Tectonic Evolution of the Tethyan Region, (A.M.C. Sengor ed.) Kluwer Academic Publishers, pp. 289-386.

Le Maitre, R.W., Bateman, P., Dudek, A., Keller, J. and others (1989). A classification of igneous rocks and glossary of terms. Blackwell, Oxford.

Leake, B.E. (1971). On aluminous and edenitic hornbledes. Mineralogical Magazine, v. 38, pp. 389-407.

Leake, B.E. (1978). Nomenclature of amphiboles. Mineralogical Magazine, v.42, pp. 533-563.

Leake, B.E., Woolley, A.R., Birch, W. D. and others (1997). Nomenclature of Amphiboles: Report of the Subcommittee on amphiboles of the International Mineralogical association Commission on New Minerals and Mineral Names. Mineralogical Magazine, v. 61, pp. 295-321

Leech, M.L., Singh, S., Jain, A.K., Klemperer, S.L. and Manickavasagm, R.M. (in review): The onset of India-Asia Continental collision: early, steep, subduction required by the timing of UHP metamorphism in the western Himalaya. Earth Planet Sci. Letters.

Ludwig, R. K. (2003). Isoplot - A Geochronological Toolkit for Microsoft Excel. Berkeley Geochronology Center. Sp. Publ., No. 4. 71p.

Lydekker, R. (1880). Geology of Ladakh and neighbouring districts being fourth notice of Geology of Ladakh and neighbouring territories. Rec. Geol. Surv. Ind. v. 3 (1), pp. 26-59.

Lydekker, R. (1883). Geology of Kasmir and Chamba territories and the British district of Khagan. Mem. Geol. Surv., v. 22, pp. 108-112.

Masuda, A. (1962). Regularities in variation of relative abundance of Lanthanide element and an attempt to analyze separation-index patterns of some minerals. J. Earth. Sc. Nagoya Univ., v.10, pp. 173-187.

Mc Intyre, G.A., Brooks, C.,Comspston, W. and Turek, A. (1966): The statistical assessment of Rb-Sr isochrons. Jour. Geophys. Res., v. 71, pp. 5459.

Middlemiss, C.A. (1910). Sections in Pir Panjal range and Sind valley, Kashmir, Rec. Geol. Surv. Ind., 41 (2), pp. 86-115.

Molnar, P. (1987). Inversion of profiles of uplift rates for the geometry of dip-slip faults at depth, with examples from Alps and Himalayas. Annales Geophysicae, 5B, pp. 6630-670.

Molnar, P. and Tapponier, P. (1975). Cenozoic tectonics of Asia: Effects of a continental collision. Science, v. 189, pp. 419-426.

Naeser C.W., and Faul, H. (1969). Fission track annealing in apatite and sphene. J. Geophys. Res., v. 74, pp. 705-710.

Naeser, C.W. (1979). Fission track dating and geologic annealing of fission tracks. In: Jager, E. and Hunziker, J.C. (eds.) Lectures in Isotope Geology, Springer- Verlag, Heidelberg, p. 154-169.

Naeser, C.W., Izett, G.A. and Obradovich, J.D. (1980). Fission track and K-Ar ages of natural glasses. U. S. Geol. Surv. Bull., v. 1489, pp. 1-31.

Nagpaul K.K., Mehta, P.P. and Gupta, M.L. (1974). Annealing studies on radiation damages in biotite, apatite and sphene and corrections to fission track ages. Pure Appl. Geophys. v. 112, pp. 131-139.

Nelson, K.D., Zhao, W., Brown, L.D., Kuo, J., Che, J., Xainwen, L., Klemperer,S., Makovsky., Y., Ni J. Nabelak, J., Chen, L., Handong, T., Wenbo, W., Hauk, M., Alsdorf, D., Ross, A., Cogan, M., Wu, C., Sandvol, E.A. and Edwards, M. (1996). Partially molten middle crust beneath southern Tibet: Synthesis of Project INDEPTH Results. Science, v. 274, 1684-1688.

O' Brien, P.J., Zotov, N. Law, R., Khan, M.A., and Jan, Q.M. (2001). Coesite in Himalayan eclogite and implications for models of India-Asia collision. Geology, v. 29, pp. 435-438.

Parrish, R.R. (1983). Cenozoic thermal evolution and tectonics of the Coast Mountains of British Columbia 1. fission track dating apparent uplift rates, and patterns of uplift. Tectonics, v. 2, p. 601-632.

Parrish, R.R. (1985). Some cautions which should be exercised when interpreting fission track and other dates with regard to uplift rate calculations. Nucl. Tracks v. 10, pp. 425.

Patariach, P. and Achache, J. (1984). India-Eurasia collision chronology has implications for crustal shortening and driving mechanism of plates. Nature, v. 311, pp. 615-621.

Patel, R.C., Singh, S., Asokan, A., Manickavasagam, R.M. and Jain, A.K. (1993) Extensional tectonics in the collisional Zanskar Himalayan belt In: Treloar, P.J. and Searle, M.P. (Eds.) Himalayan Tectonics. Geol. Soc. London Spec. Publ. No. 74, pp 445-459.

Pearce, J.A., Harris, N.B.W., and Tindle, A.G. (1984). Trace element discrimination diagrams for the tectonic interpretation of granitic rocks. Journal of Petrology, v. 25, Part 4, pp. 956-983.

Pessago, E.A., Jr. (1977). Lower cretaceous radiolaruian biostratigraphy of the Great Valley sequence and Franciscan Complex, California Coast ranges. Cushman Found. Foram. Res. Spec. Pub. No. 15, pp.87.

Philibert, J. (1963). X- ray optics and X ray microanalysis. Academic Press, New York, 329p.

Pilgrim, G.E. and West, W.D. (1928). The structure and correlation of Simla rocks. Mem. Geol. Surv. India, v. 53, 1-140p.

Potts, P. J. (1987). A handbook of Silicate rock analysis. Blackie, London.

Powell, C. McA. (1979). A speculative tectonic history of Pakistan and surroundings: some constraints from the Indian Ocean. In: Geodynamics of Pakistan (Farah, H. and DeJong, K.H. – eds.), Geological Survey of Pakistan, Quetta, pp. 5-24.

Raase, P. (1974). Al and Ti contents of hornblende, indicators of pressure and temperature of regional metamorphism. Contributions to Mineralogy and Petrology, v. 45, pp. 231-236

Rai, H. 1980. Origin and emplacement of Ladakh Batholith: present day knowledge. Him. Geol., v.10, pp.78-93.

Rai, H. (1982). Geological evidence against Shyok Paleo-Suture, Ladakh Himalaya, Nature v. 297, pp 142-144.

Rai, H. (1983). Geology of the Nubra Valley and its significance on the evolution of Ladakh Himalaya. In: Geology of Indus Suture Zone of Ladakh (V. C. Thakur and K. K. Sharma eds.), Wadia Institute of Himalayan Geology, Dehradun, pp. 79-97.

Rai, H. (1986). The geology of Ladakh Trans-Himalaya and re-evalution of paired metamorphic belt, Ophiolites and Indian Plate Margin, (eds.), N.C. Ghose and S. Vardarajan, pp. 49-61.

Rai, H. 1980. Origin and emplacement of Ladakh Batholith: present day knowledge. Him. Geol., v.10, pp.78-93.

Rai, H., and Pande, I.C. (1978). Geology of Kargil igneous complex, Jammu and Kashmir, India; Recent Res. Geol., v. 5, pp. 219-228.

Raiverman, V. and Misra, V.N. (1974). Sura tectonic axis, Kargil area, Ladakh, geol. Min. Met. Soc. Ind., Golden Jub (Abs.).

Rutherford, E. and Soddy, F.(1902.). The radioactivity of thorium compounds II. The cause and nature of radioactivity. J. Chem. Soc. Lond. V.81, pp837-860.

Raz, U. and Honneger, K. (1989). Magmatic and tectonic evolution of the Ladakh block from field studies. Tectonophysics, v. 161, pp. 107-118.

Rickwood, P.C. (1989). Boundary lines within petrologic diagrams which use oxides of major and minor elements. Lithos, v. 22, pp. 247-263.

Rolland Y. (2002). From intra-oceanic convergence to post-collisional evolution: example of the India-Asia convergence in NW Himalaya, from Cretaceous to present, India Asia convergence in NW Himalaya. Jour. of Virtual Explorer, v.8, pp. 177-199.

Rolland, Y., Pecher, A. and Picard, C. (2000). Middle Cretaceous back-arc formation and arc evolution along the Asian margin: the Shyok Suture Zone in Northern Ladakh (NW Himalaya). Tectonophysics, v. 325, pp. 145-173.

Rollinson, H. (1993). Using geochemical Data: evaluation, presentation, interpretation, Longman, London., 351p.

Rowley, D.B. (1996). Age of initiation of collision between India and Asia: a review of the stratigraphic data. Earth Planet. Sci. Lett., v. 145, pp. 1-13.

Rutherford, E. and Soddy, F. (1902). The radioactivity of thorium compounds II. The cause and nature of radioactivity. J. Chem. Soc. Lond. v. 81, pp. 837-860.

Sachan, H.K., Mukherjee, B. K., Ogasawara, Y., Maruyama, S., Ishida, H., Muko, A. and Yoshioka, N. (2004). Discovery of coesite from Indus Suture Zone, (ISZ), Ladakh, India: Evidence for deep subduction, Euro. J. Mineral v. 16, pp. 235-240.

Sahni, M.R. and Bhatnagar, N.C. (1958). Fresh water mollusca and plant remains from the Tertiaries of Kargil, Rec. Geol. Surv. Ind., v. 87 (3), pp. 467-476.

Sahni, M.R. and Shastri, V.V. (1956). A monograph of Obiotolina found in the Indian continent (Chitral, Gilgit, Kashmir, Tibet and Burma), Pal. Ind. (N.S.) Geol. Surv. Ind., v. 33 (3), pp. 1-44.

Satouru, K., Ahmed, T., Tsuyoshi, T., Bagati, T.N., Mishra, M., Kumar, R., Islam, R. and Khanna, P.P. (2001). Early cretaceous radiolarians from the Indus suture zone, Ladakh, North India. News of Osaka Micropalcontologists, Spl. Vol. No. 12, pp. 257-270.

Scharer, U., Hamet, J., and Allegre, C.J. (1984). The Transhimalaya (Gangdese) plutonism in the Ladakh region: a U-Pb and Rb-Sr study, Earth planet. Sci. Lett., v. 67, pp. 327-339.

Schlup, M., Carter, A., Cosca, M., and Steck, A. (2003). Exhumation history of eastern Ladakh revealed by 40Ar/39Ar and fission track ages: the Indus river- Tso Morari transect, NW Himalaya. Jour. Geol. Soc. London, v. 160, pp. 385-399.

Schlup, M., Carter, A., Cosca, M., and Steck, A. (2003). Exhumation history of eastern Ladakh revealed by 40Ar/39Ar and fission track ages: the Indus river- Tso Morari transect, NW Himalaya. Jour. Geol. Soc. Lond., v. 160, pp. 385-399.

Schmidt, M.W. (1992). Amphibole composition in tonalite as a function of pressure: an experimental calibration of Al barometer. Contrib. Mineral Petrol., v. 110, pp. 304- 310.

Searle, M.P. (1983). Stratigraphy, structure and evolution of the Tibetan-Tethys zone in Zanskar and the Indus suture zone in the Ladakh Himalaya. Trans. R. Soc. Edinburg Earth Sci., v. 73, pp. 205-219.

Searle, M.P. (1991). Geology and tectonics of the Karakoram mountains. John Wiley & Sons. Chichester. 385p.

Searle, M.P., Metcalfe, R.P., Rex, A.J. and Norry, M.J. (1993). Field relations, petrogenesis and emplacement of the Bhagirathi leucogranite, Garhwal Himalaya In: Treloar, P.J. and Searle, M.P. (Eds.) Himalayan Tectonics. Geol. Soc. Lond., Spec. Publ. No. 74, pp. 429-444.

Searle, M.P., Cooper, D.J.W. and Rex, A.J. (1988). Collision tectonics of the Ladakh-Zanskar Himalaya. Phil. Trans. R. Soc. London, A-326, pp. 117-150.

Searle, M.P., Crawford, M.B. and Rex, A.J. (1992). Field relation, geochemistry, origin and emplacement of Baltoro granite, Central Karakoram. Trans. R. Soc. Edinburg (Earth Sci.), v. 83, pp. 519-538.

Searle, M.P., Parrish, R.R., Tirul, R. and Rex, D.C. (1990). Age of crystallization and cooling of the K2 gneisses in the Baltoro Karakoram. Jour. Geol. Soc. Lond., v. 147, pp. 603-606.

Searle, M.P., Weinberg, R.F. and Dunlap, W.J. (1998). Transpressional tectonics along the Karakoram fault Zone, northern Ladakh. In: Holdsworth, R.E., Strachan, R.A. and Dewey, J.E. (Eds.) Continental Transpressional and Transtensional Tectonics. Geol. Soc. Lond., Spec. Publ. No. 135, pp. 307-326.

Shah S.K., Sharma, M.L., Gregan, J.T. and Tara, C.S. (1976). Stratigraphy and structure of the Indus Suture Belt, Himalayan Geology, v. 6, pp.534-556.

Shankar, R., Padhi, R. N., Parkash, G., Thusu, J. L. and Wangdus, C. (1974). Recent geological studies in Upper Indus Valley and the concept of Plate-Tectonics, inter. Semi. Tectonics metallogeny of South East Asia and Far East. Geol. Surv. Ind. (Abs).

Sharma K. K., Sinha, A. K., Baghasanian, G. P. And Gukasian, R. C. (1978). Potassium-Argon dating of Dras Volcanics and Ladakh granite, northwestern Himalay. Him. Geol., v.8, pp.288-295, .

Sharma, K.K. and Choubey, V.M. (1983). Petrology, geochemistry and geochronology of the southern margin of the Ladkah Batholith between Upshi and Chumathang. In: Thakur,V.C. and Sharma, K.K. (Eds.) Geology of Indus Suture Zone of Ladakh Wadia Institute of Himalayan Geology, Dehradun, pp. 41-60.

Sharma, K.K. and Gupta, K.R. (1983). Calc-alkaline island arc volcanism in Indus- Tsangpo suture zone. In: Geology of Indus Suture Zone of Ladakh (V. C. Thakur and K. K. Sharma eds.). Wadia Institute of Himalayan Geology, Dehradun, pp. 71-78.

Sharma, K.K. and Kumar, S. (1978). Contribution to the geology of Ladakh, Northwestern Himalaya. Himalayan Geology, v. 8, pp. 252-287.

Sharma, K.K., Choubey, V.M. and Chatti, H.R. (1991). Geological setting of the ophiolites and magmatic arc of Lohit Himalaya (Arunachal Pradesh) India with special reference to their petrochemistry. In: Sharma, K.K. (Ed.) Geology and Geodynamic Evolution of the Himalayan Collision Zone, Part-2, Phys. Chem. Earth, v. 18, pp. 221-236

Shusheng, L., and Feng, Z. (1988). Fission track ages and uplift rates of south Xiang (Tibet) region. Scientia Sinica, v. 31, p. 971-975.

Sinclair, H.D., and Jaffey, N. (2001). Sedimentology of the Indus Group, Ladakh, northern India: implications for the timing of initiation of paleo-Indus River. Jour. Geol. Soc. London, v. 158, No. 1, pp. 151-162.

Singh I.B. (1999). Tectonic control on sedimentation in Ganga Plain Foreland Basin constraints on Siwalik sedimentation models. In: Jain, A.K. and Manickavasagam, R.M. (Eds.) Geodynamics of the NW-Himalaya. Gondwana Res. Group Mem. 6, pp. 247-262.

Singh, B. (1993). Geological set up of a part of the Ladakh Granitoid Complex, Ladakh Himalaya. J. Him. Geol., v. 4 (1), pp. 57-62.

Singh, S., Barley, M.E., Jain, A.K. and Kumar, R. (2003). U-Pb SHRIMP ages and depth of emplacement of Ladakh batholith, Eastern Ladakh India, Himalayan Tectonics (The HIMPROBE Results), pp. 36-39.

Singh, S., Leech, M.L., Jain, A.K., Manickavasagam, R.M. (2003). U-Pb SHRIMP ages from the Ultrahigh-Pressure Tso-Morari Crystallines, eastern Ladakh, India. Himalayan Tectonics (HIMPROBE Results). pp 31-35.

Sorkhabi, R. B., Stump, E., Foland, K. A., and Jain, A. K. (1996). fission track and $^{40}Ar/^{39}Ar$ evidence for episodic denudation of the Gangotri granites in the Garhwal Himalaya, India. Tectonophysics, v. 260, p. 187-199.

Sorkhabi, R.B., Jain, A.K., Nishimura, S., Itaya, T., Fukui, S., Lal, N., and Kumar, A. (1997). Cooling age record of domal uplift in the core of the Higher Himalayan Crystallines (HHC), Southwest Zanskar, India. Proc. Indian Acad. Sci. (Earth Plant. Sci.), v. 106 (3), pp 169-179.

Sorkhabi, R.B., Jain, A.K., Nishimura, S., Itaya, T., Lal, N., Manickavasagam, R.M., and Tagami, T., (1994): New age constraints on the cooling and unroofing history of the Trans Himalayan Ladakh batholith (Kargil area), N. W. India. Proc. Indian Acad. Sci. (Earth Plant. Sci.), v. 103 (1), pp. 83-97.

Sorkhabi, R.B., Jain, A.K., Nishimura, S., Itaya, T., Lal, N., Manickavasagam, R.M., and Tagami, T., (1994). New age constraints on the cooling and unroofing history of the Trans Himalayan Ladakh batholith (Kargil area), N. W. India. Proc. Indian Acad. Sci. (Earth Plant. Sci.), v. 103 (1), pp 83-97.

Sorkhabi, R.B., Stump, E., Foland, K.A. and Jain, A.K. (1999). Tectonic and cooling history of the Garhwal Higher Himalaya (Bhagirathi valley): constraining from thermochronological data In: Jain, A.K. and Manickavasagam, R.M. (Eds.) Geodynamics of the NW-Himalaya. Gondwana Res. Group Mem. No. 6, pp. 217-235.

Sorkhabi, R.B., Stump, E., Foland, K.A., and Jain, A.K. (1996). fission track and $^{40}Ar/^{39}Ar$ evidence for episodic denudation of the Gangotri granites in the Garhwal Himalaya, India. Tectonophysics, v. 260, p. 187-199.

Spear, F. S. (1981). An experimental study of hornblende stability and compositional variability in amphibolite. Am. J. Sc., v. 10, pp. 317-325.

Srikantia, S.V., Ganeshan, T.M. and Wangdus, C. (1982). A note on the tectonic framework of and geological set-up of the Pangong-Chusul sector, Ladakh Himalaya. Jour. Geol. Soc. India, v. 23, pp. 354-357.

Srimal, N. (1986). India-Asia collision: Implications from the geology of the eastern Karakoram. Geology, v. 14, pp. 523- 527.

Steiger, R. And Jaeger, E. (1977). Subcommission on geochronology: Convention on the use of decay constants in geo-and cosmo-chronology. Earth Planet. Sci. Letters, v. 36, pp. 359-362.

Stoliczca, A. (1866). Summary of the geological observations during a visit to the provinces Rupshu Karnap, South Ladakh, Zanskar, Sumdo Dras and Western Tibet. Mem. Geol. Surv. India, v. 5, pp. 337-354.

Streckeisen, A.L. (1976). To each plutonic rock its proper name. Earth Sci. Rev., v. 12, pp. 1-33.

Sun, S.S., and McDonough, W.F. (1989). Chemical and isotopic systematics of oceanic basalts: implications for mantle compositions and processes. From Saunders, A. D. and Norry, M.J. (eds.) 1989, Magmatism in the Ocean Basins, Geol. Soc. London, Special Publication No. 42, pp. 313-345.

Tagami T., Ito, H. and Nishimura, S. (1990). Thermal annealing characteristics of spontaneous fission tracks in zircon. Chem. Geol (Isot. Geosci Sect.), v. 80, pp. 159-169.

Tagami, T., Lal, N., Sorkhabi, R.B., Ito, H. and Nishimura, S. (1988). Fission track dating using external detector method: a laboratory procedure, Mem. Fac. Sci., Kyoto Univ., Ser. Geol. Min., v. 53, p. 1-30..

Tahirkheli, R.A.K., Mattauer, F., Proust, F., and Tapponnier, P. (1979). The India-Eurasia Suture zone in Northern Pakistan: Synthesis and interpretation of recent data at plate scale. In: Geodynamics of Pakistan (A. Farah and K.A. DeJong, eds.) Geol. Surv. Pakistan, Quetta, pp. 125-130.

Tapponier, P. and Molnar, P. (1976). Slip-line field theory and large scale continental tectonics. Nature, v. 264, pp. 405-410.

Thakur, A. K. and Lal, N. (1993). Determination of Zeta calibration factor for fission track dating of apatite, sphene and zircon. Indain Journal of Pure and Applied Phy., v. 31, pp. 241-250.

Thakur, V.C. (1981). Regional framework and geodynamic evolution of the Indus-Tsangpo suture zone in the Ladakh Himalaya. Trans. R. Soc. Edinb. Earth. Sci. v. 72, pp. 89-97.

Thakur, V.C. (1983). Paleotectonic evolution of Indus- Tsangpo Suture zone in Ladakh and Southern Tibet. In: Geology of Indus Suture Zone of Ladakh (V. C. Thakur and K. K. Sharma eds.), Wadia Institute of Himalayan Geology, Dehradun, pp. 71-78.

Thakur, V.C. (1987). Development of major structures across the northwestern Himalaya, India. Tectonophysics, v. 135, pp. 1-13.

Thakur, V.C. (1993). Geology of the Western Himalaya. Pergamon Press, Oxford. 355p.

Thakur, V.C. and Jain, A.K. (1975). Some Observations on deformation, metamorphism and tectonic significance of the rocks of some parts of the Mishmi Hills, Lohit district (NEFA), Arunachal Pradesh. Him. Geol., v. 5, pp. 339-363

Thakur, V.C. and Misra, D.K. (1984). Tectonic framework of Indus and Shyok Suture zones in eastern Ladakh, northwestern Himalaya. Tectonophysics, v. 101, pp. 207-220.

Theil, K. and Herr, W. (1976). The 238U spontaneous fission decay constant re-determined by fission tracks, earth. Planet. Sci. Lett. v. 30, pp. 50-56.

Thomas, W.M. and Earnst, W.G. (1990). The Aluminium content of hornblende in calc alkaline granitic rocks: a mineralogic barometer calibrated experimentally to 12 kbar. In Spencer, R.J. Ming Chou, I. (eds) Fluid mineral interaction: a tribute to H.P. Eugster, Geochem Soc., Sp. Publ. v. 2, pp. 59- 63.

Thompson, T. (1852). Western Himalaya and Tibet. Foorye and Co., Honrietta Sreet, Cavent Garden, London

Upadhyaya, R., Sinha, A.K., Chandra, R. and Rai, H. (1999). Tectonic and magmatic evolution of the Eastern Karakoram, India, Geodynamica Acta, v. 12, pp.25-34.

Upadhyaya, R., and Sinha, A.K. (1998). tectonic evolution of Himalayan Tethys and subsequent Indian Plate subduction along Indus Suture Zone. In: Proc. Indian Science Academy (INSA), New Delhi 64A: 659-683.

Valdiya, K.S. (1980). Two intracrustal boundary thrusts of the Himalaya Tectonophysics, v 66, 323-348.

Valdiya, K.S. (1989). Trans-Himadri intracrustal fault and basement upwarps south of Indus-Tsangpo Suture Zone. In: Malinconico, L.L. and Lillie, R.J. (Eds.) Tectonics of the western Himalaya. Geol. Soc. Amer. Spec. Paper 232, pp.153-168.

Veevers, J.J., Powell, C.M. and Johnson, B.D. (1975). Greater India's place in Gondwanaland and in Asia. Earth Planet. Sci. Lett., v. 51, 383-387.

Virdi, N.S., Thakur, V. C. and Kumar, S. (1977). Blueschist facies metamorphism from the Indus suture zone of Ladakh and its significance. Him. Geol., v. 7, pp. 479-482.

Virdi, N.S., Thakur, V. C. and Kumar, S. (1977). Blueschist facies metamorphism from the Indus suture zone of Ladakh and its significance. Him. Geol., v. 7, pp. 479-482.

Wadia, D.N. (1937). The Cretaceous volcanic series of Astor-Deosai, Kashmir and its intrusion. Rec. Geol. Surv. India, v. 72, pp. 151-161.

Wagner, G. A. and Reimer, M., and Jager, E. (1977). Cooling ages derived by apatite fission track, mica Rb/Sr and K/Ar dating, the uplift and cooling history of the Central Alps. Memorie degli Instituti di Geologica e Mineralogia dell, Universita di Padova, p. 30.

Wagner, G. and Van Den Haute, P. (1992). Fission Track Dating. Solid Earth Sci. Lib. Vol. 6, Kluwer Acad. Pub. Derdrecht, 285p.

Wagner, G.A. and Reimer, M., and Jager, E. (1977). Cooling ages derived by apatite fission track, mica Rb/Sr and K/Ar dating, the uplift and cooling history of the Central Alps. Memorie degli Instituti di Geologica e Mineralogia dell, Universita di Padova, p. 30.

Weinberg, R.F., and Dunlap, J. (2000). Growth and deformation of the Ladakh Batholith, Northwest Himalayas: Implications for timing of continental collision and origin of calc-alkaline batholiths, J. Geol., v. 108, pp. 303-320.

Wilson, M. (1989). Igneous Petrogenesis, Unwin Hyman, London. 466p.

Windley, B. F. (1995). Geochronologic constraints on syntaxial development in the Nanga Parbat region, Pakistan. Tectonics, v. 15, pp. 1292-1308.

Windley, B.F. (1983). Metamorphism and tectonics of the Himalaya. J. Geol. Soc. London, v. 140, pp. 849-865.

Wones, D. R. (1981). Mafic silicates as indicators of intensive variables in granite magmas. Mining Geology, v. 31, pp. 191-212.

Wones, D. R., and Gilbert, M. C. (1982). Amphiboles in the igneous environment. Mineralogical Society of America Reviews in Mineralogy, v. 9B, pp. 355-390.

Yin, A. and Harrison, T. M. (2000). Geological evolution of the Himalayan- Tibetan Orogen. Annu. Rev. Earth. Planet. Sci., v. 28, 211-280.

York, D. (1966). Least Square fitting of a straight line. Canad. Jour. Phys. v. 44, pp. 1079-86..

York, D. (1969). Least square fitting of a straight line with correlated errors. Earth Planet. Sci. Letters. Earth Planet. Sci. Letters, v. 5, pp. 320-324..

Zaun, P. E. and Wagner, G.A. (1985). Fission track stability in zircons under geological conditions. Nucl. Tracks, v. 10, pp. 303-307.

Zeitler, P. K. (1985). Cooling history of the NW Himalaya, Pakistan. Tectonics, v. 4, p.127.

Zen, E-AN (1986). Aluminium enrichment in silicate melts by fractional crystallization: some mineralogic and petrographic constraints. Jour. Petrol., v. 27, pp. 1095-1117.

Zhao, W. and Nelson, K.D. and Team, P.I. (1993). Deep Seismic reflection evidence for continental underthrusting beneath southern Tibet. Nature. v. 366. pp. 557-559

APPENDIX

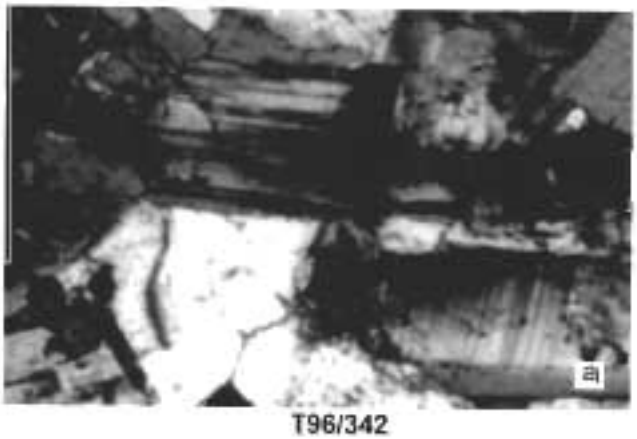

T96/342

NS 62-112

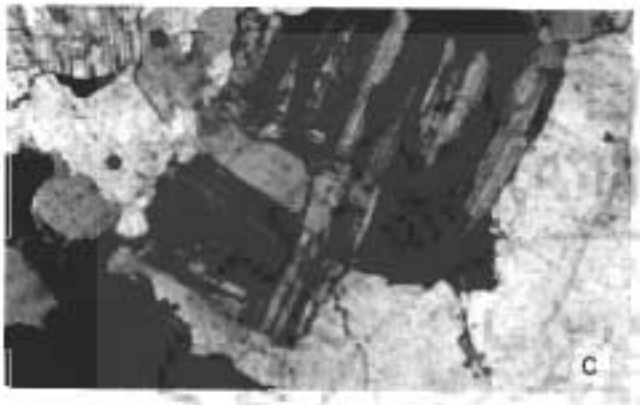

K-2

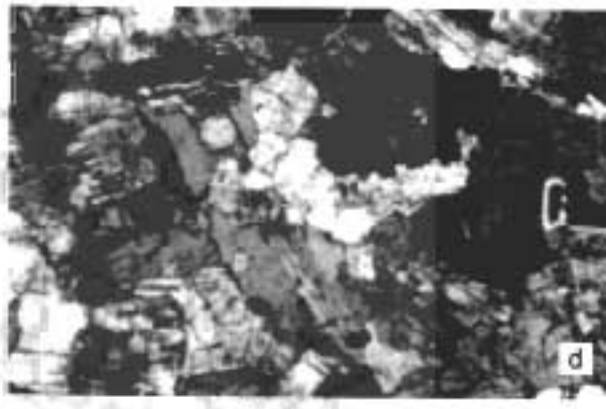

LB 17/35

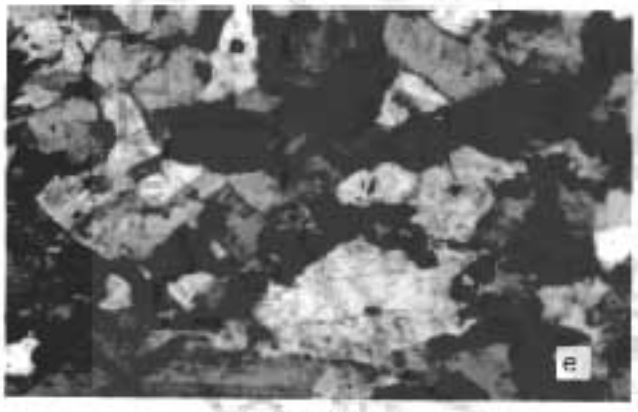

LB 18/36

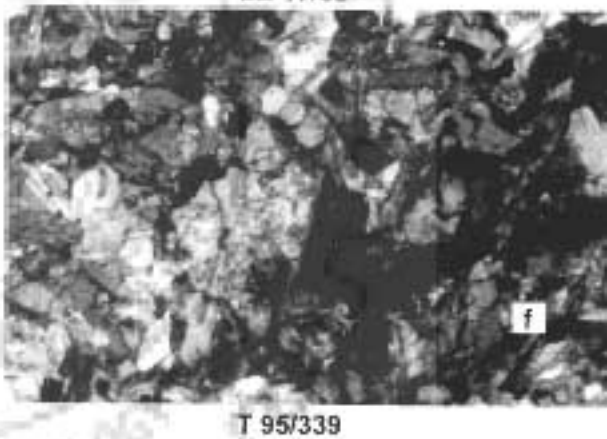

T 95/339

Photomicrographs of representative diorites from the Ladakh Batholith (all the photographs are in X-Nicol position with 20X magnification).

(a) T 96/342 : Coarse grained, plagioclase (oligoclase-andesone, 18°-20° extinction), quar biotite, hornblende. Also showing alteration.

(b)NS 62/112:Coarse grained, plagioclase, quartz, opaques, showing interlocking textu

(c) K-2 : Very coarse grained, plagioclase, quartz, hornblende, orthoclase and opaq

(d) LB 17/35 :Fine to medium grained, biotite, hornblende, plagioclase, orthoclase and quartz (very few), hypidioophic texture.

(e) LB 18/36: Medium grained hypidiomorphic texture, orthoclase, plagioclase, hornblen biotite, opaques very few.

(f) T 95/339.: Fine to medium grained, biotite, hornblende, plagioclase, orthoclase and quartz (very few), hypidiomorphic texture.

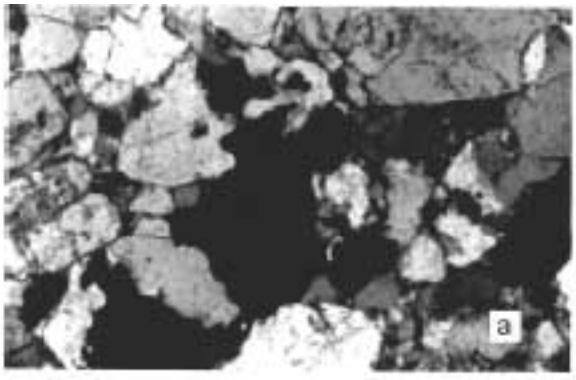

NS 3/5

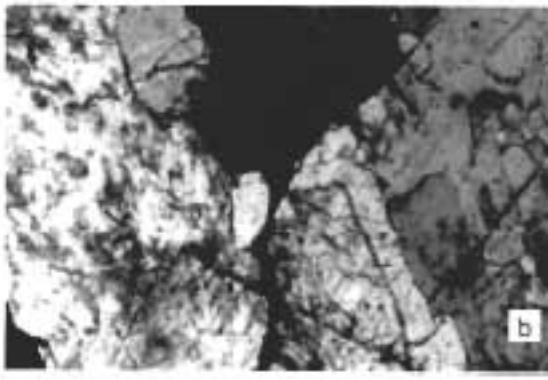

LB 10/28

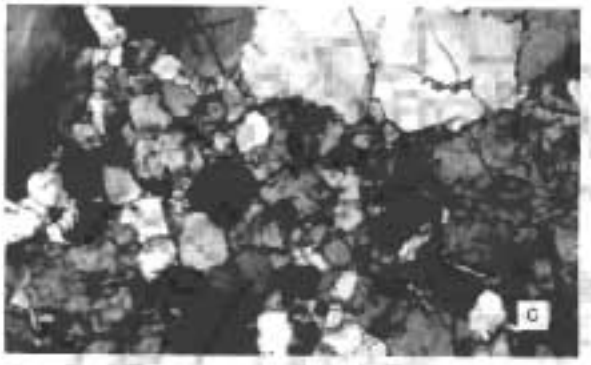

LB 14/32

LB 8/23

T 100/350

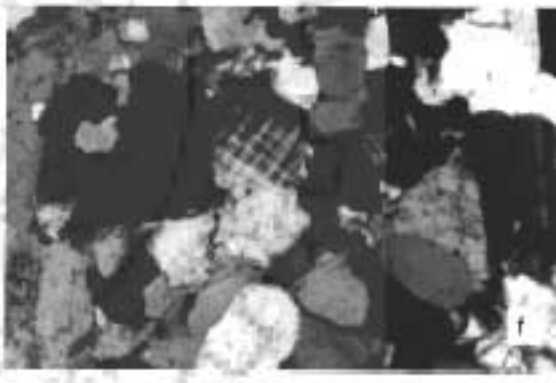

NS 5/12

Photomicrographs of representative granodiorite from the Ladakh Batholith (all the photographs are in X-Nicol position with 20X magnification).

(a)NS3/5: Medium to coarse grained, showing K-feldspar, quartz, hornblende and biotite with hypidiomorphic texture. Part of myrmekitic texture on right-bottom side of the picture.

(b)LB10/28: Coarse grained with K-feldspar, quartz, hornblende and biotite with intergranular texture.

(c)LB 14/32: Medium to fine grained, showing hypidiomorphictexture with grains of quartz, orthoclase hornblende and biotite with opaques.

(D)LB 8/23: Medium to coarse grained with quartz, plagioclase, orthoclase, biotite and opaque, hypidiomorphic texture. Also showing myrmekitic texture.

(E)T100/350: Medium grained with quartz, orthoclase, hornblende, biotite and opaque with hypidiomorphic texture. Apatite is also present.

(F)NS5/12: Medium to fine grained with orthoclase, quartz, microcline, hornblende and green biotite.

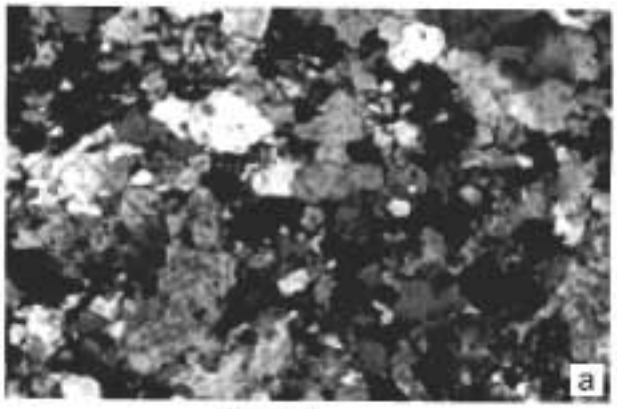

NS 1/2

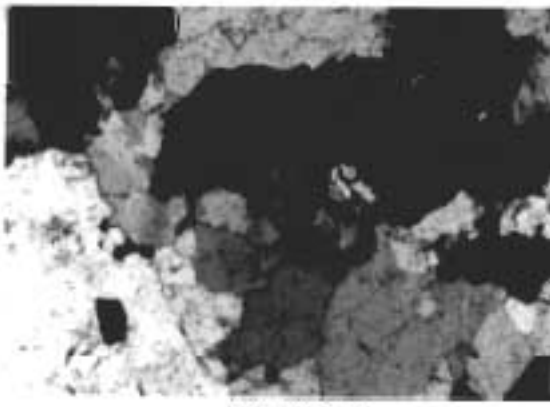

NS 84/159

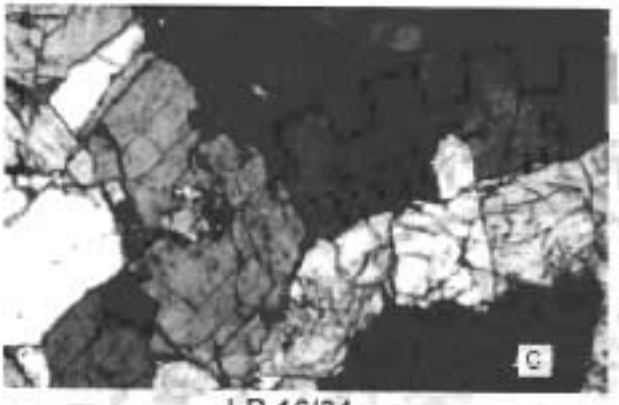

LB 16/34

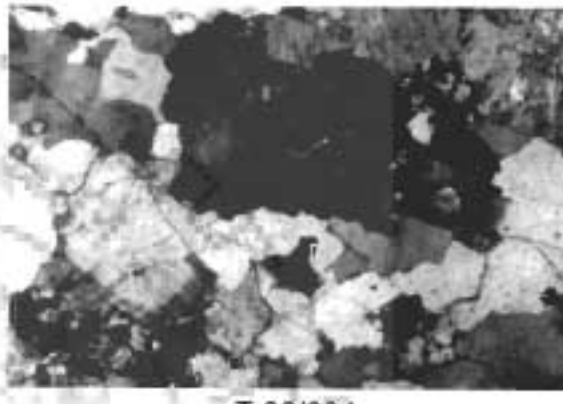

T 93/334

NS 72/128

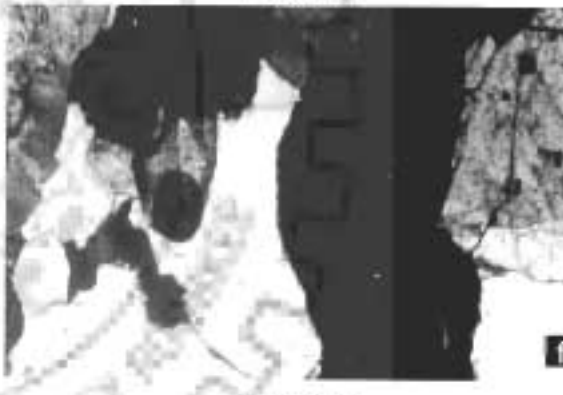

T 96/341

Photomicrographs of representative granite from the Ladakh Batholith (all the photographs are in X-Nicol position with 20X magnification).

(a)NS1/2: Fine to medium grained, hypidiomorphic texture with orthoclase, qua hornblende and biotite.

(b)NS 84/159: Medium to coarse grained interlocking texture, orthoclase, quartz, hornblende, and biotite.

(c)LB 16/34: Medium to coarse grained, orthoclase, quartz, hornblende and biotite

(d)T 93/334 : Medium grained hypidiomorphic texture, orthoclase, microcline, quartz and biotite, graphic texture. Also showing alteration.

(e)NS 72/128: Medium grained hypidiomorphic texture, orthoclase, quartz, biotite and hornblende. Also show myrmekitic intergrowth.

(f)T 96/341: Coarse grained, showing orthoclase, quartz, hornblende, biotite and opaque.